Optimisation and mechanistic investigations of visible light photocatalysed decarboxylative Giese reaction using Bi_2WO_6 semiconductor nanoparticles

Mohammed Nasser Ahmed Althuqbi

Doctor of Philosophy

University of York

Chemistry

August 2024

Abstract

Heterogenous photocatalysts based on semiconducting metal oxides serve as a sustainable alternative to expensive and toxic transition metal (photo)catalysts in organic transformations including C-C coupling. Upon absorption of a photon, semiconductors can generate excited states and charge carriers (holes and electrons) which at the surface undergo redox reactions with substrates to generate radicals.

This project aims to use visible light (405–410 nm) as the energy source to drive an organic transformation (C-C bond formation) via radical chemistry in acetonitrile. Modified Bi_2WO_6 with Pt nanoparticles was used as a model catalyst in oxidative decarboxylation of phenylacetic acid to yield benzyl radical which underwent a Giese reaction with electron-deficient alkenes. The yield of Giese adduct was 60-70 %. The main byproducts were bibenzyl, benzyl alcohol, and benzaldehyde from GC-MS. In the absence of Pt, no reaction occurred and 0.15wt% Pt was found to be optimum loading amount. Photoluminescence spectroscopy (PL) spectra showed that the platinized catalyst exhibited slightly less recombination compared to the bare catalyst, while time-resolved photoluminescence (TRPL) showed no significant difference in the lifetime of carriers in both catalysts suggesting that the role of Pt is not only to improve charge separation but also to contribute to catalysis.

Mechanistic studies focussed on catalyst surface chemistry and morphology and their influence on activity and selectivity. It was found that acid binds to the catalyst stronger than alkene or product. NMR showed that the presence of small amounts of water as source for protons on the catalyst is crucial for high reactivity and selectivity. Isotopic labelling and kinetic isotope studies showed that C-H bond formation of Giese adduct is not the rate-determining step. The selectivity of benzyl radicals with different electron withdrawing alkenes did not match that of the analogous homogeneous reactions, suggesting that the reaction occurs on the surface rather than in bulk solution. Morphological investigation revealed catalyst with high crystallinity showed better activity and selectivity compared to low crystalline (high surface area) catalysts.

The reaction scope was later explored with a variety of substrates, including different acids, e.g., 4-chlorophenylacetic acid, 4-methoxyphenylacetic acid and alkenes, e.g., acrolein, maleic anhydride, maleimide, showing the promising use of Bi_2WO_6 as a photocatalyst for obtaining valuable chemicals using the Giese reaction.

Dedication

To my mother, who grew, taught, and developed me and who had been a source of encouragement and inspiration to me throughout my life, a very special thank you for supporting me and including me in your prayers during my graduate studies. Indeed, losing you in the first year of my PhD broke my heart, and I almost lost my passion. However, I promised you I would continue my dream and make you proud of me. I miss you.

Declaration

I declare that this thesis is a presentation of my original work I conducted during my study as the University of York. This work has not previously been presented for a degree or other qualification at this University or elsewhere. All sources are acknowledged as references.

Acknowledgements

I would like to thank my supervisors Professor Victor Chechik and Professor Richard Douthwaite for their unwavering support; without them, I would not have been able to complete this research and write my thesis, and I would not have made it through my PhD degree. I am especially grateful to Professor Victor Chechik for his invaluable assistance in the modelling of the adsorption study.

A special thanks to my wife and my kids for supporting me during my study.

I would like to thank Dr. Connor Murrill for helping to perform some scanning electron microscopy data, Dr. Karl Heaton for GC-MS analysis, Dr. Laurence Abbott for time-resolved photoluminescent measurement, Dr. Heather Fish for deuterium NMR data, and Dr. Richard Gammons for microwave training.

A huge thanks to Jazan University for giving me the opportunity to study abroad, paying my tuition, and providing funding for living.

My thanks also extend to members of the VC and RED group members for helping me during my study through a scientific discussion.

Covid-19 pandemic impact statement

The Covid-19 epidemic affected my PhD project and thesis significantly. Lack of in-person interactions and training prevented me from carrying lab work for my project. Also, the limited access to labs, instruments rooms and other university facilities affected the experimental work timeline that was originally planned for the project.

Table of contents

List of figures

List of tables

List of schemes

Motivation

Nature has inspired humans throughout history to devise elegant solutions to challenging issues in their daily lives. Sunlight can drive chemical processes in the same manner that natural photosynthesis does. Photocatalysis is a nature-inspired method of collecting and converting sun energy to enable complex chemical transformations.

The utilisation of heterogeneous photocatalysts has gained substantial interest in the ongoing search for greener alternatives to thermally heated chemical reactions and soluble photoredox catalysts. More precisely, metal oxide-based semiconductors (MOSC) have emerged as attractive options for replacing costly and hazardous transition metal-based complexes and organic dyes and reducing waste.

Organic synthesis with MOSC is used in this study to promote sustainability and efficient chemical transformations. MOSC research brings together fundamental science, practical applications, and sustainable technology. It is a broad field with substantial implications, and it represents a way to efficient, environmentally friendly chemical synthesis. Furthermore, understanding MOSC and their mechanisms in organic synthesis aids in the development of efficient and ecologically friendly organic synthesis methodologies.

This work will begin with a brief background in catalysis before moving on to the project's more specific goals.

Chapter 1: Introduction

1.1 Catalysis: What is a catalysed reaction?

A catalyst is defined as a substance utilised in chemistry to accelerate a chemical reaction without undergoing consumption or incorporation into products.

Catalysts have the ability to accelerate chemical reactions by providing an alternative pathway that has a reduced activation energy (Figure 1.1). The quantity of energy needed to initiate a chemical reaction is referred to as activation energy. Failure to meet the activation energy will result in the absence of the reaction. Once the activation barrier has been overcome, the reaction will proceed. Although catalysis does not change the position of reaction equilibrium, catalysis is most often performed under non-equilibrium conditions to support selective reaction.

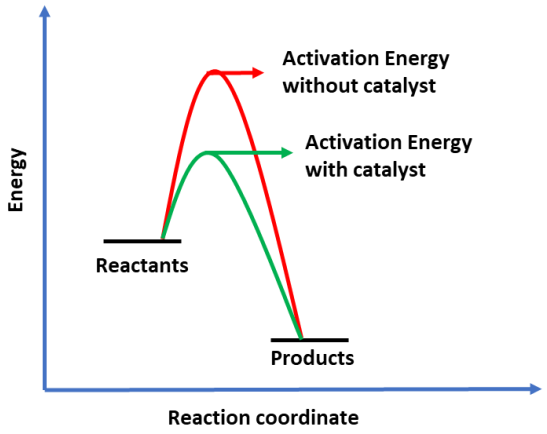

Figure 1.1: A diagram showing the difference between catalysed and noncatalyzed reaction.

1.2 Photocatalysis vs thermal catalysis

Thermal heterogeneous catalysis often relies on the reactivity of low-coordination sites on the surface of solids. These sites offer a pathway for molecules to rearrange their bonds during the breaking and reforming process necessary for a chemical reaction. Although catalysis can lower the activation energy of a reaction, the outcome of the reaction is influenced by temperature because of the differing rates of mechanistic steps that control selectivity. The operational temperature of the majority of industrially significant heterogeneous catalytic reactions typically exceeds several hundred degrees Celsius. This not only increases rates but the expense and environmental consequences of the process, and also has the potential to result in undesirable outcomes such as catalyst coking or sintering.[1]

On the other hand, photocatalysis harnesses the energy provided by light and facilitates chemical transformations usually via redox processes. It could offer a significant benefit by addressing the difficulties related to thermal reactions, and is widely recognised as using a renewable energy source either directly or via the generation of renewable electricity to power artificial light sources such as LEDs.[2]

From a thermodynamic perspective, the primary distinction between photo- and thermal catalysis lies in the fact that the latter is limited to speeding up spontaneous reactions that occur with a decrease in Gibbs free energy. Consequently, depending on the specific process, it may be necessary to raise the temperature and pressure to ensure that this criterion is satisfied. Photocatalysis can enable uphill processes, such as water splitting and CO_2 reduction with water by effectively storing some of the light energy in the new chemical bonds. Technically speaking, it is more accurate to label these processes as photosynthetic rather than photocatalytic. However, they are sometimes grouped together under the broader term of photocatalysis.[1,3]

An illustration of mild conditions that can be used to drive uphill reactions photochemically was provided by Vaiano et al., who noted that CH_4 formation (from CO_2 reduction) became observable for thermal catalytic reactions utilising 1 wt.% Pd/TiO_2 catalyst at temperatures exceeding 400 °C, with a rate of approximately 3.7 μmol h^{-1} g^{-1}. In contrast, CH_4 formation rate exhibited a substantial increase when the identical sample was exposed to UV light, even at 140 °C, culminating in a steady state value of 64 μmol h^{-1} g^{-1}.[4]

In conclusion, photocatalysis has the potential advantage of being a greener approach with mild conditions to achieve chemical transformation compared to thermal catalysis, which relies on costly transition metals and high heat.

1.3 Photocatalysis

The utilisation of coal and other hydrocarbons as energy sources for the purpose of synthesis has led to a substantial rise in carbon dioxide emissions on a global scale within the Earth's atmosphere. The emissions in question have had a significant impact on many pollution problems, notably the discharge of hazardous substances like mercury (Hg) resulting from coal burning, as well as the release of methane emissions. Therefore, the utilisation of alternative renewable energy sources is important. One potential alternative source that can be considered is solar energy. The Earth is subjected to a significant influx of solar energy on a daily basis.

The field of photocatalysis has been established since the 1970's but the proposal to use solar energy to drive chemical reactions is much older.[5] The main fundamental principle

of photolysis is the use of materials (photocatalyst) that can absorb light generating an excited state that induces electron transfer (redox processes). The use of excited states is fundamentally different to thermal based catalysis offering the opportunity to develop new reactivity in addition to improving sustainability.

Similarly, to thermal chemistry, photocatalysis can be further divided into homogenous and heterogeneous depending on the phases of the reactants and photocatalyst.

1.3.1 Heterogeneous vs homogeneous photocatalysis

Homogenous photocatalysts can efficiently use specific wavelengths of LED light and have achieved excellent results in chemical synthesis due to their well-defined electronic structure (HOMO and LUMO) and excited states for redox chemistry arising from tailored ligand design. However, they are mainly composed of expensive transition metals and ligands such as polypyridyl complexes of ruthenium and iridium and require separation from the reaction products.[6] In principle, heterogeneous photocatalysts can address these disadvantages by using Earth-abundant metal oxides and providing a simple route for product separation. However, characterising active sites in heterogeneous catalysts is difficult. Also, reproducing heterogenous reactions is also challenging. (Table 1.1) compares the advantages and disadvantages of homogeneous and heterogeneous photocatalysis.

Table 1.1: Comparison between homogenous and heterogenous photocatalysis.

Homogenous photocatalyst	Heterogenous photocatalyst
• Catalyst and reactants are in same phase, typically the liquid phase.	• Catalyst and reactants are in different phase, solid-liquid or solid-gas.
• Typically have only one type of reactive sites.	• Have many active sites with different reactivity.
• Usually expensive transition metals and many synthesis steps involved.	• Usually less expensive and can be synthesised quickly.
• High selectivity.	• Low selectivity and need modification.

• Rate of reaction is high. • Difficult to separate from reactants and products. • Low stability and not recyclable. • Characterised by their small energy gap (HOMO-LUMO).	• Rates are not fast compared to homogenous. • Easy to separate form reactants and products by physical process. • High stability and recyclable. • Their bandgap (VB-CB) energy varies.

1.3.2 Heterogenous photocatalysis

Heterogeneous photocatalysis (HetPC) has been a subject of fundamental and applied studies since the groundbreaking work of Fujishima and Honda in 1972 on the photocatalytic splitting of water into H_2 and O_2, and particularly for the oxidation of organic contaminants in air or water. A redox reaction using PC is characterised by the transfer of one or more electrons from a reductant (electron donor) to an oxidant (electron acceptor). Both the oxidant and reductant species undergo chemical change due to electron transfer, and can generate radicals for organic synthesis.[7]

There are many examples on heterogenous photocatalysts including single-atom heterogeneous photocatalysts,[8] lead-halide perovskites,[9] cadmium chalcogenide (CdS, CdSe, CdTe),[10] graphitic carbon nitrides (g-CN)[11], covalent organic frameworks (COFs)[12], metal organic frameworks (MOFs)[12,13], and relevant to this work, metal oxide semiconductors (MOSC).[14–16]

1.3.3 Metal oxide semiconductors (MOSC)

Metal oxide semiconductors (MOSC) are a class of heterogenous photocatalysts which has been used commonly due to their photochemical stability, ease of use, low toxicity and cost. They are a class of materials with an electronic structure between insulators and conductors with a bandgap on the order of 2-3 eV commensurate with the energy of solar light (Figure 1.2).

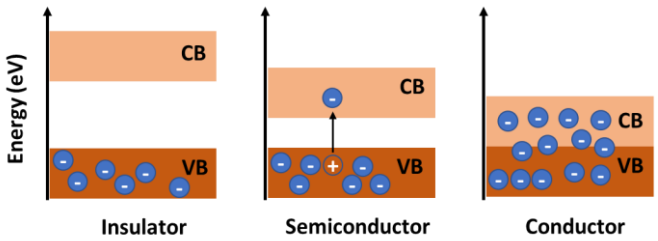

Figure 1.2: An illustration showing difference between insulator (large bandgap, Eg > 3.5 eV), semiconductor (3.5 eV > Eg > 0.1 eV) and conductor (with no gap between VB and CB). VB stands for valence band and CB stands for conduction band.

Typical examples include titanium dioxide (TiO_2), bismuth vanadate ($BiVO_4$), bismuth tungstate (Bi_2WO_6), and zinc oxide (ZnO). These MOSC are made of earth abundant elements and their stability and availability has led to their extensive use in many applications such as water splitting, organic pollutant degradation, energy storage and chemical transformations. Moreover, a great advantage of using heterogenous MOSC is the ability to remove them easily from the reaction mixture via simple physical techniques such as filtration and centrifugation.

Semiconductor oxides exposed to UV, near-UV, or visible light at room temperature and ambient pressure can generate mobile electrons and holes for redox reactions of species adsorbed on the active surface. The relative energetics of generated electron-hole potentials and the redox chemistry of substrates is a key consideration for determining if redox chemistry will occur, however many other factors control the outcome of reactions including electron-hole recombination and the surface chemistry of catalysts. The electron-hole recombination is a problem for these catalysts and this can be remedied by applying a potential as early shown by Fujishima and Honda in 1972 in the photoelectrochemical splitting of water to O_2 and H_2. This process incorporating TiO_2 photocatalyst involved the exposure of a single crystal TiO_2 anode, connected to a platinum black cathode, and irradiation with an externally applied potential to reduce electron-hole recombination. TiO_2 possesses a bandgap of 3.2 eV, necessitating the utilisation of high-energy UV photons with wavelengths below 400 nm. The ultraviolet (UV) component of sunlight comprises around 4-6% of the total solar radiation, limiting the efficiency of the process if using sunlight as the light source, but this demonstration has inspired the field over the intervening 50 years for developing other MOSC which can operate using visible light.[17]

1.3.4 Electronic structure of MOSC: bandgap

MOSC have electronic structure with bandgap energies (E_g) ranging from approximately 2-3 eV (Figure 1.3). These bandgaps values fall in UV and visible light spectrum region.

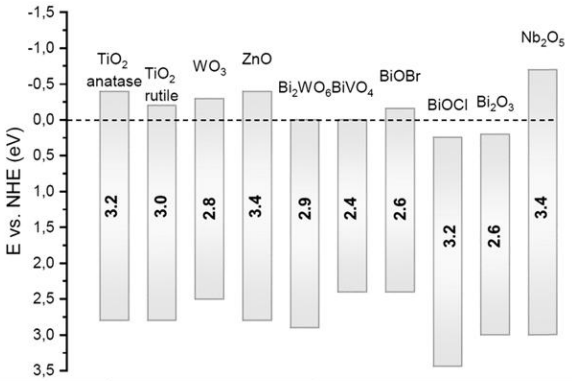

BG E (eV)	Wavelength, λ (nm)	SC
2.4 < Eg < 2.7	450 < λ < 500	$BiOBr$, $BiVO_4$, Bi_2O_3
2.7 < Eg < 3.1	400 < λ < 450	TiO_2 rutile, WO_3, Bi_2WO_6
3.1 < Eg	λ < 400	TiO_2 anatase, ZnO, BiOCl, Nb_2O_5

Figure 1.3: Bandgap energies of selected MOSC at pH 7 along with their corresponding wavelength.[18] Reused and modified with permission from ref (18). BG stands for bandgap, SC stands for semiconductor.

The MOSC bandgap is defined as the difference between the valence band (VB) maximum and conduction band (CB) minimum. The region between these two bands is forbidden, although defects introduce states within the bandgap. When a photon energy is equal to or greater than the bandgap energy, excitation of an electron (e^-) to the CB occurs leaving a positive hole (h^+) in the VB. This process eventually leads to oxidation, via h^+, and reduction, via e^-, when they are in interfacial contact with substrate at the surface (Figure 1.4). For a certain photocatalyst to do both redox reactions, the VB potential must be more positive than oxidation potential of target species whereas the CB reduction potential must be more negative than reduction potential of target species.

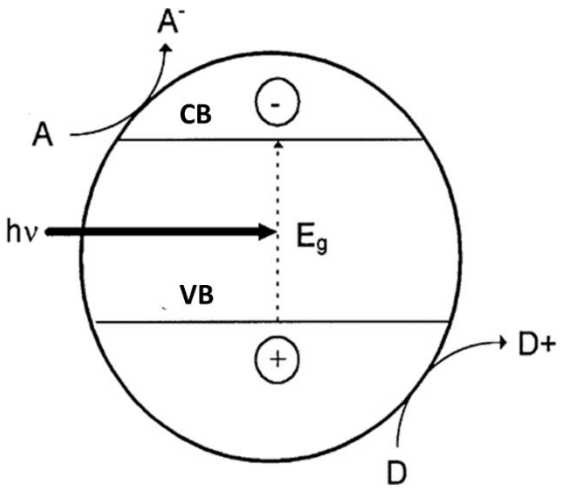

Figure 1.4: Simplified diagram showing VB-CB of MOSC and their representative oxidation-reduction pathways under irradiation.[19]

1.3.5 Visible-light activated vs. UV-light activated MOSC

The use of high energy photons such as UV is suitable for large bandgap semiconductors such as TiO_2. However, this high energy irradiation causes the formation of undesired reactive species in many reaction media including water. These highly reactive species, also called reactive oxygen species (ROS), such as hydroxyl radicals ($^{\cdot}OH$) and superoxide radicals ($O_2^{\cdot-}$) can react either with substrates (starting materials and products) or other organic molecules present in reaction media leading to non-selective reactions and consequently, leading to low product selectivity. Moreover, UV photons can react with and activate directly organic molecules present in solution resulting in bond breaking (free radicals) even without the need of photocatalyst. Thus, using visible light is an alternative option to increase reaction selectivity and also use a greater proportion of the solar spectrum.

Visible light irradiation can activate smaller bandgap MOSC, such as Bi_2O_3 (E_g = 2.6 eV), however charge separation is often limited by recombination at bulk and surface defects. To overcome this obstacle and also improve catalysis, the modification on MOSC is the key. One modification strategy is to use metal nanoparticles on the photocatalyst surface to trap electrons and catalyse reductive redox processes. A discussion on this topic will be in section 1.5.3.

1.4 Application of heterogenous metal oxide semiconductor in chemistry

MOSC have been extensively applied in many important fields including water splitting, CO_2 reduction, organic pollutant degradations and most recently organic synthesis.

1.4.1 Water splitting and CO_2 reduction

Metal oxide semiconductors have been employed in H_2 production via water splitting and hydrocarbons fuels via CO_2 reduction. For water splitting, the uphill energetics of the reaction and its positive Gibbs energy (~ 237 kcal/mol) make water splitting challenging to accomplish.[20] Overall water splitting requires that under standard conditions the top of the VB is more positive than the oxidation potential of H_2O to O_2 (1.23 V vs. NHE) and the bottom of the CB is more negative than the reduction potential of H^+ to H_2 (0 V vs. NHE). In general, total water splitting over a photocatalyst particle can be promoted by combining the photocatalyst with an appropriate metal cocatalyst to produce an active redox site for proton reduction to H_2 (Figure 1.5.) The co-catalyst can capture the photoinduced electrons promoting charge separation in semiconductor and also can promote proton reduction to hydrogen. The role of co-catalyst will be discussed later in section 1.5.3.

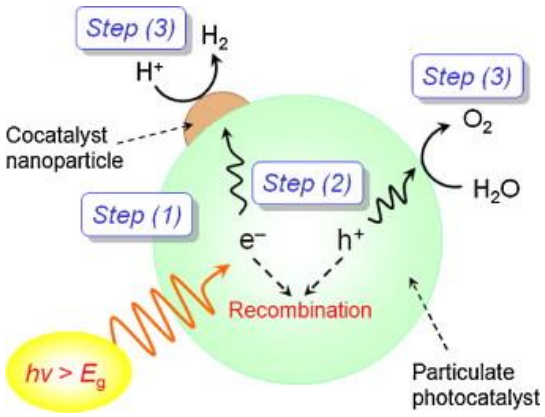

Figure 1.5: Schematic diagram of water splitting for H_2 production, step 1) where a suitable light energy matches semiconductor (SC) bandgap result in electron-hole (e^-/h^+) separation, step 2) migration of e-h to surface of SC, step 3) e is captured by cocatalyst and converts protons to H_2 gas, step 4) water is oxidised by holes producing O_2.[21] Reused with permission from ref (21).

For CO_2 reduction to hydrocarbons and oxygenates, strong C=O σ- and π-bonds must be broken requiring a significant amount of energy. H_2O abundance and non-toxicity make it a common reducing agent in photocatalytic CO_2 conversion processes mimicking photosynthesis. The photo-generated electrons in the conduction band should have a more negative potential than the product/CO_2 redox potential in order to have enough energy to reduce the adsorbed CO_2 molecule to HCOOH, HCHO, CH_3OH, and CH_4 etc. In a similar vein, to produce protons, electrons and oxygen, the potential of the photo-generated holes in the valence band must be higher than the O_2/H_2O redox potential (Figure 1.6).

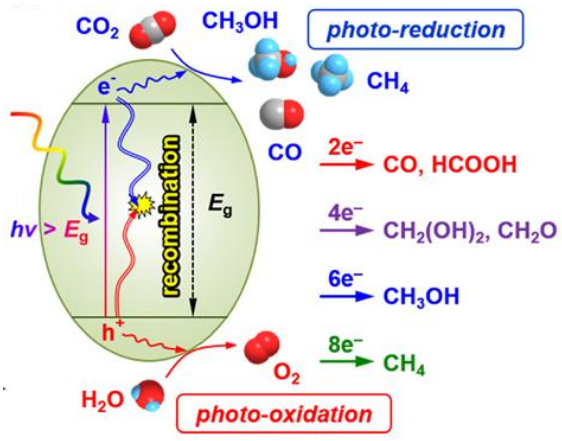

Figure 1.6: CO_2 reduction mechanism over MOSC.[22] Reused with permission from ref (22).

Both water splitting and CO_2 reduction are similar with respect to the oxidation catalysis requiring the oxidation of water. Reduction of H^+ to H_2, and CO_2 to organic products have similar potentials resulting in similar thermodynamics, however the kinetics of CO_2

reduction are much more challenging because multiple intermediates and products are involved.

1.4.2 Pollutant degradation

MOSC have been used extensively in environmental remediation eliminating various pollutant such as pesticides, dyes, and other industrial waste, e.g. pharmaceuticals and agrochemicals. Long-term environmental persistence of some pesticides, particularly in water, may have negative consequences. The main oxidising chemical pieces in pollutant degradation are reactive oxygen species (ROS), e.g., OH radicals. Figure 1.7 illustrates a typical degradation mechanism. The ideal product of degradation is complete mineralisation to CO_2, however incomplete oxidation can give rise to compounds that may also be toxic.

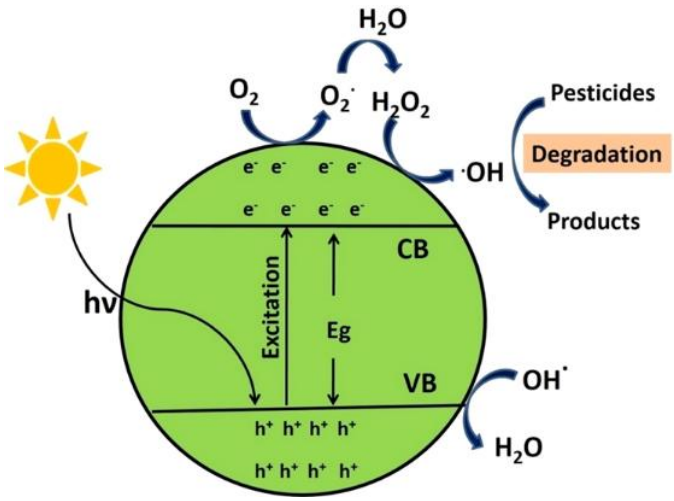

Figure 1.7: mechanism of pesticide degradation over MOSC.[23] Reused with permission from ref (23).

1.4.3 Organic synthesis

Organic chemicals play a crucial role in the production of medicines, insecticides, and food additives, that are fundamental to our daily lives. Traditional industrial processes sometimes necessitate severe operating conditions, such as elevated temperature and pressure. Therefore, the development of photocatalytic synthesis methods that utilise light as an energy source to facilitate chemical processes under less severe reaction conditions is greatly sought after.

The utilisation of heterogeneous photocatalysis for the synthesis of organic molecules is increasing and becoming of importance. The research field is currently in a state of ongoing development, with ongoing basic research being conducted in this area. So far,

it is evident that a variety of valuable organic molecules can be created using this method, both through processes involving oxidation and reduction.[24]

1.4.3.1 Alcohol oxidation

From bulk chemicals to fine chemicals to pharmaceuticals, selective oxidation reactions form a significant fraction of synthetic processes in chemical industry.[25] Selective oxidation catalysts based on MOSC can be used to prepare a wide range of chemicals and intermediates including alcohols, epoxides, aldehydes, ketones and organic acids. TiO_2 is the most popular photocatalyst that has been used in such applications due to its low cost, low toxicity, thermo and chemo stability and most important, it is a very efficient photocatalyst.

In their work on the photocatalytic oxidation of benzyl alcohol into benzaldehyde, Shinya et al. demonstrated high conversion > 99% and selectivity > 99% on a TiO_2 photocatalyst by O_2 under visible light irradiation (Figure 1.8 A).[26] They proposed that the absorption of visible light and special selective photocatalytic reaction depend much on surface complex generated by the interaction of benzyl alcohol with the Ti sites and/or surface OH groups of TiO_2 (Figure 1.8 B).

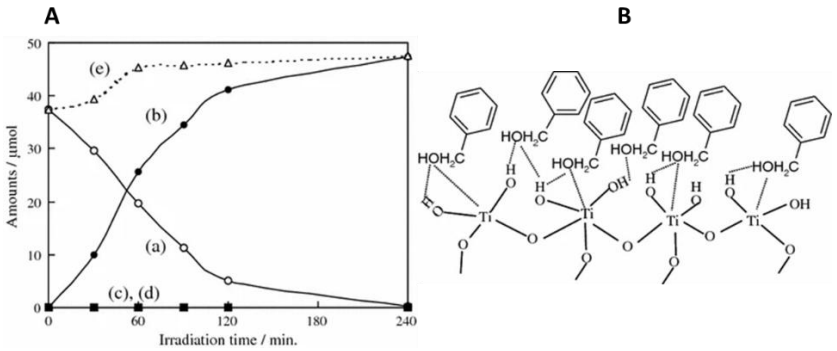

Figure 1.8: A) Under visible light output from the LED lamp, photocatalytic oxidation of benzyl alcohol (50 μmol) on TiO_2 (50 mg). (a) benzyl alcohol, (b) benzaldehyde, (c) benzoic acid, (d) CO_2, and (e) both benzyl alcohol and benzaldehyde evolved in solution. B) Proposed surface structure of benzyl alcohol adsorbed on TiO_2 surface.[26]

Using dioxygen as oxidant, Unsworth et al. also showed that bismuth vanadate nanoparticles (nano-$BiVO_4$) have selectively photo-oxidised benzyl alcohols to benzaldehydes under visible light irradiation, blue LED (λ_{max} = 470 nm) in presence of oxygen as oxidant. For several situations, nano-$BiVO_4$ produced yields 30 times more than bulk $BiVO_4$ with >99% selectivity. The proposed mechanism is illustrated in Figure 1.9 where benzyl alcohol is oxidised by valence band holes (h^+) to produce alkoxy

intermediate that could bind to surface and undergoes second oxidation to yield the corresponding aldehyde, benzaldehyde.

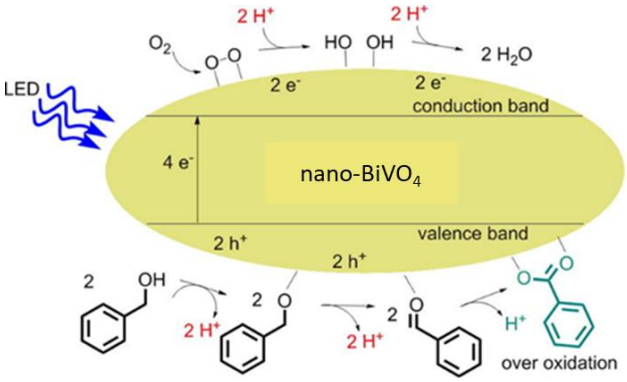

Figure 1.9: Suggested mechanism for aerobic oxidation of benzyl alcohol under visible light irradiation using nano-$BiVO_4$.[27]

Bi_2WO_6 which is the focus of this thesis has been used in alcohol oxidation. One of its first applications in photocatalysis was selective oxidation of alcohols to corresponding carbonyl compounds. Xu et al. conducted a study on the selective oxidation of glycerol to dihydroxyacetone (DHA) in water using Bi_2WO_6 crystals with a flower-like structure.[28] The crystals were exposed to visible light with a wavelength greater than 420 nm. The target chemical was obtained with the yield of 87% of DHA and the reaction exhibited a high level of selectivity (91%) (scheme 1.1). The byproduct observed was glyceraldehyde.

The hypothesised mechanism is based on the direct oxidation of the adsorbed glycerol by the positive holes created by light on the valence band of Bi_2WO_6, resulting in the creation of the corresponding intermediate. The required DHA product is obtained through the reaction between the intermediate and oxygen, or activated oxygen such as $O_2^{\cdot -}$.

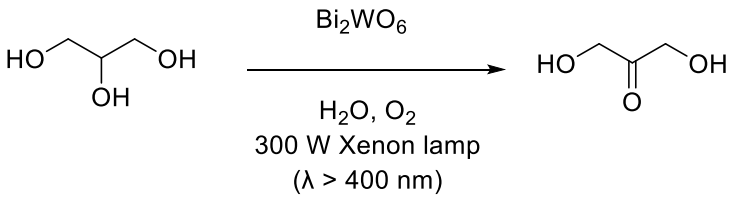

Scheme 1.1: oxidation of glycerol to dihydroxyacetone (DHA) in water using Bi_2WO_6 crystals with a flower-like structure.[28]

1.4.3.2 C-C bond formation

Another example of using MOSC in organic synthesis is C-C bond formation where many valuable products can be obtained using this approach. C–C bonds are formed via free radicals produced by reduction or oxidation of organic substrate under specific conditions. These radicals can then add to unsaturated bonds and combine with other radicals which results in C-C bond formation. C-C bond forming reactions often involve both reduction and oxidation. Redox-combined processes in which intermediates produced by one redox centre become the substrates for another are made possible by the charge separation that takes place on the photoexcited surface of MOSC.[29,30]

Yoshida et al. reported the cross-coupling between tetrahydrofuran (THF) and a variety of alkanes in the presence of Pt-TiO_2 as photocatalyst and using a Xenon lamp as light source (λ ≥ 350 nm). [31] This approach was based on direct activation of sp^3 C-H bonds of both THF and cyclohexane via oxidising holes of TiO_2 to generate radical species that cross-couple (Scheme 1.2). Long reaction times resulted in product degradation. They also observed homo-coupling product which reduced selectivity. They argued that Pt cocatalyst could have two roles: (i) decreasing the recombination of the electron-hole pairs created by light and (ii) serving as a metal catalyst to initiate the activation of the Csp^3-H bond in THF or alkane molecules.

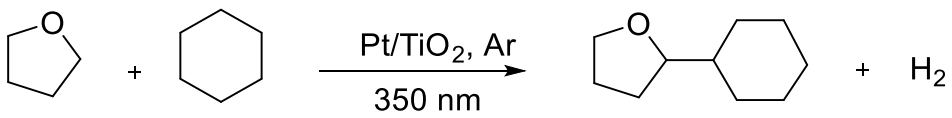

Scheme 1.2: Pt/TiO_2 photocatalyst is used to facilitate a direct cross-coupling reaction between tetrahydrofuran (THF) and cyclohexane.[31]

Scaiano et al. reported that they were able to couple two aryl iodides (Ullmann reaction), Scheme 1.3, to produce corresponding biaryl compound using Pd-TiO_2 as catalyst under UV and visible light irradiation.[32] The reaction is started by UVA excitation causing the electron-hole pair to form on the TiO_2 surface. Like other metal nanoparticles, palladium nanoparticles (PdNPs) help to collect electrons from the conduction band (CB), which, by spatial isolation, extends the lifespan of the electron-hole pair (Scheme 1.3).

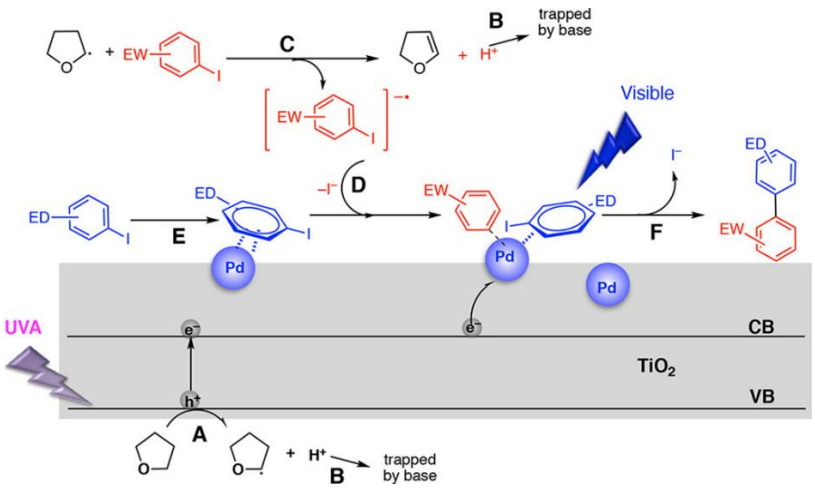

Scheme 1.3: Proposed mechanism of Ullman reaction using irradiated Pd-TiO_2.[32] *Reused with permission from ref (32).*

THF first traps the hole in the valence band (VB) producing THF• (A) and a proton, which the base (B) scavenges. Either of the two aryl-iodides, which are found in the system in similar amounts, can accept an electron from THF•. In step (C) the reduction of aryl iodide with an electron withdrawing group (EWG) is more favourable than that of the iodide with an electron donating group (EDG). Expected to be extremely short-lived, the aryl radical anion generated by electron capture (C) loses iodide either before or simultaneously with the aryl radical interacting with the Pd@TiO_2 surface (D). The presence of EDG facilitates adsorption of the corresponding aryl iodide on the Pd@TiO_2 surface (E). By a photoreductive elimination, the second aryl halide can be added oxidatively (with THF• assistance via abstracting H). Visible light facilitates the last step of electron transfer from the PdNP to the residual iodide, therefore enabling the synthesis of cross-coupling products (F).

The authors proposed that combining both UV and visible light enhance starting material conversion and cross-coupling product selectivity. Using UV light only induced conversion however visible light was necessary for product selectivity.

Also shown by Feng and Chen that Suzuki coupling under visible light irradiation was feasible with modified TiO_2 with less expensive silver nanoparticles (AgNP).[33] The main advantage of doping with AgNP was to enable visible light absorption. Aryl halides (specifically bromobenzene) and phenylboronic acid were reacted at room temperature and atmospheric pressure, resulting in the successful formation of a C-C bond between two aryl rings. The reaction was carried out under visible light illumination and achieved a 95% conversion of bromobenzene, with a 92% yield of biphenyl. Toluene was used as the solvent. When exposed to visible light (20 W LED, λ >420 nm), the TiO_2 semiconductor only was less excited due to large bandgap (Eg = 3.2 eV, λ <388 nm) so

electrons do not have sufficient energy to reach CB but when doped with 2% Ag, semiconductor activity increased because doping with Ag enables absorption of visible light. The holes were used to oxidise phenylboronic acid at VB and produce the phenyl radical. The energised electrons from the CB were subsequently transported to AgNP, which then used these electrons for aryl halide reduction (Scheme 1.4).

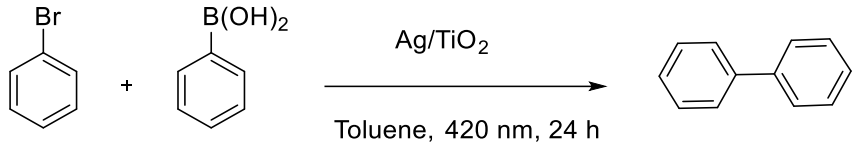

Scheme 1.4: The Suzuki coupling reaction between bromobenzene and phenylboronic acid catalysed by Ag/TiO_2 under visible light irradiation.[33]

Despite the usefulness of the above reactions, two of them used alkyl halide as a radical precursor. These halogen-containing compounds are toxic for the environment. Therefore, there is a need to use other alternative green precursors, such as carboxylic acids.

Walton et al. reported the process of carboxylic acid decarboxylation through photolysis utilising TiO_2 (P25 Degussa) under UVA irradiation (15 W Cleo tubes, λ = 350 nm). This method resulted in the production of several C-C compounds via photo Kolbe reaction.[34] The photocatalytic method was effectively used to break down various carboxylic acids, resulting in the production of the appropriate homocoupled products with moderate to good yields (38-83%) and great selectivity. In this instance, Pt (0.1wt.%) was employed to augment the photocatalytic efficacy of the TiO_2. In addition, they expanded the range of the decarboxylation reaction to facilitate the alkylation of electron-deficient alkenes using TiO_2 (P25). A reaction between carboxylic acid and maleimide, for example, is shown in Scheme 1.5.

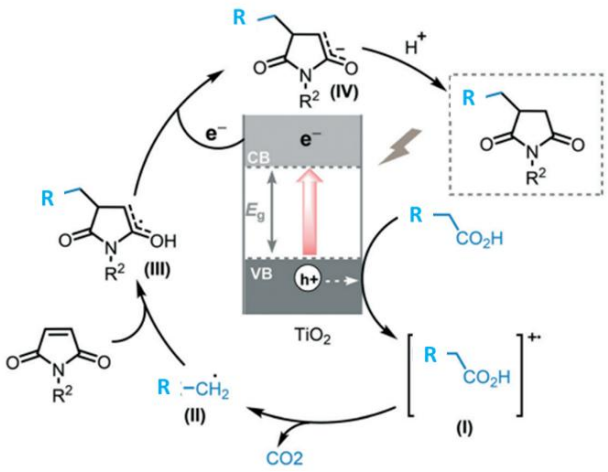

Scheme 1.5: Alkylation of maleimides with carboxylic acids promoted by platinised titanium oxide.[18,34]

The hypothesised mechanism entails the oxidation of the carboxylic acid by the photogenerated holes on the valence band (VB) of the TiO_2, resulting in the formation of the corresponding radical cation (I). The radical species undergoes deprotonation, followed by decarboxylation, resulting in the formation of an alkyl radical (II). This alkyl radical then adds across the double bond of the alkene. The alkylated alkene was formed through electron transfer from Pt/TiO_2 followed by protonation.

Most of C-C bond formation reactions were reported with TiO_2 as described above but bismuth containing metal oxide photocatalyst are used more rarely. The advantage of Bi is that the bandgap is in the visible range. Buglioni et al. conducted an experiment to assess the practicality of using Bi_2O_3 to promote the arylation of heteroarenes when exposed to visible light irradiation from a 23 W CFL (compact fluorescent lamp) source (Scheme 1.6).[35]

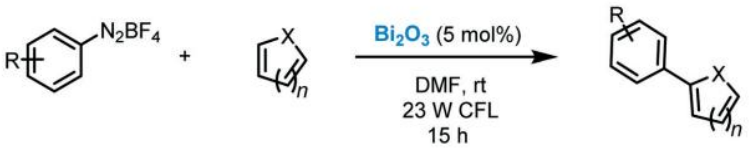

Scheme 1.6: reduction of the diazonium salt by photo-irradiated Bi_2O_3.[35]

This transformation involved the use of various heteroarenes, such as pyridine, thiophene, furan, and N-protected pyrrole. The result was the production of heterobiaryls with yields ranging from moderate to excellent (32% to 97%). A proposed reaction mechanism involves the reduction of the diazonium salt by the electrons generated by light in the conduction band of Bi_2O_3, resulting in the formation of the aryl radical. The

aryl radical will subsequently react with the heteroarene, resulting in the formation of an intermediate radical. This radical is then oxidised by the photogenerated holes, leading to the production of the intermediate cation. The final step is the deprotonation of the cation, resulting in the formation of the desired arylated product. In addition, they noted the occurrence of radical chain propagation as an alternative reaction pathway.

TiO_2 has many applications and examples in C-C formation, however there is no report on C-C bond formation using Bi_2WO_6. This opens an opportunity to utilise this catalyst in organic synthesis of valuable chemicals using visible light.

The general use of metal oxides in organic transformations is promising; however, understanding the reaction mechanism is not straightforward because it includes complex surface chemistry and photophysics. The following topics will discuss the main themes for using MOSC's for heterogenous photocatalysis.

1.5 Mechanism of photocatalysis using MOSC and factors affecting MOSC efficiency

The mechanism of photocatalytic reactions is complex and involves multiple steps. The mechanism can be divided into two main contributions, first, charge carrier generation in MOSC and second, heterogenous redox process on MOSC surfaces. The mechanism regarding charge formation inside semiconductor includes: (1) light absorption; (2) electron excitation and electron-hole separation; and (3) electron-hole mobility to the surface. Heterogeneous redox catalysis consists of (1) adsorption and diffusion of organic molecules to the surface of the semiconductor, (2) oxidation or reduction of these organic molecules (reactants) via photogenerated electron transfer of holes/electrons on the semiconductor, and (3) desorption and diffusion of products from the semiconductor surface.[36,37] A minimum total of six processes are crucial for a successful photocatalytic reaction.

Therefore, successful heterogenous reaction will depend on structure and composition of the semiconductor material and chemical structure of the organic molecules. (Figure 1.10) summarizes the photocatalytic reaction mechanism and other side pathways.

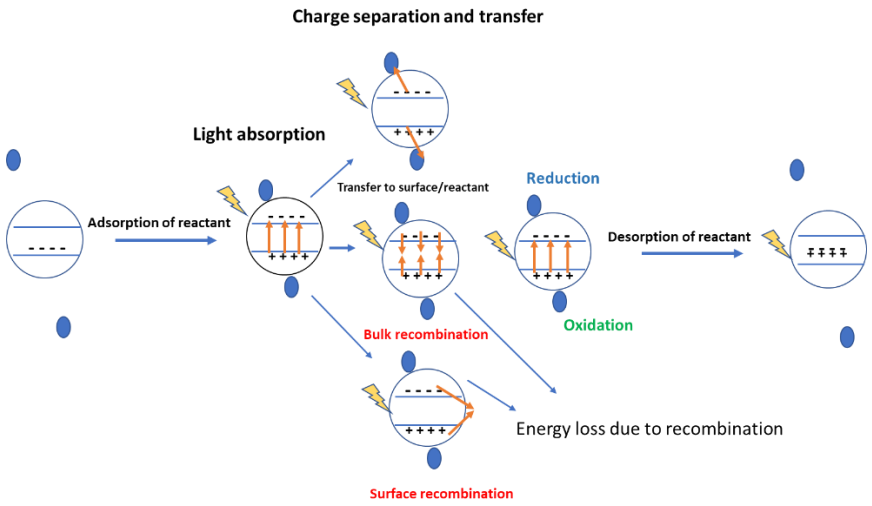

Figure 1.10: diagram showing the ideal/ typical photocatalytic mechanism over metal oxide semiconductors.[38]

A major challenge in photocatalytic activity of MOSC is effective light absorption and separation of photoexcited charges. These highly energetic species can drive catalytic reaction on the surface. In order to generate these charges, an appropriate light with wavelength and enough intensity is a necessity.

1.5.1 Light absorption and scattering and light intensity

The photocatalytic process begins with the absorption of a photon (with energy, hυ) by a semiconductor having a bandgap energy (Eg) smaller than the photon energy (hυ ≥ Eg). Charge transfer reactions across the semiconductor/solution interface are made possible by the redox characteristics of the semiconductor surface being altered by this photoexcitation.[39] Charge separation and recombination are commonly considered the main factors that affect the catalytic activity, and this is true especially in photocatalysis, where light energy would play a crucial role in formation of these charges and light intensity would affect their formation rate.

Regarding light intensity, if MOSC with a known bandgap is irradiated with an appropriate wavelength, one would expect reaction to occur. However, if light intensity is weak or if light does not reach the catalyst surface for any reason, photocatalytic efficiency will be low. However, too high light intensity can produce electrons-holes at a rate which increases recombination. The optimum light intensity is also determined by the probability of light absorption resulting from electronic structure of the bandgap. A direct bandgap is formally allowed increasing the probability of absorption, but also conversely increasing the probability of direct recombination.

When talking about light absorption by photocatalysts, there are also practical factors that can reduce absorption efficiency. A co-catalyst on the surface could prevent light absorption, particularly at high loadings. Solvents could also reduce light penetration by creating a reflectance layer. The reactor design and length of the light path would also affect the light intensity. More importantly, catalyst morphology could also affect light absorption.

A study by Calza et al.[39] revealed that different TiO_2 samples (P25 vs UV100) had different transmitted light intensities. The less transmittance value, the more scattered and absorbed light is expected. As there is more light scattering and absorption, the more catalytic activity is expected, as more light reaches and penetrates through catalyst particles. Both catalysts showed a decrease in transmittance with high catalyst loading (Figure 1.11 A). P25, which is the standard catalyst used in pollutant degradation and other photocatalytic applications, however, showed a significant loss in transmittance (more light absorption) due to its high scattering property. In contrast, the UV100 sample showed less absorption at the same catalyst loading, but started to absorb more when more catalyst was used.

Thus, when they tested both catalysts with formic acid degradation at low acid concentrations (0.2 mM), P25 showed a higher degradation rate (Figure 1.11 B). The lower activity in the UV100 TiO_2 sample was attributed to the high recombination rate in this sample compared to P25 TiO_2. When they increased the formic acid concentration (1 mM), UV100 TiO_2 showed superior activity (Figure 1.11 C). In both experiments (low and high acid concentrations), P25 showed a similar degradation rate.

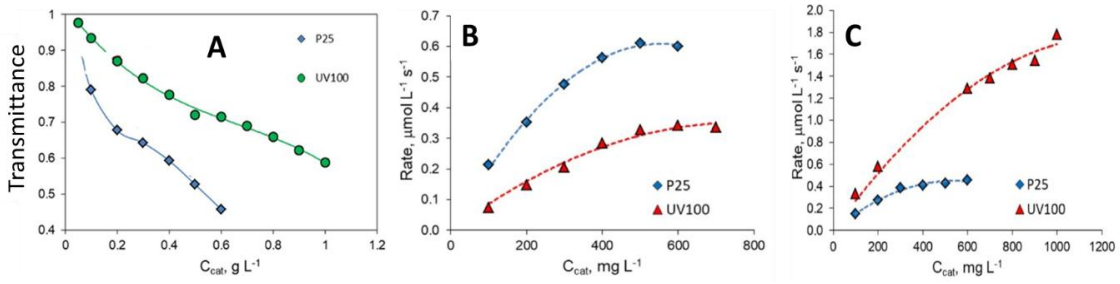

Figure 1.11: Relationship between transmitted light intensity and catalyst loading for different TiO_2 samples (A). photocatalytic activities of both samples at low formic acid loading (B) and high formic acid loading (C).[39] Reprinted and adapted with permission from ref (39).

They suggested that high substrate concentrations could trigger indirect electron transfer, where the fundamental mechanism of electron transfer shifts from the surface complexation-favoured direct mechanism (at the interface) at low concentration to an indirect mechanism (through the interface), in which the substrate is unbound at high

concentration. This explanation was based on a previous study by Montoya et al. on phenol photodegradation by TiO_2.[40] However, as mentioned in the study, phenol is not expected to adsorb as strongly as formic acid, so it might not be appropriate to propose an indirect mechanism here. Also, phenol would absorb more UV light compared to formic acid due to presence of benzene ring, which could result in photodegradation without the presence of TiO_2.

Another reason they did not mention can explain their observation, which is associated with the catalyst's morphology. It is that at low acid concentrations, P25 was active could be due to its unique crystal structure and its high scattering coefficient despite its low surface area (50 m^2/g) compared to UV100 (348 m^2/g). In high concentrations, P25 was probably deactivated due to acid poisoning the catalyst surface.

In conclusion, it is important for any photocatalyst to be able to carry out chemical transformation to have optimum light absorption but this is very reaction and apparatus dependent.

1.5.2 Charge separation, transportation, trapping and recombination

After absorbing light with sufficient energy, a charge separation event happens when electrons get excited from the CB to VB, leaving holes with positive charge in the VB (Figure 1.12). Surface photoactivity requires charge carriers to stabilise at the surface for electron transfer processes to occur between photocatalyst and substrate(s) and recombination events to be minimised.[41] Photogenerated charge separation and transfer is a major challenge in heterogeneous photocatalysis.

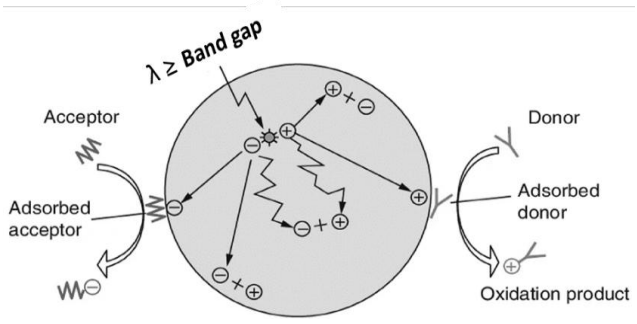

Figure 1.12: Charge recombination in bulk and or near surface.[42] Reused with permission from ref (42).

The fate of these separated charges depends on MOCS morphology and other modifications, such as co-catalysts. In pure MOSC, there is a high chance that these charges will recombine (either radiatively or non-radiatively) in bulk or on the surface.[41] Most MOSC contain defects that can trap photogenerated charges and transfer their

energy into heat via recombination. Bulk defects such as metal and oxygen vacancies, hinder photoactivity because electrons or holes do not reach the surface for redox chemistry.

1.5.3 Role of co-catalyst-metal on surface.

Despite the frequent use of MOSC photocatalysts in organic synthesis, their ability to induce chemical transformations in their unmodified form is hindered. The fast recombination of photogenerated electrons-holes inhibits the photocatalytic activity by minimizing interaction with adsorbed substrates decreasing efficiency of redox reactions.

The role of the cocatalyst is crucial in promoting photocatalytic efficiency. There are three main effects of cocatalysts in MOSC mechanisms. First, it can act as an electron trap, which increases the lifetime of electrons and holes. Second, co-catalysts can promote the thermal reactions of intermediates (chemical catalysis) to the final product, such as by protonation. Lastly, some metal nanoparticles can also augment light absorption (Figure 1.13).

Metal nanoparticles, such as bismuth (Bi), silver (Ag), or gold (Au), can be attached to the surface of semiconductor photocatalysts to expand their ability to absorb light over a wider range. Absorption of light at the resonance wavelength in these metals can excite surface plasmons. Localised surface plasmon resonance (LSPR) refers to the synchronised movement of conducting electrons at the boundary between a metal and a dielectric material, which occurs when it matches the frequency of the incident electromagnetic waves.[43–47]

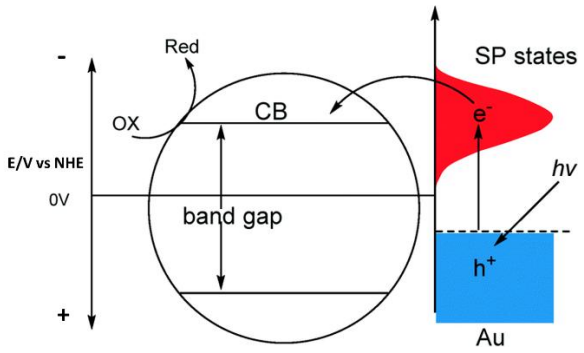

Figure 1.13: simplified diagram showing surface plasmon and its contribution in enhancing charge movement and redox reaction in semiconductor.[48] SP stands for surface plasmon. Reused with permission from ref (48).

Metal nanoparticles like Pd and Pt display plasmonic phenomena in a different region of electromagnetic spectrum based on particle size. Pd particles (50-60 nm) show their plasmonic band below 300 nm. However, palladium nanoparticles with a size above 120

nm exhibit an extinction band that spans from the ultraviolet (UV) to the infrared (IR) range. Pt nanoparticles on the other hand, the plasmonic absorption peak can be adjusted within the range of approximately 400 to 494 nm by varying the size of the Pt nanoparticles from 73 to 107 nm.[49] The optical absorption of metal nanoparticles at other wavelengths, such as Pt nanoparticles, can also be explained by the process of intraband excitations. This involves the movement of conduction electrons from their lowest energy state to higher energy states.

Mainly, cocatalyst nanoparticles are decorated over MOSC by methods such as chemical reduction and photodeposition. Identifying the optimum amount of metal NPs on MOSC is always challenging, as low metal loading could lead to a slow reaction rate, and high loading could also inhibit photocatalytic activity (Figure 1.14).

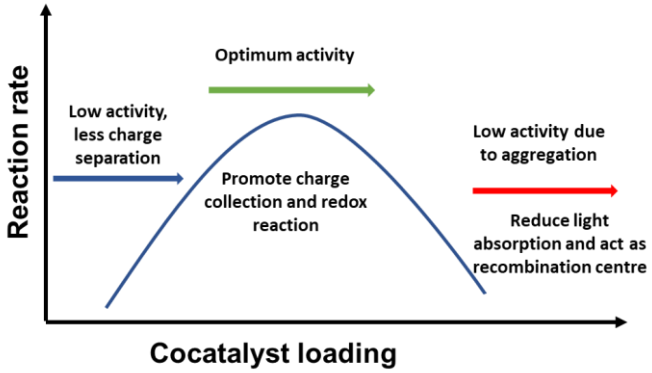

Figure 1.14: Schematic diagram showing effect of cocatalyst (metal NPs) loading.[21]

1.5.4 Synergistic role of metal nanoparticles and oxygen vacancies in enhancing photocatalytic activity

Oxygen vacancies (OVs) are imperfections in the arrangement of atoms in a crystal lattice, resulting from the absence of oxygen atoms. These vacancies generate additional energy levels within the bandgap, enabling the semiconductor to capture light in the visible spectrum. OVs can expand the range of wavelengths that can be absorbed, going beyond the natural limit of the material's absorption band.[50,51]

The concurrent use of metal nanoparticles (MNPs) and OVs results in a synergistic effect that improves the separation of electric charges. Metal nanoparticles capture electrons, whereas oxide vacancies capture holes. This dual trapping method serves to inhibit recombination, hence enhancing the efficiency of using photogenerated charges for catalytic processes.

The existence of OVs and MNPs can have an impact on the surface chemistry of the photocatalyst. For instance, these OVs can generate active sites that facilitate specific processes, whereas metal nanoparticles have the ability to selectively enhance particular redox reactions. This collaboration results in enhanced specificity in the creation of products.[52]

Ma et al. examined the catalytic performance of $SrTiO_3$ (STO) and 15% Ag-$SrTiO_3$ (STO-Ag-15%) for NO removal under visible light illumination. They found that both STO and 15% Ag-$SrTiO_3$ (STO-Ag-15%) showed good activity toward NO oxidation, with slightly better performance when using Ag-modified catalysts (50% and 70%, respectively). High concentration and high stability of oxygen vacancies in STO-Ag-15% were given as the main reasons for the observed increased photocatalytic activity.[53]

Upon catalyst characterization, UV-Vis diffuse reflectance spectroscopy (UV-Vis DRS) showed a visible light response due to Ag surface plasmon. EPR measurements showed the presence of unpaired free electrons signal at g = 2.000, demonstrating the generation of vacancies (Figure 1.15). Both STO and STO-Ag-15% showed this signal in the dark and under illumination; however, STO signal is weaker compared to STO-Ag-15% indicating increase in OVs formation.

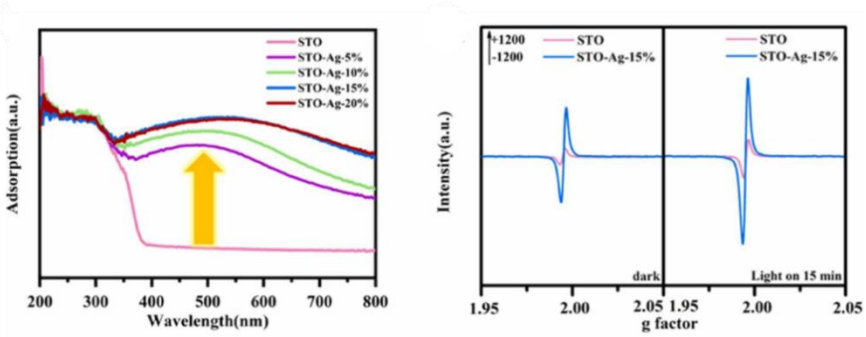

Figure 1.15: UV-Vis DRS and EPR spectra of STO and STO-Ag-15%. Reprinted with permission from ref (53).

Additionally, they suggested that the use of Ag metal not only improves absorption of light and transfer of charges to metal oxide, but also prevents the deactivation of OVs by molecular oxygen upon contact with air. This was explained by when Ag nanoparticle is subjected to the LSPR effect, it produces hot electrons and hot holes. These hot electrons could stay at metal-semiconductor interface while hot holes could be effectively transferred to a defect state near the surface resulting in the continuous formation of OVs with high energy and extending their lifespan.

Moreover, the interaction between metal and semiconductor interfaces creates new sites (OVs) which could be used for different purpose based on reaction conditions used such as adsorption and activation of H_2O to promote production of reactive oxygen species as was explained in a report by Li et al. (Figure 1.16).[54] They proposed that the electroconductivity of Au/TiO_2-x is improved by an increase in OVs, which reduces back transfer recombination and extends the lifetime of hot holes in Au NPs which facilities water oxidation. Also, as plasmonic hole lifetime is extended by the transfer of Au NPs' d-band holes to TiO_2-x defect states, this increases holes density (from both metal and semiconductor) which could also facilitate water oxidation.

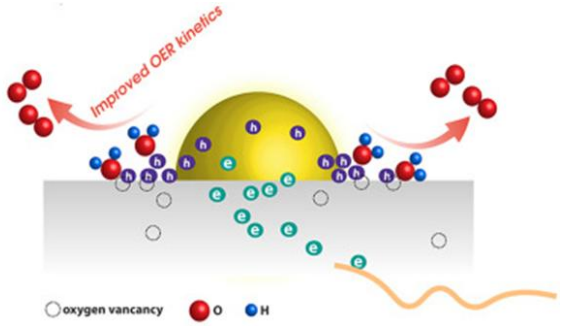

Figure 1.16: Graphical representations of the functions oxygen vacancies performed in plasmon-induced water oxidation. Reprinted with permission from ref (54)

Liu et al. conducted a study where they successfully loaded Ag nanoparticles onto bismuth molybdate (Bi_2MoO_6) in order to increase the surface OVs and improve the conversion of nitrogen to ammonia. The researchers came to the conclusion that the addition of Ag NPs increased the spectrum of light absorption and enhanced the effectiveness of separating photogenerated carriers by acting as electron trapping agents. Moreover, the incorporation of Ag NPs increases the concentration of OVs in Bi_2MoO6, which further enhances the photocatalytic activity by the adsorption of reactants.[55]

1.5.5 Substrate ligand-to-photocatalyst metal-charge transfer (LMCT)

Photocatalysis is usually described in terms of the photocatalyst as the only species that is absorbing light in photocatalytic system. However, adsorbed species on photocatalyst surface such as dyes can also absorb light. In the case of TiO_2, which does not absorb visible light, the dye can absorb visible light and acting as an antenna to enhance photocatalytic reactions (Figure 1.17).

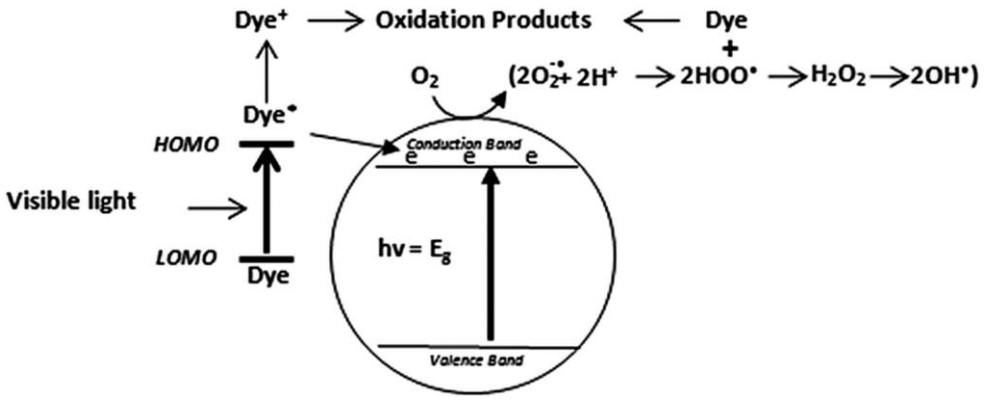

Figure 1.17: Illustration depicting the process of direct dye degradation.[56] Reused with permission form ref. (56).

Photon absorption by the dye of visible light photons with a wavelength greater than 400 nm, causes transition from its ground state (Dye) to a higher energy triplet excited state (Dye*). The dye species in an excited state injects an electron into the conduction band of TiO_2 to give the oxidized radial cation ($Dye^{+\bullet}$). This can be reduced to support further photoinduced electron injection or undergo degradation.[57]

There are other molecules that may not absorb visible light as effectively as dyes, but upon binding with the catalyst surface, they might transfer electrons to metal oxide upon illumination, and this is called substrate-ligand-to-photocatalyst metal-charge transfer (LMCT).[58]

In the LMCT mechanism, when organic molecules bind to the catalyst surface through metal centres, the metal's oxidation state changes (for example, from M^{3+} to M^{2+}). This alters the surface chemistry and electronic structure by adding new levels of defects. These new defects near VB alter the bandgap (which becomes narrow), thus enabling absorption of visible light.

Yoshida et al. studied the effect of adding noble metals such as Pd to the surface of TiO_2 and how it increased the catalytic activity and reaction selectivity of the C-C cross-coupling reaction between benzene and cyclohexane (Figure 1.18).[59] First, they ran the reaction under UV light irradiation. They proposed that, upon irradiation, the photogenerated electrons gain sufficient energy and are excited to CB, leaving photogenerated holes in VB that oxidise both benzene and cyclohexane to phenyl and cyclohexyl radicals, respectively, which are coupled together, producing the desired compound. Pd's role here is to capture e^- in CB, preventing charge recombination and enabling the oxidation of starting materials. However, the use of UV light resulted in low selectivity of the desired compound, phenylcyclohexane (PCH), due to formation of homo-coupled products, bicyclohexyl (BCH) and biphenyl (BP). When they studied the

effect of visible light, they found a remarkable improvement in product selectivity of >99%.

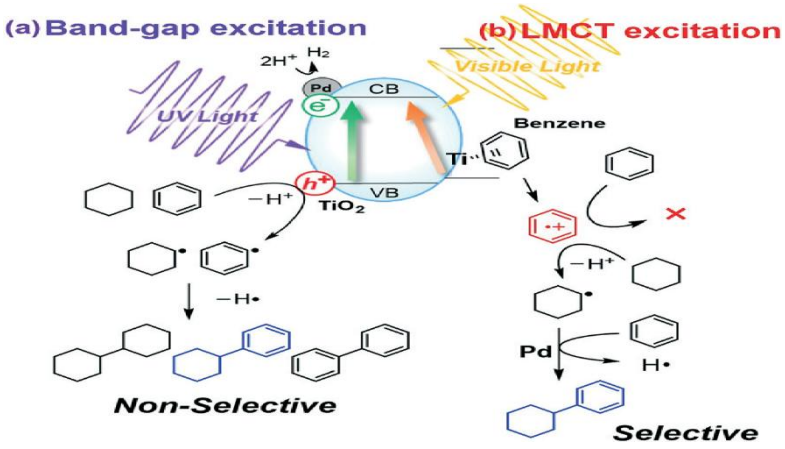

Figure 1.18: Schematic diagram showing reaction mechanism of C-C coupling between benzene and cyclohexane using UV-Vis irradiated Pd-TiO_2, LMCT = Ligand-to-metal-charge transfer.[59] *Reprinted with permission from ref (59).*

They proposed that the benzene molecule interacts with TiO_2 through π-interaction, (LMCT) which could move the VB position, promoting electrons to CB under visible light excitation and producing a benzene radical cation that can activate cyclohexane, yielding a cyclohexyl radical. This cyclohexyl would react with another benzene molecule via addition-elimination in the presence of Pd. So, the metal and the LMCT effect can work together to enhance both catalyst activity and reaction selectivity.

1.5.6 Morphology of MOSC

It has long been actively sought to engineer semiconducting functional materials into desired morphologies. This is because surface atomic structures, which may be precisely controlled via morphological control, affect various applications including heterogeneous catalysis, gas detection and sensing, molecule adsorption, energy conversion and storage. Important progress in this field has been made possible by the decade-long focused research on morphology-controlled materials.[60] MOSC can be fabricated in different morphologies including 0, 1, 2, 3-dimensional structure. The production of lower dimensional structures has traditionally relied on the use of structure-directing agents such as aqueous fluoride ions. These agents attach to particular facets of the developing TiO_2 nanoparticles, effectively inhibiting crystal growth in this direction.

In addition to morphology, the surface chemical composition may not reflect the bulk composition potentially giving a range of surface energies and catalytic activity.

1.5.6.1 0-D Quantum dots (QDs)

The idea of "artificial atoms," or quantum dots (QDs), was first proposed many years ago when semiconductors were first reduced in dimensionality. Nobel prize in chemistry in 2023 was awarded for discovery of QDs. With dimensions of nanometres, these semiconductor nanocrystals show quantum size effects in their electrical and optical characteristics. Several of these uses are now commercially available and part of our everyday life, like QD-based displays.[61]

One additional benefit of QD catalysts, especially for organic transformations, is their colloidal nature. This enables effective interactions between the catalysts and substrates due to their high surface to volume ratio (high surface area) and removal from the reaction solution system. As a result, QD catalysts can combine the advantages of both homogeneous and heterogeneous catalysts.[62]

1.5.6.2 1-D nanostructures

A one-dimensional nanostructure has a high aspect ratio, meaning its length is much greater than its diameter. The diameter of such nanostructures often falls within the range of 1 to 100 nm. They can take various shapes, including tube-like, rod-like, wire-like, fibre-like, or belt-like. For example, 1D TiO_2 nanostructured materials possess the characteristic properties of TiO_2 nanoparticles and exhibit a significant specific surface area, facilitating the efficient transfer of photogenerated carriers in the axial direction.[63]

1.5.6.3 Two-dimensional (2D)

In recent times, there has been a significant amount of interest in two-dimensional (2D) materials, specifically nanosheets and nanoflakes. These materials have high aspect ratios and are only a few atomic layers thick. The discovery of graphene in 2004 paved the path for the exploration of other two-dimensional structures. The 2D metal oxides are very thin, allowing most of the atoms to be easily reached on the surfaces.[64]

1.5.6.4 Three-dimensional (3D)

Low-dimensional nanostructured building blocks can self-assemble into three-dimensional (3D) nanostructures, such as 3D hierarchical architectures and 3D mesoporous nanostructures including flower-like, networks, and dendritic structures. Because they facilitate reactant adsorption and light harvesting, these 3D hierarchical nanostructures and linked porous networks with large specific surface areas find extensive application in photocatalysis. Furthermore, they can be easily loaded with other components such as metal nanoparticles into 3D hierarchical nanostructures to create heterojunctions.[65,66]

3D hierarchical nanomaterials have been used in the field of photocatalysis for decades due to their unique structures and increased specific surface area. These materials are effective in degrading organic contaminants. Lee et al. showed that 3D hierarchical TiO_2 nanostructures outperform 2D TiO_2 in terms of photoinduced degradation of methylene blue (MB). They enhance performance by providing a high surface area, and reducing the distance between the location of excitation and reactive surface. Additionally, it was observed that catalysts with a 3D structure can be more effectively retrieved and reused compared to those with a 2D structure.[67]

1.5.7 Crystal facets and surface atoms arrangement

Coordinatively-unsaturated atoms with dangling bonds create distinct electronic structures on the surface of a semiconductor. Different atomic arrangements and terminations of a semiconductor can lead to different properties of crystal facets in terms of the adsorption of organic molecules, the transfer of the photogenerated carriers, electron-hole recombination, and the desorption of product molecules during photocatalytic processes.[68]

Crystal facets have different surface energy as a result of their unique atomic configurations. High-energy surfaces or facets exhibit greater reactivity compared to low-energy surfaces. For instance, the surface of anatase (TiO_2) is mostly composed of the thermodynamically stable (101) facets, which make up about 94% of the crystal surface according to the Wulff construction (Figure 1.19).[69] In contrast, the (001) facets, which are more reactive, are less dominant. Nevertheless, the presence of the highly reactive (001) facets significantly influences both the process of photocatalysis and the mechanism of gas sensing.[70]

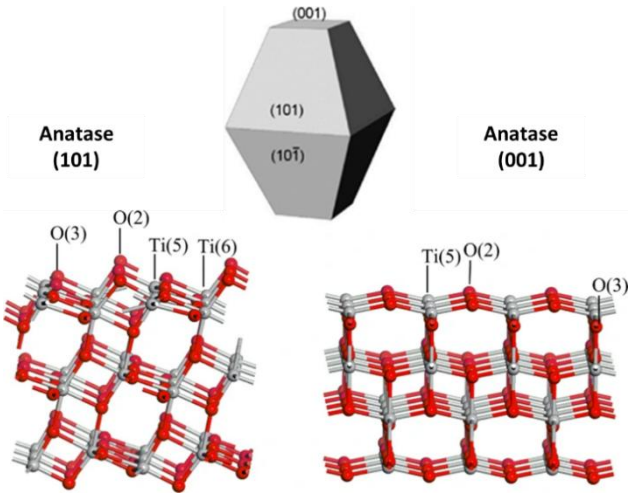

Figure 1.19: Crystal facet of anatase TiO_2 showing (101) (most stable) and 001 facet (most reactive) and according to Wulff construction. Titanium atoms are represented as grey spheres,

whereas oxygen atoms are represented as red spheres. [41,69,71,72] *Reprinted with permission from ref (69).*

The Arienzo group synthesised TiO_2 with (001) and (101) exposed facets using a morphology guiding agent. Both theoretically and practically, it has been demonstrated that the (001) surface exhibits higher activity for photocatalytic oxidation reactions, whilst the exposed (101) surface acts as a reductive surface.[73] Under vacuum conditions, the trapped holes (O^- centres) become more concentrated as the surface area and photoactivity of the (001) surface increase. On the other hand, the amount of Ti^{3+} centres increase with the specific surface area of (101) facets. These findings indicate that (001) surfaces can be primarily regarded as places where oxidation occurs, playing a crucial role in the photoxidation process. On the other hand, (101) surfaces act as sites where reduction takes place.

The pronounced photoactivity of the (001) surface in this study may be attributed to efficient light scattering as discussed in section 1.5.1. The light scattering feature is well recognised as a crucial factor in affecting the efficiency of light harvesting and it is a consequence of morphology. In addition, it has been found that there is a relationship between the percentage of (001) facets exposed to light and the 3D flower-like structure. As morphology changes to be more spherical or flower-like, the (001) facets percentage increases (Figure 1.20).[74]

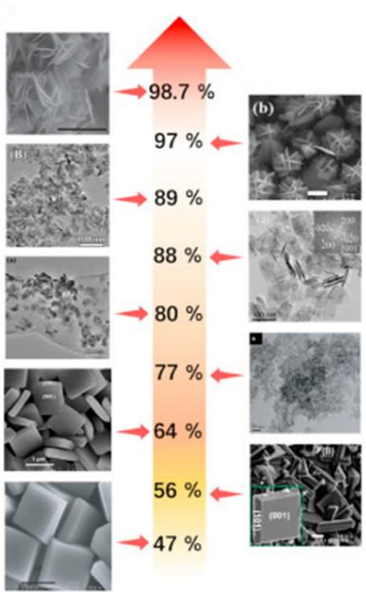

Figure 1.20: Photographs depicting TiO_2 samples showing varying proportions of exposed (001) facets in relation to particle morphology. As morphology changes to 3D, (001) ratio increase.[74] *Reprinted with permission from reference (74).*

1.6 Understanding chemical factors affecting heterogenous photocatalyst selectivity in organic transformations

Despite green credentials of heterogeneous photocatalysts, their applications to organic synthesis are often limited by reaction selectivity. This section will focus on the selectivity of C-C bond formation as it is the main application of this work. Surface chemistry of metal oxides with different crystallinity, adsorption/desorption of organic molecules, and the effect of water on catalysis will also be discussed.

1.6.1 Metal oxide surface chemistry

Since photocatalytic reactions occur on the surface of the photocatalyst, selective adsorption of the reactants and products on the photocatalyst play an important role in catalysis. Strong adsorption of reactants and weak binding of products increase the rate of catalytic reaction. This binding can be affected by surface morphology, crystallinity and surface modification. Apart from affecting binding of reactants and products, surface functional groups can also affect catalysis such as presence of OH groups that can act as Lewis acidic or basic sites.[75]

1.6.2 Surface area and crystallinity

The level of surface crystallinity has a substantial impact on the activity of metal oxide photocatalysts. The enhancement of photocatalytic efficiency through increased crystallinity is commonly attributed to the elimination of dangling bonds and distorted lattice structures that serve as locations for charge trapping and/or recombination. On the other hand, higher crystallinity might also result in the negative consequences of reduced surface OH coverage and overall surface area (Figure 1.21) shows advantage and disadvantage of crystalline and amorphous structure.

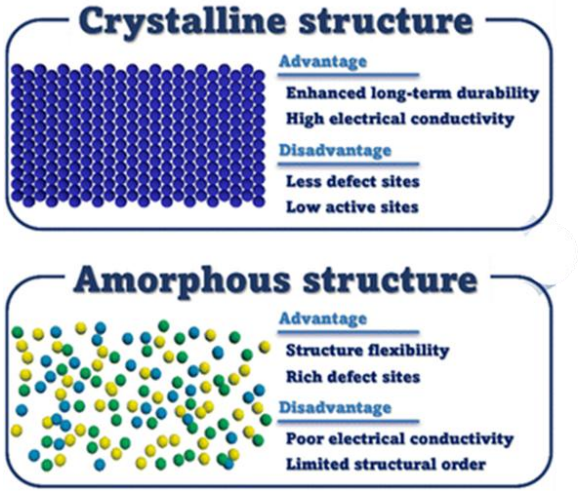

Figure 1.21: Comparison between crystalline and amorphous catalysts properties in photocatalysis.[76] Reprintend and modified with permission from ref (76).

When comparing activity of different polymorphs and amorphous MOSCs, we need to consider three factors: (1) light absorption and charge transport; (2) charge trapping and charge carrier mobility; and (3) adsorption of reactants on the MOSCs and catalytic reactions including electron transfer.

The first factor depends on the bulk crystalline structure of the material, such as the bandgap. For example, the TiO_2 anatase phase has a 3.2 eV bandgap, while the TiO_2 rutile has a 3.0 eV bandgap.

The other two factors depend on the surface properties of different polymorphs. For example, Komaguchi et al. examined the relative surface reducibility of TiO_2 anatase and TiO_2 rutile. Understanding surface's reducibility helps to determine the type of catalytic activity because it shows how well TiO_2 can keep charge carriers that affect the redox chemistry on the surface. Komaguchi et al. used vacuum annealing and reaction with H_2 at 773 K. Using EPR, they monitored the Ti^{3+} profile on the surface. They found that the rutile phase showed reduced Ti^{3+} at 77 K, while no signal was detected in the anatase phase. A Ti^{3+} signal indicates the formation of subsurface traps. These traps can capture electrons and could induce or inhibit photocatalytic activity, depending on redox chemistry.

On the other hand, the third factor, which is related to the adsorption of reactants and presence of active sites on surfaces, also influence photocatalytic activity. For example, Anderson et al. found that rates of phenol photodegradation were higher for anatase nanoparticles (surface area (SA) = 256 m^2/g) than for suspended rutile nanoparticles (SA = 39 m^2/g).[77] In contrast, another study by Sun et al. showed that rutile nanoparticles activity toward phenol degradation was higher than that of anatase nanoparticles with similar surface area (SA = 174 m^2/g for rutile vs 184 m^2/g for anatase) . The noticeable photocatalytic activity of rutile sample was attributed to higher content of hydroxyl groups compared to anatase one.[78] Therefore, it is beneficial to have high surface area but the nature of active sites present on the surface may be the dominant factor.

1.6.3 Surface Hydroxyl groups

The presence of surface hydroxyl groups can enhance photocatalysis by several mechanisms. For instance, hydroxyl groups can enhance the separation of charges by capturing positive holes, and extending the lifetime of the excited state. This role is analogous to that of oxygen vacancies, which serve as defects either within the bulk or on the surface.[79] In addition, hydroxyl groups establish hydrogen bonds with adjacent atoms on semiconductor surfaces. These surface effects can give rise to a depletion layer on the order on nm for MOSCs which can modify the bulk electronic structure of particles < 5 nm resulting in a change in the bandgap.

The other very important aspect of hydroxyl groups is that the equilibrium between protonated and non-protonated states determines the surface charge of the particle. The point at which the adsorbent's surface has a net electrical charge of zero is referred to as the point of zero charge (PZC). At this particular pH, the surface of the adsorbent is electrically neutral, which can have a substantial impact on its ability to adsorb substances. Below PZC, the adsorbent's surface possess a positive charge, enabling it to attract anions such as carboxylates. Above the PZC, the surface retains a negative charge, which causes it to attract cations. The effect of surface charge becomes noticeable in aqueous media that facilitate the ionisation state of the substrate. However, when a non-aqueous solvent like acetonitrile is used instead, the alteration of surface charge is probably not that important. In addition to have more or less OH on surface which will affect substrate binding as mentioned above, the presence of OH groups will also affect the surface chemistry through increasing the availability of protons which will participate in reactions such as the promoting final protonation step.

In the current study, hydroxyl groups may also play a role in catalysis by facilitating the transfer of protons. Hydroxyl groups can act as either acidic or basic sites (e.g., by helping to deprotonate carboxylic acids). Chapter 3, Section 3.6 describes the adsorption of phenylacetic acid on Bi_2WO_6 studied in this thesis.

The formation of acidic and basic hydroxyl groups on metal oxide semiconductor surfaces occurs through distinct pathways. One is through hydrogen bonding between protons of adsorbed water with lattice oxygen atoms, resulting in bridging hydroxyl groups (OH_B), while the other arises from the interaction of water with Lewis acid sites, yielding terminal hydroxyl groups (OH_T) (Figure 1.22).[80]

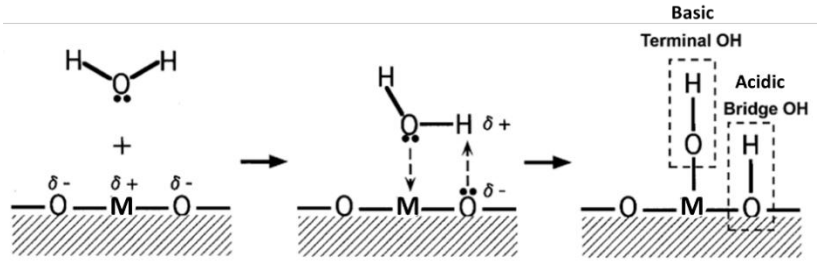

Figure 1.22: Formation of basic and acidic surface OH on titanium oxide through the adsorption of water molecules.[81] Adapted from ref (81).

Water can promote the formation of hydroxyl groups on the catalyst surface, which act as linker sites for substrate binding and active sites in catalytic reactions. Tamura et al. propose an alternative mechanism where the hydroxyl groups formed can be classified into two types: the acidic OH (a) that results from the protonation of lattice oxide and the

basic OH (b) of the original water molecules.[82] In this mechanism, the acid hydroxyl groups (a) serve as the cation exchange sites, while the base hydroxyl groups (b) function as the anion exchange sites (Figure 1.23). The difference in this mechanism is that basic OH originates from water (the water hydroxyl group) rather than terminal OH bound to the metal centre.

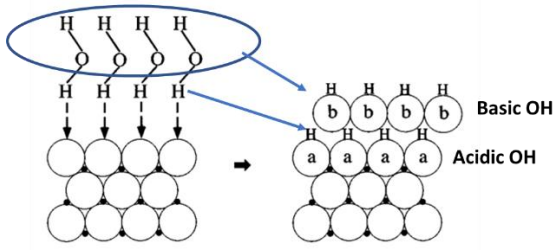

Figure 1.23: formation of acidic and basic hydroxyl groups via conjugated acid of lattice oxide ions and the conjugated base of adsorbed water.[82] Reused with permission from ref (82).

In addition to facilitating formation of surface hydroxyl groups which are important for substrate binding, water can block active sites. For instance, the presence of water in photocatalysis on TiO_2 is commonly regarded as a site blocker. There are two forms of site blockage that can be considered. The first type involves water filling up important adsorption and/or reaction sites on the surface. The second type involves water forming a multilayer film on the catalyst surface preventing reactants from reaching the oxide-solution interface. Therefore, the presence of water layers atop TiO_2 surfaces can restrict the access of a reactant to the TiO_2 surface by creating hydrogen-bonded networks in physisorbed conditions.

Henderson showed that water hindered the process of acetone conversion to acetate by exposure to light on a TiO_2 surface at 100 K. This hindrance was observed by measuring the synthesis of ketene in a post-irradiation temperature programmed desorption (TPD) experiment (Figure 1.24).[83] The reason why water inhibits the photochemistry of acetone on rutile TiO_2(110) is likely due to water molecules at high coverage forming hydrogen bonds with the surface and neighbouring water molecules, causing acetone to unbound or become weakly adsorb.

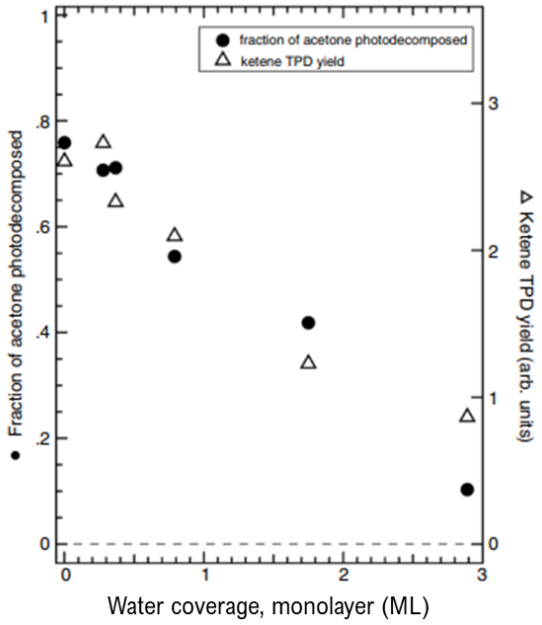

Figure 1.24: The percentage of acetone that undergoes photodecomposition (measured on the left axis) and the amount of ketene produced from the thermal decomposition of acetate generated by light (measured on the right axis) are both shown against the coverage of water coadsorption on the TiO_2(110) surface. ML stands for monolayer. Reused with permission from ref (83).

1.6.4 Adsorption of substrates on MOSC surface

The structure of the adsorbate (organic molecules) plays a crucial role in binding to MOSC. The surface of pure MOSC is composed of metal cations, oxide anions and hydroxyl group. Organic molecules bearing functional groups such as OH, e.g. alcohols and carboxylic acids, have strong affinity for MOSC. The binding mode could vary based on atoms involved in binding and type of bonds resulting in physisorption or chemisorption. Physisorption includes electrostatic interactions and weak hydrogen bonding. Chemisorption includes monodentate (ester-like linkage), bidentate bridging and bidentate chelating (Figure 1.25).

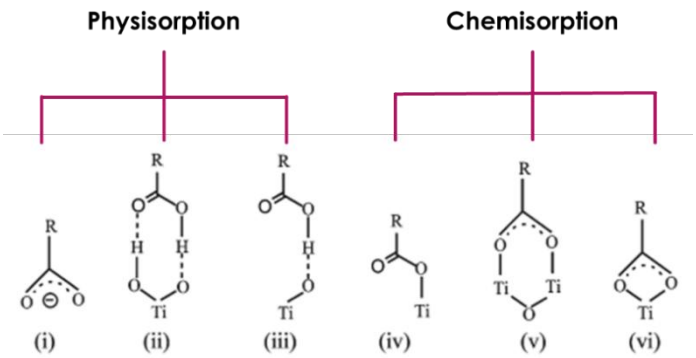

Figure 1.25: (i) Electrostatic Attraction, (ii, iii) H-Bonding, (iv) Monodentate (Ester-like Linkage), (v) Bidentate Bridging and (vi) Bidentate Chelating.[84] Adapted from ref (84).

Wu and colleagues tracked the relative photoreactivity of mono and bidentate-bonded alkoxy groups produced by the dissociative adsorption of methanol or ethanol on TiO_2 using Fourier transformed infrared spectroscopy (FTIR) (Figure 1.26).

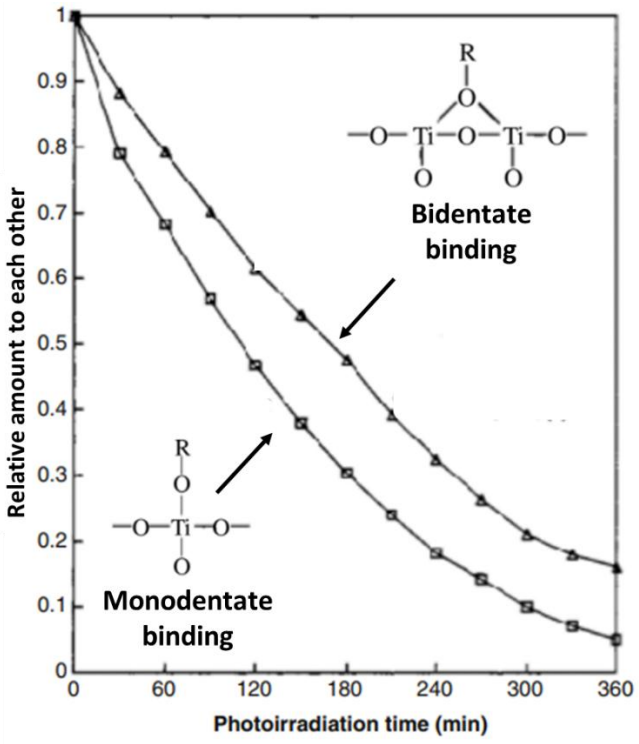

Figure 1.26: The proportions of monodentate and bidentate alkoxy groups vary with the duration of UV exposure over TiO_2.[85] Reuse from permission from ref (85).

These authors demonstrated that the bidentate form's relative rate of disappearance was lower than that of monodentate ethoxy groups by observing the variation of their integrated IR absorptions with UV irradiation time where alcohols peak disappeared and by-product, water and bound carboxylic acid evolved over time. These results imply that

an alkoxy group on TiO_2 was around 1.5 times more reactive in its mono-dentate form than bidentate.[85] This study suggests that substrate binding to MOSC could negatively affect decomposition rate if substrate binds strongly via different binding mode or binding to multiple sites.

Surface coverage by substrate also plays a crucial role in photocatalytic activity. A study done by Henderson showed that acetone photodecomposition on rutile titanium dioxide (R TiO_2) showed distinct coverage dependency; rates fell by ten times as the surface got saturated with acetone. In this instance, O_2 was required for the reaction, but acetate, a photodecomposition product, built up on the surface and prevented O_2 from getting into TiO_2 surface.[86]

1.6.5 Desorption of intermediates and products

While adsorption concerns starting materials, desorption concerns intermediates, if any, and products. The desorption of the product is no less important for catalysis than adsorption.[87] Products that don't readily desorb or stick permanently block catalytic sites, which prevent new molecules from adsorbing on surfaces and, as a result, deactivate catalytic reactions. Also, if the product desorbs slowly from the surface, it will slow the reaction rate.

Blocking catalytic sites would affect reactions that involve several pathways or intermediates. For instance, following the initial photoreaction, the reactive intermediate can desorb, and the consequent reaction would take place in the bulk solution. Alternatively, reactive intermediates could undergo further reactions on the surface, either with surface-adsorbed reactants or with reactants in solution. These two pathways can have different selectivities and have different reaction kinetics.

The reaction of organic molecules on solid surfaces, in general, may follow one of the following mechanisms: Langmuir-Hinshelwood and Eley-Rideal (Figure 1.27).[88] In the Langmuir-Hinshelwood mechanism, two molecules are adsorbed on the surface. Then these two molecules diffuse and react with each other, producing the product. Finally, the product desorbs from the surface. On the other hand, in the Eley-Rideal mechanism, one of the reactants adsorbs on the surface while the other one remains in solution. Then, the unbound molecules react with the adsorbed molecules, forming the product that desorbs from the surface.

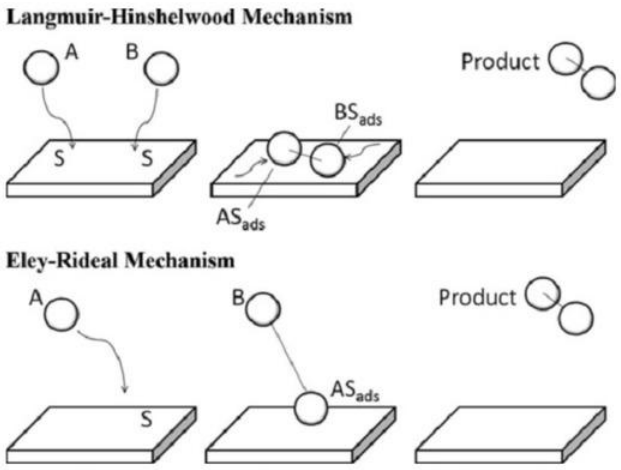

Figure 1.27: Illustration showing difference between Langmuir-Hinshelwood and Eley-Rideal mechanisms. Reprinted with permission from ref (89).[89]

In both mechanisms, the state of the intermediate, which facilitates the formation of the final product, could play an important role in reaction kinetics because it could have different binding affinity and reactivity. For instance, if this intermediate (like an aryl radical that is generated from aryl carboxylic acid) desorbs slowly from the surface, presumably it follows the Eley-Rideal mechanism or takes time to react with other molecules, it will contaminate the surface and make it less accessible to new acid molecules, which as a result lowers the reaction rate. If this intermediate binds strongly or permanently without reacting further, it may block or poison surface active sites and stop the reaction completely.

Moreover, this intermediate may undergo different mechanisms, either to yield the desired product or to produce competitive side products, depending on its binding affinity to the catalyst surface. For instance, when a benzyl radical adheres firmly to the catalyst surface, holes can facilitate a second electron transfer, transforming it into a benzyl cation. This benzyl cation is electron deficient and would be expected to react differently from a benzyl radical.

To conclude, all mechanisms will depend on the adsorption and desorption phenomena, but the precise mechanism will determine how each of these processes, adsorption and desorption, will affect the reaction rate. For a photocatalytic reaction to happen, the substrate and catalyst must be able to interact well so that electrons can move over a short distance. However, the adsorption and desorption states may not be important for other parts of the reaction pathway.

1.7 Aims of the project

The objective of this project is to obtain deep mechanistic understanding of how the factors mentioned in the literature review affect yield and selectivity of a heterogeneously catalysed organic photochemical coupling reaction. This will be done using Bi_2WO_6 as a model photocatalyst to facilitate chemical transformation, the formation of C-C bonds. Bi_2WO_6 is chosen because its bandgap lies at the edge of visible/UV boundary and it is known for photocatalytic properties in addition to its low cost and sustainability compared to precious metal polypyridyl complexes. The Giese reaction, addition of benzyl radical to electron deficient alkene, will be used as a model reaction. Giese reaction is chosen for its simplicity, comprising single electron oxidation of carboxylate to generate the intermediate radical on spontaneous decarboxylation. We aim to obtain mechanistic understanding of the factors affecting the efficiency and selectivity of this reaction, and use this understanding to optimise conditions for practical use of Bi_2WO_6 and other MOCS for organic photocatalysis. We will probe how metal oxide surface chemistry and structure affect activity and selectivity. In addition, the investigation will focus on the structure of the substrate and how it bonds to the solid surface in order to establish a relationship with the catalytic activity and selectivity.

In Chapter 2, Bi_2WO_6 nanoparticles with different crystallinity and surface area will be synthesised, and their crystal structure and morphology will be studied by powder X-ray (XRD) and scanning electron microscopy (SEM). Optical properties will be also examined by UV-Vis diffuse reflectance spectroscopy (UV-Vis DRS). The Giese reaction will assess the efficacy of synthesised nanoparticles in C-C bond formation. An investigation will be conducted to examine the impact of including a co-catalyst, specifically Pt, on optical characteristics using DRS.

Following this, Chapter 3 will involve experiments to elucidate the reaction pathways and unravel mechanistic features, with the aim of achieving enhanced selectivity. Photoluminescent spectroscopy (PL) will be utilised to compare pristine and platinised catalysts and uncover the role of the co-catalyst in catalytic efficiency. Subsequently, deuterium exchange and kinetic isotope studies using ^2H NMR and ^1H NMR, respectively, will be conducted in order to probe the reaction pathway and the rate-determining step. Additionally, the identification of radical intermediates will be conducted using electron paramagnetic resonance (EPR). Finally, adsorption of the reactants, phenylacetic acid and methacrolein, onto the Bi_2WO_6 surface will be studied with the help of ^1H NMR to determine which substrates exhibit strong binding and establish a correlation with reaction selectivity.

Chapter 4 will concentrate on reaction optimisation, specifically investigating the impact of Pt loading, catalyst quantity, and substrate electronic structure. This analysis aims to enhance our understanding of the variables that influence catalytic activity and reaction selectivity. Finally, in order to obtain some valuable fine chemicals, the reaction scope will be explored.

References

(1) Fresno, F.; Iglesias-Juez, A.; Coronado, J. M. Photothermal Catalytic CO2 Conversion: Beyond Catalysis and Photocatalysis. *Top. Curr. Chem.* **2023**, *381* (4), 21. https://doi.org/10.1007/s41061-023-00430-z.

(2) Zhu, S.; Wang, D. Photocatalysis: Basic Principles, Diverse Forms of Implementations and Emerging Scientific Opportunities. *Adv. Energy Mater.* **2017**, *7* (23), 1700841. https://doi.org/10.1002/aenm.201700841.

(3) Osterloh, F. E. Photocatalysis versus Photosynthesis: A Sensitivity Analysis of Devices for Solar Energy Conversion and Chemical Transformations. *ACS Energy Lett.* **2017**, *2* (2), 445–453. https://doi.org/10.1021/acsenergylett.6b00665.

(4) Vaiano, V.; Sannino, D.; Ciambelli, P. Steam Reduction of CO2 on Pd/TiO2 Catalysts: A Comparison between Thermal and Photocatalytic Reactions. *Photochem. Photobiol. Sci.* **2015**, *14* (3), 550–555. https://doi.org/10.1039/C4PP00252K.

(5) Ciamician, G. The Photochemistry of the Future. *Science* **1912**, *36* (926), 385–394. https://doi.org/10.1126/science.36.926.385.

(6) Prier, C. K.; Rankic, D. A.; MacMillan, D. W. C. Visible Light Photoredox Catalysis with Transition Metal Complexes: Applications in Organic Synthesis. *Chem. Rev.* **2013**, *113* (7), 5322–5363. https://doi.org/10.1021/cr300503r.

(7) Friedmann, D.; Hakki, A.; Kim, H.; Choi, W.; Bahnemann, D. Heterogeneous Photocatalytic Organic Synthesis: State-of-the-Art and Future Perspectives. *Green Chem.* **2016**, *18* (20), 5391–5411. https://doi.org/10.1039/C6GC01582D.

(8) Xia, Y.; Sayed, M.; Zhang, L.; Cheng, B.; Yu, J. Single-Atom Heterogeneous Photocatalysts. *Chem Catal.* **2021**, *1* (6), 1173–1214. https://doi.org/10.1016/j.checat.2021.08.009.

(9) Zhu, X.; Lin, Y.; San Martin, J.; Sun, Y.; Zhu, D.; Yan, Y. Lead Halide Perovskites for Photocatalytic Organic Synthesis. *Nat. Commun.* **2019**, *10* (1), 2843. https://doi.org/10.1038/s41467-019-10634-x.

(10) Xiang, X.; Wang, L.; Zhang, J.; Cheng, B.; Yu, J.; Macyk, W. Cadmium Chalcogenide (CdS, CdSe, CdTe) Quantum Dots for Solar-to-Fuel Conversion. *Adv. Photonics Res.* **2022**, *3* (11), 2200065. https://doi.org/10.1002/adpr.202200065.

(11) López-Salas, N.; Albero, J. CxNy: New Carbon Nitride Organic Photocatalysts. *Front. Mater.* **2021**, *8*. https://doi.org/10.3389/fmats.2021.772200.

(12) Wang, H.; Wang, H.; Wang, Z.; Tang, L.; Zeng, G.; Xu, P.; Chen, M.; Xiong, T.; Zhou, C.; Li, X.; Huang, D.; Zhu, Y.; Wang, Z.; Tang, J. Covalent Organic Framework Photocatalysts: Structures and Applications. *Chem. Soc. Rev.* **2020**, *49* (12), 4135–4165. https://doi.org/10.1039/D0CS00278J.

(13) Navalón, S.; Dhakshinamoorthy, A.; Álvaro, M.; Ferrer, B.; García, H. Metal–Organic Frameworks as Photocatalysts for Solar-Driven Overall Water Splitting. *Chem. Rev.* **2023**, *123* (1), 445–490. https://doi.org/10.1021/acs.chemrev.2c00460.

(14) Araújo, E. S.; Pereira, M. F. G.; da Silva, G. M. G.; Tavares, G. F.; Oliveira, C. Y. B.; Faia, P. M. A Review on the Use of Metal Oxide-Based Nanocomposites for the Remediation of Organics-Contaminated Water via Photocatalysis: Fundamentals, Bibliometric Study and Recent Advances. *Toxics* **2023**, *11* (8), 658. https://doi.org/10.3390/toxics11080658.

(15) Danish, M. S. S.; Estrella, L. L.; Alemaida, I. M. A.; Lisin, A.; Moiseev, N.; Ahmadi, M.; Nazari, M.; Wali, M.; Zaheb, H.; Senjyu, T. Photocatalytic Applications of Metal Oxides for Sustainable Environmental Remediation. *Metals* **2021**, *11* (1), 80. https://doi.org/10.3390/met11010080.

(16) Karthikeyan, C.; Arunachalam, P.; Ramachandran, K.; Al-Mayouf, A. M.; Karuppuchamy, S. Recent Advances in Semiconductor Metal Oxides with Enhanced Methods for Solar Photocatalytic Applications. *J. Alloys Compd.* **2020**, *828*, 154281. https://doi.org/10.1016/j.jallcom.2020.154281.

(17) Zhang, N.; Ciriminna, R.; Pagliaro, M.; Xu, Y.-J. Nanochemistry-Derived Bi2WO6 Nanostructures: Towards Production of Sustainable Chemicals and Fuels Induced by Visible Light. *Chem. Soc. Rev.* **2014**, *43* (15), 5276–5287. https://doi.org/10.1039/C4CS00056K.

(18) Riente, P.; Noël, T. Application of Metal Oxide Semiconductors in Light-Driven Organic Transformations. *Catal. Sci. Technol.* **2019**, *9* (19), 5186–5232. https://doi.org/10.1039/C9CY01170F.

(19) Litter, M. I. Heterogeneous Photocatalysis: Transition Metal Ions in Photocatalytic Systems. *Appl. Catal. B Environ.* **1999**, *23* (2), 89–114. https://doi.org/10.1016/S0926-3373(99)00069-7.

(20) Wang, S.; Lu, A.; Zhong, C.-J. Hydrogen Production from Water Electrolysis: Role of Catalysts. *Nano Converg.* **2021**, *8* (1), 4. https://doi.org/10.1186/s40580-021-00254-x.

(21) Maeda, K. Photocatalytic Water Splitting Using Semiconductor Particles: History and Recent Developments. *J. Photochem. Photobiol. C Photochem. Rev.* **2011**, *12* (4), 237–268. https://doi.org/10.1016/j.jphotochemrev.2011.07.001.

(22) Lee, Y. Y.; Jung, H. S.; Kang, Y. T. A Review: Effect of Nanostructures on Photocatalytic CO2 Conversion over Metal Oxides and Compound Semiconductors. *J. CO2 Util.* **2017**, *20*, 163–177. https://doi.org/10.1016/j.jcou.2017.05.019.

(23) Vaya, D.; Surolia, P. K. Semiconductor Based Photocatalytic Degradation of Pesticides: An Overview. *Environ. Technol. Innov.* **2020**, *20*, 101128. https://doi.org/10.1016/j.eti.2020.101128.

(24) Friedmann, D.; Hakki, A.; Kim, H.; Choi, W.; Bahnemann, D. Heterogeneous Photocatalytic Organic Synthesis: State-of-the-Art and Future Perspectives. *Green Chem.* **2016**, *18* (20), 5391–5411. https://doi.org/10.1039/C6GC01582D.

(25) Yadav, G. D.; Mewada, R. K.; Wagh, D. P.; Manyar, H. G. Advances and Future Trends in Selective Oxidation Catalysis: A Critical Review. Catal. Sci. Technol. 2022, 12 (24), 7245–7269. https://doi.org/10.1039/D2CY01322C.

(26) Higashimoto, S.; Okada, K.; Morisugi, T.; Azuma, M.; Ohue, H.; Kim, T.-H.; Matsuoka, M.; Anpo, M. Effect of Surface Treatment on the Selective Photocatalytic Oxidation of Benzyl Alcohol into Benzaldehyde by O2 on TiO2 Under Visible Light. *Top. Catal.* **2010**, *53* (7), 578–583. https://doi.org/10.1007/s11244-010-9490-z.

(27) Unsworth, C. A.; Coulson, B.; Chechik, V.; Douthwaite, R. E. Aerobic Oxidation of Benzyl Alcohols to Benzaldehydes Using Monoclinic Bismuth Vanadate Nanoparticles under Visible Light Irradiation: Photocatalysis Selectivity and Inhibition. *J. Catal.* **2017**, *354*, 152–159. https://doi.org/10.1016/j.jcat.2017.08.023.

(28) Zhang, Y.; Zhang, N.; Tang, Z.-R.; Xu, Y.-J. Identification of Bi2WO6 as a Highly Selective Visible-Light Photocatalyst toward Oxidation of Glycerol to Dihydroxyacetone in Water. *Chem. Sci.* **2013**, *4* (4), 1820–1824. https://doi.org/10.1039/C3SC50285F.

(29) Kou, J.; Lu, C.; Wang, J.; Chen, Y.; Xu, Z.; Varma, R. S. Selectivity Enhancement in Heterogeneous Photocatalytic Transformations. *Chem. Rev.* **2017**, *117* (3), 1445–1514. https://doi.org/10.1021/acs.chemrev.6b00396.

(30) Maldotti, A.; Molinari, A. Design of Heterogeneous Photocatalysts Based on Metal Oxides to Control the Selectivity of Chemical Reactions. *Top. Curr. Chem.* **2011**, *303*, 185–216. https://doi.org/10.1007/128_2011_140.

(31) Tyagi, A.; Yamamoto, A.; Kato, T.; Yoshida, H. Bifunctional Property of Pt Nanoparticles Deposited on TiO2 for the Photocatalytic sp3C–sp3C Cross-Coupling Reactions between THF and Alkanes. *Catal. Sci. Technol.* **2017**, *7* (12), 2616–2623. https://doi.org/10.1039/C7CY00535K.

(32) Marina, N.; Lanterna, A. E.; Scaiano, J. C. Expanding the Color Space in the Two-Color Heterogeneous Photocatalysis of Ullmann C–C Coupling Reactions. *ACS Catal.* **2018**, *8* (8), 7593–7597. https://doi.org/10.1021/acscatal.8b02026.

(33) Chen, Y.; Feng, L. Silver Nanoparticles Doped TiO2 Catalyzed Suzuki-Coupling of Bromoaryl with Phenylboronic Acid under Visible Light. *J. Photochem. Photobiol. B* **2020**, *205*, 111807. https://doi.org/10.1016/j.jphotobiol.2020.111807.

(34) Manley, D. W.; McBurney, R. T.; Miller, P.; Howe, R. F.; Rhydderch, S.; Walton, J. C. Unconventional Titania Photocatalysis: Direct Deployment of Carboxylic Acids in Alkylations and Annulations. *J. Am. Chem. Soc.* **2012**, *134* (33), 13580–13583. https://doi.org/10.1021/ja306168h.

(35) Buglioni, L.; Riente, P.; Palomares, E.; Pericàs, M. A. Visible-Light-Promoted Arylation Reactions Photocatalyzed by Bismuth(III) Oxide. *Eur. J. Org. Chem.* **2017**, *2017* (46), 6986–6990. https://doi.org/10.1002/ejoc.201701242.

(36) Ibhadon, A. O.; Fitzpatrick, P. Heterogeneous Photocatalysis: Recent Advances and Applications. *Catalysts* **2013**, *3* (1), 189–218. https://doi.org/10.3390/catal3010189.

(37) Wen, J.; Xie, J.; Chen, X.; Li, X. A Review on G-C3N4-Based Photocatalysts. *Appl. Surf. Sci.* **2017**, *391*, 72–123. https://doi.org/10.1016/j.apsusc.2016.07.030.

(38) Khan, A. A.; Tahir, M. Recent Advancements in Engineering Approach towards Design of Photo-Reactors for Selective Photocatalytic CO2 Reduction to Renewable Fuels. *J. CO2 Util.* **2019**, *29*, 205–239. https://doi.org/10.1016/j.jcou.2018.12.008.

(39) Calza, P.; Minella, M.; Demarchis, L.; Sordello, F.; Minero, C. Photocatalytic Rate Dependence on Light Absorption Properties of Different TiO2 Specimens. *Catal. Today* **2020**, *340*, 12–18. https://doi.org/10.1016/j.cattod.2018.10.013.

(40) Montoya, J. F.; Velásquez, J. A.; Salvador, P. The Direct–Indirect Kinetic Model in Photocatalysis: A Reanalysis of Phenol and Formic Acid Degradation Rate Dependence on Photon Flow and Concentration in TiO2 Aqueous Dispersions. *Appl. Catal. B Environ.* **2009**, *88* (1), 50–58. https://doi.org/10.1016/j.apcatb.2008.09.035.

(41) Henderson, M. A. A Surface Science Perspective on TiO2 Photocatalysis. *Surf. Sci. Rep.* **2011**, *66* (6), 185–297. https://doi.org/10.1016/j.surfrep.2011.01.001.

(42) Hassaan, M. A.; El-Nemr, M. A.; Elkatory, M. R.; Ragab, S.; Niculescu, V.-C.; El Nemr, A. Principles of Photocatalysts and Their Different Applications: A Review. *Top. Curr. Chem.* **2023**, *381* (6), 31. https://doi.org/10.1007/s41061-023-00444-7.

(43) Gharibshahi, E.; Saion, E.; Johnston, R. L.; Ashraf, A. Theory and Experiment of Optical Absorption of Platinum Nanoparticles Synthesized by Gamma Radiation. *Appl. Radiat. Isot.* **2019**, *147*, 204–210. https://doi.org/10.1016/j.apradiso.2019.02.015.

(44) Mayer, K. M.; Hafner, J. H. Localized Surface Plasmon Resonance Sensors. *Chem. Rev.* **2011**, *111* (6), 3828–3857. https://doi.org/10.1021/cr100313v.

(45) Clavero, C. Plasmon-Induced Hot-Electron Generation at Nanoparticle/Metal-Oxide Interfaces for Photovoltaic and Photocatalytic Devices. *Nat. Photonics* **2014**, *8* (2), 95–103. https://doi.org/10.1038/nphoton.2013.238.

(46) Feng, L.; Fu, H.; Zhang, T.; Zhang, Q.; Ren, S.; Cheng, J.; Liang, Q.; Xiao, X. Synergy of Oxygen Vacancies and Bi Nanoparticles on BiOBr Nanosheets for Enhanced Photocatalytic H2O2 Production. *New J. Chem.* **2024**, *48* (5), 1998–2007. https://doi.org/10.1039/D3NJ03815G.

(47) Chen, P.; Liu, H.; Cui, W.; Lee, S. C.; Wang, L.; Dong, F. Bi-Based Photocatalysts for Light-Driven Environmental and Energy Applications: Structural Tuning, Reaction

Mechanisms, and Challenges. *EcoMat* **2020**, *2* (3), e12047. https://doi.org/10.1002/eom2.12047.

(48) Chen, J.; Cen, J.; Xu, X.; Li, X. The Application of Heterogeneous Visible Light Photocatalysts in Organic Synthesis. *Catal. Sci. Technol.* **2016**, *6* (2), 349–362. https://doi.org/10.1039/C5CY01289A.

(49) Bigall, N. C.; Härtling, T.; Klose, M.; Simon, P.; Eng, L. M.; Eychmüller, A. Monodisperse Platinum Nanospheres with Adjustable Diameters from 10 to 100 Nm: Synthesis and Distinct Optical Properties. *Nano Lett.* **2008**, *8* (12), 4588–4592. https://doi.org/10.1021/nl802901t.

(50) Deng, H.; Zhu, X.; Chen, Z.; Zhao, kai; Cheng, G. Oxygen Vacancy Engineering of TiO2-x Nanostructures for Photocatalytic CO2 Reduction. *Carbon Lett.* **2022**, *32* (7), 1671–1680. https://doi.org/10.1007/s42823-022-00385-z.

(51) Zhang, J.; Li, J. The Oxygen Vacancy Defect of ZnO/NiO Nanomaterials Improves Photocatalytic Performance and Ammonia Sensing Performance. *Nanomaterials* **2022**, *12* (3), 433. https://doi.org/10.3390/nano12030433.

(52) Li, J.; Zhang, M.; Guan, Z.; Li, Q.; He, C.; Yang, J. Synergistic Effect of Surface and Bulk Single-Electron-Trapped Oxygen Vacancy of TiO2 in the Photocatalytic Reduction of CO2. *Appl. Catal. B Environ.* **2017**, *206*, 300–307. https://doi.org/10.1016/j.apcatb.2017.01.025.

(53) Ma, H.; Yang, W.; Tang, H.; Pan, Y.; Li, W.; Fang, R.; Shen, Y.; Dong, F. Enhance the Stability of Oxygen Vacancies in SrTiO3 via Metallic Ag Modification for Efficient and Durable Photocatalytic NO Abatement. *J. Hazard. Mater.* **2023**, *452*, 131269. https://doi.org/10.1016/j.jhazmat.2023.131269.

(54) Li, H.; Wang, S.; Tang, J.; Xie, H.; Ma, J.; Chi, H.; Li, C. Roles of Oxygen Vacancies in Surface Plasmon Resonance Photoelectrocatalytic Water Oxidation. *Cell Rep. Phys. Sci.* **2023**, *4* (5), 101386. https://doi.org/10.1016/j.xcrp.2023.101386.

(55) Liu, Z.; Luo, M.; Meng, L.; Su, S.; Ding, W.; Yuan, S.; Li, H.; Li, X. Plasma Ag Nanoparticles Loaded on Bi2MoO6 to Enhance Surface Oxygen Vacancies for Efficient Nitrogen Conversion to Ammonia. *J. Mater. Chem. C* **2024**. https://doi.org/10.1039/D4TC01521E.

(56) Ajmal, A.; Majeed, I.; Malik, R. N.; Idriss, H.; Nadeem, M. A. Principles and Mechanisms of Photocatalytic Dye Degradation on TiO2 Based Photocatalysts: A Comparative Overview. *RSC Adv.* **2014**, *4* (70), 37003–37026. https://doi.org/10.1039/C4RA06658H.

(57) Zhao, J.; Chen, C.; Ma, W. Photocatalytic Degradation of Organic Pollutants Under Visible Light Irradiation. *Top. Catal.* **2005**, *35* (3), 269–278. https://doi.org/10.1007/s11244-005-3834-0.

(58) Juliá, F. Ligand-to-Metal Charge Transfer (LMCT) Photochemistry at 3d-Metal Complexes: An Emerging Tool for Sustainable Organic Synthesis. *ChemCatChem* **2022**, *14* (19), e202200916. https://doi.org/10.1002/cctc.202200916.

(59) Yamamoto, A.; Ohara, T.; Yoshida, H. Visible-Light-Induced Photocatalytic Benzene/Cyclohexane Cross-Coupling Utilizing a Ligand-to-Metal Charge Transfer Benzene Complex Adsorbed on Titanium Oxides. *Catal. Sci. Technol.* **2018**, *8* (8), 2046–2050. https://doi.org/10.1039/C7CY02566A.

(60) Liu, G.; Yu, J. C.; Lu, G. Q. (Max); Cheng, H.-M. Crystal Facet Engineering of Semiconductor Photocatalysts: Motivations, Advances and Unique Properties. *Chem. Commun.* **2011**, *47* (24), 6763–6783. https://doi.org/10.1039/C1CC10665A.

(61) Cotta, M. A. Quantum Dots and Their Applications: What Lies Ahead? *ACS Appl. Nano Mater.* **2020**, *3* (6), 4920–4924. https://doi.org/10.1021/acsanm.0c01386.

(62) Yuan, Y.; Jin, N.; Saghy, P.; Dube, L.; Zhu, H.; Chen, O. Quantum Dot Photocatalysts for Organic Transformations. *J. Phys. Chem. Lett.* **2021**, *12* (30), 7180–7193. https://doi.org/10.1021/acs.jpclett.1c01717.

(63) Ge, M.; Cao, C.; Huang, J.; Li, S.; Chen, Z.; Zhang, K.-Q.; Al-Deyab, S. S.; Lai, Y. A Review of One-Dimensional TiO2 Nanostructured Materials for Environmental and Energy Applications. *J. Mater. Chem. A* **2016**, *4* (18), 6772–6801. https://doi.org/10.1039/C5TA09323F.

(64) Kumbhakar, P.; Chowde Gowda, C.; Mahapatra, P. L.; Mukherjee, M.; Malviya, K. D.; Chaker, M.; Chandra, A.; Lahiri, B.; Ajayan, P. M.; Jariwala, D.; Singh, A.; Tiwary, C. S. Emerging 2D Metal Oxides and Their Applications. *Mater. Today* **2021**, *45*, 142–168. https://doi.org/10.1016/j.mattod.2020.11.023.

(65) He, X.; Zhang, C. Recent Advances in Structure Design for Enhancing Photocatalysis. *J. Mater. Sci.* **2019**, *54* (12), 8831–8851. https://doi.org/10.1007/s10853-019-03417-8.

(66) Boccalon, E.; Gorrasi, G.; Nocchetti, M. Layered Double Hydroxides Are Still out in the Bloom: Syntheses, Applications and Advantages of Three-Dimensional Flower-like Structures. *Adv. Colloid Interface Sci.* **2020**, *285*, 102284. https://doi.org/10.1016/j.cis.2020.102284.

(67) Lee, K.; Yoon, H.; Ahn, C.; Park, J.; Jeon, S. Strategies to Improve the Photocatalytic Activity of TiO 2 : 3D Nanostructuring and Heterostructuring with Graphitic Carbon Nanomaterials. *Nanoscale* **2019**, *11* (15), 7025–7040. https://doi.org/10.1039/C9NR01260E.

(68) Zhou, X.; Dong, H. A Theoretical Perspective on Charge Separation and Transfer in Metal Oxide Photocatalysts for Water Splitting. *ChemCatChem* **2019**, *11* (16), 3688–3715. https://doi.org/10.1002/cctc.201900567.

(69) Lazzeri, M.; Vittadini, A.; Selloni, A. Structure and Energetics of Stoichiometric ${\mathrm{TiO}}_{2}$ Anatase Surfaces. *Phys. Rev. B* **2001**, *63* (15), 155409. https://doi.org/10.1103/PhysRevB.63.155409.

(70) Kusior, A.; Synowiec, M.; Zakrzewska, K.; Radecka, M. Surface-Controlled Photocatalysis and Chemical Sensing of TiO2, α-Fe2O3, and Cu2O Nanocrystals. *Crystals* **2019**, *9* (3), 163. https://doi.org/10.3390/cryst9030163.

(71) Chávez-Rocha, R.; Mercado-Sánchez, I.; Vargas-Rodriguez, I.; Hernández-Lima, J.; Bazán-Jiménez, A.; Robles, J.; García-Revilla, M. A. Modeling Adsorption of CO2 in Rutile Metallic Oxide Surfaces: Implications in CO2 Catalysis. *Molecules* **2023**, *28* (4), 1776. https://doi.org/10.3390/molecules28041776.

(72) Tan, R.; Lv, Z.; Tang, J.; Wang, Y.; Guo, J.; Li, L. Theoretical Study of the Adsorption Characteristics and the Environmental Influence of Ornidazole on the Surface of Photocatalyst TiO2. *Sci. Rep.* **2019**, *9* (1), 10891. https://doi.org/10.1038/s41598-019-47379-y.

(73) D'Arienzo, M.; Carbajo, J.; Bahamonde, A.; Crippa, M.; Polizzi, S.; Scotti, R.; Wahba, L.; Morazzoni, F. Photogenerated Defects in Shape-Controlled TiO2 Anatase Nanocrystals: A Probe To Evaluate the Role of Crystal Facets in Photocatalytic Processes. *J. Am. Chem. Soc.* **2011**, *133* (44), 17652–17661. https://doi.org/10.1021/ja204838s.

(74) Li, G.; Fang, K.; Ou, Y.; Yuan, W.; Yang, H.; Zhang, Z.; Wang, Y. Surface Study of the Reconstructed Anatase TiO2 (001) Surface. *Prog. Nat. Sci. Mater. Int.* **2021**, *31* (1), 1–13. https://doi.org/10.1016/j.pnsc.2020.11.002.

(75) Dai, Y.; Xiong, Y. Control of Selectivity in Organic Synthesis via Heterogeneous Photocatalysis under Visible Light. *Nano Res. Energy* **2022**, *1*, e9120006. https://doi.org/10.26599/NRE.2022.9120006.

(76) Singh, M.; Chan Cha, D.; Ibomcha Singh, T.; Maibam, A.; Ram Paudel, D.; Hwan Nam, D.; Hyeong Kim, T.; Yoo, S.; Lee, S. A Critical Review on Amorphous–Crystalline Heterostructured Electrocatalysts for Efficient Water Splitting. *Mater. Chem. Front.* **2023**, *7* (24), 6254–6280. https://doi.org/10.1039/D3QM00940H.

(77) Andersson, M.; Österlund, L.; Ljungström, S.; Palmqvist, A. Preparation of Nanosize Anatase and Rutile TiO2 by Hydrothermal Treatment of Microemulsions and Their Activity for Photocatalytic Wet Oxidation of Phenol. *J. Phys. Chem. B* **2002**, *106* (41), 10674–10679. https://doi.org/10.1021/jp025715y.

(78) Sun, J.; Gao, L.; Zhang, Q. Synthesizing and Comparing the Photocatalytic Properties of High Surface Area Rutile and Anatase Titania Nanoparticles. *J. Am. Ceram. Soc.* **2003**, *86* (10), 1677–1682. https://doi.org/10.1111/j.1151-2916.2003.tb03539.x.

(79) Pan, M.; Teng, X.; Li, M.; Pan, X.; Liao, Q.; Cheng, W.; Yang, R. A Facile Approach for Surface Modification of TiO2 Nanosheets to Enhance Photocatalytic Hydrogen Evolution Activity. *J. Nanoparticle Res.* **2021**, *23* (12), 260. https://doi.org/10.1007/s11051-021-05369-0.

(80) Xu, X.; Liu, H.; Wang, J.; Chen, T.; Ding, X.; Chen, H. Insight into Surface Hydroxyl Groups for Environmental Purification: Characterizations, Applications and Advances. *Surf. Interfaces* **2021**, *25*, 101272. https://doi.org/10.1016/j.surfin.2021.101272.

(81) Hanawa, T. Biofunctionalization of Metallic Materials: Creation of Biosis–Abiosis Intelligent Interface. In *Interface Oral Health Science 2014*; Sasaki, K., Suzuki, O., Takahashi, N., Eds.; Springer Japan: Tokyo, 2015; pp 53–64. https://doi.org/10.1007/978-4-431-55192-8_5.

(82) Tamura, H.; Mita, K.; Tanaka, A.; Ito, M. Mechanism of Hydroxylation of Metal Oxide Surfaces. *J. Colloid Interface Sci.* **2001**, *243* (1), 202–207. https://doi.org/10.1006/jcis.2001.7864.

(83) Henderson, M. A. Effect of Coadsorbed Water on the Photodecomposition of Acetone on TiO2(110). *J. Catal.* **2008**, *256* (2), 287–292. https://doi.org/10.1016/j.jcat.2008.03.020.

(84) Qu, Q.; Geng, H.; Peng, R.; Cui, Q.; Gu, X.; Li, F.; Wang, M. Chemically Binding Carboxylic Acids onto TiO2 Nanoparticles with Adjustable Coverage by Solvothermal Strategy. *Langmuir* **2010**, *26* (12), 9539–9546. https://doi.org/10.1021/la100121n.

(85) Wu, W.-C.; Chuang, C.-C.; Lin, J.-L. Bonding Geometry and Reactivity of Methoxy and Ethoxy Groups Adsorbed on Powdered TiO2. *J. Phys. Chem. B* **2000**, *104* (36), 8719–8724. https://doi.org/10.1021/jp0017184.

(86) Henderson, M. A. Photooxidation of Acetone on TiO2(110): Conversion to Acetate via Methyl Radical Ejection. *J. Phys. Chem. B* **2005**, *109* (24), 12062–12070. https://doi.org/10.1021/jp0507546.

(87) Yang, Q.; Dong, L.; Su, R.; Hu, B.; Wang, Z.; Jin, Y.; Wang, Y.; Besenbacher, F.; Dong, M. Nanostructured Heterogeneous Photo-Catalysts for Hydrogen Production and Water Splitting: A Comprehensive Insight. *Appl. Mater. Today* **2019**, *17*, 159–182. https://doi.org/10.1016/j.apmt.2019.07.016.

(88) Zheng, J.; Zhao, W.; Song, L.; Wang, H.; Yan, H.; Chen, G.; Han, C.; Zhang, J. Advances of Manganese-Oxides-Based Catalysts for Indoor Formaldehyde Removal. *Green Energy Environ.* **2023**, *8* (3), 626–653. https://doi.org/10.1016/j.gee.2022.01.008.

(89) Bratan, V.; Vasile, A.; Chesler, P.; Hornoiu, C. Insights into the Redox and Structural Properties of CoOx and MnOx: Fundamental Factors Affecting the

Catalytic Performance in the Oxidation Process of VOCs. *Catalysts* **2022**, *12* (10), 1134. https://doi.org/10.3390/catal12101134.

Chapter 2: Synthesis and characterisation of bismuth tungstate and modified bismuth tungstate

2.1 Introduction

2.1.1 Bismuth tungstate (Bi_2WO_6): structure and properties

Bi_2WO_6 belongs to the Aurivillius family and is distinguished by its distinctive structure. The compound is comprising alternating layers of perovskite-like $[WO_4]^{2-}$ anions and bismuth oxide $[Bi_2O_2]^{2+}$ cations (Figure 2.1).[1–3] This configuration offers benefits in terms of assisting the efficient separation of photogenerated charge carriers, notably electron-hole pairs, and enhancing the creation of internal electric fields between the layers. Consequently, the photocatalytic performance is improved.

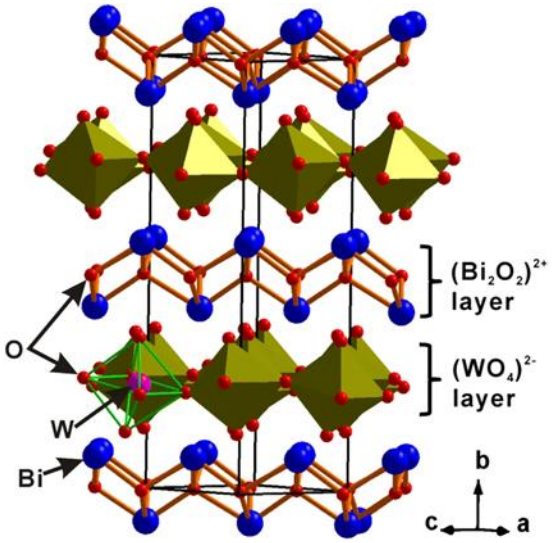

Figure 2.1: Crystal structure of Bi_2WO_6 (Reprinted form Ref. [2] with permission from Springer Nature).[2]

The analysis of the band structure reveals that the process of charge transfer in Bi_2WO_6, which is triggered by photoexcitation, involves the movement of electrons from the hybrid orbitals formed by the combination of O 2p and Bi 6s orbitals in the valence band (VB) to the unoccupied W 5d orbitals in the conduction band (CB) (Figure 2.2). This separation is key to increasing the photocatalytic efficacy of Bi_2WO_6.

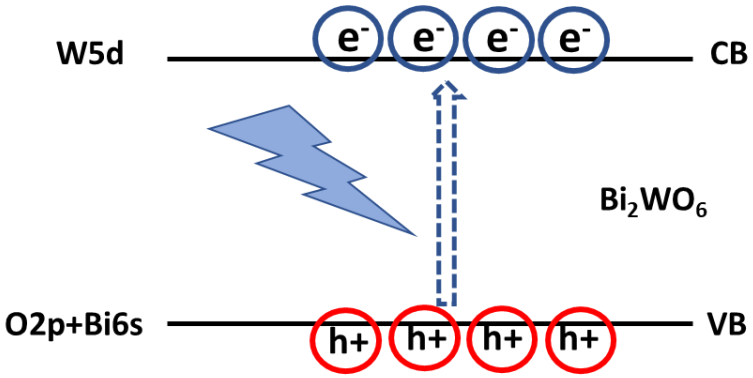

Figure 2.2: Simplified systematic diagram showing valance and conduction bands of unmodified Bi_2WO_6.[4]

2.1.2 Electrical properties of Bi_2WO_6

Bi_2WO_6 materials exhibit unique properties, including piezoelectricity and ferroelectricity. Piezoelectricity is a characteristic shown by specific crystal phases that undergo electrical polarisation when subjected to mechanical stress, and conversely, deform when an electric field is applied to them.[5] This feature is utilised in sensors that detect acoustic, shock, and vibration waves. On the other hand, ferroelectricity is the property of a material to display an electrical polarisation in its natural state, which can be reversed by an external electric field.[6,7]

2.1.3 Micro/nanostructure of Bi_2WO_6

Despite the importance of obtaining a single crystal of Bi_2WO_6, which is good for electrical applications, these crystals lack high surface area, which is an important feature for photocatalytic applications. Thus, the synthesis of nanostructured Bi_2WO_6 has been successfully achieved by researchers, who have subsequently explored its potential uses in many fields including water splitting, carbon dioxide reduction, pollutant degradation, and chemical synthesis.[3] The main advantage of having a nanostructure semiconductor is the increase in surface area and energy. The increase in surface energy is correlated with increase in surface area. As particle size decreases, surface area (SA) increases. As a result, semiconductor activity will increase as more active and binding sites (high surface area) are available for adsorbed substrate. Before describing the synthesis methods of nanostructured Bi_2WO_6, a brief background about the Bi_2WO_6 formation mechanism is discussed.

2.1.4 Bismuth tungstate particles formation mechanism

The proposed chemical reactions for Bi_2WO_2 is described in (Equation 2.1). Upon mixing bismuth nitrate with water, the bismuth nitrate undergoes hydrolysis and releases

bismuth oxynitrate and nitric acid. The bismuth oxynitrate is insoluble in water. The formed nitric acid in situ reacts with dissolved sodium tungstate to form tungstic acid. The oxynitrate would also form a complex with water resulting in multilayer bismuth nitrate which would react later with tungstic acid to form final bismuth tungstate.[8,9]

Equation 2.1

$$2\,Bi(NO_3)_3 + Na_2WO_4 + 2\,H_2O \xrightarrow[180\ ^oC\ -\ 24\ h]{H_2O} Bi_2WO_6 + 2\,NaNO_3 + 4\,HNO_3 \quad (1)$$

$$Bi(NO_3)_3 + H_2O \rightleftharpoons BiONO_3 + 2\,HNO_3 \quad (1.1)$$

$$Na_2WO_4 + 2\,HNO_3 \longrightarrow H_2WO_4 + 2\,NaNO_3 \quad (1.2)$$

$$BiONO_3 + H_2O \rightleftharpoons Bi_2O_2(OH)NO_3 + HNO_3 \quad (1.3)$$

$$Bi_2O_2(OH)NO_3 + H_2WO_4 \longrightarrow Bi_2WO_6 + HNO_3 + H_2O \quad (1.4)$$

The crystal formation of Bi_2WO_6 is also proposed which could proceed via several steps during hydrothermal treatment (scheme 2.1).[10]

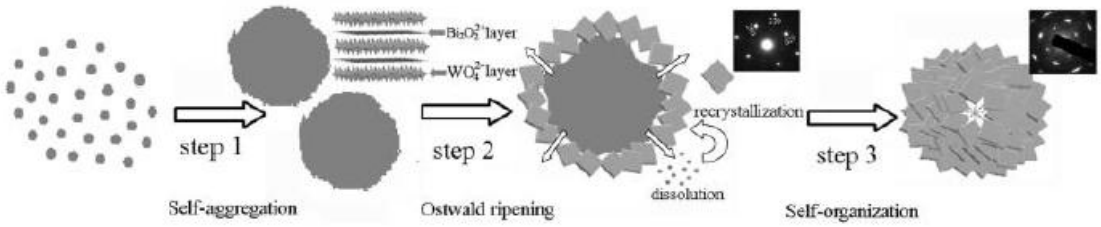

Scheme 2.1: flower-like bismuth tungstate formation steps. [10]

In the early stages of the hydrothermal process, the nanoparticles self-aggregate, which leads to the formation of spherical microparticles (step 1, scheme 2.1).

The hydrothermal treatment procedure leads to the dissolution of smaller crystallites that are found on the surface of spherical microparticles. This dissolution generates $(Bi_2O_2)^{2+}$ and $(WO_4)^{2-}$ ions in an acid aqueous medium. The solid microspheres contain numerous microscopic protrusions on their surfaces, (step 2, scheme 2.1), which provide a significant number of high-energy sites for the growth of nanocrystals.

The occurrence of dissolution and recrystallization, also referred to as Ostwald ripening, is a commonly seen crystallisation phenomenon. In the course of this particular procedure, it is observed that the ions of $(Bi_2O_2)^{2+}$ and $(WO_4)^{2-}$ in the solution display a tendency for migrating towards and adhering to the surfaces of microparticles possessing a spherical morphology. In addition, the nanocrystals of Bi_2WO_6 develop two-

dimensional plate-like formations with a single-crystal composition when subjected to hydrothermal conditions. This behaviour can be attributed to the considerable intrinsic anisotropic properties exhibited by these nanocrystals. The crystalline structure of Bi_2WO_6 consists of orthorhombic arrangements, wherein $(Bi_2O_2)^{2+}$ layers and perovskite-like $(WO_4)^{2-}$ layers are arranged in an alternating manner.

The reduction in the quantity of solid spherical microparticles is a result of mass diffusion and Ostwald ripening when the hydrothermal process is prolonged.[11,12] As a result, a considerable number of Bi_2WO_6 nanoplates are produced, which act as the primary building blocks for the creation of a three-dimensional flower-like morphology, (step 3, scheme 2.1).

2.2 Bi_2WO_6 synthesis methods

There are different synthesis methods employed to obtain Bi_2WO_6 microparticles including solid-state synthesis,[11–13] sol-gel,[14–17] hydrothermal[10,18–20] or solvothermal[20] and microwave-assisted methods.[21–24] Among all these, hydrothermal synthesis using conventional heating or microwave-assisted heating are considered environmentally friendly as water is used as the most common solvent and microwave one assists hydrothermal synthesis by reducing the time of reaction. Also, both methods, conventional and microwave-assisted hydrothermal, have minimum synthesis steps compared to the other methods.

2.2.1 Hydrothermal metal oxide synthesis

Hydrothermal synthesis is employed for compounds that exhibit insolubility at standard temperature and pressure conditions, typically below 100 °C and 1 atm. Upon increasing temperature, the solvent properties such as dielectric constant undergo significant alterations. The critical temperature and pressure values for water are reported as 374 °C and 22.1 MPa, respectively.[25] However, hydrothermal synthesis using Teflon liners is often conducted at temperatures below 300 °C as Teflon softens considerably above 220 ºC. While microwave assisted hydrothermal synthesis carried out using glass container can go above 300 ºC, there is a risk of volatility of reactant and pressure build up. At room temperature, water has a dielectric constant of 78, promoting the solubility of polar inorganic salts in water but has a negative correlation with temperature, whereby an increase in temperature leads to a reduction in its dielectric constant.[26] Therefore, at high hydrothermal temperature (≈ 200 ºC) and with decrease in dielectric constant (≈ 35), solubility will decrease, promoting crystal growth.[27]

The hydrothermal method for synthesising bismuth tungstate involves the use of either an autoclave or a sealed Teflon container with bismuth and tungsten precursors in a

water-based solution under conditions of elevated temperature and pressure. Upon heating nitric acid is evolved therefore in terms of safety, a closed system is advantageous. Importantly, hydrothermal synthesis tends to have a high level of reproducibility to obtain crystals with specific morphology. This should also support reproducible photocatalysis.

2.2.1.1 Hydrothermal and solvothermal synthesis of Bi_2WO_6

The predominant morphology observed in Bi_2WO_6 is characterised by a flower-like structure. This three-dimensional (3D) structure has been shown to photocatalytically degrade a wide range of organic contaminants. The microstructure is generally crystalline whilst achieving a reasonable surface area. For example, Zhao et al.[20] synthesised Bi_2WO_6 nanoflower structures by a hydrothermal (water as solvent) and solvothermal (ethylene glycol (EG) as solvent) methods using conventional heating (CH), employing $Bi(NO_3)_3.5H_2O$ and $Na_2WO_4.2H_2O$ as precursor materials. The maximum surface area achieved was 26 m^2 / g for Bi_2WO_6 prepared in water which they attributed to nanoplates on Bi_2WO_6 surface. For photocatalytic applications, the antibiotic ceftriaxone was degraded 70% with sample prepared in water compared to 63% for the sample synthesised in EG. They concluded the high photocatalytic activity of water-synthesised sample is because of morphology.

L. Zhang et al.[10] also employed a hydrothermal method to synthesise a Bi_2WO_6 material with a flower-like morphology. In this study, they demonstrated the effect of crystallinity and surface area. They prepared Bi_2WO_6 using CH and examined the impact of varying calcination temperature on the surface area. The uncalcined sample exhibited a surface area (SA) of 33.68 m^2 / g (Figure 2.3), while the calcined sample displayed a surface area of 4.33 m^2 / g.

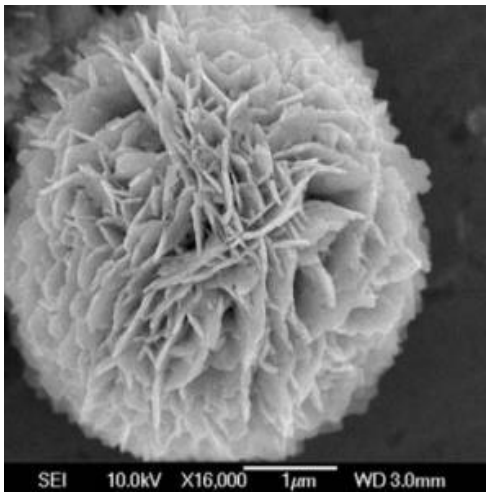

Figure 2.3: SEM image of uncalcined Bi_2WO_6 synthesised as 160 °C for 20 h showing flower-like morphology.[10]

Calcination was shown to enhance the degree of crystallinity. Photocatalytic degradation of Rhodamine B (RhB) showed both uncalcined and calcined samples exhibited significant photocatalytic activity in the breakdown of the dye (84% vs 97% RhB conversion, respectively). Hydrothermal synthesis method still showed good photocatalytic activity even without calcination post treatment.

Despite having different surface areas low surface area with high crystallinity could degrade the dye as efficiently as Bi_2WO_6 with higher surface area but lower crystallinity. Although the authors did not give compelling reasons for comparable reactivity better separation of photogenerated charges is expected with greater crystallinity.

2.2.2 Microwave-assisted synthesis of metal oxide

The utilisation of microwave radiation for the synthesis of metal oxide nanomaterials has experienced significant advancements. This is mostly due to the ability of microwave radiation to rapidly heat the reaction system, leading to an accelerated reaction rate and a consequent reduction in the overall reaction time.

2.2.2.1 Microwave-assisted synthesis of Bi_2WO_6

In general, the utilisation of microwave-assisted methods for the synthesis of metal oxides results in the production of small particles especially when organic solvent such as EG is used. EG stabilises these small particles by inhibiting agglomeration. Consequently, this approach enables the acquisition of a catalyst with a high surface area. There were some reports on microwave assisted synthesis of Bi_2WO_6. For instance, Cao et al.[23] employed a microwave-assisted technique to synthesise Bi_2WO_6 nanoparticles with a flower-like morphology. The initial substances employed in this study consisted of $Bi(NO_3)_3.5H_2O$ and Na_2WO_4. Additionally, hexamethylene tetraamine (HMT) was included to regulate pH. The duration of the reaction was 5 minutes, with a temperature of 180 °C. The reaction mixture was immediately cooled to room temperature using compressed air. Rapid cooling could help stop nucleation. The powder that was obtained exhibited a crystalline phase of Bi_2WO_6 with an orthorhombic structure. The elemental analysis revealed the presence of an additional carbon peak in the energy-dispersive X-ray spectroscopy (EDS) spectrum, potentially originating from the absorption of HMT. The SEM image related to the synthesised catalyst is depicted in (Figure 2.4).

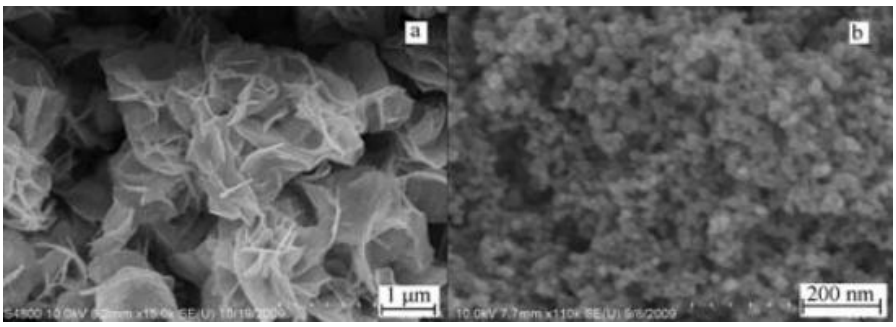

Figure 2.4: SEM image of Bi_2WO_6 nanoparticles prepared (a) without and (b) with HTM.[23] Reused with permission from ref. (23).

They also examined the impact of reaction temperature variation where they observed that elevated temperatures are conducive to the formation of flower-like microstructures. Furthermore, it is evident that the utilisation of HMT had a significant impact on final morphology by reducing particles size. In addition, the researchers investigated the impact of calcination temperature on the crystallinity and morphology of Bi_2WO_6. It was observed that an increase in the calcination temperature resulted in an enhancement of crystallinity. It is important to mention that Bi_2WO_6 has high thermal stability where its melting temperature is above 800 ºC. Nevertheless, the floral morphology disappeared after elevating the calcination temperature to 500 °C. Here, while high annealing temperature could induce crystallinity, it will affect morphology negatively. The researchers assessed the photocatalytic performance of Bi_2WO_6 using Rhodamine B (RhB), a representative chemical dye, as a model pollutant for this purpose. The researchers discovered that Bi_2WO_6 in the form of flower-like structures had a significantly higher dye removal efficiency of 99% when compared to other morphologies.

In addition, the above paper describes preparation of the flower type structure without HTM which exhibited high photocatalytic activity compared to sample that prepared with HTM. Despite having high surface area with HTM sample (44 m^2/g), the morphology of the sample prepared without HTM showed improved crystallinity and had higher activity. This paper also confirmed that both morphology and crystallinity are important in photocatalytic activity.

Phu et al.[21] conducted a study in which they employed the microwave-assisted approach to synthesise of Bi_2WO_6 nanoparticles. In their experimental procedure, they utilised water as the main solvent. The microwave power utilised in the experiment was 500 watts but they did not explain what temperature was used. The duration of the reaction was 30 minutes. The acquired sample was subjected to a drying process, followed by calcination at various temperatures in air. The researchers observed a correlation between calcination temperature and the development of crystallinity, whereby

increasing the annealing temperature resulted in improved crystallinity which was confirmed by XRD and uncalcined material was found to be amorphous. Furthermore, it was observed that an increase in the calcination temperature resulted in an increase in the particle size. The annealed sample at 400 °C exhibited the maximum surface area of 17.63 m^2 / g, while a further increase in calcination temperature resulted in a decrease in surface area. Furthermore, it was observed that the optical bandgap exhibited a decrease with an increase in the annealing temperature. This is probably due to the increase in the particle size. The corresponding SEM image of the sample is shown in (Figure 2.5).

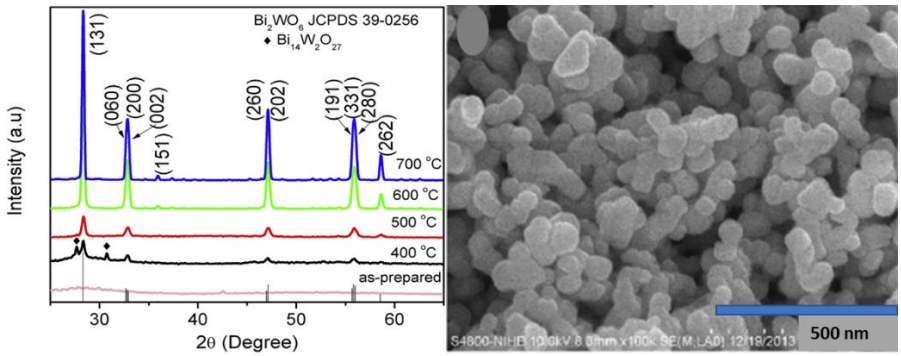

Figure 2.5: XRD pattern and SEM image of Bi_2WO_6 nanoparticles annealed at 500 ºC.[21] Reused with permission from ref. (21).

The particles exhibit agglomeration which leads to bigger particles because of sintering and did not have a flower-type morphology. In order to evaluate the photocatalytic properties of the nanoparticles, they investigated decoloration of methylene blue (MB) in an aqueous solution, utilising visible-light irradiation. The researchers discovered that the sample subjected to a temperature of 500 °C had superior photocatalytic activity compared to the sample calcined at 400 °C, despite the latter having a greater surface area. The observed phenomenon could be ascribed to the reduced efficiency of charge separation in photoexcited states, which can be related to the presence of defects in less crystalline sample. Another factor could be due to pore size where mesoporous sample could degrade MB better than microporous. MB would stay longer in microporous. [28]

The above results from Phu et al. paper showed that poor crystallinity and the presence of impurities are a major factor behind the photocatalytic activity decline of sample calcined at 400 ºC as surface area is more important for adsorption, photocatalytic reactivity could be determined by crystallinity. The sample treated at 400 ºC has higher SA than the one calcinated at 500 ºC. However, there is no big variation in SA of all samples (18 m^2/g – 11 m^2/g). The bandgap absorption of 400 ºC annealed sample was greater than that for the sample annealed at 500 ºC but the numbers have not been

reported. The conclusion of this study was that crystallinity is the major factor behind Bi_2WO_6 photocatalytic activity.

In a recent report by Liu et al., microwave heating was used to synthesise high-surface area (138 m^2/g) Bi_2WO_6 using ethylene glycol as a solvent. They used the synthesised sample to oxidise alkenes through the oxidative cleavage of C=C bonds to ketones in water at room temperature.[29]

The conclusion taken from all above studies is that Bi_2WO_6 samples that possess both flower-like morphology and high crystallinity and high surface area show better photocatalytic activity compared to high surface area amorphous Bi_2WO_6. Therefore, preparation of Bi_2WO_6 with flower-type structure attaining both high crystallinity and high surface area will be the aim of this chapter.

2.3 Synthesis of Bi_2WO_6 with flower-like morphology and high surface area

Bi_2WO_6, with its flower-like three-dimensional structure, is recognised for having the maximum photocatalytic activity compared to other morphologies attributed to diffusion channels and the effective separation and migration of photoexcited charge carriers on absorption of light.[30]

Therefore, it was decided to synthesise Bi_2WO_6 using hydrothermal and solvothermal methods employing conventional and microwave heating for the Giese reaction as a model reaction for the organic synthesis of fine chemicals. Understanding the mechanisms and factors affecting this reaction will be the main aim of this project.

2.3.1 Hydrothermal and solvothermal synthesis of Bi_2WO_6 using conventional heating (CH)

The hydrothermal synthesis of bismuth tungstate (Bi_2WO_6) was conducted by employing bismuth nitrate pentahydrate ($Bi(NO_3)_3.5H_2O$) as the source of bismuth and sodium tungstate dihydrate ($Na_2WO_4.2H_2O$) as the source of tungsten.[31] The solvents employed in the experiment were water (hydrothermal) and EG (solvothermal). The synthesis conditions of Bi_2WO_6 using hydrothermal synthesis is shown in (Figure 2.6). When EG was used, the reaction time was 2 hours (step 2) as longer period of time resulted in the decomposition of EG.

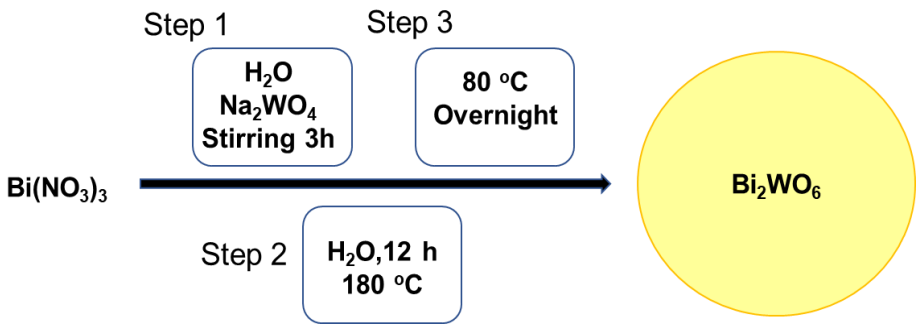

Figure 2.6: General scheme for Bi_2WO_6 synthesis using hydrothermal approach using conventional heating (CH).

The compound $Na_2WO_4.2H_2O$ exhibited high solubility in water, whereas the bismuth nitrate produced a white suspension. Grinding $Bi(NO_3)_3$ into a fine powder and employing sonication aids in achieving a uniform suspension of $Bi(NO_3)_3$. The hydrothermal synthesis process is advantageous due to the use of elevated temperatures, which is good for facilitating crystal formation with small particles. After reaction, separation of Bi_2WO_6 was achieved using a centrifuge, resulting in a 97% yield of pale-yellow powder of Bi_2WO_6. This sample is denoted as Bi_2WO_6 (Hydro_CH).

The solvothermal method was also utilised to synthesise Bi_2WO_6, with ethylene glycol serving as the solvent. Upon completion of the reaction, the resulting supernatant had brownish colour potentially due to EG oxidation. Furthermore, the powder was washed several times with water in order to eliminate any traces of organic solvent. It is widely recognised that organic solvents possessing OH group have the ability to bind with inorganic materials (metal oxide) to form complexes. As a result, the formed Bi_2WO_6 particles are suspended in the solvent, and indicating the possible formation of small nanoparticles. This sample is denoted as Bi_2WO_6 (EG_CH).

2.3.2 Hydrothermal and solvothermal synthesis of Bi_2WO_6 using microwave-assisted heating method (MW)

The microwave-assisted technique employed identical salt precursors as those utilised in conventional hydrothermal methods with water and ethylene glycol serving as the solvents. The primary rationale for employing this approach is to efficiently generate a photocatalyst with a large surface area in a short time. The reactor utilised in the experiment was composed of glass material which is suitable for MW transmittance and was fitted with a magnetic stirrer which is an extra feature allowing a good mixing of reactants which helps to reduce the formation of hot spots.[32] The selection of the solvent for microwave synthesis is determined by considering the dielectric and loss tangent properties of the solvent, as previously mentioned. Thus, it was suitable to use EG in

MW. The resultant product was observed to be in a state of suspension inside the reaction solution and not precipitating quickly when EG was used, suggesting the presence of small nanoparticles. The washing stages were done multiple times to ensure thorough removal of the organic solvent. The centrifugation time was also long (≈ 1 h) at 3400 (rpm) to achieve complete separation of nanoparticles to give Bi_2WO_6 in 95%. This sample is denoted as Bi_2WO_6 (EG_MW)

When water was used as solvent, the separation was better compared to EG sample. This may suggest that EG binds to the surface and blocks crystallites growth which results in formation of very small particles. This sample is denoted as Bi_2WO_6 (Hydro_MW).

The powders obtained with both methods (hydrothermal and solvothermal) are summarised in (Table 2.1). These samples will be characterised to compare their crystallinities, morphologies and surface areas which will be carried out in the next section.

Table 2.1: Bi_2WO_6 samples synthesis conditions with their labels.

Sample synthesis conditions	Label
Bi_2WO_6 synthesised in water using conventional heating (CH)	Bi_2WO_6 (Hydro_CH)
Bi_2WO_6 synthesised in water using microwave heating (MW)	Bi_2WO_6 (Hydro_MW)
Bi_2WO_6 synthesised in ethylene glycol using conventional heating (CH)	Bi_2WO_6 (EG_CH)
Bi_2WO_6 synthesised in ethylene glycol using microwave heating (MW)	Bi_2WO_6 (EG_MW)

2.4 Bismuth tungstate characterization

The characterization of prepared bismuth tungstate was carried out using powder X-ray diffraction (PXRD) to check crystallinity, scanning electron microscopy (SEM) to reveal the morphology, UV-Vis diffuse reflectance spectroscopy (UV-Vis DRS) to study the optical properties, and surface area measurement (BET) to calculate the specific surface area and pores size.

2.4.1 Catalyst crystallinity

As the crystallinity is an important factor in photocatalytic activity, the synthesised catalyst was initially characterised using PXRD to determine the crystal structure and confirm the identity of the resulting material as bismuth tungstate. The PXRD pattern of Bi_2WO_6 synthesised using hydrothermal method with conventional heating (CH), referred to as Bi_2WO_6 (Hydro_CH), is depicted in (Figure 2.7 A) while sample synthesised hydrothermally using MW is shown in (Figure 2.7 B).[33]

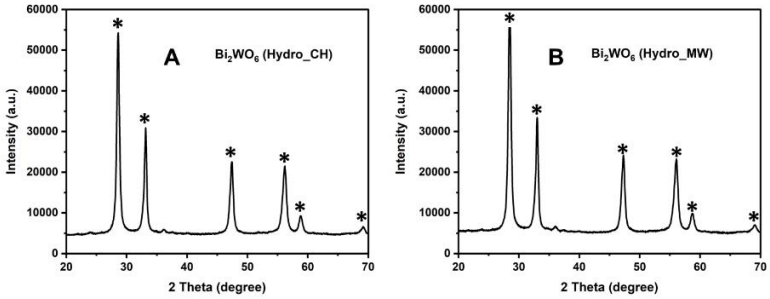

Figure 2.7: PXRD pattern of A) Bi_2WO_6 synthesised hydrothermally using conventional heating, Bi_2WO_6 (Hydro_CH) and B) Bi_2WO_6 synthesised hydrothermally using MW, Bi_2WO_6 (Hydro_MW). Asterisk indicates peaks match with reference data according to literature with JCPDS card no. 39-0256 ref. (33).

The crystal structure of the Bi_2WO_6 aligns with previously documented crystal structures of Bi_2WO_6. All peaks that correspond to the expected diffraction patterns are observed; yet, these peaks exhibit a certain level of broadening. The phenomenon of broadening in X-ray diffraction (XRD) can be attributed to various sources. One of the factors is associated with the size of the crystallites. A direct relationship exists between the size of the crystallite and the width of the diffraction peak. Specifically, as the size of the crystallite decreases, the diffraction peak becomes broader, due to presence of lattice strains or dislocation due to large volume of defects could also affect peak broadening.[34]

The crystallite size of the hydro-synthesized sample utilising conventional heating (CH) was determined to be approximately 14.2 nm based on most intense peak at 28 (2θ degree), using Scherrer's equation (1). Crystallite size values produced by Scherrer's method are sometimes underestimated due to other effects that can contribute to an increase in full width at half maximum (FHWM) such as instrumental factors.

$$D = \frac{K\lambda}{\beta \cos\theta} \quad (1)$$

D = average crystallite size or crystal length

K = Scherrer constant (0.98)

λ = X-ray wavelength (1.54 Å)

β = line broadening (FWHM)

θ = Bragg angle in degree

The hydrothermally synthesised sample using MW, referred to as Bi_2WO_6 (Hydro_MW), exhibits the crystal structure of bismuth tungstate, with a crystallite size estimated at 13.2 nm (Figure 2.7 B). In conclusion, it can be stated that both conventional heating (CH) and microwave heating methods yield crystalline Bi_2WO_6 when water is used as solvent with little difference in crystallite size as judged by PXRD.

On the other hand, the synthesised Bi_2WO_6 in ethylene glycol (EG) using CH, Bi_2WO_6 (EG_CH) and MW, Bi_2WO_6 (EG_MW) are shown in (Figure 2.8 A and B). The concepts again behind employing EG is to facilitate the creation of small metal oxide particles.

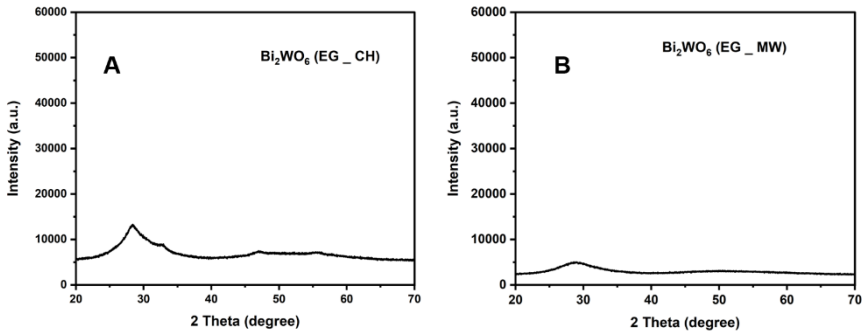

Figure 2.8: PXRD pattern of Bi_2WO_6 synthesised via solvothermal (ethylene glycol) using conventional heating (CH) (A) and microwave (MW) (B).

The literature has established that ethylene glycol (EG) could work as a surfactant to prevent NPs agglomeration by lowering surface energy and as a result, enhancing the stability of small metal oxides nanoparticles.[35] Moreover, ethylene glycol (EG) is favoured in microwave synthesis owing to its physical properties such as high boiling point, high dielectric constant and large loss tangent in comparison to alternative solvents, such as water. The utilisation of ethylene glycol (EG) in conventional hydrothermal (CH) synthesis has resulted in the absence of a pure Bi_2WO_6 crystal phase as confirmed by XRD pattern in (Figure 2.8 A). This phenomenon can be attributed to the inhibitory effect of EG on crystal nucleation, leading to the development of amorphous material instead. Furthermore, it can be observed that EG supernatant became brown indicative of EG

oxidation, possibly, or dehydration of EG would give acetaldehyde which would then oligomerise to coloured impurities.

The synthesised samples in ethylene glycol (EG) utilising both microwave (MW) and conventional heating (CH) exhibited the formation of an amorphous material. However, XRD pattern displayed a broad peak with shoulder and other very-weak peaks for sample synthesised in EG using CH (Figure 2.8 A) compared to Bi_2WO_6 synthesised in EG using MW that only shows broad peak (Figure 2.8 B). This shows again that the obtained bismuth tungstate is not in a pure crystal or polycrystal phase, but has a significantly reduced degree of crystallinity. Therefore, it is evident that samples made utilising EG are largely amorphous but may retain small crystallite sizes consistent with the broadening of diffraction peaks. Also, the lack of crystallinity in EG samples could be the result of lack of structure ordering due to presence of many defects. According to some researchers, solvent molecules have the ability to specifically adhere to the crystallographic facets of crystals, which in turn inhibits the growth of these facets.[36,37]

To conclude, utilising water as solvent in Bi_2WO_6 synthesis facilitates the formation of crystalline structure while using ethylene glycol inhibits crystal growth.

Due to the observed low crystallinity or amorphous nature of samples synthesised in EG, which suggests the presence of small particles, it was determined that a post-treatment method with secondary hydrothermal heating would be employed to improve crystallinity instead of common high-temperature annealing (calcination) method reported in literature.[38] It is important for a semiconductor to be crystalline or show some crystallinity, as this feature would affect photoelectrical properties such as charge mobility and separation inside the structure.[39] The presence of defects (poor crystalline structure) could suppress the transmission of charge carriers, so improving crystallinity could eliminate these defects.[40] Whilst increasing crystallinity, calcination would lead to a decrease in surface area, samples prepared in EG using MW were subjected to additional hydrothermal treatment in an attempt to increase crystallinity whilst retaining small particle size. That was done by taking Bi_2WO_6 (EG_MW) dry powder, transferring it into a Teflon tube with the addition of water, and reheating it at 180 ºC for 2 hours. The XRD pattern (Figure 2.9) illustrates the characteristics of Bi_2WO_6 (EG_MW) powder that has undergone hydrothermal post-treatment. This particular sample is referred to as Bi_2WO_6 (EG_MW)_Hydro, where hydrothermal step was carried out on dry powder.

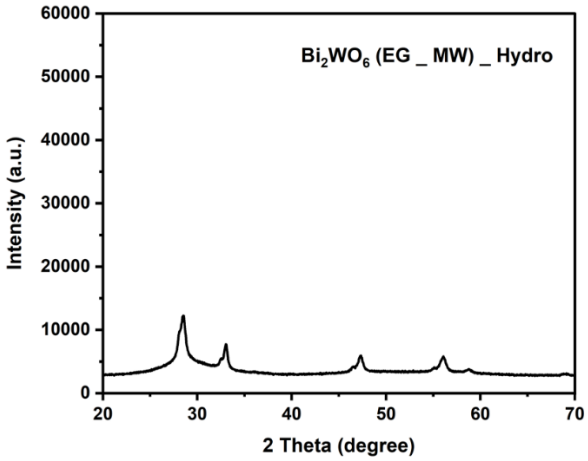

Figure 2.9: PXRD pattern of Bi_2WO_6 (EG_MW)_Hydro. Suffix ''Hydro'' after bracket indicates that post treatment was performed on dry powder.

The provided XRD pattern of Bi_2WO_6 in the present sample suggests the occurrence of recrystallization in the sample that was synthesised using EG after being treated hydrothermally. There is an obvious increase in diffraction peaks intensities compared to Bi_2WO_6 (EG_MW) where the only peak can be seen is the one at ca. 28 (2θ degree) and it is very broad. The observed increase in peak intensity indicates improvement in crystallinity.

Another synthesised sample, Bi_2WO_6 (EG_MW) was post treated hydrothermally just after being obtained and before drying out, designated as Bi_2WO_6 (EG_MW_Hydro) (Figure 2.10).

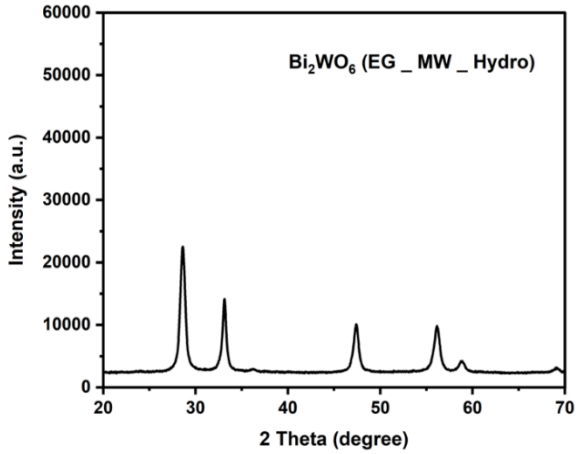

Figure 2.10: PXRD pattern of Bi_2WO_6 (EG_MW_Hydro). Suffix ''Hydro'' inside bracket indicates that post treatment was performed on wet powder immediately after initial synthesis.

It can be clearly seen that crystallinity is enhanced after treating immediately after initial synthesis, and the crystallite size has increased to 12.2 nm using the Scherrer equation, which is close to the value of Bi_2WO_6 (Hydro_MW), 13.2 nm. This sample shows better crystallinity compared to previous one, Bi_2WO_6 (EG_MW)_hydro, despite both of them being reheated in water. The reason for this is not clear but it could be due to effectiveness of eliminating EG in still-wet sample or that 2nd sample dissolved in water more efficiently and recrystallised. However, both treatments with water enhanced crystallinity presumably due to higher solubility of Bi_2WO_6 in water than in EG.

To conclude, it is obvious that hydrothermal method is superior to the solvothermal (using EG) method for the synthesis of crystalline Bi_2WO_6. The next important factor in photoactivity of MOSC is their morphology.

2.4.2 Catalyst morphology

The utilisation of scanning electron microscopy is a highly effective method employed to reveal the morphology of materials on the micro-nanoscale. SEM analysis was conducted on both water and EG synthesised samples in order to investigate the catalyst morphology. As previously stated, the structures of Bi_2WO_6 that resemble flakes or flowers exhibit the highest level of activity when employed as photocatalysts for organic molecule degradation. The hydrothermal synthesis of the sample utilising both CH and MW resulted in the flower-like morphology of Bi_2WO_6, as depicted in (Figure 2.11).

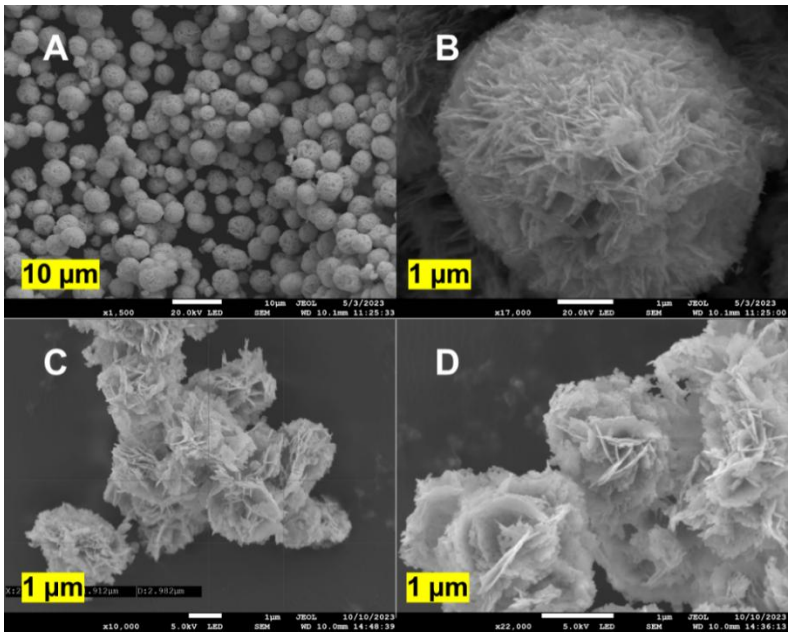

Figure 2.11: SEM of Bi_2WO_6 synthesised hydrothermally using conventional heating (CH), Bi_2WO_6 (Hydro_CH) (A and B) and microwave heating (MW), Bi_2WO_6 (Hydro_MW) (C and D). Value in yellow box represents value of original scale bar.

The SEM image presented above illustrates the successful synthesis of Bi_2WO_6 in an aqueous solution utilising a Teflon container within a standard heating oven. The resulting morphology of the synthesised material exhibits a distinctive flower-like structure, Bi_2WO_6 (Hydro_CH) as depicted in (Figures 2.11, A and B). Furthermore, Bi_2WO_6 synthesised in water by microwave irradiation, Bi_2WO_6 (Hydro_MW) as in (Figures 2.11, C and D), still exhibits a comparable flower-like structure. However, the particles tend to aggregate rather than form distinct entities. One potential explanation for the disparity in morphologies could be attributed to changes in the conditions of synthesis. The Bi_2WO_6 (Hydro_CH) sample was subjected to thermal treatment for a duration of 12 hours, a considerably longer period of time, facilitating the full development of this morphology resembling a flower. Longer reaction time could lead to crystallisation which is a slow process. Also, longer reaction times increase temperature gradually allowing crystals to grow, whereas fast heating as in case of microwave heating could lead to rapid stop of crystal growth and formation of amorphous phase.

Nevertheless, the overall morphology of both samples exhibits a comparable organisation. The surface area of Bi_2WO_6 (Hydro_CH) was measured to be 21 m^2/g, whereas Bi_2WO_6 (Hydro_MW) exhibited a surface area of 25 m^2/g. Furthermore, the obtained result from SEM is consistent with the XRD analysis (Figure 2.7 A and B), respectively which also indicates that the flower-like structure exhibits a high degree of crystallinity.

The samples produced utilising ethylene glycol (EG), Bi_2WO_6 (EG_CH) and Bi_2WO_6 (EG_MW) are shown in (Figure 2.12) lack a recognisable higher ordered structure and are characterised by their small size. Both samples exhibit an PXRD pattern characterised by an amorphous structure (Figures 2.8 A and B). This observation is consistent with the findings from SEM images that the absence of ordered flower like structure leads to poor crystallinity. On the other hand, previous observation in Figure 2.11 indicating that the flake-like structure of the flower is accountable for the elevated level of crystallinity in Bi_2WO_6 synthesised in an aqueous medium.

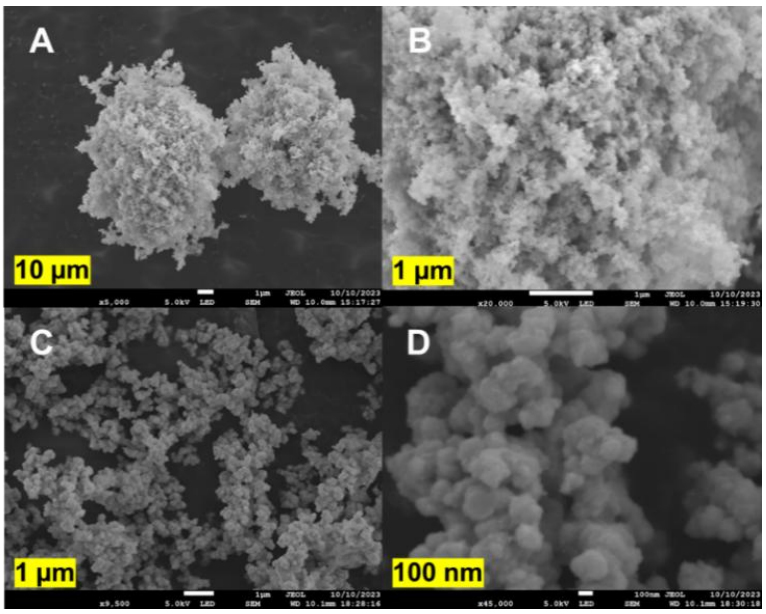

Figure 2.12: SEM of Bi_2WO_6 synthesised in EG using conventional heating (CH), Bi_2WO_6 (EG_CH) (A and B) and microwave heating (MW), Bi_2WO_6 (EG_MW) (C and D). Value in yellow box represents value of original scale bar.

The PXRD data (Figure 2.9 and 2.10) have demonstrated the impact of water on the crystallinity evolution of Bi_2WO_6. In order to investigate the alterations in morphology resulting from this treatment, SEM was also employed. Figures 2.13, A and B depict the sample of Bi_2WO_6 (EG_MW)_Hydro, whereas Figures 2.13, C and D illustrate Bi_2WO_6 (EG_MW_Hydro) sample.

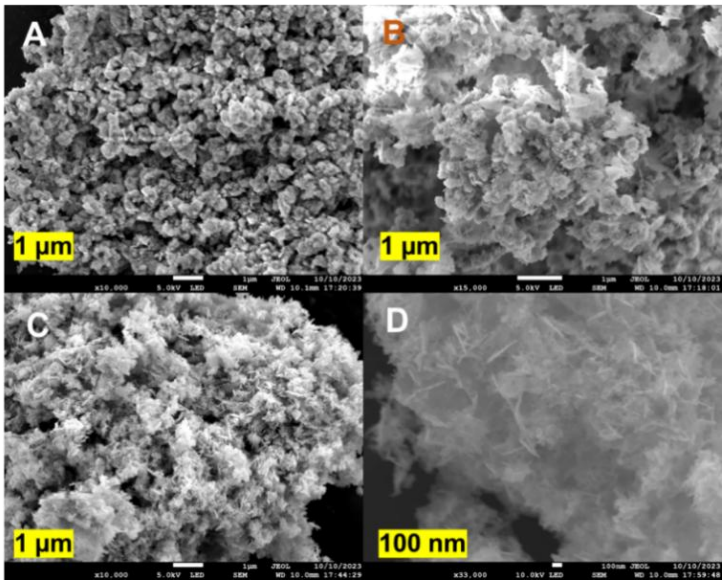

Figure 2.13: SEM of Bi_2WO_6 synthesised in EG using MW then treated hydrothermally A, B) with dry sample, Bi_2WO_6 (EG_MW)_Hydro and C, D) with wet sample, Bi_2WO_6 (EG_MW_Hydro). Value in yellow box represents value of original scale bar.

The XRD analysis (Figure 2.9) revealed that the crystallinity of Bi_2WO_6 (EG_MW)_Hydro was only slightly improved while Bi_2WO_6 (EG_MW_Hydro) was much improved in crystallinity (Figure 2.10). The SEM image above indicates the presence of a novel aggregation phase, however, the expected organised flower-like morphology remains absent, instead, clustered spherical particles are present. In contrast, the sample that was treated hydrothermally just after synthesis, Bi_2WO_6 (EG_MW_Hydro), has an enhanced level of ordering in its structure when compared to the sample that was treated hydrothermally after being dried, Bi_2WO_6 (EG_MW)_Hydro. However, both samples have not yet achieved the same degree of flower-like structure as the original hydrothermally synthesised sample, Bi_2WO_6 (Hydro_CH) sample.

2.4.3 Catalyst surface area

Surface areas of different Bi_2WO_6 samples were acquired using BET technique. This surface area measurement is associated with the adsorption of N_2 gas (physisorption) onto solid material surfaces. This physisorption phenomenon is caused by van der Waals forces between the adsorbate (N_2) and the adsorbent (solid). A layer of N_2 molecules are formed on the surface of a solid particle, and the number of adsorbed molecules can be correlated with surface area of solid.[41,42] The N2 adsorption-desorption isotherms for Bi_2WO_6 samples synthesised via different methods and conditions are shown in Figure 2.14.

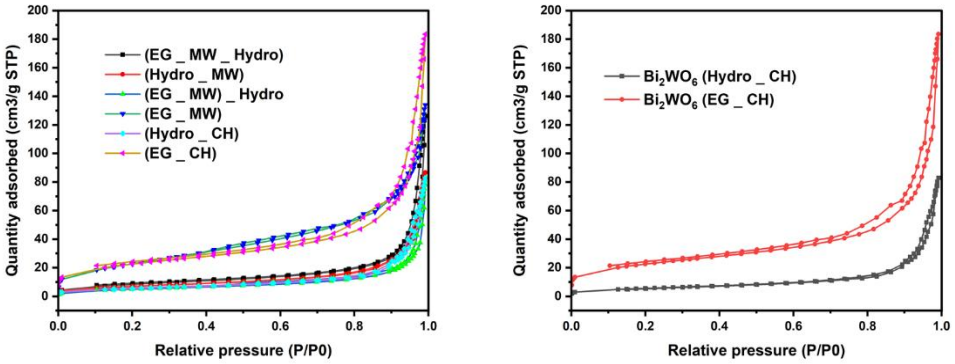

Figure 2.14: N_2 adsorption-desorption isotherms of Bi_2WO_6 synthesised at different conditions (left). Comparison between N_2 adsorption-desorption isotherm of Bi_2WO_6 (Hydro–CH) and Bi_2WO_6 (EG–CH) samples (right).

It can be seen that Bi_2WO_6 that was synthesised in EG shows a higher capacity for gas adsorption, which reflects the high surface area (SA) these samples possess. The calculated SA by BET method of Bi_2WO_6 (EG_CH) and Bi_2WO_6 (EG_MW) were 79 and 86 m^2/g, respectively. The other samples, synthesised in water using conventional

heating, show similar isotherms but smaller N_2 adsorption. Their surface areas are 21, 25, 18, and 31 m^2/g for Bi_2WO_6 (Hydro_CH), Bi_2WO_6 (Hydro_MW), Bi_2WO_6 (EG_MW)_hydro, and Bi_2WO_6 (EG_MW_hydro), respectively. In terms of adsorption-desorption curve, there is no obvious hysteresis between adsorption and desorption for hydrothermal synthesised samples however samples synthesised in EG showed small hysteresis.[43] This small variation might suggest the sample is porous or presence of different pore sizes. A comparison between Bi_2WO_6 samples synthesised in water and EG in terms of surface area and FHWM value is shown in (Table 2.2). FHWM is a function of crystallinity, the smaller the number, the sharper the diffraction peak, the more the crystalline phase the solid retains. On the other hand, the higher the surface area, the smaller the particles.

Table 2.2: surface area and FHWM values of Bi_2WO_6 prepared in water and ethylene glycol

Synthesis conditions	**Catalyst**	**Surface area (m^2/g)**	**FHWM (º) of peak at 28 *2 theta***
Originally synthesised samples	Bi_2WO_6 (Hydro_CH)	21	0.57
	Bi_2WO_6 (Hydro_MW)	25	0.61
	Bi_2WO_6 (EG_CH)	79	6.88
	Bi_2WO_6 (EG_MW)	86	7.07
Treated Samples with Water	Bi_2WO_6 (EG_MW)_Hydro	18	1.69
	Bi_2WO_6 (EG_MW_Hydro)	31	0.66

It can be concluded from the adsorption characterisation that while hydrothermally-synthesised Bi_2WO_6 samples have flower-like morphology with high crystallinity, they show lower surface area compared to samples synthesised in EG. While those samples prepared in EG as solvent show high surface area, they lack flower-like morphology and crystallinity. Thus, based on these results, Bi_2WO_6 synthesised hydrothermally was chosen as the model catalyst.[44]

2.4.4 Optical properties

UV-Vis DRS is one of the spectroscopic techniques used to measure reflected light in the UV or visible region of solid materials such as heterogeneous metal oxide photocatalysts. It is a powerful tool for studying optical properties of semiconductors. [45] Considering MOSC is not a transparent material and a powder, reflectance is measured instead of transmittance and absorption. Bi_2WO_6 prepared under different conditions was measured by DRS, and the corresponding spectra are shown in (Figure 2.15) and corresponding bandgap energy calculated using Tauc plot is shown in (Table 2.3).

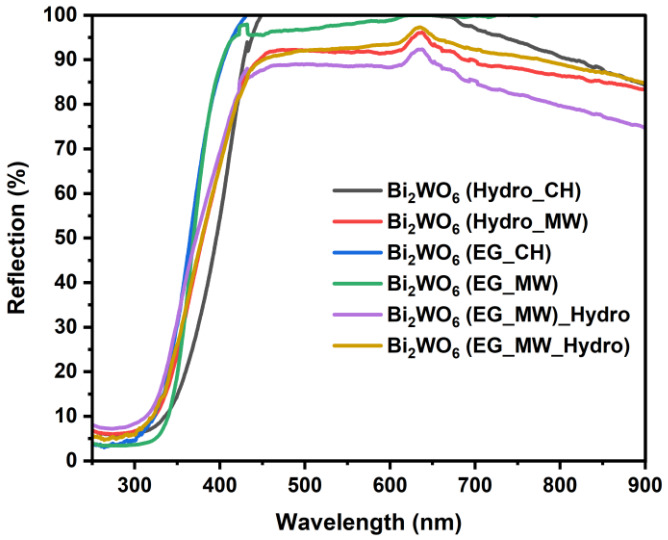

Figure 2.15: UV-Vis Diffuse reflectance spectrum of prepared Bi_2WO_6 via hydrothermal and solvothermal methods.

Table 2.3**:** Bandgap energy of Bi_2WO_6 powders synthesised with different methods.

Catalyst	Bandgap energy (eV)
Bi_2WO_6 (Hydro_CH)	2.97
Bi_2WO_6 (Hydro_MW)	3.06
Bi_2WO_6 (EG_CH)	3.22
Bi_2WO_6 (EG_MW)	3.29
Bi_2WO_6 (EG_MW)_Hydro	3.13
Bi_2WO_6 (EG_MW_Hydro)	3.09

It can be seen from the above UV-Vis DRS results that Bi_2WO_6 (Hydro_CH) shows more absorption of visible light compared to Bi_2WO_6 (EG_CH) and Bi_2WO_6 (EG_MW) that show less visible light absorption. The bandgap energy of Bi_2WO_6 (Hydro_CH) is less

than that of those samples that were synthesised in EG. The increase in bandgap could be related to particle sizes. As particle size decreases, the bandgap increases.[46-48] There are some explanations for this behaviour. First, as particles become smaller, the distance between electrons (e^-) and holes (h^+) and excitons becomes smaller, which makes them hold together strongly, and as a result, more energy (shorter λ) is needed to induce charge separation. Another explanation is regarding the number of atoms (electrons) available in small particles. When the size of the particle is reduced, there are fewer atomic orbitals to overlap and form VB and CB thus leading to increased bandgap (Figure 2.16).[49]

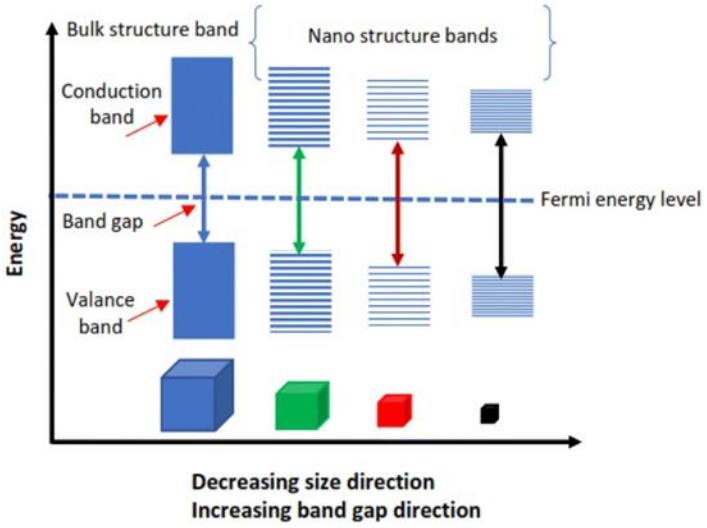

Figure 2.16: illustration showing difference between bulk and nano-structure of semiconductor with emphasis on number of energy levels. Reused with permission from ref. (49)

Bi_2WO_6 (Hydro_MW), Bi_2WO_6 (EG_MW)_ Hydro, and Bi_2WO_6 (EG_MW_Hydro) are showing better absorption than samples synthesised in EG only and could be related to crystallinity enhancement after hydrothermal treatment. Also, Bi_2WO_6 (Hydro _ MW) has a similar SA value to Bi_2WO_6 (Hydro _ CH), but its absorption band edge is smaller, and again, that could be due to the crystallinity effect.

2.5 Modification of bismuth tungstate, the use of platinum as electron-capture centre.

2.5.1 Modification on semiconductors NPs

MOSC have demonstrated significant potential in facilitating chemical reactions due to their distinctive electronic structures, namely the valence band (VB) and conduction band (CB), as previously mentioned. Nevertheless, the use of this characteristic poses challenges due to the tendency of photoexcited charge carriers to recombine and return

to their lowest energy state, resulting in the dissipation of acquired energy as heat. The lifetimes of electrons and holes created during photoexcitation are very short due to rapid recombination. Recombination may occur either within the bulk or at the surface. The rapid recombination of electrons (e^-) and holes (h^+) is a well-documented concern in MOSC devices, and this phenomenon is also observed in Bi_2WO_2.

Various strategies can be employed to enhance the efficiency of MOSC, both in terms of optical properties and catalytic performance. These strategies encompass the incorporation of metal and non-metal nanoparticles through doping, the formation of heterojunction structures by coupling MOSC with another MOSC, and the application of metal nanoparticles for surface modification purposes.[50-52]

The introduction of doping agents into a MOSC structure could alter its composition, leading to the formation of a different material exhibiting different morphological characteristics and physical and chemical properties in comparison to the original parent material. However, this approach necessitates a series of sequential procedures, a greater number of chemical substances, and additional refinement in order to obtain the ultimate outcome.

On the other hand, the application of metal nanoparticles for the purpose of surface modification of MOSC does not require complicated equipment and can be done quickly and easily, while simultaneously preserving the inherent crystal structure. Furthermore, a minimal quantity of metal particles is required for deposition on MOSC surface, hence minimising wastage.

2.5.2 Photodeposition of metal nanoparticles on surface of Bi_2WO_6

Various techniques can be employed to deposit metal nanoparticles onto MOSC surfaces, including wet impregnation, chemical reduction utilising reducing chemicals, precipitation, atomic layer deposition, sputtering, electrodeposition, and photodeposition.[53-57] The latter strategy exhibits certain advantages in comparison to alternative approaches. One notable advantage is in the deposition of metal nanoparticles (MNPs) onto the catalyst surface using light (mild and more sustainable energy source), as opposed to chemical reduction methods that employ a harsh reducing agent like $NaBH_4$. The latter approach carries the risk of reducing the metal oxide (MO) and altering its oxidation state. Also, photodeposition does not require the application of high electrical potential (electrodeposition) and an elevated temperature (impregnation).

2.5.2.1 Photodeposition mechanism

The photodeposition method is a straightforward approach for the synthesis of noble metal/semiconductor materials changing the optical properties the semiconductor. The

photo-induced reduction method needs just the exposure to a light source for the metal reduction to occur. Therefore, in this approach, MOSC works as a template facilitating the adsorption sites for metal nanoparticles (MNPs) and acts as source of energy to drive reduction or oxidation reaction.

Several parameters must be met in order to facilitate photodeposition. Firstly, it is essential for the precursor of metal nanoparticle (MNP) to come into contact with the active sites of a MOSC, where the reduction can occur. Additionally, in order for electron transfer to take place, it is necessary for the energy of light to be equal to or greater than the bandgap of the semiconductor. Furthermore, it is imperative to ensure some separation of photogenerated electrons and holes for surface reduction to occur. Moreover, in order for metal nanoparticles to be deposited, the bandgap position of MOSC must match the corresponding reduction potential. Similarly, the valence band should enable oxidation of the species to be oxidised, such as water or sacrificial agents including alcohols.

2.5.3 Modification of Bi_2WO_6 with platinum nanoparticles

The modification of flower-like Bi_2WO_6 with platinum is carried out using H_2PtCl_6 as a Pt source. Platinum is one of the most common noble metals for MOSC modification. It is used as an electron sink due to its relatively high work function and the creation of the Schottky barrier, which prevents electrons from reversing to the semiconductor CB.[58-61] The deposition of Pt on Bi_2WO_6 is done by using the photodeposition technique, as illustrated in Figure 2.17. H_2PtCl_6 is one of the most common Pt sources used in the synthesis of Pt NP due to its ionic character, which is important in adsorption onto the catalyst surface through electrostatic forces.[53] The metal oxides, including Bi_2WO_6, may have acidic and basic hydroxyl groups on their surfaces, which means they are amphoteric under mild conditions and at room temperature. This surface chemistry facilitates binding between the complex $[PtCl_6]^{2-}$, and the Bi_2WO_6. The mechanism of photodeposition of Pt NPs on the Bi_2WO_6 surface is based on the reduction of Pt (IV) to Pt (0) is accessible via CB electrons.

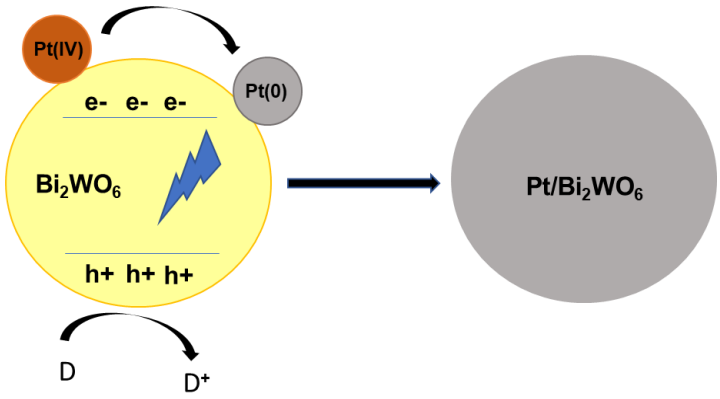

Figure 2.17: Systematic diagram showing platinization mechanism of Bi_2WO_6 using photo-deposition approach.

Some studies reported Bi_2WO_6 platinization, such as Wu et al.[62] In their study, they used H_2PtCl_6 as a Pt precursor and ethanol as an electron donor for photoexcited holes at Bi_2WO_6 VB. They used UV light to drive such transformations which directly excites $[PtCl_6]^{2-}$ via charge transfer bands towards reduction in solution to form nanoparticles directly. The synthesised Pt/Bi_2WO_6 with different Pt loadings shows enhanced photocatalytic activity towards ciprofloxacin (CIP), an antibiotic, photodegradation using 150 W-Xenon lamps. However, when high Pt loading is used, photocatalytic activity decreases as more Pt NPs on the surface could prevent absorption of light by MOSC. UV-vis diffuse reflectance shows an enhancement in visible light absorption for the platinised catalyst compared to the unmodified one attributed to a change in bandgap from 2.7 eV for the unmodified catalyst to 2.4 eV for the modified catalyst. They did not explain how surface addition of nanoparticles modifies the bulk electron structure of Bi_2WO_6.

Another study in similar fashion was carried out by Qamar et al.[63], where a 230 W tungsten-halogen lamp was used. There was no difference in UV-Vis diffuse absorbance between the unmodified and platinized catalysts. The bandgap energy for both was 2.8 eV. The synthesised Pt/Bi_2WO_6 was used to transform alcohol into the corresponding aldehyde. The authors attributed the enhanced photocatalytic activity of Pt/Bi_2WO_6 to the formation of Schottky barrier without further explanation. To explain the role of Schottky barrier, metal-semiconductor (M-SC) junction with high Schottky barrier will prevent electrons to move back to semiconductor CB and as a result enhancing charges separation and suppressing e-/h+ recombination.

Both studies used high power UV lamps to deposit Pt on the Bi_2WO_6 surface; however, in this work, which is adapted from work done by previous researcher, Unsworth [31] and

study performed by Zhang et al,[64] visible-light is used to reduce $[PtCl_6]^{2-}$ via Bi_2WO_6 so that deposition occurs at the location where e^- emerge at the surface.

The Pt loading is also crucial. Both literature reports found that Bi_2WO_6 loaded with 0.1 - 0.2 wt.%Pt gave superior photocatalytic activity to unmodified Bi_2WO_6. Also, this small loading probably will not affect the original crystal structure and morphology of Bi_2WO_6 and should not prevent light absorption by the MOSC, which is the driving force for catalytic performance. So, it was decided to platinise Bi_2WO_6 with initially with 0.15wt.% Pt using visible light LED to give 0.15wt.%Pt/Bi_2WO_6 (0.15Pt/Bi_2WO_6).

The general methodology of this project is also to use green solvents, to utilise mild reaction condition, and to minimise chemical waste. A 30 W LED lamp (410–450 nm) was used as energy source to induce platinisation of Bi_2WO_6 (bandgap, Eg = 3.00 – 2.7 eV). Ethanol was used as a sacrificial agent instead of methanol because it is considered more environmentally friendly.[59] In general, the role of a sacrificial agent is crucial. In order to generate electrons at CB, holes at VB need to be consumed. Therefore, sacrificial agents such as alcohol can be used. Water can also be used to quench holes via oxidation of hydroxyl ions (^-OH) to hydroxyl radicals ($\cdot OH$); however, the hole conversion rate will be lower when using water. The reason alcohol is more favourable than water is that alcohols have a lower oxidation potential compared to water.[53,54,66,67]

2.5.4 Characterization of Platinised bismuth tungstate (Pt/Bi_2WO_6)

The characterization of platinised bismuth tungstate was carried out using PXRD (Figure 2.18), SEM equipped with energy dispersive X-ray spectroscopy (EDX) for elemental composition quantification (Figure 2.19), and UV-Vis DRS (Figure 2.21). It can be seen that there is no obvious difference between bare and platinized Bi_2WO_6 in XRD pattern, which indicates the crystal structure remains unchanged.

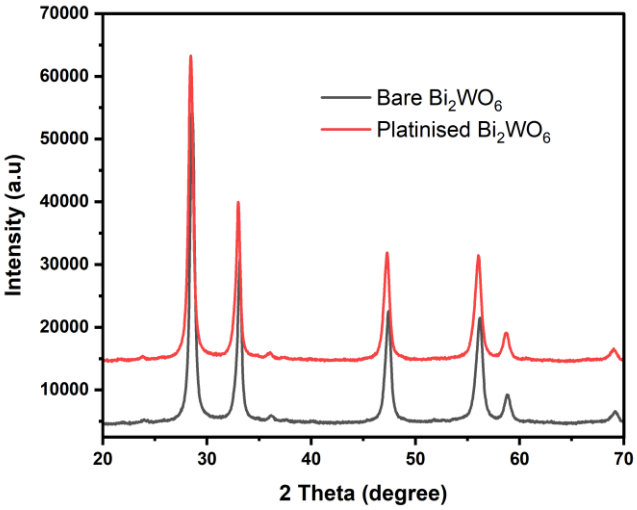

Figure 2.18: pXRD pattern of Bi_2WO_6 and 0.15Pt/Bi_2WO_6

There is no sign of Pt crystallites and also there is no significant change in FWHM unmodified Bi_2WO_6 and platinised Bi_2WO_6, showing that photodeposition is a mild technique and its effect on crystal structure is minimal. The morphology details of Pt/Bi_2WO_6 and the corresponding elemental analysis by EDX are shown in (Figure 2.19).

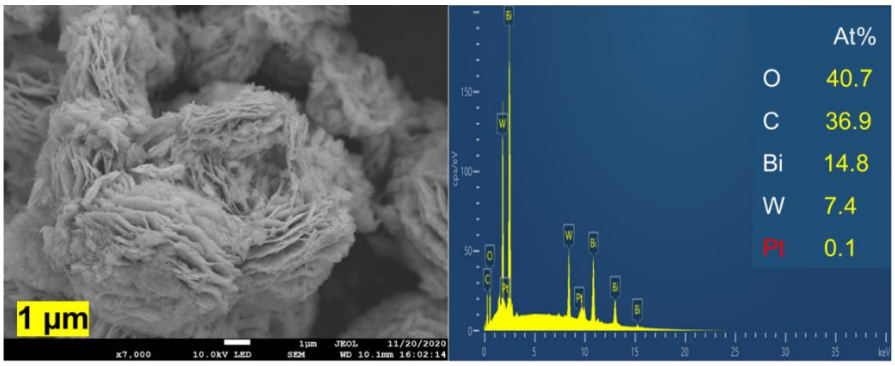

Figure 2.19: SEM image of 0.15Pt/Bi_2WO_6 (left) and corresponding elemental analysis by EDX (right). Value in yellow box represents value of original scale bar.

It can be seen from the above SEM image that Pt/ Bi_2WO_6 retains the flower-type structure. The EDX spectrum shows that bismuth (Bi) atom % was twice as high as tungsten (W) amount (2 Bi: 1W) while Pt is around 0.1 atom % confirming the presence of Pt. Further quantitative measurement of Pt was carried out using inductive plasma optical emission spectroscopy (ICP-OES). The amount of Pt in platinised catalyst was found to be 0.14 Wt.%. There was no loss of Pt after washing with water and ethanol which suggests that Pt could be reduced to Pt metal nanoparticles on MOSC surface.

Surface areas of Bi_2WO_6 and 0.15Pt/Bi_2WO_6 are 21 and 19 m^2/g, respectively. The isotherm adsorption plot is shown in Figure 2.20.

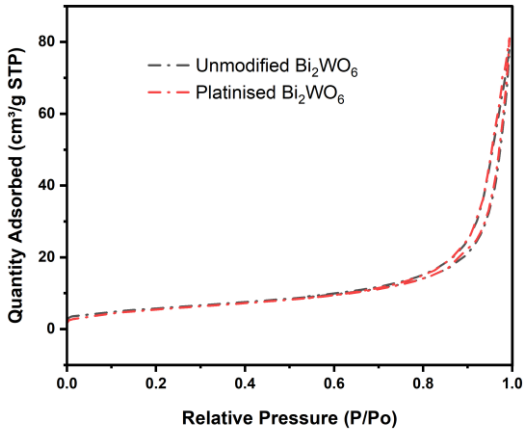

Figure 2.20: Isotherm plot of unmodified Bi_2WO_6 and 0.15Pt/Bi_2WO_6.

It can be clearly seen from the above isotherm diagram that bare and modified bismuth tungstate do not differ from each other, which indicates that the addition of Pt does not significantly affect microstructure or morphology, however, the small reduction in surface area may suggest that the presence of Pt NPs on the surface which may block some surface porosity.

Whilst PXRD and SEM results suggest that there is no major difference between unmodified and platinised catalysts, UV-Vis DRS shows an obvious difference between platinised and unmodified Bi_2WO_6 (Figure 2.21).

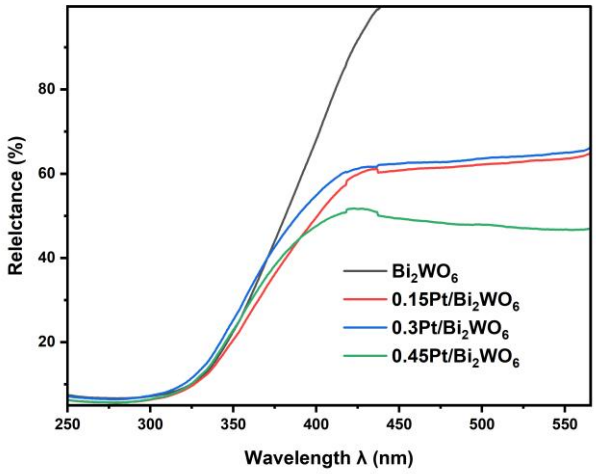

Figure 2.21: UV-Vis DRS of unmodified and platinised bismuth tungstate with different Pt wt. (%) loadings.

It can be clearly seen that the platinized sample with different Pt loadings exhibits a considerably wider absorption band in the visible light region than the unmodified sample. Such enhancement in visible light absorption could be attributed to the surface plasmon resonance of metal nanoparticles.[59,68-70] Illumination of noble metal nanoparticles excites surface plasmons, which in turn generates a non-uniform electromagnetic field in close proximity to the metal particles. The transfer of this energy to the semiconductor occurs via plasmon-induced resonance energy transfer. Surface plasmon resonance is observed in many metal nanoparticles; however, it is best known in gold (Au) and silver (Ag). For gold, for instance, smaller nanoparticles have a plasmon peak at about 520 nm, whereas larger nanoparticles demonstrate enhanced scattering and have a plasmon peak that shifts towards longer wavelengths, a phenomenon known as red-shifting. Other metals, such as Pt, typically show plasmonic peak in UV region. However, surface plasmon absorption can be extended into visible light upon increasing Pt particle size.[71] Therefore, low reflectance in platinised bismuth tungstate could due to the aggregation of Pt NPs (formation of bigger particles) on Bi_2WO_6 surface which may extend absorption band to visible light region. The sample looks darker as Pt loading increases (Figure 2.22).

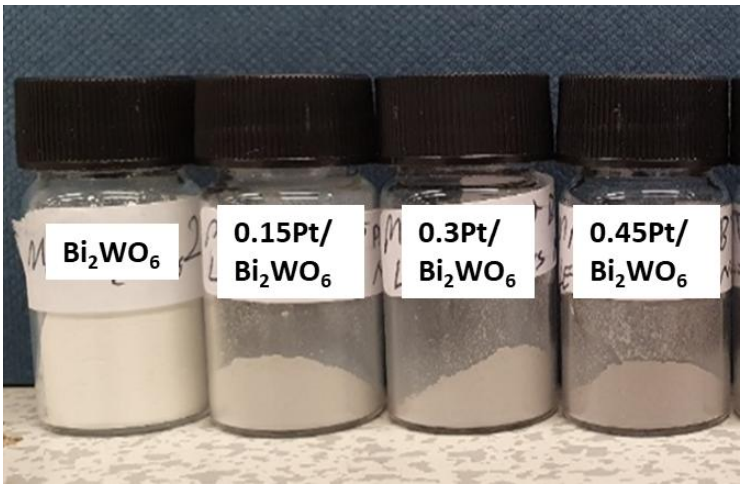

Figure 2.22: Photograph of unmodified Bi_2WO_6 and platinised Bi_2WO_6 with different Pt loadings, 0.15, 0.3 and 0.45wt.%Pt.

In addition, this enhancement in optical characteristic (absorption in visible light) due to presence of Pt NPs probably caused by d-d interband transitions within the metal structure and between the metal and semiconductor heterojunction and not by plasmonic effect such as the case in gold and silver.[72-75]

2.6 Conclusion

Bismuth tungstate nanoparticles were synthesised hydrothermally and solvothermally using conventional and microwave-assist heating techniques. Samples synthesized in water using either conventional or microwave heating revealed a crystalline structure, while samples synthesised in ethylene glycol with both conventional and microwave methods displayed poor crystallinity.

Morphology investigations revealed that samples synthesized in water using conventional and microwave heating had a flower-like structure, whereas those synthesized in ethylene glycol did not have such a structure. However, samples prepared in ethylene glycol have a larger surface area than those prepared in water. Due to lack of time, other synthesis methods, including using different surfactants, were not possible. There is room to further optimize the structure of Bi_2WO_6 using different solvents and surfactants to achieve a balance between crystallinity and surface area without the need for high-temperature treatment. However, secondary hydrothermal heating of amorphous samples showed that this method can increase crystallinity whilst retaining surface area > 30 m^2/g.

The addition of Pt showed enhancement in light absorption based on diffuse reflectance spectroscopy. The use of the photodeposition method to deposit different metal particles is promising and can be applied to different photocatalysts. The microwave synthesis is favourable because it requires less energy and time; however, scaling limits its application. As a result, designing a proper reactor or using more advanced equipment with more capacity could enable scaling.

In the following chapter, the applicability of platinised and modified Bi_2WO_6 for use in organic synthesis application is explored. The organic reaction model that will be used is Giese reaction. Then, the mechanism of this reaction will be studied.

References

(1) Zhang, N.; Ciriminna, R.; Pagliaro, M.; Xu, Y.-J. Nanochemistry-Derived Bi2WO6 Nanostructures: Towards Production of Sustainable Chemicals and Fuels Induced by Visible Light. Chem. Soc. Rev. 2014, 43 (15), 5276–5287. https://doi.org/10.1039/C4CS00056K.

(2) Liang, Y.; Shi, J. Effect of Halide Ions on the Microstructure of Bi2WO6 with Enhanced Removal of Rhodamine B. J. Inorg. Organomet. Polym. Mater. 2020, 30 (8), 2872–2880. https://doi.org/10.1007/s10904-019-01437-0.

(3) Elaouni, A.; Ouardi, M. E.; BaQais, A.; Arab, M.; Saadi, M.; Ahsaine, H. A. Bismuth Tungstate Bi2WO6: A Review on Structural, Photophysical and Photocatalytic Properties. RSC Adv. 2023, 13 (26), 17476–17494. https://doi.org/10.1039/D3RA01987J.

(4) Yi, H.; Qin, L.; Huang, D.; Zeng, G.; Lai, C.; Liu, X.; Li, B.; Wang, H.; Zhou, C.; Huang, F.; Liu, S.; Guo, X. Nano-Structured Bismuth Tungstate with Controlled Morphology: Fabrication, Modification, Environmental Application and Mechanism Insight. Chem. Eng. J. 2019, 358, 480–496. https://doi.org/10.1016/j.cej.2018.10.036.

(5) Zeng, T.; Yan, H.; Ning, H.; Zeng, J.; Reece, M. J. Piezoelectric and Ferroelectric Properties of Bismuth Tungstate Ceramics Fabricated by Spark Plasma Sintering. J. Am. Ceram. Soc. 2009, 92 (12), 3108–3110. https://doi.org/10.1111/j.1551-2916.2009.03344.x.

(6) McDowell, N. A.; Knight, K. S.; Lightfoot, P. Unusual High-Temperature Structural Behaviour in Ferroelectric Bi2WO6. Chem. – Eur. J. 2006, 12 (5), 1493–1499. https://doi.org/10.1002/chem.200500904.

(7) Takeda, H.; Han, J. S.; Nishida, M.; Shiosaki, T.; Hoshina, T.; Tsurumi, T. Growth and Piezoelectric Properties of Ferroelectric Bi2WO6 Mono-Domain Crystals. Solid State Commun. 2010, 150 (17), 836–839. https://doi.org/10.1016/j.ssc.2010.02.011.

(8) Tian, Y.; Hua, G.; Xu, W.; Li, N.; Fang, M.; Zhang, L. Bismuth Tungstate Nano/Microstructures: Controllable Morphologies, Growth Mechanism and Photocatalytic Properties. J. Alloys Compd. 2011, 509 (3), 724–730. https://doi.org/10.1016/j.jallcom.2010.09.010.

(9) Wang, D.; Zhen, Y.; Xue, G.; Fu, F.; Liu, X.; Li, D. Synthesis of Mesoporous Bi2WO6 Architectures and Their Gas Sensitivity to Ethanol. J. Mater. Chem. C 2013, 1 (26), 4153–4162. https://doi.org/10.1039/C3TC30189C.

(10) Zhang, L.; Wang, W.; Chen, Z.; Zhou, L.; Xu, H.; Zhu, W. Fabrication of Flower-like Bi2WO6 Superstructures as High Performance Visible-Light Driven Photocatalysts. J. Mater. Chem. 2007, 17 (24), 2526–2532. https://doi.org/10.1039/B616460A.

(11) Nishida, M.; Takeda, H.; Nishida, T.; Shiosaki, T. Syntheisis and Characterization of Bismuth Tungstate Crystals by Solution Growth Technique. Key Eng. Mater. 2007, 350, 81–84. https://doi.org/10.4028/www.scientific.net/KEM.350.81.

(12) Zhang, C.; Zhu, Y. Synthesis of Square Bi2WO6 Nanoplates as High-Activity Visible-Light-Driven Photocatalysts. Chem. Mater. 2005, 17 (13), 3537–3545. https://doi.org/10.1021/cm0501517.

(13) Amano, F.; Nogami, K.; Abe, R.; Ohtani, B. Facile Hydrothermal Preparation and Photocatalytic Activity of Bismuth Tungstate Polycrystalline Flake-Ball Particles. Chem. Lett. 2007, 36 (11), 1314–1315. https://doi.org/10.1246/cl.2007.1314.

(14) Basaleh, A. S.; El-Hout, S. I. Sol-Gel Synthesis of Photoactive PtO/Bi2WO6 Nanocomposites for Improved Photoreduction of Hg (II) Ions under Visible Illumination. Mol. Catal. 2023, 547, 113413. https://doi.org/10.1016/j.mcat.2023.113413.

(15) Zhang, G.; Lü, F.; Li, M.; Yang, J.; Zhang, X.; Huang, B. Synthesis of Nanometer Bi2WO6 Synthesized by Sol–Gel Method and Its Visible-Light Photocatalytic Activity for Degradation of 4BS. J. Phys. Chem. Solids 2010, 71 (4), 579–582. https://doi.org/10.1016/j.jpcs.2009.12.041.

(16) Liu, Y.; Li, Z.; Lv, H.; Tang, H.; Xing, X. Synthesis of Hierarchical Bi2WO6 Microspheres with High Visible-Light-Driven Photocatalytic Activities by Sol–Gel-Hydrothermal Route. Mater. Lett. 2013, 108, 84–87. https://doi.org/10.1016/j.matlet.2013.06.064.

(17) El-Shishtawy, R. M.; Shawky, A.; Alorfi, H. S.; Hussein, M. A.; Mohamed, R. M. Efficient Visible-Light-Driven H2 Evolution over Sol-Gel Processed Bi2WO6 Nanocrystals Anchored with Ag2O Support. Ceram. Int. 2023, 49 (9, Part A), 14274–14280. https://doi.org/10.1016/j.ceramint.2023.01.014.

(18) Zhong, X.; Liu, Y.; Hou, T.; Zhu, Y.; Hu, B. Effect of Bi2WO6 Nanoflowers on the U(VI) Removal from Water: Roles of Adsorption and Photoreduction. J. Environ. Chem. Eng. 2022, 10 (2), 107170. https://doi.org/10.1016/j.jece.2022.107170.

(19) Luo, S.; Ke, J.; Yuan, M.; Zhang, Q.; Xie, P.; Deng, L.; Wang, S. CuInS2 Quantum Dots Embedded in Bi2WO6 Nanoflowers for Enhanced Visible Light Photocatalytic Removal of Contaminants. Appl. Catal. B Environ. 2018, 221, 215–222. https://doi.org/10.1016/j.apcatb.2017.09.028.

(20) Zhao, Y.; Wang, Y.; Liu, E.; Fan, J.; Hu, X. Bi2WO6 Nanoflowers: An Efficient Visible Light Photocatalytic Activity for Ceftriaxone Sodium Degradation. Appl. Surf. Sci. 2018, 436, 854–864. https://doi.org/10.1016/j.apsusc.2017.12.064.

(21) Phu, N. D.; Hoang, L. H.; Chen, X.-B.; Kong, M.-H.; Wen, H.-C.; Chou, W. C. Study of Photocatalytic Activities of Bi2WO6 Nanoparticles Synthesized by Fast Microwave-Assisted Method. J. Alloys Compd. 2015, 647, 123–128. https://doi.org/10.1016/j.jallcom.2015.06.047.

(22) Xie, H.; Shen, D.; Wang, X.; Shen, G. Microwave Hydrothermal Synthesis and Visible-Light Photocatalytic Activity of Bi2WO6 Nanoplates. Mater. Chem. Phys. 2007, 103 (2), 334–339. https://doi.org/10.1016/j.matchemphys.2007.02.040.

(23) Cao, X.-F.; Zhang, L.; Chen, X.-T.; Xue, Z.-L. Microwave-Assisted Solution-Phase Preparation of Flower-like Bi2WO6 and Its Visible-Light-Driven Photocatalytic Properties. CrystEngComm 2010, 13 (1), 306–311. https://doi.org/10.1039/C0CE00031K.

(24) Yao, S.; Wei, J.; Huang, B.; Feng, S.; Zhang, X.; Qin, X.; Wang, P.; Wang, Z.; Zhang, Q.; Jing, X.; Zhan, J. Morphology Modulated Growth of Bismuth Tungsten Oxide Nanocrystals. J. Solid State Chem. 2009, 182 (2), 236–239. https://doi.org/10.1016/j.jssc.2008.09.016.

(25) Hayashi, H.; Hakuta, Y. Hydrothermal Synthesis of Metal Oxide Nanoparticles in Supercritical Water. Materials 2010, 3 (7), 3794–3817. https://doi.org/10.3390/ma3073794.

(26) Adschiri, T.; Hakuta, Y.; Sue, K.; Arai, K. Hydrothermal Synthesis of Metal Oxide Nanoparticles at Supercritical Conditions. J. Nanoparticle Res. 2001, 3 (2), 227–235. https://doi.org/10.1023/A:1017541705569.

(27) Luong, D.; Sephton, M. A.; Watson, J. S. Subcritical Water Extraction of Organic Matter from Sedimentary Rocks. Anal. Chim. Acta 2015, 879, 48–57. https://doi.org/10.1016/j.aca.2015.04.027.

(28) Sheng, L.; Zhang, Y.; Tang, F.; Liu, S. Mesoporous/Microporous Silica Materials: Preparation from Natural Sands and Highly Efficient Fixed-Bed Adsorption of

Methylene Blue in Wastewater. Microporous Mesoporous Mater. 2018, 257, 9–18. https://doi.org/10.1016/j.micromeso.2017.08.023.

(29) Liu, T.; Xue, F.; Wang, B.; Wang, R.; Cao, W.; Zhao, X.; Xia, Y.; Jin, W.; Zhang, Y.; Lin, H.; Liu, C. Rapid Microwave Synthesis of Bi2WO6 for C=C Bonds Oxidative Cleavage to Ketones with Visible Light Irradiation in Aerobic Micellar Medium. J. Catal. 2023, 417, 41–51. https://doi.org/10.1016/j.jcat.2022.11.034.

(30) Liu, Y.; Yang, B.; He, H.; Yang, S.; Duan, X.; Wang, S. Bismuth-Based Complex Oxides for Photocatalytic Applications in Environmental Remediation and Water Splitting: A Review. Sci. Total Environ. 2022, 804, 150215. https://doi.org/10.1016/j.scitotenv.2021.150215.

(31) Unsworth, C. A. The Use of Visible Light Absorbing Bismuth-Containing Semiconductors as Heterogeneous Photocatalysts for Selective Chemical Transformations. phd, University of York, 2017. https://etheses.whiterose.ac.uk/19361/ (accessed 2023-08-15).

(32) Hu, Y.; Ma, D.; Ma, J. Microwave Hotspots: Thermal Nonequilibrium Dynamics from the Perspective of Quantum States. J. Phys. Chem. A 2021, 125 (12), 2690–2696. https://doi.org/10.1021/acs.jpca.0c11594.

(33) Chen, Y.; Zhang, Y.; Liu, C.; Lu, A.; Zhang, W. Photodegradation of Malachite Green by Nanostructured Bi 2WO 6 Visible Light-Induced Photocatalyst. Int. J. Photoenergy 2012, 2012 (1), 510158. https://doi.org/10.1155/2012/510158.

(34) Muhammed Shafi, P.; Chandra Bose, A. Impact of Crystalline Defects and Size on X-Ray Line Broadening: A Phenomenological Approach for Tetragonal SnO2 Nanocrystals. AIP Adv. 2015, 5 (5), 057137. https://doi.org/10.1063/1.4921452.

(35) Cartwright, A.; Jackson, K.; Morgan, C.; Anderson, A.; Britt, D. W. A Review of Metal and Metal-Oxide Nanoparticle Coating Technologies to Inhibit Agglomeration and Increase Bioactivity for Agricultural Applications. Agronomy 2020, 10 (7), 1018. https://doi.org/10.3390/agronomy10071018.

(36) Wang, H.; Lin, Q.; Dou, X.; Yang, T.; Han, Y. A Different View of Solvent Effects in Crystallization. Crystals 2017, 7 (12), 357. https://doi.org/10.3390/cryst7120357.

(37) Ouyang, J.; Pei, J.; Kuang, Q.; Xie, Z.; Zheng, L. Supersaturation-Controlled Shape Evolution of α-Fe2O3 Nanocrystals and Their Facet-Dependent Catalytic and Sensing Properties. ACS Appl. Mater. Interfaces 2014, 6 (15), 12505–12514. https://doi.org/10.1021/am502358g.

(38) Wang, L.; Liu, G.; Xi, X.; Yang, G.; Hu, L.; Zhu, B.; He, Y.; Liu, Y.; Qian, H.; Zhang, S.; Zai, H. Annealing Engineering in the Growth of Perovskite Grains. Crystals 2022, 12 (7), 894. https://doi.org/10.3390/cryst12070894.

(39) Bansal, N.; Reynolds, L. X.; MacLachlan, A.; Lutz, T.; Ashraf, R. S.; Zhang, W.; Nielsen, C. B.; McCulloch, I.; Rebois, D. G.; Kirchartz, T.; Hill, M. S.; Molloy, K. C.; Nelson, J.; Haque, S. A. Influence of Crystallinity and Energetics on Charge Separation in Polymer–Inorganic Nanocomposite Films for Solar Cells. Sci. Rep. 2013, 3 (1), 1531. https://doi.org/10.1038/srep01531.

(40) Xu, K.; Yao, M.; Chen, J.; Zou, P.; Peng, Y.; Li, F.; Yao, X. Effect of Crystallization on the Band Structure and Photoelectric Property of SrTiO3 Sol–Gel Derived Thin Film. J. Alloys Compd. 2015, 653, 7–13. https://doi.org/10.1016/j.jallcom.2015.09.017.

(41) Ambroz, F.; Macdonald, T. J.; Martis, V.; Parkin, I. P. Evaluation of the BET Theory for the Characterization of Meso and Microporous MOFs. Small Methods 2018, 2 (11), 1800173. https://doi.org/10.1002/smtd.201800173.

(42) Walton, K. S.; Snurr, R. Q. Applicability of the BET Method for Determining Surface Areas of Microporous Metal−Organic Frameworks. J. Am. Chem. Soc. 2007, 129 (27), 8552–8556. https://doi.org/10.1021/ja071174k.

(43) Thommes, M.; Kaneko, K.; Neimark, A. V.; Olivier, J. P.; Rodriguez-Reinoso, F.; Rouquerol, J.; Sing, K. S. W. Physisorption of Gases, with Special Reference to the Evaluation of Surface Area and Pore Size Distribution (IUPAC Technical Report). Pure Appl. Chem. 2015, 87 (9–10), 1051–1069. https://doi.org/10.1515/pac-2014-1117.

(44) Giese, B.; González-Gómez, J. A.; Witzel, T. The Scope of Radical CC-Coupling by the “Tin Method.” Angew. Chem. Int. Ed. Engl. 1984, 23 (1), 69–70. https://doi.org/10.1002/anie.198400691.

(45) Raza, W.; Faisal, S. M.; Owais, M.; Bahnemann, D.; Muneer, M. Facile Fabrication of Highly Efficient Modified ZnO Photocatalyst with Enhanced Photocatalytic, Antibacterial and Anticancer Activity. RSC Adv. 2016, 6 (82), 78335–78350. https://doi.org/10.1039/C6RA06774C.

(46) Alivisatos, A. P. Perspectives on the Physical Chemistry of Semiconductor Nanocrystals. J. Phys. Chem. 1996, 100 (31), 13226–13239. https://doi.org/10.1021/jp9535506.

(47) Abdullah, B. J. Size Effect of Band Gap in Semiconductor Nanocrystals and Nanostructures from Density Functional Theory within HSE06. Mater. Sci. Semicond. Process. 2022, 137, 106214. https://doi.org/10.1016/j.mssp.2021.106214.

(48) Singh, M.; Goyal, M.; Devlal, K. Size and Shape Effects on the Band Gap of Semiconductor Compound Nanomaterials. J. Taibah Univ. Sci. 2018, 12 (4), 470–475. https://doi.org/10.1080/16583655.2018.1473946.

(49) Rabouw, F. T.; de Mello Donega, C. Excited-State Dynamics in Colloidal Semiconductor Nanocrystals. Top. Curr. Chem. 2016, 374 (5), 58. https://doi.org/10.1007/s41061-016-0060-0.

(50) Mohtar, S. S.; Aziz, F.; Ismail, A. F.; Sambudi, N. S.; Abdullah, H.; Rosli, A. N.; Ohtani, B. Impact of Doping and Additive Applications on Photocatalyst Textural Properties in Removing Organic Pollutants: A Review. Catalysts 2021, 11 (10), 1160. https://doi.org/10.3390/catal11101160.

(51) Ali, S.; Abdul Nasir, J.; Nasir Dara, R.; Rehman, Z. Modification Strategies of Metal Oxide Photocatalysts for Clean Energy and Environmental Applications: A Review. Inorg. Chem. Commun. 2022, 145, 110011. https://doi.org/10.1016/j.inoche.2022.110011.

(52) Pascariu, P.; Gherasim, C.; Airinei, A. Metal Oxide Nanostructures (MONs) as Photocatalysts for Ciprofloxacin Degradation. Int. J. Mol. Sci. 2023, 24 (11), 9564. https://doi.org/10.3390/ijms24119564.

(53) Wenderich, K.; Mul, G. Methods, Mechanism, and Applications of Photodeposition in Photocatalysis: A Review. Chem. Rev. 2016, 116 (23), 14587–14619. https://doi.org/10.1021/acs.chemrev.6b00327.

(54) Chen, G.; Li, R.; Huang, L. Advances in Photochemical Deposition for Controllable Synthesis of Heterogeneous Catalysts. Nanoscale 2023, 15 (34), 13909–13931. https://doi.org/10.1039/D3NR02475J.

(55) Lee, Y.; Kim, E.; Park, Y.; Kim, J.; Ryu, W.; Rho, J.; Kim, K. Photodeposited Metal-Semiconductor Nanocomposites and Their Applications. J. Materiomics 2018, 4 (2), 83–94. https://doi.org/10.1016/j.jmat.2018.01.004.

(56) Rao, V. N.; Reddy, N. L.; Kumari, M. M.; Cheralathan, K. K.; Ravi, P.; Sathish, M.; Neppolian, B.; Reddy, K. R.; Shetti, N. P.; Prathap, P.; Aminabhavi, T. M.; Shankar, M. V. Sustainable Hydrogen Production for the Greener Environment by Quantum Dots-Based Efficient Photocatalysts: A Review. J. Environ. Manage. 2019, 248, 109246. https://doi.org/10.1016/j.jenvman.2019.07.017.

(57) Zhou, X.; Qian, K.; Zhang, Y.; Li, D.; Wei, Z.; Wang, H.; Ye, R.; Liu, J.; Ye, B.; Huang, W. Tuning the Size of Photo-Deposited Metal Nanoparticles via Manipulating Surface Defect Structures of TiO2 Nanocrystals. Chem. Commun. 2020, 56 (13), 1964–1967. https://doi.org/10.1039/C9CC09642F.

(58) Majumdar, A.; Pal, A. Recent Advancements in Visible-Light-Assisted Photocatalytic Removal of Aqueous Pharmaceutical Pollutants. Clean Technol. Environ. Policy 2020, 22 (1), 11–42. https://doi.org/10.1007/s10098-019-01766-1.

(59) Xue, J.; Ma, S.; Zhou, Y.; Zhang, Z.; He, M. Facile Photochemical Synthesis of Au/Pt/g-C3N4 with Plasmon-Enhanced Photocatalytic Activity for Antibiotic Degradation. ACS Appl. Mater. Interfaces 2015, 7 (18), 9630–9637. https://doi.org/10.1021/acsami.5b01212.

(60) Zhang, G.; Guan, W.; Shen, H.; Zhang, X.; Fan, W.; Lu, C.; Bai, H.; Xiao, L.; Gu, W.; Shi, W. Organic Additives-Free Hydrothermal Synthesis and Visible-Light-Driven Photodegradation of Tetracycline of WO3 Nanosheets. Ind. Eng. Chem. Res. 2014, 53 (13), 5443–5450. https://doi.org/10.1021/ie4036687.

(61) Shiraishi, Y.; Tsukamoto, D.; Sugano, Y.; Shiro, A.; Ichikawa, S.; Tanaka, S.; Hirai, T. Platinum Nanoparticles Supported on Anatase Titanium Dioxide as Highly Active Catalysts for Aerobic Oxidation under Visible Light Irradiation. ACS Catal. 2012, 2 (9), 1984–1992. https://doi.org/10.1021/cs300407e.

(62) Wu, Y.; Zhang, X.; Zhang, G.; Guan, W. Visible Light-Assisted Synthesis of Pt/Bi2WO6 and Photocatalytic Activity for Ciprofloxacin. Micro Nano Lett. 2014, 9 (2), 119–122. https://doi.org/10.1049/mnl.2013.0705.

(63) Qamar, M.; Elsayed, R. B.; Alhooshani, K. R.; Ahmed, M. I.; Bahnemann, D. W. Highly Efficient and Selective Oxidation of Aromatic Alcohols Photocatalyzed by Nanoporous Hierarchical Pt/Bi2WO6 in Organic Solvent-Free Environment. ACS Appl. Mater. Interfaces 2015, 7 (2), 1257–1269. https://doi.org/10.1021/am507428r.

(64) Zhang, S.; Pu, W.; Chen, A.; Xu, Y.; Wang, Y.; Yang, C.; Gong, J. Oxygen Vacancies Enhanced Photocatalytic Activity towards VOCs Oxidation over Pt Deposited Bi2WO6 under Visible Light. J. Hazard. Mater. 2020, 384, 121478. https://doi.org/10.1016/j.jhazmat.2019.121478.

(65) Prat, D.; Wells, A.; Hayler, J.; Sneddon, H.; McElroy, C. R.; Abou-Shehada, S.; Dunn, P. J. CHEM21 Selection Guide of Classical- and Less Classical-Solvents. Green Chem. 2015, 18 (1), 288–296. https://doi.org/10.1039/C5GC01008J.

(66) Nakamatsu, H.; Kawai, T.; Koreeda, A.; Kawai, S. Electron-Microscopic Observation of Photodeposited Pt on TiO2 Particles in Relation to Photocatalytic Activity. J. Chem. Soc. Faraday Trans. 1 Phys. Chem. Condens. Phases 1986, 82 (2), 527–531. https://doi.org/10.1039/F19868200527.

(67) Advances and Significances of Nanoparticles in Semiconductor Applications – A Review. Results Eng. 2023, 19, 101347. https://doi.org/10.1016/j.rineng.2023.101347.

(68) Lehmann, J.; Merschdorf, M.; Pfeiffer, W.; Thon, A.; Voll, S.; Gerber, G. Surface Plasmon Dynamics in Silver Nanoparticles Studied by Femtosecond Time-Resolved Photoemission. Phys. Rev. Lett. 2000, 85 (14), 2921–2924. https://doi.org/10.1103/PhysRevLett.85.2921.

(69) Leong, K. H.; Gan, B. L.; Ibrahim, S.; Saravanan, P. Synthesis of Surface Plasmon Resonance (SPR) Triggered Ag/TiO2 Photocatalyst for Degradation of Endocrine Disturbing Compounds. Appl. Surf. Sci. 2014, 319, 128–135. https://doi.org/10.1016/j.apsusc.2014.06.153.

(70) Su, Y.-H.; Ke, Y.-F.; Cai, S.-L.; Yao, Q.-Y. Surface Plasmon Resonance of Layer-by-Layer Gold Nanoparticles Induced Photoelectric Current in Environmentally-Friendly Plasmon-Sensitized Solar Cell. Light Sci. Appl. 2012, 1 (6), e14–e14. https://doi.org/10.1038/lsa.2012.14.

(71) Qin, L.; Wang, G.; Tan, Y. Plasmonic Pt Nanoparticles—TiO2 Hierarchical Nano-Architecture as a Visible Light Photocatalyst for Water Splitting. Sci. Rep. 2018, 8 (1), 16198. https://doi.org/10.1038/s41598-018-33795-z.

(72) Lee, C.; Park, Y.; Park, J. Y. Hot Electrons Generated by Intraband and Interband Transition Detected Using a Plasmonic Cu/TiO2 Nanodiode. RSC Adv. 2019, 9 (32), 18371–18376. https://doi.org/10.1039/C9RA02601K.

(73) Lyu, P.; Espinoza, R.; Nguyen, S. C. Photocatalysis of Metallic Nanoparticles: Interband vs Intraband Induced Mechanisms. J. Phys. Chem. C 2023, 127 (32), 15685–15698. https://doi.org/10.1021/acs.jpcc.3c04436.

(74) Brown, A. M.; Sundararaman, R.; Narang, P.; Goddard, W. A. I.; Atwater, H. A. Nonradiative Plasmon Decay and Hot Carrier Dynamics: Effects of Phonons, Surfaces, and Geometry. ACS Nano 2016, 10 (1), 957–966. https://doi.org/10.1021/acsnano.5b06199.

(75) Clavero, C. Plasmon-Induced Hot-Electron Generation at Nanoparticle/Metal-Oxide Interfaces for Photovoltaic and Photocatalytic Devices. Nat. Photonics 2014, 8 (2), 95–103. https://doi.org/10.1038/nphoton.2013.238.

Chapter 3: Mechanistic study of Giese Reaction Photocatalysed by Bismuth Tungstate

3.1 Introduction

The model reaction system chosen for this study is the Giese reaction which has not been previously reported for Bi_2WO_6 photocatalysis but has been reported for TiO_2 under UV light. The Giese reaction is a simple and efficient C-C coupling reaction which is valuable in organic chemistry. Preliminary results[1] showed the feasibility of using Bi_2WO_6 as a photocatalyst in this reaction. Thus, the main goal of this chapter is to study factors affecting the reaction, which leads to improved understanding of the mechanism. Trying different reaction conditions does not necessarily lead to optimum yield. However, by understanding the reaction mechanism, designing experiments would be easier, which would lead to further improvement through suitable optimisation and expand the scope of the reaction. In addition, understanding the mechanism of this particular reaction will help in designing other reactions in the future. This justifies the mechanistic study from an organic point of view. From an inorganic point of view, a suitable catalyst can be chosen or synthesised to meet photocatalysis requirements. Also, structure and surface modifications can be applied to improve catalysis when the mechanism is understood. The mechanistic study will be carried out using techniques such as proton nuclear magnetic resonance (^{1}H NMR), electron paramagnetic resonance spectroscopy (EPR), deuterium nuclear magnetic resonance spectroscopy (^{2}H NMR), photoluminescent spectroscopy (PL) and time-resolved photoluminescent spectroscopy (TRPL). The current study will focus on factors affecting the efficiency of photocatalysis using Bi_2WO_6 nanoparticles. The surface chemistry of Bi_2WO_6 and how it affects catalytic activity are some of these factors. Others include the adsorption of starting materials (such as acids and alkenes) and products on the catalyst surface, and the impact of water on catalytic activity. H/D isotopic labelling was also performed to study how the intermediate radical is transformed to final product via net addition of a hydrogen atom.

3.1.1 Giese reaction

The Giese reaction is one of the most useful reactions in radical chemistry. Giese radical addition is a reaction between a nucleophilic carbon-centred radical and an electron-deficient alkene, Michael acceptor. The name came after the German chemist professor Bernd Giese's work titled “The Scope of Radical C-C Coupling by the Tin Method." In his study, he showed that alkyl radicals can be formed from alkyl halides using tributyltin hydride as a mediator.[2] The carbon-centred radical (I) that formed undergoes an addition to electron-deficient alkenes to form the corresponding radical adducts (II) (Figure 3.1).

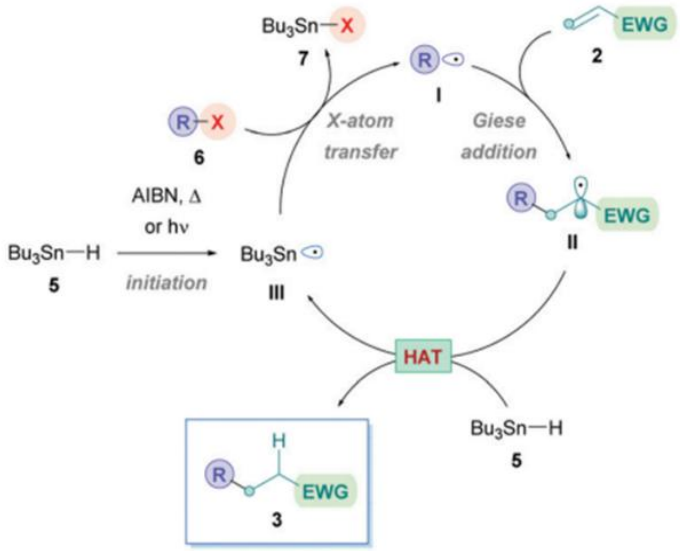

Figure 3.1: Traditional Giese reaction mechanism using AIBN as initiator and Bu_3SnH as a mediator and alkyl halide as radical precursors.[2,3]

The Giese reaction is a regioselective reaction and is considered in some literature as 1,4 addition pathway resembling addition of nucleophile (here carbon centred radical is a nucleophilic species) to a double bond in conjugation with carbonyl group as electron withdrawing group (2). This addition forms a new radical intermediate (II), which is subsequently either trapped by a hydrogen atom transfer (HAT) to form Giese adduct (3) or, alternatively, this radical intermediate can undergo single electron transfer (SET) to yield a carbanion (enolate) followed by protonation to form Giese adduct. The rate at which carbon-centered radical adds to electron-deficient alkene is approximately 10^6 M^{-1} s^{-1}.[4] Fortunately, this rate is higher than that of the typical counterproductive reactions, such as atom-transfer reactions involving delicate functional groups like alcohols and amines, as well as carbonyl additions, which have a rate of approximately 10^2 M^{-1} s^{-1}. The variation in rates highlights the chemoselective property of radical conjugate additions, which can occur even when there are unprotected functional groups present.

Traditionally, the Giese reaction uses toxic tin hydride reagents as a radical mediator and is initiated by AIBN (azobisisobutyronitrile) that needs light or heat, with alkyl halides or selenides as alkyl radical precursors.

It is challenging to obtain high yields in Giese reaction because the yields of desired products are often reduced by competing side reactions. Such reactions include addition of tin radicals to the Michael acceptor, a process called hydrostannylation; (Figure 3.2 A), oligomerisation of the Michael acceptor (Figure 3.2 B), or premature abstraction of hydrogen from Bu_3SnH (Figure 3.2 C). Nevertheless, by employing appropriate reaction conditions, those limitations can be reduced.

The limited range of possible radical precursors has also added to the limitations brought about by biggest issue, the toxicity of tin compounds. There has been a noticeable upsurge in the development of innovative strategies that are eco-friendly and employ more sustainable radical precursors in order to tackle these issues such as using carboxylic acids.

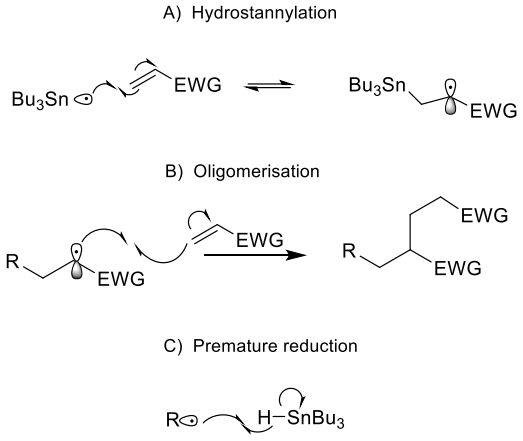

Figure 3.2: Possible competitive side reactions in Giese reaction. A) hydrostannylation, B) oligomerisation, C) premature reduction.[3]

3.1.2 Carboxylic acids as a versatile radical precursor

Carboxylic acids have become a great alternative source of alkyl radicals. They are inexpensive, bench-stable, nontoxic, and widely used. Carboxylic acids can undergo deprotonation easily. These carboxylate ions can be readily oxidised to a carboxyl radical, which undergoes selective spontaneous fragmentation to yield an alkyl radical and release carbon dioxide (CO_2) as a by-product. This creates a driving force for alkyl radical formation. Carboxylic acids, due to their wide range of structural variations, are present in various organic molecules, such as amino acids, fatty acids, and sugar acids. This characteristic makes them ideal feedstock for the production of valuable chemicals, including pharmaceuticals. As this project aims to develop greener approaches, carboxylic acids will be used as a radical precursor.

3.1.3 Photocatalysis vs electrochemistry

The classical route of generation of alkyl radicals by oxidative decarboxylation is through electrolysis (Kolbe reaction).[5,6] These radicals can undergo dimerization, addition to alkene (i.e., Giese reaction), and radical chain reactions. Alternatively, carboxylates can be oxidised to alkyl radicals photocatalytically. Both electrolysis and photocatalysis (photoredox) are considered greener methods in terms of using mild reaction conditions, renewable energy sources (electricity and light), and minimum toxic waste. However,

electrolysis needs complex cell design and includes other components in the system, such as electrolytes (Figure 3.3). In photocatalysis, on the other hand, fewer components are used, which is good in terms of atom economy. Also, electrical power in electrolysis needs to be controlled to avoid overoxidation or overreduction of substrates. Most importantly, the electrodes (anode and cathode) in electrosynthesis are separated by distance, which affects oxidation and reduction via a drop in voltage due to solution resistance. On the other hand, the photoredox cycle happens simultaneously on the same particle. In addition, while electrochemistry allows to control energy by changing the potential, electrochemistry requires the electrodes to be conductive which may limit the possibilities for catalysis.

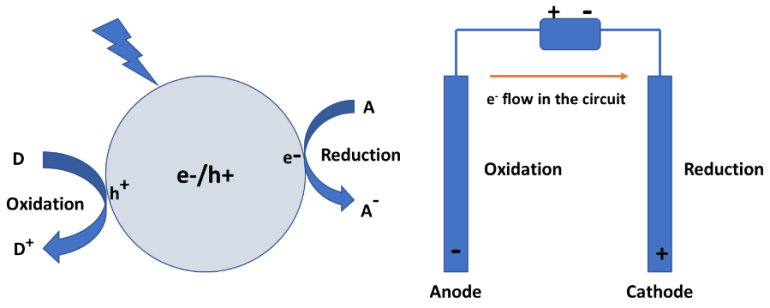

Figure 3.3: Schematic diagram comparing photocatalysis with electrolysis. [7]

3.1.4 Photocatalysis in decarboxylative Giese reaction

Carbon-centred free radical formation via decarboxylation of carboxylic acids using homogeneous photocatalysis has attracted huge attention. Many studies have been published on photoredox-mediated decarboxylative Giese reactions using iridium and ruthenium-based photocatalysts.[8-11] However, recently metal oxide semiconductors (MOSC) have emerged as an alternative approach as they are considered greener photocatalysts because they generate less or non-toxic waste, they can be recovered and reused. There are however only a few studies in the literature on photoredox-mediated decarboxylative Giese reactions using metal oxide semiconductors.

3.1.4.1 Homogenous photocatalysts in Giese reaction

Miyake et. al.[11] demonstrated the decarboxylation of arylacetic acids and the formation of corresponding benzyl radicals which subsequently added to ethyl (E)-2-cyano-3-phenylpropenoate, affording 85% of the benzylated adducts using the iridium polypyridyl complex $[Ir(ppy)_2(dtbbpy)][BF_4]$ as a visible-light photocatalyst (Figure 3.4).[12] This reaction proceeds through radical pathway where aminoarylacetic acid is subjected to an excited photo-catalyst-induced oxidation process, followed by decarboxylation,

benzyl radical production, and reduction of intermediate radical to corresponding intermediate anion which later is protonated to yield product (3). The reduction step of the intermediate radical converts reduced catalyst back to its original state.

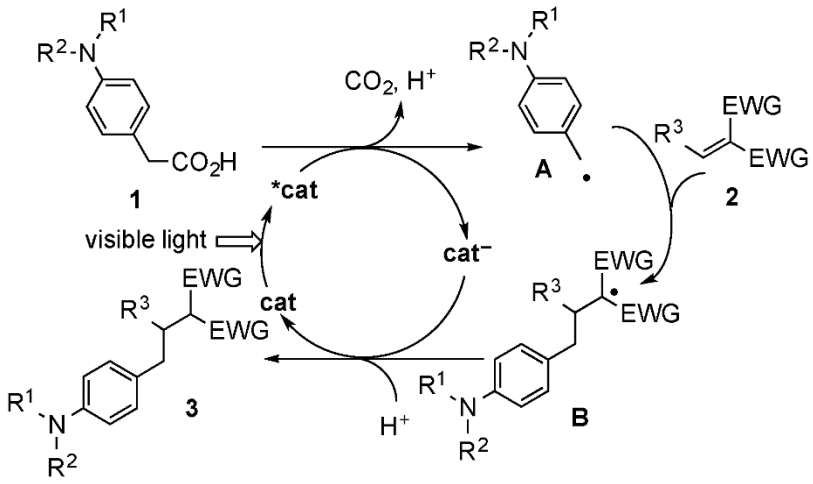

Figure 3.4: proposed mechanism by Miyake for formation of Giese adduct using photo-irradiated [Ir(ppy)2(dtbbpy)][BF4].[12] Reused with permission from ref. (12)

Another similar study was carried out by Chu et al[13] where an iridium catalyst, $[Ir(df(CF_3)ppy)_2(dtbbpy)][PF_4]$, was used to obtain the corresponding 1,4-addition Giese product using a broad scope of carboxylic acids and Michael acceptors. In this work, a base such as CsF and K_2HPO_4 was needed to deprotonate the carboxylic acid. A wide range of substrates (acids, including aliphatic acid, and alkene were utilised) with high selectivity compared to previous work.

3.1.4.2 Disadvantages of homogeneous catalysts in Giese reaction

Homogeneous photocatalysts can have higher selectivity and require lower loading, yet their toxicity and cost are disadvantages. Their separation from the reaction mixture is also challenging, and the complete removal of metal is very difficult. On the other hand, MOSC is less toxic and cheaper. Besides, they can be separated easily and recovered for further use as described in the introduction.

3.1.4.3 Metal oxide semiconductors in Giese reaction

A report on using MOSC was carried out by Zhu and Nocera using TiO_2 in Giese radical addition (Figure 3.5).[14,15] Surface-adsorbed acetate undergoes decarboxylation due to photogenerated holes when photoexcitation induces the formation of electrons and holes within the TiO_2 particles. After migrating to the surface, the holes oxidise the adsorbed acetate. A reduced catalyst (C) and a free methyl radical are the outcomes of this. Intermediate enolate (E) is created by the reduction of radical (D) by reduced TiO_2 (C).

This also brings TiO_2 back to its original oxidation state. The catalytic cycle is closed by proton transfer from acetic acid. The authors also tried other metal oxides, such as ZnO, but this oxide did not work because ZnO was not stable in acidic conditions. Acetonitrile was found to be the best solvent to yield the desired product in up to 86% yield. Three equivalents of acid were needed to reach this yield based on the alkene substrate. The scope was applied to a wide range of carboxylic acids and olefins and required intense UV light.

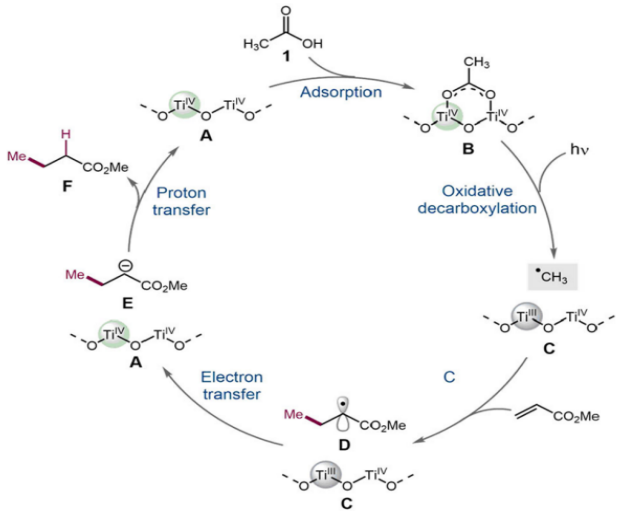

Figure 3.5: proposed mechanism by Zhu and Nocera of photocatalysed Giese reaction using TiO2 nanoparticles. [14] Reused with permission from ref. (14).

Another example of using MOSC in the Giese addition reaction was carried out by Kuwana et al.[16] using TiO_2 as photocatalyst but with the addition of Pt as a co-catalyst (Figure 3.6). They did not explain the use of Pt but it could have increased the activity of TiO_2 under violet LED (390 nm) illumination by absorbing light or Pt could have acted as a sink for photogenerated electrons. In addition to Giese addition product, this work investigated the formation of dimers as an alternative reaction pathway in the absence of alkene and an 87 % yield of the dimer was achieved with Pt-doped TiO_2 catalyst. This work also studied oxygenated substrates where alkoxy carboxylic acids were used. The obtained diastereomeric dimers yields were moderate (50 %).

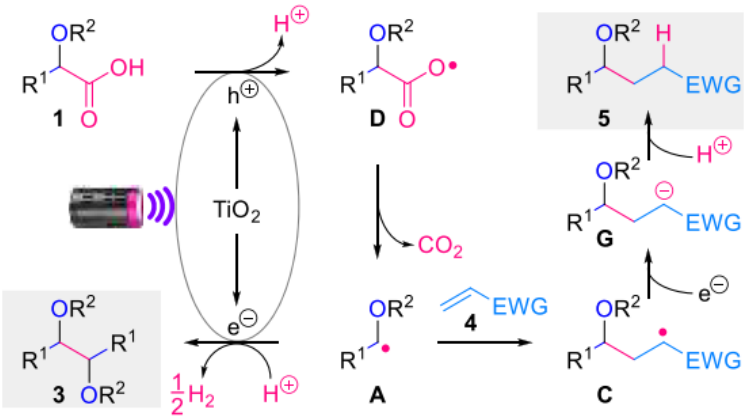

Figure 3.6: Plausible mechanism of formation of Giese adduct and radical dimerization as a side reaction.[16] Reused with permission from ref. (16)

The above examples of photocatalysed Giese reactions, which can be driven by homogeneous or heterogeneous photocatalysts, support the theory that photoexcited catalysts facilitate oxidation of carboxylates which decarboxylate to yield carbon-centred radicals and carbon dioxide. Then, these radicals can undergo addition to alkene to produce the desired adduct.

However, the use of heterogenous MOSCs is favourable due to their sustainability, which makes them stable, recyclable, and cost-effective compared to homogenous photocatalysts. The surface chemistry of MOSCs is what makes them a good alternative in organic synthesis. In the following section, we will try to understand the surface chemistry of MOSCs and highlight its importance in organic synthesis.

3.2 Bi_2WO_6 in photo induced Giese reaction

Bi_2WO_6 nanoparticles are known for their applications in water oxidation and dye degradation. Bi_2WO_6 has relatively small bandgap compared to TiO_2, which makes it an alternative to TiO_2 for use with visible light. The main goal of this chapter is to utilise Bi_2WO_6 nanoparticles in the Giese reaction and then try to understand factors affecting photocatalytic activity and reaction selectivity through mechanistic study. This chapter starts by developing the methodology for monitoring photocatalytic Giese reaction by Bi_2WO_6. In the beginning, the model reaction of an arylacetic acid (phenylacetic acid, PAAH) and an electron-deficient alkene (methacrolein, MAC) with Bi_2WO_6 under irradiation in an oxygen-free environment (Scheme 3.1), will be used to test the feasibility of this reaction. Then, mechanistic experiments such as radical trapping, deuterium exchange and catalyst hydration (addition of water) will be carried out to monitor the factors affecting catalytic activity and reaction selectivity and to try to elucidate the reaction pathways.

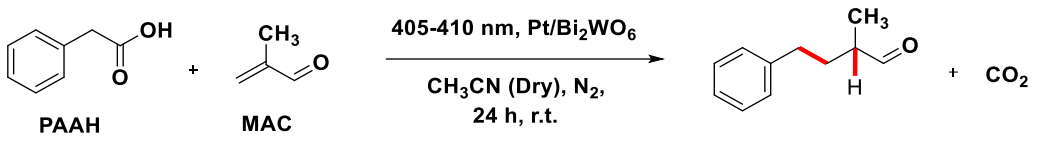

Scheme 3.1: General scheme of Giese reaction in presence of Irradiated Bi_2WO_6 nanoparticles.

3.2.1 Unmodified Bi_2WO_6 vs platinised Bi_2WO_6: control experiment

In this experiment, bare and platinised Bi_2WO_6 were used in Giese reaction to compare their activities and investigate the role of co-catalyst. Pt/Bi_2WO_6 was used, the desired product was obtained in 64 % with complete conversion of phenylacetic acid. The corresponding ^1H NMR spectrum is shown in **(**Figure 3.7 A). Unmodified photoirradiated Bi_2WO_6 was also used in the decarboxylation of phenylacetic acid in the presence of methacrolein, and the corresponding ^1H NMR spectrum is shown in (Figure 3.7 B). There is no evidence of reaction product, and only the starting material is observed. The spectral pattern (Figure 3.7 A) is complicated by the presence of a stereogenic centre, which makes both black CH_2 with asterisk and red CH_2 diastereotopic.

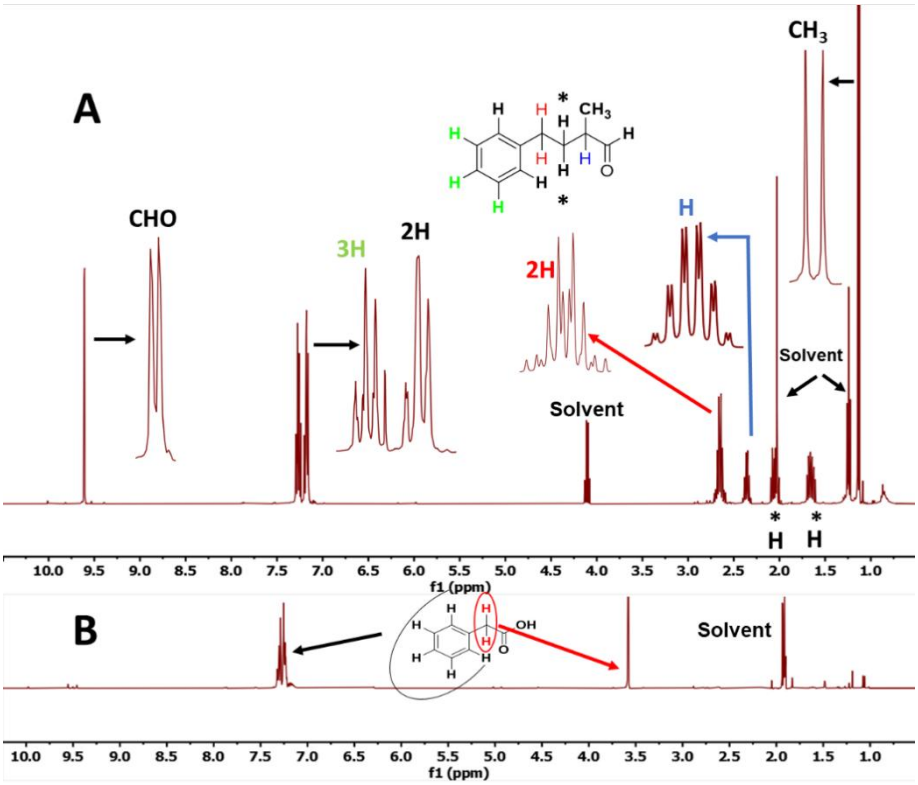

Figure 3.7: Typical ^1H NMR spectrum of A) Giese adduct resulted from reaction between phenylacetic acid (PAAH) and methacrolein (MAC) in presence of photo-irradiated 0.15Pt/ Bi_2WO_6 nanoparticles. B) Reaction outcome between PAAH and MAC in presence of photo-irradiated Bi_2WO_6 nanoparticles.

It can be clearly seen from ^{1}H NMR that the $0.15Pt/Bi_2WO_6$ is more active than Bi_2WO_6, in which the starting material (PAAH) was not consumed, (Figure 3.7 B). Other side products resulting from Giese reaction using $0.15Pt/Bi_2WO_6$ (Figure 3.7 A), including bibenzyl, benzyl alcohol, and benzaldehyde, are confirmed by GC-MS (Figure 3.8). The major peak is assigned to the target product, 4-phenyl-2-methylbutanal. The remaining unidentified compounds could be the result of multiple radical addition reactions.

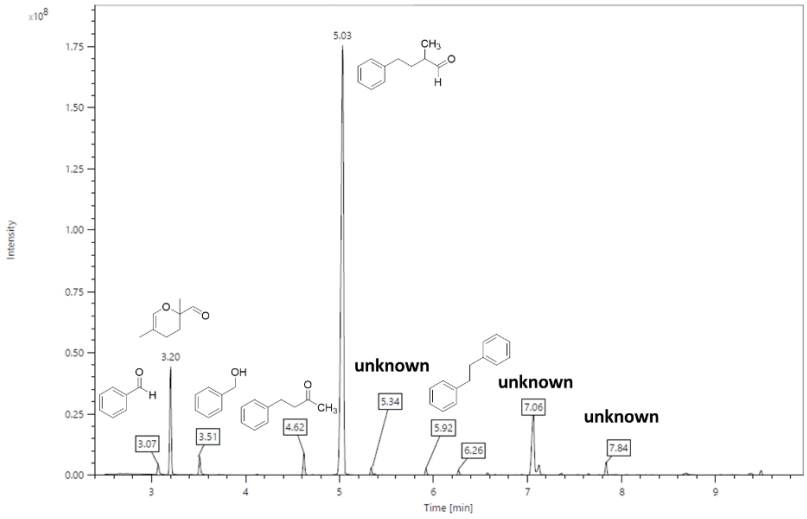

Figure 3.8: GC-MS chromatogram showing the major product, the Giese adduct, and other side products including benzaldehyde, benzyl alcohol, bibenzyl, and products as result of multiple radical additions.

The optimum condition of the reaction was 3 equivalents of alkene, 60 mg of platinised catalyst with around 0.15-2 wt.% Pt and 24 hrs reaction length. These conditions are described in chapter 4, optimisation chapter.

The conclusion of this section is that Pt is important for catalytic activity and reaction selectivity. The following section is to investigate the role of Pt in adding such activity and selectivity.

3.3 Importance of addition of metal NPs as co-catalyst

As discussed in section 1.5.3, metal NPs can enhance metal oxides photoactivity in different ways. They can act as charge trapping centres facilitating redox chemistry, help enhancing light absorption via surface plasmon phenomena of intraband transition and aid in promoting chemical catalysis. Here we are trying to explore each of these possibilities.

3.3.1 The role of Pt in charge separation and light absorption

One of the most important factors affecting the efficiency of MOS in photocatalysts is the mobility of charge carriers, electrons (e^-) and holes (h^+), and how well they are separated to reach the surface and carry out corresponding redox reactions on the surface. Lifetime of these charge carries and their recombination rate control the ability to drive redox reactions. The modified catalyst is more active than the bare catalyst, as seen in (Figure 3.7 A). Without the use of Pt, the desired adduct was not obtained, and most of the starting material remained unchanged. So, the use of Pt is important for both, catalytic activity and reaction selectivity and can contribute in (i) charge separation, (ii) light absorption, and (iii) chemical catalysis. The use of noble metal (Pt), as mentioned in Chapter 2, could enhance Bi_2WO_6 optical properties by promoting the absorption of visible light, as the catalyst looks grey after platinization, which in turn would affect photocatalyst activity. However, there is no obvious significant change in bandgap energy between bare and platinized Bi_2WO_6 with 0.15 wt. Pt (2.97 eV vs 3.02 eV) indicating broad band light absorption is confined to the surface. The UV-Vis diffuse reflectance spectroscopy (UV-Vis DRS) spectrum is shown in section 2.5.4 (Figure 2.21) of this thesis. The noticeable activity could be attributed to the successful separation of holes and electrons in semiconductors and lowering the recombination. PL results showed that modified Bi_2WO_6 with Pt exhibited a lower photoluminescent intensity as an indicator of a less charge recombination, meaning these charges are trapped and prevented from recombining (Figure 3.9).

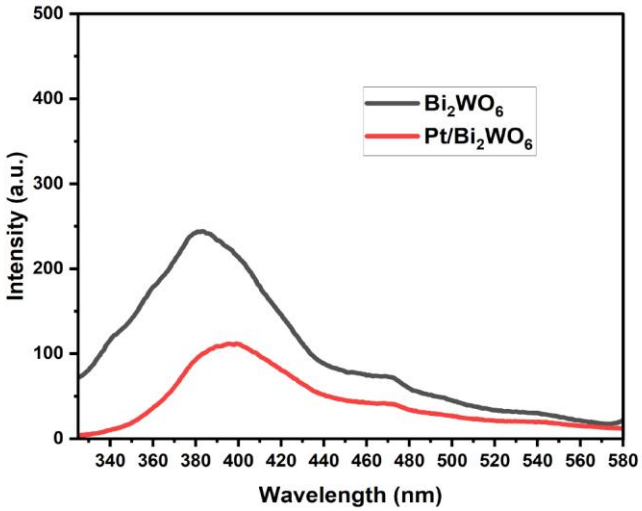

Figure 3.9: Steady state photoluminescent spectra of Bi_2WO_6 and platinised Bi_2WO_6.

The higher the intensity of the emission, the higher the recombination. Therefore, from this experiment, the presence of Pt may be helping catalytic activity (conversion of PAAH) by trapping the photogenerated electrons and acting as electron sinks, therefore making photogenerated holes in semiconductors available for the oxidation of phenylacetic acid. However, the absolute intensity in this experiment is not very reliable as it depends on the exact amount of the sample being illuminated. There was a variation in particles settling rate between bare and modified catalyst suspension during measurement. This can affect the intensity of light reaching NPs. In addition, the presence of Pt on the surface might block absorption of light or in other words the amount of light that reaches the catalyst is less which result in less emission intensity. So, while PL results suggest that Pt may be helping to reduce recombination, they are not conclusive. Thus, it was decided to run time-resolved photoluminescent (TRPL) as it can give direct comparison between life time of excited species of the two catalysts.

3.3.2 Charge carrier's life time

In this experiment, TRPL spectra of unmodified and platinised Bi_2WO_6 were compared. There is no significant difference in relaxation curve and charge carrier's lifetime between Bi_2WO_6 and Pt/ Bi_2WO_6, as seen by TRPL measurement in (Figure 3.10) and (Table 3.1**)**, respectively. The Pt-modified catalyst was expected to show longer relaxation if charge recombination is suppressed. This observation suggests that the presence of Pt may not reduce the rate of charge recombination, but it could also have other catalytic roles, such as the reduction of protons making Pt/Bi_2WO_6 more active than Bi_2WO_6.

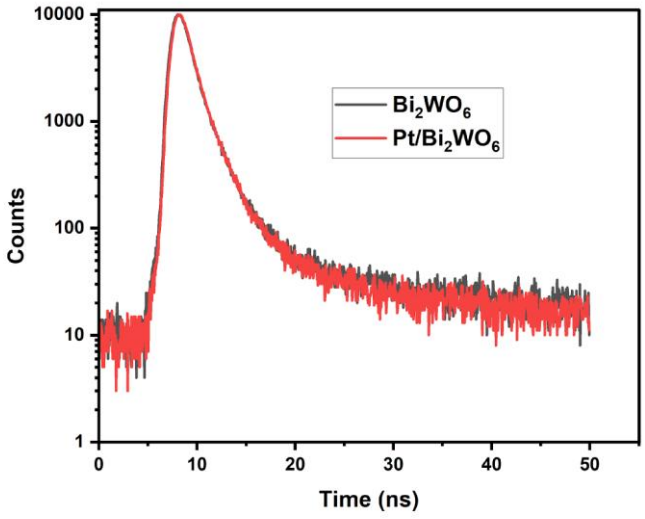

Figure 3.10: Time-resolved photoluminescent spectra of Bi_2WO_6 and platinised Bi_2WO_6 in solution.

Table 3.1: Comparison of lifetime in nanosecond between Bi_2WO_6 and 0.15Pt/Bi_2WO_6. Data collected with 317 nm laser pulse as excitation wavelength and double exponential fitting.

Sample	Bi_2WO_6	0.15Pt/Bi_2WO_6
τ ns (contribution %)	1.19 (94 %)	1.16 (94.05 %)
τ ns (contribution %)	10.12 (6 %)	8.56 (5.95 %)

However, if proton reduction was the rate determining step (RDS), it would probably show a kinetic isotope effect (KIE), but that was not observed as seen in section 3.5.2. A study carried out by Tse et al. revealed that precious metals such as Pt and Pd did not show KIE, while non-precious metals such as Ni showed primary KIE.[17] It is not clear what could make a platinized catalyst more reactive and selective. One possible explanation is that oxygen vacancies could act as electron trapping states, and the presence of Pt could enhance the stability of these vacancies.[18] It may be a synergistic effect of Pt, acting as a co-catalyst and an oxygen vacancy promoter.

The conclusion from this experiment is that charge separation by the presence of Pt does not appear to dominate the reactivity. This prompted estimation of the surface coverage of Pt (0.15%) on the catalyst surface, which might explain why charge carrier lifetime does not significantly increase for the platinised catalysts. It might also suggest that the non-emissive state could be responsible for the activity.

3.3.3 Pt nanoparticles size, coverage, and electron trapping

Aggregates of Bi_2WO_6 particles vary in size between 1 µm and 5 µm, as seen from SEM. If light is absorbed far away from the particle surface (in the bulk), it will be difficult for electrons and holes to migrate to the surface due to the large diffusion length required. Charge carrier diffusion length depends on how fast they are moving and their lifetime. The lifetime of charge carriers is very short, as seen from time-resolved measurements. The distance the carriers have to travel to reach the surface will depend on the thickness of the Bi_2WO_6 flower-like flakes, where Pt is presumably deposited. If the flake is too thick, photogenerated electrons and holes will not be able to reach the surface. If the distance between Pt NPs on the surface is large, the probability for these carriers to be trapped by Pt is low especially with their very short lifetime. Absorbing light near the surface, where it is close to Pt, can cause excitons to be generated near Pt, where they can be captured and separated.

To estimate the distance between Pt NPs (Equation 3.1) can be used, where *N* is the estimated number of Pt NPs in 1 g of catalyst. This number can be calculated as the total

volume of Pt NPs *V* in 1 g of catalyst ($\frac{0.0015\ \mathrm{g}}{d}$, where *d* is bulk Pt density, *d* = 21.5 g cm^{-3} so V = 7×10^{-5} cm^3) divided by volume of each individual Pt NP$v_{Pt} = \frac{4}{3}\pi r^3$ where *r* is the estimated NP radius in cm (Equation 3.2).

Equation 3.1

$$Distance\ between\ \ Pt\ NPs\ = \sqrt{\frac{Surface\ area\ of\ \ catalyst\ per\ g\ (SA)}{Number\ of\ particles\ per\ g\ (N)}}$$

Equation 3.2

$$\text{Estimated number of Pt NPs } (N)\ = \frac{V}{v_{Pt}} = \frac{7\times10^{-5}\ \mathrm{cm}^3}{\frac{4}{3}\pi r^3}$$

The area covered by Pt particles on the catalyst surface can be obtained by multiplying the number of Pt NPs by the cross-sectional area of Pt NP assuming that particles have spherical shape (Equation 3.3). Where r is NPs radius.

Equation 3.3

$$Area\ covered\ by\ Pt\ NPs = N \times \pi r^2$$

The obtained value form above equation is then used to calculate the surface coverage of catalyst (Equation 3.4) by Pt using ratio between value obtained from above equation and total surface area of Bi_2WO_6. The estimated distance between Pt NPs and their surface coverage % are shown in (Table 3.2).

Equation 3.4

$$Surface\ coverage\ of\ Pt = \frac{Area\ covered\ by\ Pt\ NPs}{Surface\ area\ of\ Bi_2WO_6} \times 100\%$$

Table 3.2: Estimated Pt NPs dimeter size and the corresponding distance between them

Estimated Pt NP diameter (nm)	Estimated Distance between Pt NPs (nm)	Surface coverage of co-catalyst (%)
2	34.617	0.26
3	63.600	0.175
5	136.845	0.1
10	387	0.05

Table 3.2 suggests that a small change in Pt NPs diameter makes a significant change in the distance between particles, which in turn could affect the separation of charge carriers to reach Pt NPs and being trapped. So, as the size of Pt NPs increases, there is a bigger chance that electrons and holes will recombine. So, the role of Pt might not prevent recombination as discussed above in section 3.3.2 but likely its role as co-catalyst. The following section discusses a study of reaction intermediates to understand and uncover the reaction pathways.

3.4 Investigation of intermediate species

The identification of reaction intermediates is a crucial step in understanding the reaction pathway. The following experiments are to check if this reaction proceeds via radical chemistry.

3.4.1 The formation of intermediate radicals

As seen from previous studies, adduct formation in the Giese reaction proceeds via free radical intermediates. An alternative mechanism for the reaction would be catalytic decarboxylation of the carboxylate anion to give a carbanion which would undergo nucleophilic addition to the Michael acceptor. In order to test whether the reaction proceeds via an ionic or a radical process, a spin trapping experiment was performed. The reaction mixture between phenylacetic acid and methacrolein in the presence of platinized bismuth tungstate was spiked with one equivalent of spin trap molecules such as α-phenyl N-t-butyl nitrone (PBN) and 5,5-dimethyl-pyrroline N-oxide (DMPO) to produce spin adducts (Scheme 3.2).

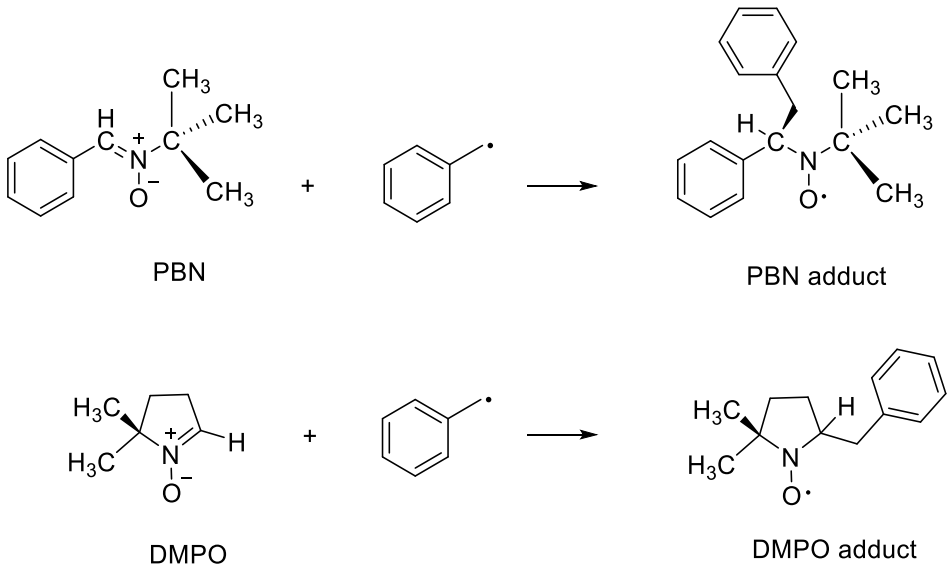

Scheme 3.2: structure of spin taps (PBN and DMPO) before and after addition of benzyl radical.

The intermediate benzyl radicals, are likely to be too short-lived to be directly detectable by EPR but the spin adducts are persistent radicals (nitroxides) so they can accumulate to detectable concentrations. The control experiment, where the reaction mixture was stirred with a trap in the dark, was also performed, and no EPR signal was observed. The main three experiments were as follows:

1. Solvent + photocatalyst + spin trap
2. Solvent + photocatalyst + acid + spin trap
3. Solvent + photocatalyst + acid + alkene + spin trap

The photo-irradiated reaction mixture was subsequently subjected to EPR analysis, and the corresponding spectra are shown in Figure 3.11.

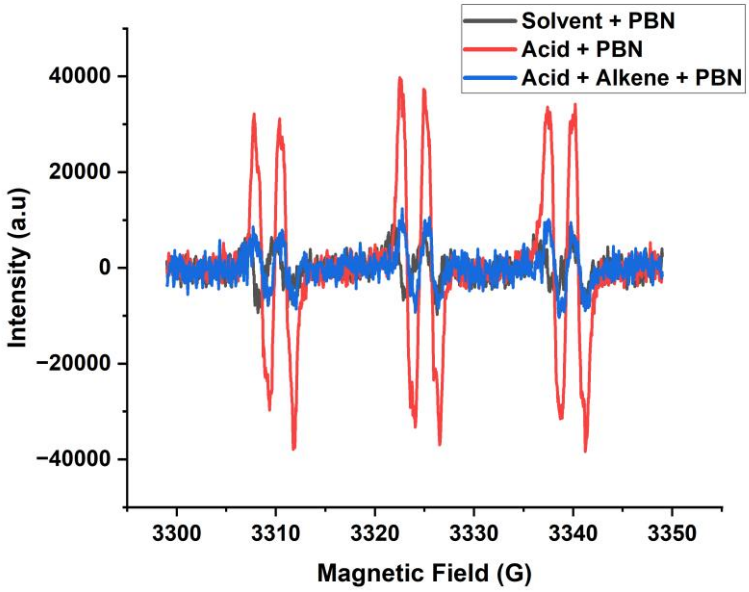

Figure 3.11: X-band EPR spectra of spin adducts obtained using PBN spin trap. 10 min irradiation of Pt/Bi_2WO_6 in acetonitrile and PBN (black), 10 min irradiation of Pt/Bi_2WO_6 in acetonitrile in presence of phenylacetic acid and PBN (red), 10 min irradiation of Pt/B.

After the samples were irradiated for 10 minutes with an LED torch (405–410 nm), the EPR signal was recorded. The spectrum shows a triplet of doublets, consistent with the structure of a PBN radical adduct. The triplet splitting is due to hyperfine interaction with ^{14}N nucleus of the nitroxide adduct whereas the doublet is due to the interaction with the hydrogen of the α-CH group. So, the observation of the EPR signal of PBN adducts confirms the formation of intermediate radical in this reaction. The intensity of the signal was in the order of 2 > 3 > 1. So, the low signal intensity seen in the reaction with acid

and alkene (3) could be due to the fact that the intermediate benzyl radical is being trapped by alkene. The reason for the signal that was generated in (1) was not clear, as there was no acid in the system. If the system is not sufficiently dry, there may be some photogenerated hydroxyl radicals, which may give rise to an EPR signal. The spectra of the reaction between acid and photocatalyst can be simulated as follows: (Figure 3.12).

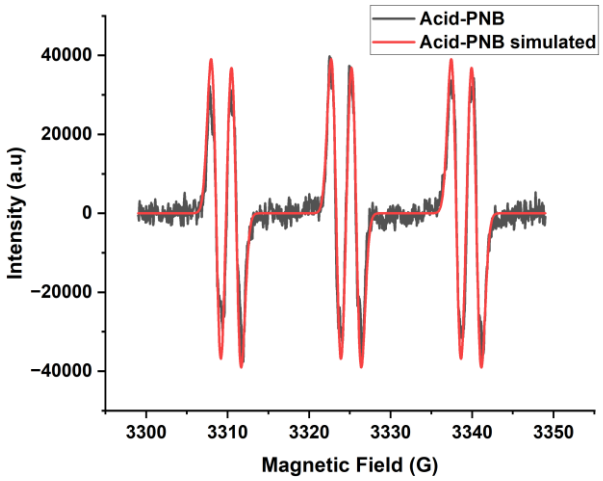

Figure 3.12: EPR spectrum of phenylacetic acid in presence of photo-irradiated Pt/Bi_2WO_6 indicating the formation of benzyl radical adduct. Hyperfine values: a_N 14.72, a_H 2.46 G.

PBN adducts of carbon and oxygen-centred radicals have similar hyperfine values. For instance, a_H = 3.3 G for trapped methyl radical and a_H = 3 G for ·OH in acetonitrile.[19,20] Therefore, it is hard to tell from the EPR spectra in Figure 3.13 whether the trapped radical is a carbon or oxygen-centred radical In nitroxides, hyperfines (a_H) strongly depend on the dihedral angle between the orbital with the unpaired electron and the C-H bond. All PBN adducts have similar hyperfines because they are flexible, and the dihedral angle is averaged out when they freely rotate around the C-N bond. Therefore, cyclic spin traps like DMPO are better suited to distinguish between different types of trapped radicals, as they show no free rotation around the C-N bond; hence, different adducts have different hyperfines. For example, this can be used to distinguish between carbon and oxygen centred radicals, (a_H = 20.4 G for ·C_6H_5 and a_H = 13.6 G for ·OH) in acetonitrile.[21] Thus, the same trapping experiment (solvent + photocatalyst + acid + spin trap) was performed with DMPO, and the spectra can be simulated as follows: (Figure 3.13).

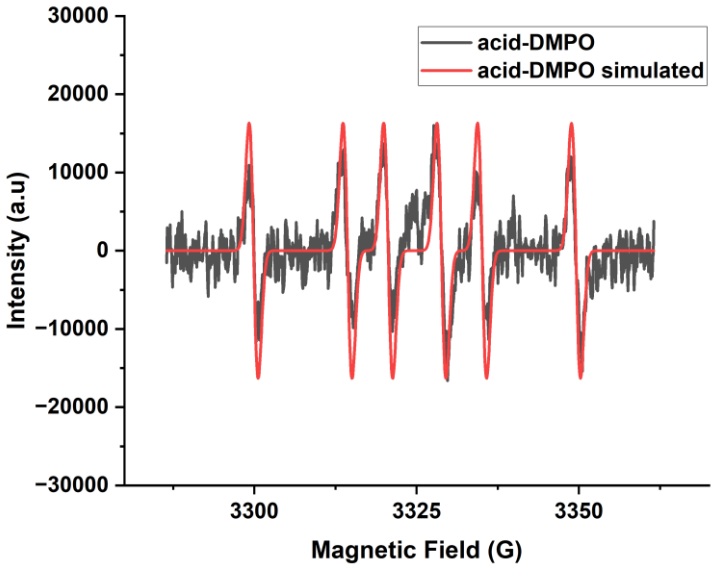

Figure 3.13: EPR spectrum of phenylacetic acid in presence of photo-irradiated Pt/Bi_2WO_6 indicating the formation of benzyl radical. Hyperfines: a_N 14.45, a_H 20.70 G. DMPO has characteristic spectra for C and O-centred radicals.

The above spectrum also shows similar splitting pattern (triplets of doublets) however the distance between splitting lines is different which is a fingerprint of DMPO adduct that is formed by benzyl radical (carbon-centred radical). Also, the hydrogen hyperfine value is typical of a carbon-centred radical. Based on this experiment, the trapped radical is a carbon-centred radical. This carbon-centre radical could be a benzyl radical or another similar carbon-centre radical intermediate. These results confirm that this reaction proceeds via radical intermediate and not ionic intermediate where no EPR signal will arise.

3.4.2 Formation of homocoupling product (bibenzyl)

The other evidence that this reaction proceeds via a radical mechanism is the formation of bibenzyl (BB), as seen in the ^{1}H NMR spectrum of the reaction of PAAH only with Pt/Bi_2WO_6 (Figure 3.14). This means that homocoupling is possible when benzyl radicals are formed and radical acceptor molecules such as methacrolein are not present. The acid conversion was around 57 % and that yielded 23 % BB. As two benzyl radicals are needed to produce one BB molecule, this corresponds to the selectivity of 80 %. Other side product is benzaldehyde (5 %). The total area of aromatic protons is 106 % which matches the expected yield within the 10 % error of NMR measurement and suggests complete recovery of PAAH-derived products.

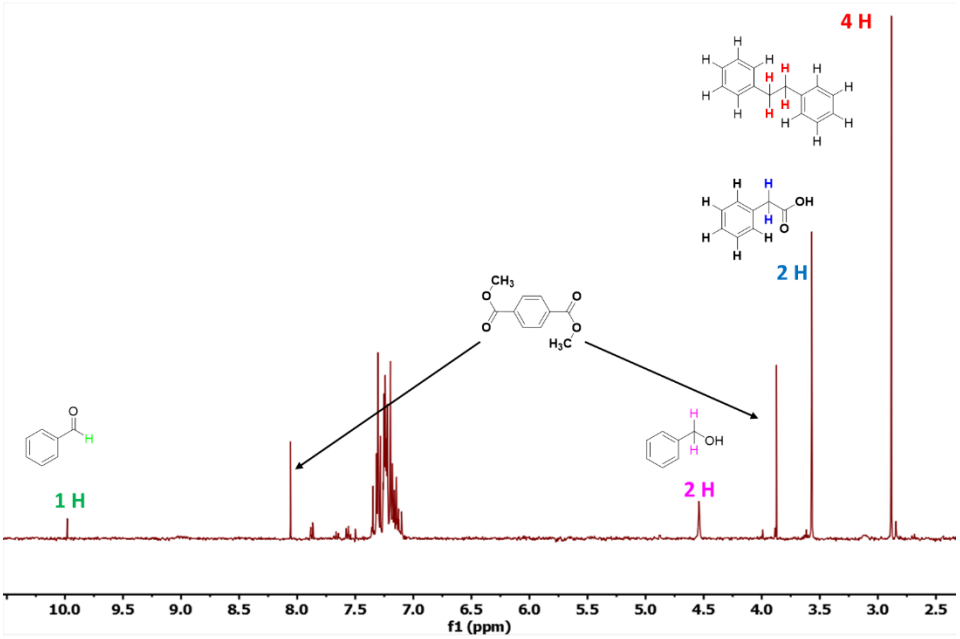

Figure 3.14: ^{1}H NMR spectrum of reaction outcome of PAAH with photo-irradiated Pt/Bi_2WO_6 in absence of methacrolein showing the main product is bibenzyl.

3.5 Isotope labelling experiment

The process of replacing one or more atoms in a molecule with an isotope of the same element is known as isotope labelling. Isotopically labelled substances thus produced can function as distinct tracers or markers. Researchers can follow the routes of chemical reactions by using isotope labelling. In addition, labelled substrates can be used to determine the kinetic isotope effect (see Section 3.5.2).

3.5.1 Deuteration of acid and catalyst and the addition of D_2O into the reaction

A reaction between generated benzyl radical and electron deficient alkene would result in formation of an intermediate radical. The catalytic cycle is closed by formal addition of a hydrogen atom. This could occur in a single step via HAT or reaction with a Pt-H moiety. Alternatively, the radical adduct could undergo stepwise addition of an electron (reduction) and proton. Reduction presumably occurs at Pt creating an intermediate enolate. This intermediate enolate could be protonated by phenylacetic acid, surface OH groups or water. Labelling experiments were undertaken to try and identify the source of protons in the product (Scheme 3.3).

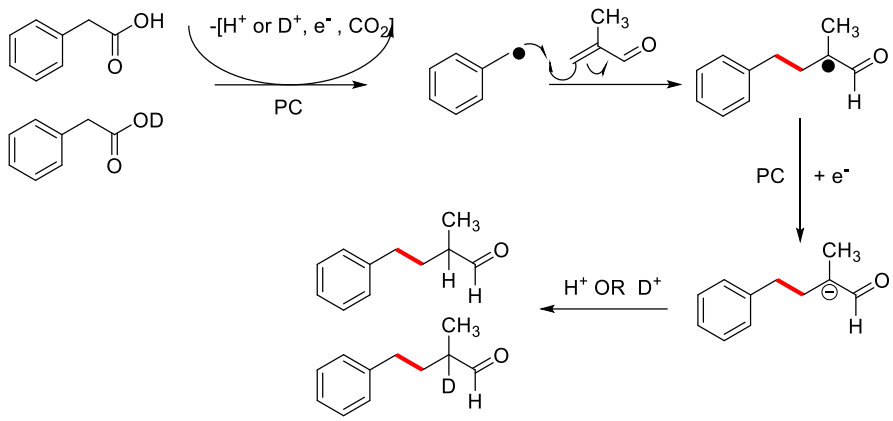

Scheme 3.3: Proposed mechanism of formation of protonated and deuterated Giese adduct.

The first step was to deuterate the starting material (phenylacetic acid) by refluxing in deuterium oxide (D_2O). It was found that the majority of the acid has been deuterated as seen by the significant reduction of the OH proton peak, and a representative ^1H NMR spectrum is shown in (Figure 3.15). It was challenging to get full deuteration of acid as the O-H proton is labile and rapidly exchanges with any labile protons present in the system or from the surrounding environment, such as the presence of humidity.

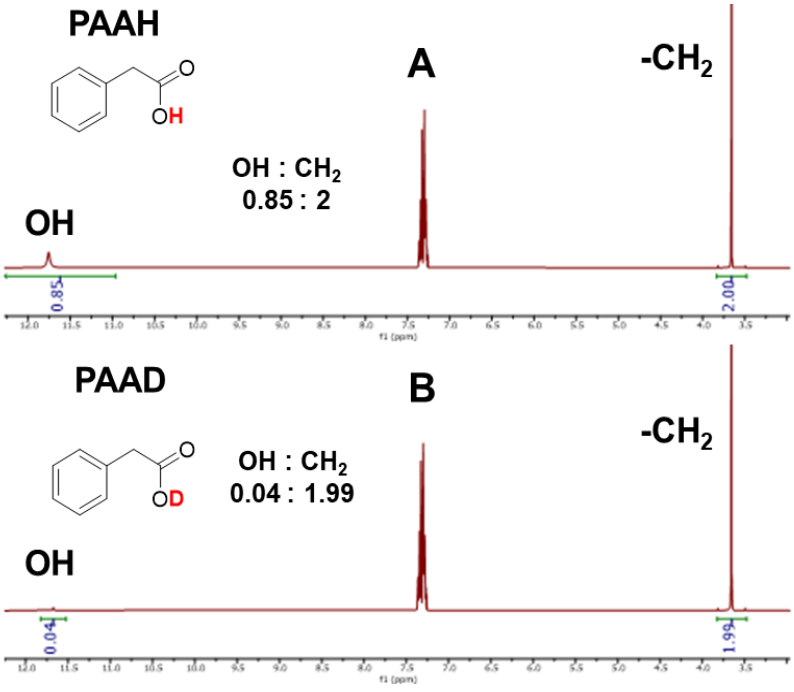

Figure 3.15: ^1H NMR of normal protonated phenylacetic acid (A) and as deuterated phenylacetic acid (B).

A reaction between the deuterated phenylacetic acid (PAAD) and methacrolein under standard conditions (dry solvent, oven dry catalyst) resulted in almost same ^{1}H NMR of product with small variation in yield (~7% more for protonated product) (Figure 3.16).

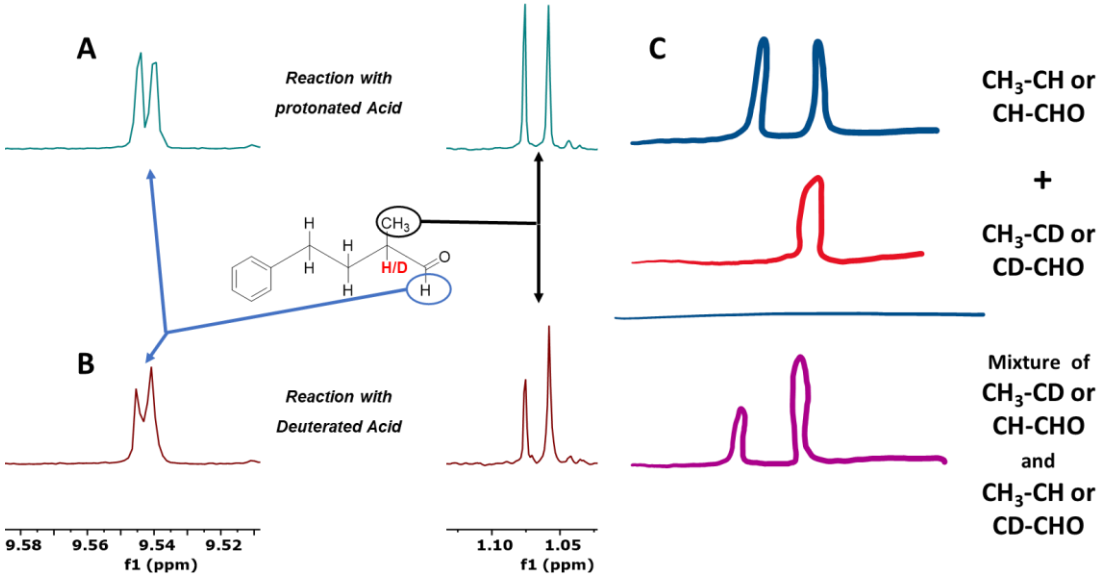

Figure 3.16: ^{1}H NMR stacked spectra of Giese adduct by reacting normal (A) and deuterated (B) phenylacetic acid with methacrolein in presence of photoirradiated 0.15Pt/Bi_2WO_6. (C) Explanation of D incorporation effect in splitting pattern of methyl and aldehyde doublet intensity of Giese adduct.

To distinguish between protonated and deuterated product, the NMR peaks must be resolved, however, the NMR peaks of the exchanged proton overlap. However, deuteration changes the splitting of the nearby protons and it was found that the most accurate way of determining the extent of D incorporation is to analyse the methyl peak at 1 ppm. Unexchanged product gives a doublet at this chemical shift, whereas deuterated product gives a broad singlet which overlaps with one component of the doublet. By separate integration of the two components of the doublet, the extent of D incorporation can be calculated. The difference in integral values of deuterium to proton ((H+D) -H) in the adduct was about 0.7 based on two components of the methyl doublet of the adduct, $H_{integral}$ and $(H+D)_{integral}$ which equals to 1 and 1.70, respectively. This gives 41% of D incorporated in the product, (0.7/ 1.7 = 0.41 * 100 = 41%).

These results show that only partial D incorporation into the C-H position of the product. That is probably due to the presence of other proton sources such as adventitious water in the system, which is hard to avoid completely. Thus, the formation of CH or CD product is affected by kinetic isotope effect where the CH product will form faster by a factor of

about 8. Water will exchange protons with acid before or during the catalytic reaction. The other possible source of protons is the catalyst, Bi_2WO_6, as these metal oxides have oxygen and hydroxyl groups on their surface, which attract water, and this water layer acts as a proton source. In order to check whether D is incorporated at any other positions of the product molecules, a ^2H NMR spectrum was recorded.

The ^2H NMR spectrum of PAAD reaction mixture showed the methyl peak at 2.3 ppm, as it is the only peak present in the spectrum (Figure 3.17). Since the chemical shifts of H and D in ^1H and ^2H NMR, are similar, this peak could be attributed to the proton attached to β-carbon (-CH-) in ^1H NMR. This result confirms that the only position of D incorporation in the product is β-CH and the starting material (phenylacetic acid) is the source of H/D atoms at this position in the product.

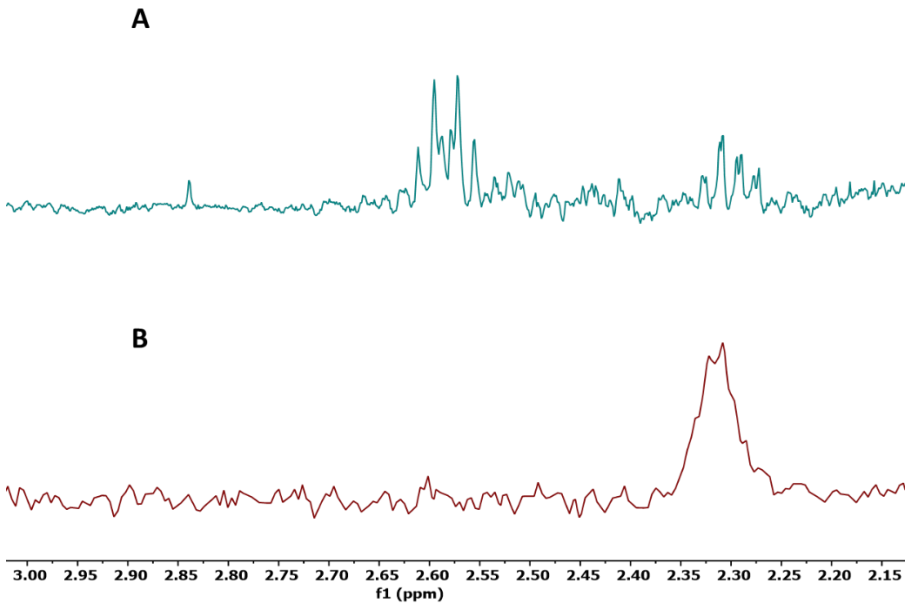

Figure 3.17: Stacked NMR spectra of standard reaction with deuterated acid (a) ^1H NMR, (b) ^2H NMR.

To investigate whether incomplete D incorporation is due to the presence of OH group or water on the catalyst or due to other factors, the catalyst was deuterated the same way PAAH was, refluxing with D_2O overnight and dried under vacuum. By doing this, presumably OH can be replaced with OD. Then, a reaction was performed with both deuterated catalyst and deuterated acid, and the methyl doublet is still visible, but the difference in integral values of deuterium to proton ((H+D) -H) in the adduct was about 1.1 based on two components of the methyl doublet of the adduct, $H_{integral}$ and $(H+D)_{integral}$ equals 1 and 2.1, respectively. This gives 52% of D incorporated in the product.

This increase in D incorporation suggests that water/surface OH groups of the catalyst are a source of protons for the enolate protonation. When dry protonated solvent (acetonitrile) was replaced with dry deuterated solvent, no major change was observed, confirming that the protons of the methyl group of the solvent are not involved in the reaction. So, after deuteration of both acid and catalyst, the protonation of enolate is likely subject to kinetic isotope effect (i.e., protonation could be up to 8 times faster than deuteration). Hence, a significant amount of non-deuterated product could form even if most proton sources in the reaction have been deuterated.

In order to investigate if catalyst is source of protons (presence of moisture), a representative ^{1}H NMR spectrum of the reaction carried out under normal and dry conditions, Table 3.4, are shown in Figure 3.18. It can be seen that drying the catalyst in the oven at (80 ºC) does not remove all water while drying in oven under vacuum and higher temperature (150 ºC) remove water.

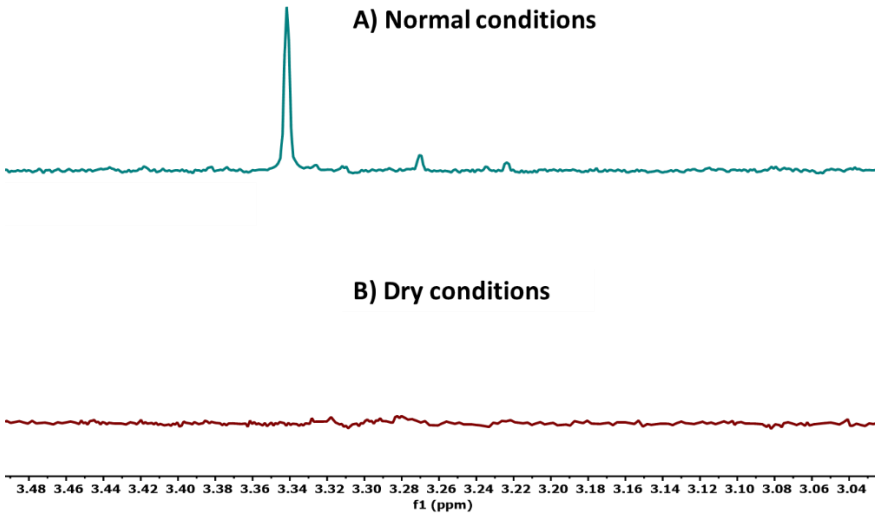

Figure 3.18: 1H NMR spectrum showing water peak at 3.34 ppm in standard reaction (A) and dry condition (B).

It can be noted from the above spectrum that under normal conditions, the water peak is present at 3.34 ppm, which is attributed to the water content of CH_3CN, which could arise from the catalyst.[22] Under dry conditions, that peak disappeared and probably this water peak comes from the catalyst.

Another observation regarding the relationship between water and catalyst was noticed during the adsorption experiment of phenylacetic acid with Bi_2WO_6 (Figure 3.19). The intensity of water peak is directly proportional to amount of catalyst used in the titration

experiment (Figure 3.20). It is clear that as the amount of catalyst increases, so does the intensity of the water peak.

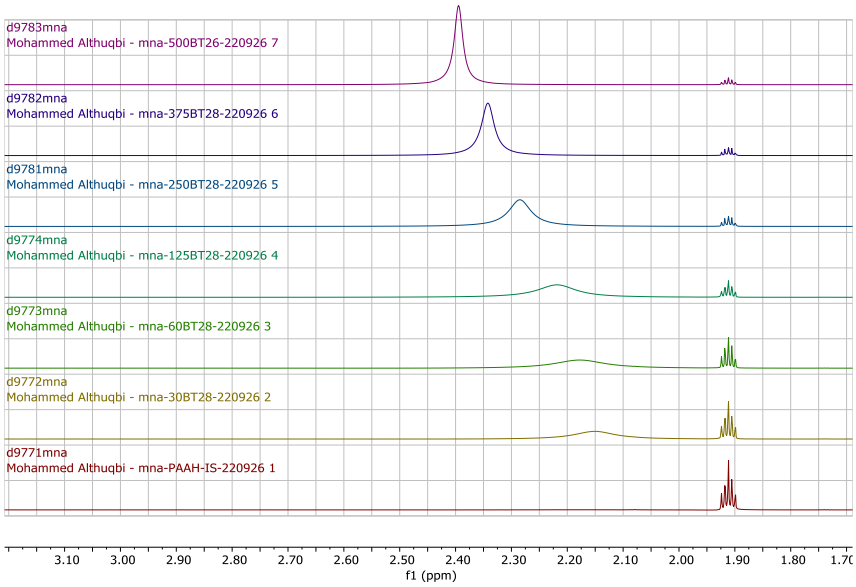

Figure 3.19: ^{1}H NMR spectra of stock PAAH solution, 18 mM (1st spectrum at bottom) and titration with different amount of Bi_2WO_6 , 30 – 500 mg (2nd – 7th spectrum). Peaks at range of 2.15 -2.40 ppm represent water.

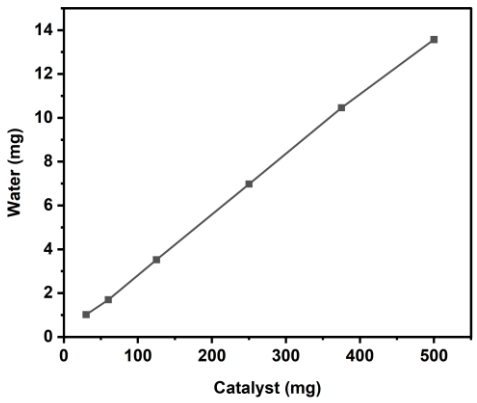

Figure 3.20: Linear relation between amount of catalyst and amount of water released in solution.

The evolution of water could be due to the excess water on the catalyst surface that could be released in the solvent.

In order to confirm that exchangeable protons are the only proton source for enolate protonation, it was then decided to spike the reaction with 100 µL of D_2O to see if this could enhance the deuteration. Almost full deuteration of β-carbon in the Giese adduct

was obtained. This affected the splitting pattern of both methyl and aldehyde peaks by changing them from doublet to broad singlet, which is confirmed by ^{1}H NMR (Figure 3.21). The difference in integral values of deuterium to proton ((H+D) -H) in the adduct was about 10 based on two components of the methyl doublet of the adduct, $H_{integral}$ and $(H+D)_{integral}$ equals 1 and 11, respectively. This gives around 90% of D incorporated in the product. This experiment suggests that exchangeable protons are the dominant source of protons for C-H group in the product. Incomplete D incorporation in reactions where all components had been rigorously deuterated is surprising. One possible explanation is that enolate formation and protonation takes place on the catalytic sites which may have a relatively slow proton exchange rate. This could explain incomplete D incorporation in the adduct.

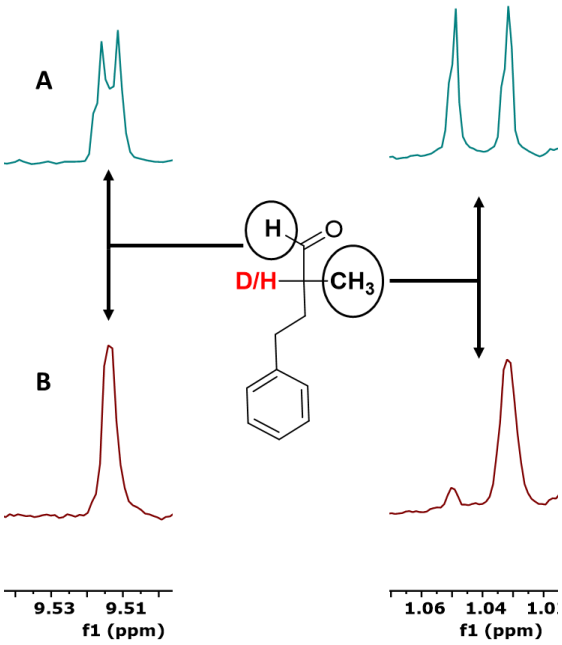

Figure 3.21: ^{1}H NMR spectra of Giese adduct showing the change of both aldehyde and methyl splitting pattern from doublet to broad singlet upon D_2O addition (b). Addition of H_2O did not affect doublet pattern of methyl (a). The change in splitting pattern after D_2O addition indicated deuteration of β-carbon in the adduct.

3.5.2 Kinetic isotope effect study (KIE)

The target bond reorganisations the formation of a Giese adduct is C-H bond. In order to determine if a formation of a C-H bond is the rate-determining step (RDS), the kinetic isotope effect (KIE) can be used. KIE is done using different isotopes to study their effect on reaction rate. The most commonly used isotope is deuterium (D). If KIE = $k_H/k_D > 2$, then the O-H/C-H bond is broken or formed in the RDS (this is called primary KIE). If KIE

< 2, the O-H/C-H bond is not broken or formed in the RDS. Table 3.3 shows the reaction outcomes after adding H_2O and D_2O to different reaction mixtures under the same conditions, using dry acetonitrile and ambient catalyst. The measurement assumes that the difference in acid conversion and product yield will be exclusively due to the KIE. Based on acid conversion, normal KIE (KH/KD = 1.06) is observed. This suggests that the breakage of the O-H bond in PAAH is not the rate-determining step. Also, the yields of the product are quite similar for H_2O and D_2O (KH/KD = 1.39), which also suggests that the formation of the C-H bond in the adduct is also not the rate-determining step. The conclusion from this study is that enolate protonation is not the RDS in this reaction. Based on this study we do not know what the RDS is but carboxylate oxidation is likely to be the slowest step (rate-determining step).

Table 3.3: Isotope effect with addition of H_2O and D_2O.

Conditions	***Yield (%)***	***Conversion (%)***	***Selectivity (%)***
Addition of H_2O	32	78	41
Addition of D_2O	23	73	31

Conditions: Phenylacetic acid (200 mM), methacrolein (600 mM), 24 h, 405-410 nm, sealed under N_2.

3.5.3 Role of water in catalytic activity: ambient vs dry catalyst

Based on the results of the deuterium labelling and KIE experiments, it can be seen that water has an effect on reactivity as the original (reaction at standard condition) PAAH conversion (94%) dropped to (78%) after adding water (Table 3.3). The possible explanation for that is that water could block surface active sites, preventing good adsorption for PAAH. In an attempt to investigate this effect, reactions with dry conditions were performed, and the results are shown in (Table 3.4).

Table 3.4: Effect of water in catalytic efficiency and reaction selectivity.

Conditions	***Yield (%)***	***Conversion (%)***	***Selectivity (%)***
ambient conditions	63	94	67
dry conditions	30	61	49

Ambient conditions: 60 mg oven dried catalyst at 80 ºC overnight, phenylacetic acid (0.2 mmol), alkene (0.6 mmol). Dry conditions: 60 mg Vacuum dried catalyst at 150 ºC for 3 hrs, vacuumed dried phenylacetic acid (0.2 mmol), alkene (0.6 mmol).

When the reaction components were dried (the catalyst was subjected to further drying), both the catalytic reactivity and selectivity dropped. This result confirms that the presence of water is essential for catalytic activity. The reaction was spiked with different amounts of water (5–20 µL) in order to restore the activity as in ambient condition; yet, that did not bring full conversion as before (94 %), and selectivity also was not completely restored, (Table 3.5). however, addition of water to the dry catalyst did enhance the activity.

Table 3.5: Addition of water to dry catalytic system

Water (uL)	Yield (%)	Conversion (%)	Selectivity (%)
0	30	61	49
5	36	89	40
10	41	83	50
20	40	79	51

Conditions: 60 mg of vacuum-dried catalyst at 150 ºC for 3 hrs, vacuum-dried phenylacetic acid (0.2 mmol), alkene (0.6 mmol), N_2, 405-410 nm LED torch, 24 h.

Optimising the water content in the reaction is not straightforward because water could have a dual effect on catalytic activity by either inhibiting or promoting activity. Too little water gives poor conversion and yield as seen with dry catalyst and addition of water to normal catalyst (ambient condition) also reduced conversion and yield. The possible inhibiting effect of water is that excess water (a small molecule compared to acid) could block the surface-active site and compete with the adsorption of acid. Due to time constraint, further optimisation of water amount was limited. On the other hand, water on the MO surface could promote the formation of hydroxyl groups when adsorbed onto the surface. Typically, hydroxyl groups are formed when water molecules dissociate over the surface and form a linkage with surface oxide, as discussed previously in (section 1.6.3, Figure 1.22). When washing/refluxing catalyst with D_2O, there is the possibility of forming O-D on surface instead of O-H. A simplified possible mechanism of deuteration of surface hydroxyl group by D_2O is illustrated in (Figure 3.22).

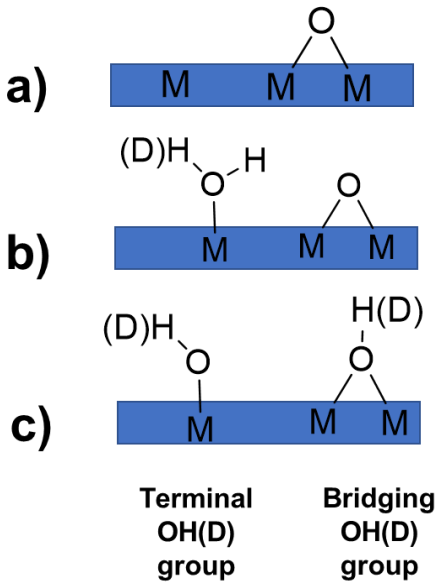

Figure 3.22: schematic diagram explaining the formation of OH(D) group on metal oxide surface aiding by adsorbed H_2O /D_2O. a) cation sites (M) and anion sites (O) on surface. b) water hydroxyl adsorbed on cation sites while water protons adsorbed on anion sites. c) formation of terminal hydroxyl and bridging hydroxyl.[23]

The presence of D_2O instead of H_2O would form O-D on the surface. However, this exchange process may not be very fast as observed in the deuterium labelling experiment. However, surface O-H can still serve as Bronsted acid active sites where they can donate their labile protons to enolate or other anion species, as seen in a photocatalytic reaction with a deuterated catalyst.

These newly formed hydroxyl groups are very important for catalytic activity because they could facilitate the adsorption of PAAH via hydrogen bonding. This binding is a key for electron transfer from substrate to surface.

In conclusion, water plays two roles in this reaction. Small amount of water speeds up the reaction by making it easier for hydroxyls to form. It can also help to close the catalytic cycle by protonation. Large amount of water, however, inhibits the reaction, potentially by blocking active sites on the surface.

As an important step in catalytic reaction is substrate adsorption, the following section will study the adsorption of staring materials (phenylacetic and methacrolein) on the Bi_2WO_6 surface.

3.6 Organic molecules binding onto catalyst surface

The process of adsorption of carboxylic acids on metal oxides occurs through the contact between the carboxyl group of the acid and the metal sites on the surface of the oxide.

Typically, this contact causes the carboxylic acid to separate into its components, with the carboxylate anion attaching to the metal sites and the proton joining with surface oxygen atoms. Take oleic acid as an example, which is a common carboxylic acid. It undergoes dissociation on the surface of a metal oxide, resulting in the creation of a connection between the carboxylate and the metal sites. On the other hand, alkenes can also bind to metal oxides. In this process, the alkene molecule transfers its π-electrons to the unoccupied d-orbitals of the metal atoms present on the surface of the oxide.[24]

3.6.1 Phenylacetic acid and methacrolein binding with Bi_2WO_6

Adsorption and desorption of substrates are key to a successful heterogenous catalytic reaction. The purpose of this section is to check if substrates bind to the nanoparticle surface in the presence of the solvent. In order to achieve a good catalytic reaction, the binding of molecules should be strong enough to enable electron transfer to/from the catalyst. Also, this binding should be reversible so that products can leave the surface easily.

The concentration of substrates in solution can be measured by room-temperature NMR before and after addition to a solid catalyst. Thus, the binding of phenylacetic acid and alkene on the Bi_2WO_6 surface was studied using quantitative ^1H NMR. We attempted to use infrared (IR) spectroscopy, thermogravimetric analysis (TGA) and TGA-MS to quantify the amount of acid being adsorbed onto a solid surface, but saw no evidence of strong adsorption. The amount of adsorbed acid was around 0.1 mg for 60 mg of catalyst, ~ 0.1 Wt. % (as measured by solution ^1H NMR, see below) which is a very small amount to detect by TGA.

It has been found that phenylacetic acid adsorbs more strongly on Bi_2WO_6 compared to methacrolein, and this conclusion is based on measuring the amount of substrate left unbound and remaining in the solution after exposure to a solid catalyst for 5 minutes (Figure 3.23). As the amount of catalyst increased, the amount of alkene did not change significantly, while the amount of acid dropped dramatically. A possible binding mode of carboxylic acid onto the Bi_2WO_6 surface is predicted to be similar to that of other metal oxides, such as TiO_2. These binding modes could be either physisorption, via H-bonding, or chemisorption as discussed in section 1.6.4, Figure 1.25. However, TGA and IR are indicative of limited OH groups in contrast to TiO_2 which is known to strongly bind carboxylate groups.

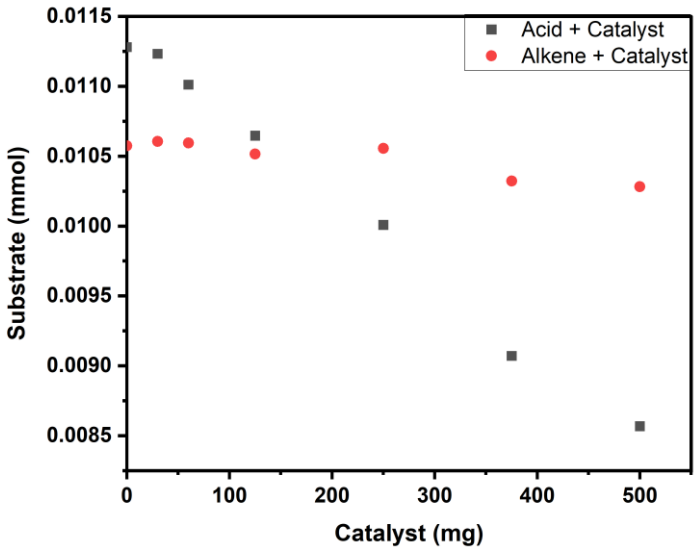

Figure 3.23: A graph representing the relationship between the amount of phenylacetic acid (18 mM) and methacrolein (17.6 mM) analysed by ^{1}H NMR in CD_3CN (10 mL) remains in solution after mixed with different amounts of catalyst (30, 60, 125, 250, 375, 500 mg).

Since the acid is binding more strongly to the surface than the alkene in acetonitrile solvent, it would be useful to measure the binding constant and the number of binding sites. Quantifying the binding constant helps to predict the reactivity of different carboxylic acids. In addition, knowing the number of binding sites, different catalysts (bare vs platinised) can be compared to understand the effect of adding cocatalyst. Also, catalytic parameters such as turn over number (TON) can be calculated if the number of binding sites is known.

To achieve this goal, a separate adsorption experiment of phenylacetic acid only with Bi_2WO_6 was performed. In this experiment, a fixed amount of catalyst is used (125 mg) and spiked with different acid amounts. By using quantitative ^{1}H NMR with help of internal standard, the amount of acid detected in solution can be measured. The corresponding ^{1}H NMR titration spectra and binding curve with fitting are shown in (Figures 3.24 and 3.25), respectively.

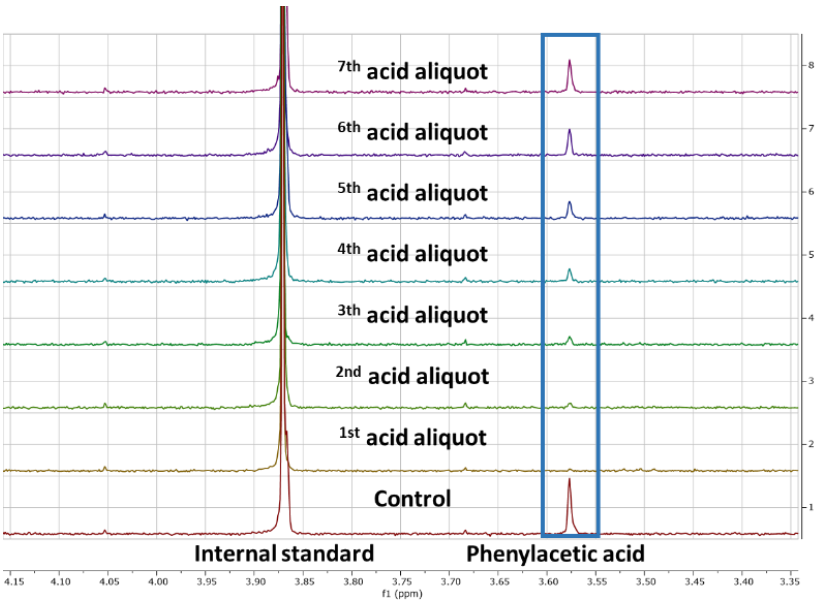

Figure 3.24: Acid titration with Bi_2WO_6 (125 mg) and phenylacetic acid (0.5 mM). Control = no catalyst. IS = dimethyl terephthalate (DMT), δ 3.88 ppm (6H).

The first acid aliquot addition to the catalyst resulted in the almost full disappearance of acid according to the ^{1}H NMR acid profile. After the second acid aliquot addition, methylene protons (-CH_2) started to appear. With further acid addition to the catalyst, the acid peak grew, which was an indication of surface saturation.

The molar concentration of acid remaining in solution can be correlated with moles of adsorbed acid and fit to a model describing equilibrium between solution and adsorption as will be explained in the following section.

3.6.2 Calculating number of binding sites and binding constant using Langmuir adsorption model

Reversible adsorption of molecules on surfaces can be described by simple equilibrium (Equation 3.5). The model assumes that substrates bind to solid surfaces in a distinct way with one type of binding sites, and this binding is reversible.[25] This model is used to estimate the binding constant, K (Equation 3.6) and the number of binding sites. These values can be used to compare the binding strength of different substrates. The estimated binding strength can be used to correlate substrate activity with their structures.

Equation 3.5 $$S + L \leftrightarrow SL$$

Equation 3.6 $$K = \frac{[SL]}{[S][L]}$$

Here, S represents the free sites on the surface of nanoparticle, L is ligand or molecule (acid) and SL is site-ligand complex or the occupied sites. θ parameter is introduced here to simplify the formula, and it is the ratio of occupied binding sites [SL] to the total number of binding sites (SL/S+SL), while 1-θ is the proportion of the free binding sites (Equation 3.7).

Equation 3.7 $$K = \frac{\theta}{(1-\theta)[A]}$$

Where $[A_0]$ and [A] is acid molar concentration before and after adsorption, respectively. By combining this equation with the total amount of acid (mass balance), a new formula can be derived to calculate the binding constant (K) and the number of binding sites (Z), (Equation 3.8).

Equation 3.8 $$[A] = \frac{ZK[A0]-Z-K+\sqrt{(ZK[A0]-Z-K)^2+4Z^2K[A0]}}{2ZK}$$

Using the molar concentration of acid from titration experiments, binding curve with fitting can be obtained (Figure 3.25), and K and Z can be solved. Their values were found to be $1.20 * 10^{4}$ and $1.60 * 10^{-6}$ mol, respectively, for phenylacetic acid.

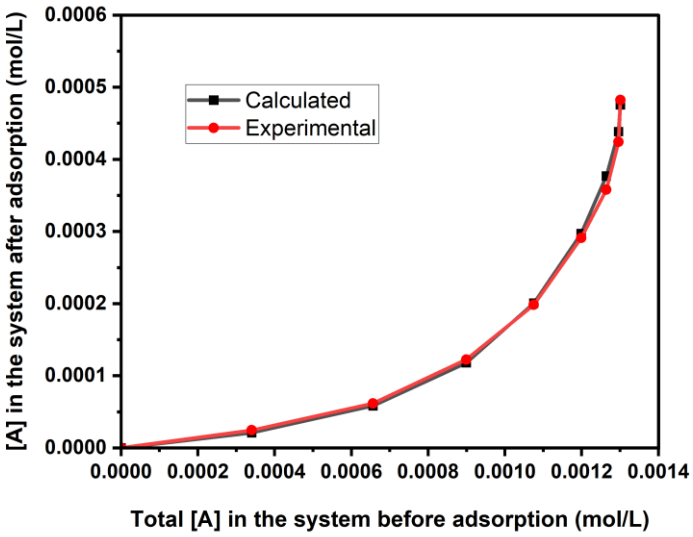

Figure 3.25: Binding curve with fitting of phenylacetic acid with Bi_2WO_6 nanoparticles. Bi_2WO_6 (125 mg), phenylacetic acid (0.5 mM). CD_3CN (10 mL) as solvent.

In order to compare the binding strengths of different substrates, different phenylacetic acids with different substitutions were used, such as 4-methoxyphenylacetic acid and 4-chlorophenylacetic acid. A comparison of these acids in terms of number of binding sites and binding strength is presented in Figures 3.26 and 3.27, respectively.

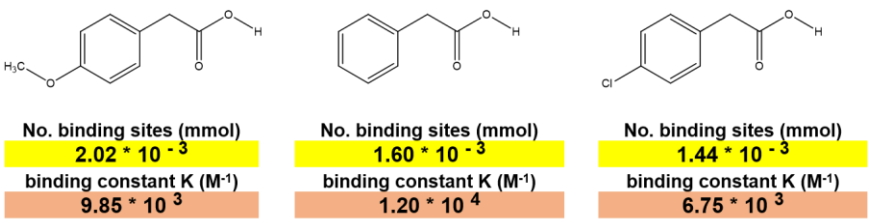

Figure 3.26: Schematic diagram showing number of binding sites and binding constant (K) of phenylacetic acid (PAAH), 4-meoxyphenylacetic acid and 4-chlorophenylacetic acid.

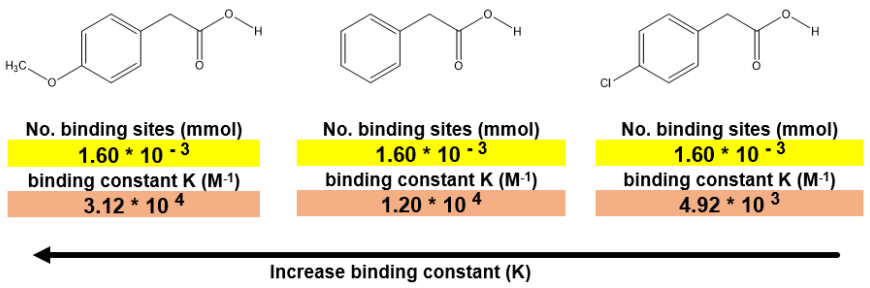

Figure 3.27: Schematic diagram showing acids binding strength order by freezing number of binding sites.

The estimated numbers of binding sites for all three acids are close similar. The number of binding sites should be independent of the type of acid, but there are some deviations. These deviations could be due to artificial error in modelling, as the model is based on one type of binding site but the real system may have a range of different binding sites. The number of binding sites can be fixed during fitting to allow a comparison between the binding strengths of three acids (Figure 3.27). These numbers suggest that methoxyphenylacetic acid (MeO-PAAH) is binding stronger than other acids, and the order is MeO-PAAH > PAAH > Chloro-PAAH. In terms of catalytic activity, PAAH and chloro-PAAH gave similar conversions of ~ 100%. However, MeO-PAAH conversion was reduced to ~ 79%. It is expected that strong binding might be beneficial for the conversion; however, that is not the result here. It was not clear why the presence of methoxy substituents reduced activity. In terms of yield, methoxyphenylacetic acid is lower in yield than PAAH and Chloro-PAAH by ~ 22%. Apparently, the strength of binding does not correlate with the reaction yield

In terms of low conversion of 4-methoxyphenylacetic acid, since this acid could bind stronger than other acids, some binding sites might not be available for incoming acid molecules to bind, resulting in low conversion of 4-methoxyphenylacetic acid. The same effect could also be related to low yield and selectivity, it might be speculated that overoxidation of the 4-methoxybenzylic radical is possible as this radical might bind strongly to the surface. As a result, low conversion and selectivity were observed.

3.6.3 Calculating turnover number (TON) and substrate packing density

We can compare the estimated number of binding sites to nitrogen adsorption data (surface area) in order to calculate TON. TON might be used to compare between different catalysts and predict their catalytic performance.

The first step is to convert the moles of binding sites to their absolute number:

- *Number of binding sites = 1.60 × 10^{-3} mmol = 1.60 × 10^{-6} mol (moles of binding sites) × 6.0221408 × 10^{23} molecules * mol^{-1} (Avogadro's number) = 9.6354 × 10^{17} binding sites (BS) or (molecules).*
- *TON = acid molecules consumed / binding sites (molecules) = 1.20 × 10^{20} (molecules) / 9.6354 × 10^{17} BS (molecules) = 124.540.* This value is larger than 1 which confirms the reaction is catalytic.

The surface coverage which represents the substrate packing density can also be estimated as follows.

- *Substrate (carboxylate) packing density = BS / SA of catalyst in reaction tube =9.6354 × 10 [17] BS (molecules) / 2.512 × 10 [18] nm^2 = 0.3835 sites (molecules) / nm^2*

Despite the quite high number of binding sites, the carboxylate monolayer is not tightly packed at saturation compared to values reported by Liu et al which was around 1- 4 carboxylate molecules / nm^2.[26]

3.6.4 Substrates binding with platinised Bi_2WO_6

The presence of Pt on the surface is essential for Bi_2WO_6 catalytic activity and reaction selectivity. However, Pt deposited on the surface could block the binding sites, reducing the chance for acid to access these sites. Thus, in order to check if Pt could block binding sites on Bi_2WO_6 surface, an adsorption experiment was performed with platinised Bi_2WO_6. The adsorption of alkene was much weaker compared to carboxylic acid, as seen in (Figure 3.23). The adsorption of Giese adduct was also much weaker compared to phenylacetic acid (Table 3.6). Thus, for both compounds, the binding was so weak that estimating the binding constant was not possible.

Table 3.6: Amount of phenylacetic acid, methacrolein, and Giese adduct remaining in solution before and after mixing with Bi_2WO_6 and platinised Bi_2WO_6 powder.

	Amount of acid remaining in solution (µmol)	***Amount of methacrolein remaining in solution (µmol)***	***Amount of Giese adduct remaining in solution (µmol)***
No catalyst (control)	0.365	0.051	0.037
Bi_2WO_6	0.005	0.050	0.031
Pt/Bi_2WO_6	0.056	0.050	0.031

Conditions: All reagents were dissolved in CD_3CN. 1 mL of reagent stock (PAAH 0.60 mM. Methacrolein 0.08 mM, Giese adduct 0.06 mM) solution was mixed with 125 mg of catalyst and subjected to further mixing using vortex.

The carboxylic acid adsorbed on both unmodified and platinised catalysts, but platinisation noticeably reduced the amount of adsorbed acid. This suggests that Pt on the surface could block the binding sites, which agrees with the observed result from Chapter 4, where higher Pt loading led to lower activity. It can be concluded from this study that the presence of Pt on the surface could reduce substrate binding; however, this needs additional investigation with different Pt loadings to correlate with substrate binding.

3.7 Proposed mechanism

Based on the outcome of this chapter, the role of Pt, the presence of water, and substrate binding, the proposed mechanism could be given (Scheme 3.4). In general, when a photocatalyst absorbs light, it gets excited, and electrons move from the valence band to the conduction band, leaving holes (h^+) with oxidising power. However, if Pt NPs are present in high amounts, they can block substrate adsorption and light from reaching the catalyst surface, which could lower the charge carriers generation rate and, as a result, slow down reactivity.

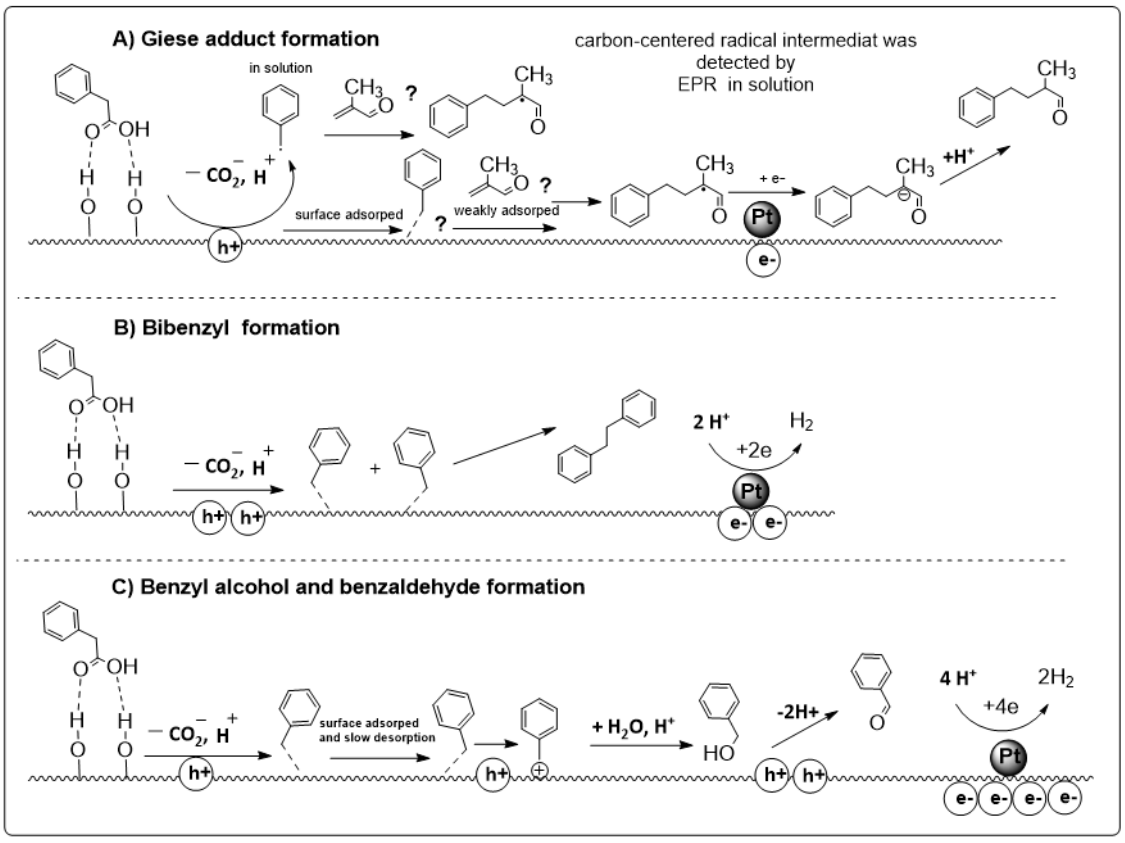

Scheme 3.4: Proposed mechanism of photo-Giese reaction by photoirradiated Pt/Bi_2WO_6.

Phenylacetic acid is adsorbed onto the Pt/Bi_2WO_6 surface, mainly via H-bonding between phenylacetate ions (via carboxylate) and surface hydroxyl groups (Scheme 3.4 A), resulting in the deprotonation of phenylacetic acid. Phenylacetate is oxidised through single electron transfer (SET) that is facilitated by holes (h^+) in the Bi_2WO_6 valance band (VB), which leads to the formation of the phenylacetate radical. CO_2 gas, a thermodynamically stable species, is released following decarboxylation of the phenylacetate radical, which facilitates the formation of benzyl radical. Alkene binds weakly to the catalyst; nonetheless we cannot determine whether addition to alkene

requires both benzyl radical and alkene to be adsorbed on the catalyst surface, or this reaction proceeds between desorbed radical and solution phase alkene.

An electron-deficient alkene (methacrolein) traps this benzyl radical, creating an intermediate radical at the β-carbon. Electrons (e-) at the Bi_2WO_6 conduction band (CB) or those trapped by Pt nanoparticles could reduce this radical intermediate to enolate that gets protonated by H^+ present in solution or on the catalyst surface as seen in deuterium exchange experiment. The source of these protons could be either acid, water adsorbed on surfaces, or surface-hydroxyl groups.

The formation of the bibenzyl (BB) by-product suggests the direct coupling of two benzyl radicals competes with the addition of alkene (Scheme 3.4 B). The rate of the radical-radical homocoupling reaction is fast compared to the rate of radical addition to alkene, but a high concentration of alkene favours the addition pathway. Another reason that could explain BB formation is the poor adsorption of alkene onto the catalyst surface, as shown by the adsorption experiment, which could allow two adsorbed benzyl radicals on surface to diffuse and react with each other.

If this benzyl radical does not desorb rapidly, it could undergo a second SET oxidation, forming a benzyl cation (Scheme 3.4 C). On the surface, this benzyl cation would react with adsorbed water and form the corresponding benzyl alcohol. Further oxidation of benzyl alcohol would result in the formation of benzaldehyde.

3.8 Conclusion and future work

The formation of Giese adducts via decarboxylation of phenylacetic by visible-light-irradiated Bi_2WO_6 decorated with Pt co-catalyst nanoparticles in the presence of methacrolein was successful. It was found that the presence of Pt is important for photocatalytic reactivity in the first instance, as no reaction happens in the absence of Pt. Pt role is not only to facilitate charge separation; it is also essential for visible light absorption and catalysis. Furthermore, the optimum amount of Pt provides a distance of tens of nm between Pt nanoparticles.

The presence of water is also crucial for catalytic activity and needs to be in the optimum amount, as excess water would slow down the reaction significantly. Water could facilitate both the formation of surface OH groups and the protonation of enolate, as seen in reactions performed in dry conditions. Thus, some water is needed for efficient catalysis (which facilitates the formation of surface OH or acts as protons surface), but very drying conditions could remove surface OH groups, which is also critical for catalysis. Deuterium exchange experiments showed that it is difficult to completely replace labile protons which suggests that some catalyst surface sites undergo proton

exchange relatively slowly. Nonetheless, nearly complete deuterium incorporation was achieved when D_2O was added to the reaction mixture. KIE studies showed that O-H bond breaking and C-H bond formation are not the RDS in the overall reaction. It is likely that oxidation of carboxylic acid is the slowest step.

Substrate binding is also a crucial step in the current mechanism. It was demonstrated that acid has a stronger binding affinity than alkene and Giese adduct. However, the strength of binding does not directly correlate to acid conversion as even weakly-binding acids form a complete layer on the catalyst surface under reaction conditions used in this study. Both alkene and product do not bind or bind too weakly to the surface, so the dissociation of the product is unlikely to be a major factor in the overall reaction. The estimated number of binding sites for phenylacetic adsorption is quite high, although the carboxylate monolayer is not tightly packed at saturation. However, the TON is bigger than 1, so the reaction is definitely catalytic.

Despite the complexity of heterogenous photocatalysis reactions, we hope that this chapter has shed some light on the mechanism of heterogenous catalysis by Bi_2WO_6 in organic transformation. This understanding can be applied to other metal oxide semiconductors. For future work, further optimisation of catalyst morphology can be investigated and tested against substrate binding. For example, a dry catalyst can be compared with a normal catalyst to determine acid binding constant and number of binding sites and to correlate with the role of surface OH and water in either aiding or obstructing substrate binding. Also, different acids with different functional groups and moiety sizes can be used to study functional group and molecule size effects.

References

(1) Unsworth, C. A. The Use of Visible Light Absorbing Bismuth-Containing Semiconductors as Heterogeneous Photocatalysts for Selective Chemical Transformations. phd, University of York, 2017. https://etheses.whiterose.ac.uk/19361/ (accessed 2023-08-15).

(2) Giese, B.; González-Gómez, J. A.; Witzel, T. The Scope of Radical CC-Coupling by the "Tin Method." *Angew. Chem. Int. Ed. Engl.* **1984**, *23* (1), 69–70. https://doi.org/10.1002/anie.198400691.

(3) Kitcatt, D. M.; Nicolle, S.; Lee, A.-L. Direct Decarboxylative Giese Reactions. *Chem. Soc. Rev.* **2022**, *51* (4), 1415–1453. https://doi.org/10.1039/D1CS01168E.

(4) Giese, B. Formation of CC Bonds by Addition of Free Radicals to Alkenes. Angew. Chem. Int. Ed. Engl. 1983, 22 (10), 753–764. https://doi.org/10.1002/anie.198307531

(5) Lindsey, A. S.; Jeskey, H. The Kolbe-Schmitt Reaction. *Chem. Rev.* **1957**, *57* (4), 583–620. https://doi.org/10.1021/cr50016a001.

(6) Teetz, N.; Holtmann, D.; Harnisch, F.; Stöckl, M. Upgrading Kolbe Electrolysis—Highly Efficient Production of Green Fuels and Solvents by Coupling Biosynthesis and Electrosynthesis. *Angew. Chem. Int. Ed.* **2022**, *61* (50), e202210596. https://doi.org/10.1002/anie.202210596.

(7) Verschueren, R. H.; De Borggraeve, W. M. Electrochemistry and Photoredox Catalysis: A Comparative Evaluation in Organic Synthesis. *Molecules* **2019**, *24* (11), 2122. https://doi.org/10.3390/molecules24112122.

(8) Tucker, J. W.; Stephenson, C. R. J. Shining Light on Photoredox Catalysis: Theory and Synthetic Applications. *J. Org. Chem.* **2012**, *77* (4), 1617–1622. https://doi.org/10.1021/jo202538x.

(9) Prier, C. K.; Rankic, D. A.; MacMillan, D. W. C. Visible Light Photoredox Catalysis with Transition Metal Complexes: Applications in Organic Synthesis. *Chem. Rev.* **2013**, *113* (7), 5322–5363. https://doi.org/10.1021/cr300503r.

(10) Koike, T.; Akita, M. Visible-Light Radical Reaction Designed by Ru- and Ir-Based Photoredox Catalysis. *Inorg. Chem. Front.* **2014**, *1* (8), 562–576. https://doi.org/10.1039/C4QI00053F.

(11) Teegardin, K.; Day, J. I.; Chan, J.; Weaver, J. Advances in Photocatalysis: A Microreview of Visible Light Mediated Ruthenium and Iridium Catalyzed Organic Transformations. *Org. Process Res. Dev.* **2016**, *20* (7), 1156–1163. https://doi.org/10.1021/acs.oprd.6b00101.

(12) Miyake, Y.; Nakajima, K.; Nishibayashi, Y. Visible Light-Mediated Oxidative Decarboxylation of Arylacetic Acids into Benzyl Radicals: Addition to Electron-

Deficient Alkenes by Using Photoredox Catalysts. *Chem. Commun.* **2013**, *49* (71), 7854–7856. https://doi.org/10.1039/C3CC44438D.

(13) Chu, L.; Ohta, C.; Zuo, Z.; MacMillan, D. W. C. Carboxylic Acids as A Traceless Activation Group for Conjugate Additions: A Three-Step Synthesis of (±)-Pregabalin. *J. Am. Chem. Soc.* **2014**, *136* (31), 10886–10889. https://doi.org/10.1021/ja505964r.

(14) Zhu, Q.; Nocera, D. G. Photocatalytic Hydromethylation and Hydroalkylation of Olefins Enabled by Titanium Dioxide Mediated Decarboxylation. *J. Am. Chem. Soc.* **2020**, *142* (42), 17913–17918. https://doi.org/10.1021/jacs.0c08688.

(15) Manley, D. W.; McBurney, R. T.; Miller, P.; Howe, R. F.; Rhydderch, S.; Walton, J. C. Unconventional Titania Photocatalysis: Direct Deployment of Carboxylic Acids in Alkylations and Annulations. *J. Am. Chem. Soc.* **2012**, *134* (33), 13580–13583. https://doi.org/10.1021/ja306168h.

(16) Kuwana, D.; Komori, Y.; Nagatomo, M.; Inoue, M. Photoinduced Decarboxylative Radical Coupling Reaction of Multiply Oxygenated Structures by Catalysis of Pt-Doped TiO2. *J. Org. Chem.* **2022**, *87* (1), 730–736. https://doi.org/10.1021/acs.joc.1c02736.

(17) Tse, E. C. M.; Varnell, J. A.; Hoang, T. T. H.; Gewirth, A. A. Elucidating Proton Involvement in the Rate-Determining Step for Pt/Pd-Based and Non-Precious-Metal Oxygen Reduction Reaction Catalysts Using the Kinetic Isotope Effect. *J. Phys. Chem. Lett.* **2016**, *7* (18), 3542–3547. https://doi.org/10.1021/acs.jpclett.6b01235.

(18) Zhu, Z.; Wan, S.; Zhao, Y.; Qin, Y.; Ge, X.; Zhong, Q.; Bu, Y. Recent Progress in Bi2WO6-Based Photocatalysts for Clean Energy and Environmental Remediation: Competitiveness, Challenges, and Future Perspectives. *Nano Sel.* **2021**, *2* (2), 187–215. https://doi.org/10.1002/nano.202000127.

(19) Okhlobystina, L. V.; Cherkasova, T. I.; Tyurikov, V. A. Study of the Formation of Free Radicals in Reactions of Aliphatic Nitro Compounds by the Method of Radical Trapping. 4. Formation of Short-Lived Radicals When Nucleophilic Reagents Are Reacted with Difluorodinitromethane in Aprotic Solvents. *Bull. Acad. Sci. USSR Div. Chem. Sci.* **1979**, *28* (10), 2036–2043. https://doi.org/10.1007/BF00947548.

(20) Schaich, K. M.; Borg, D. C. EPR Studies in Autoxidation. In *Autoxidation in Food and Biological Systems*; Simic, M. G., Karel, M., Eds.; Springer US: Boston, MA, 1980; pp 45–70. https://doi.org/10.1007/978-1-4757-9351-2_4.

(21) Barker, P.; Beckwith, A. L. J.; Cherry, W. R.; Huie, R. Characterization of Spin Adducts Obtained with Hydrophobic Nitrone Spin Traps. *J. Chem. Soc. Perkin Trans. 2* **1985**, No. 8, 1147–1150. https://doi.org/10.1039/P29850001147.

(22) Kang, E.; Park, H. R.; Yoon, J.; Yu, H.-Y.; Chang, S.-K.; Kim, B.; Choi, K.; Ahn, S. A Simple Method to Determine the Water Content in Organic Solvents Using the

1H NMR Chemical Shifts Differences between Water and Solvent. *Microchem. J.* **2018**, *138*, 395–400. https://doi.org/10.1016/j.microc.2018.01.034.

(23) Henderson, M. A. The Interaction of Water with Solid Surfaces: Fundamental Aspects Revisited. *Surf. Sci. Rep.* **2002**, *46* (1), 1–308. https://doi.org/10.1016/S0167-5729(01)00020-6.

(24) Deblock, L.; Goossens, E.; Pokratath, R.; De Buysser, K.; De Roo, J. Mapping out the Aqueous Surface Chemistry of Metal Oxide Nanocrystals: Carboxylate, Phosphonate, and Catecholate Ligands. *JACS Au* **2022**, *2* (3), 711–722. https://doi.org/10.1021/jacsau.1c00565.

(25) B. Greytak, A.; L. Abiodun, S.; M. Burrell, J.; N. Cook, E.; P. Jayaweera, N.; Moinul Islam, M.; E Shaker, A. Thermodynamics of Nanocrystal–Ligand Binding through Isothermal Titration Calorimetry. *Chem. Commun.* **2022**, *58* (94), 13037–13058. https://doi.org/10.1039/D2CC05012A.

(26) Liu, J.; Shekhah, O.; Stammer, X.; Arslan, H. K.; Liu, B.; Schüpbach, B.; Terfort, A.; Wöll, C. Deposition of Metal-Organic Frameworks by Liquid-Phase Epitaxy: The Influence of Substrate Functional Group Density on Film Orientation. *Materials* **2012**, *5* (9), 1581–1592. https://doi.org/10.3390/ma5091581.

Chapter 4: Optimisation of Giese reaction and reaction scope

4.1 Optimisation

Reaction optimisation, at its core, facilitates a more profound comprehension of the reaction mechanism, a critical factor in the progression of chemical synthesis, the development of novel reactions, and the enhancement of preexisting ones. It determines the optimal parameters that govern the progression of a chemical reaction with maximum efficiency and selectivity. In terms of importance for industrial applications, researchers can increase the yield of the desired product while minimising or eliminating potential side reactions by optimising the reaction. It is critical to comprehend the mechanism via optimisation in order to facilitate the transition of the reaction from laboratory settings to industrial production. The utilisation of optimised reactions can yield mechanistic insights that can be applied to the development of more selective and efficient catalysts.

This chapter aims to investigate the reaction parameters and how they may affect the Giese reaction, the model reaction between phenylacetic acid and methacrolein. This chapter also explores reaction scope by using different acids and alkenes. Pt loading on catalyst, catalyst mass, reaction time, and substrate stoichiometry are the main optimisation parameters that will undergo investigation. We will also show how crystallinity affects catalytic activity and reaction selectivity compared to surface area.

4.1.1 Pt loading on Bi_2WO_6

As shown in the previous chapter, the presence of Pt is crucial for reaction reactivity and selectivity, as the reaction did not proceed in the absence of Pt. It was found in chapters 2 and 3 that Pt did not significantly affect the bandgap (but enhance visible light absorption) or charge carrier lifetime in Bi_2WO_6. However, it could act as a co-catalyst where (i) intermediate radical could be reduced at the catalyst surface to enolate (and this could be catalysed by Pt) or (ii) protons can be reduced to surface H atoms on the Pt surface (Pt-H), with Pt catalysis, and abstracted by the intermediate radical to yield the product. Photogenerated electrons that convert protons to Pt-H could also facilitate hydrogen production, however, the GC gas analysis of Giese reaction showed no hydrogen evolution, suggesting that the reaction consumed any hydrogen produced likely in reduction of excess alkene or carbonyl moieties. The source of protons could be acid or water, as discussed in Chapter 3.

Thus, the first parameter to optimise is the amount of Pt on the catalyst surface. Different Pt loadings were used, and (Table 4.1) shows the corresponding conversion and yield.

Table 4.1: Pt loading on Bi_2WO_6 and its effect on yield, conversion and selectivity.

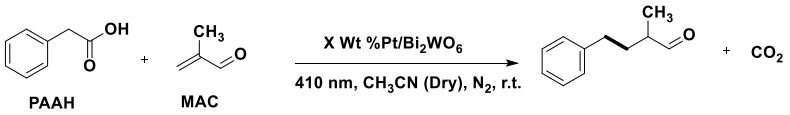

PAAH MAC

Entry	Pt (Wt. %)	Yield (%)	Conversion (%)	Selectivity (%)
1	0.075	35	66	53
2	0.15	55	99	56
3	0.3	40	70	57
4	0.45	11	51	22

Reaction conditions: Pt/Bi_2WO_6 (20 mg), phenylacetic acid, PAAH (0.1 mmol) and methacrolein, MAC (0.25 mmol), reaction time (24 hours), 405-410 nm LED torch, N_2. Yield and conversion were calculated by ^1H NMR using dimethyl terephthalate (DMT) as internal standard. Selectivity is ratio of yield to conversion.

Table 4.1 shows that when using the smallest amount of Pt (0.075 Wt.%), the conversion was 66%, and when using relatively high Pt (0.3 Wt.%), the conversion was 70% (Table 4.1, entries 1 and 3). The decrease in conversion for catalysts with high Pt loading could be explained by more Pt on surface may prevent photo absorption by bulk Bi_2WO_6 but light absorption at surface still observed and this could be due intraband absorption in Pt at the surface as mentioned in chapter 2. Pt in high loading could also block catalyst binding and active sites, which could prevent acid adsorption on the surface. The experiment done in Chapter 3 confirmed that there was a reduction in the number of binding sites and less acid adsorbed on the platinized catalyst compared to the bare catalyst. On the other hand, the decrease in conversion and yield associated with very low Pt loading was expected as Pt is needed for activity and selectivity.

To conclude, the presence of Pt is critical and assists in reaction reactivity and product selectivity. Low Pt loading (below 0.15%) may not provide sufficient Pt for light absorption and optimised catalysis, and so yield and conversion are low. The optimum Pt amount was found to be around 0.15 wt.%. Above this value, catalytic activity starts to decline due to surface blocking.

The other parameter to investigate is the amount of catalyst required to drive the reaction. It is usually preferred to use a small amount of catalyst to enable catalyst separation and it is cheaper and more sustainable.

4.1.2 Amount of Catalyst

Here, optimal amount of catalyst was determined. It is common that increasing the amount of catalyst (and hence the number of available surface sites for substrate binding) causes the reaction rate to increase. Table 4.2 shows the different catalyst amounts used, as well as the corresponding conversion and selectivity.

Table 4.2: Amount of Bi_2WO_6 used in reaction and its effect on yield, conversion and selectivity.

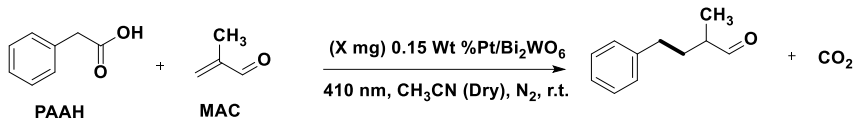

PAAH MAC

Entry	*Catalyst (mg)*	*Yield (%)*	*Conversion (%)*	*Selectivity (%)*
1	20	16	43	37
2	40	53	90	53
3	60	63	94	67
4	80	63	99	63

Reaction conditions: 0.15 Pt/Bi_2WO_6 (X mg), phenylacetic acid, PAAH (0.2 mmol) and methacrolein, MAC (0.6 mmol), reaction time (24 hours), 405-410 nm LED torch, N_2. Yield and conversion were calculated by ^1H NMR using dimethyl terephthalate (DMT) as internal standard. Selectivity is ratio of yield to conversion.

In Table 4.2 entry 1, using 20 mg of catalyst gave low conversion and selectivity, (43 % & 37 %). Table 4.2, entry 2 clearly shows that 40 mg of catalyst resulted in high acid conversion and moderate selectivity. Using 60 mg of catalyst yielded the best selectivity, which was approximately 67%. There are two values to discuss: conversion and selectivity, and how the amount of catalyst affects them. Fewer catalyst sites for starting material binding can explain low conversion with less catalyst. The fact that selectivity increases with catalyst loading used suggests the presence of different catalytic sites: some lead to the desired reaction (“good” selective catalytic sites), and some result in overoxidation (non-selective catalytic sites).

High catalyst loading makes many catalytic sites available for acid oxidation, resulting in high conversion. However, high catalyst loading may prevent light penetration the mixture which can limit catalysis or cause it to plateau. At high catalyst loading, there are plenty of good sites, which gives good selectivity. At low catalyst loading, deactivation of

"good" sites results in the reaction occurring at non-selective catalytic sites giving side products such as multiple radical adducts, bibenzyl, benzyl alcohol, and benzaldehyde.

From this optimisation, 60 mg of catalyst looks optimal and can consume PAAH in 24 hours. Next, we tested concentration of substrates to determine the optimum reaction conditions.

4.1.3 Concentration of substrates

Another reaction set was performed to study the impact of acid amount on conversion and selectivity, (Table 4.3).

Table 4.3: The effect of increasing the amount of acid on yield, conversion and selectivity.

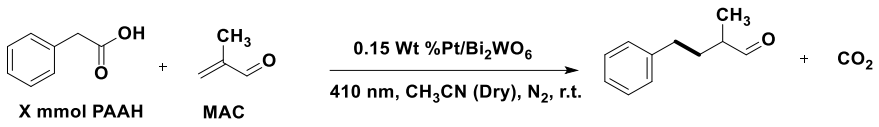

Entry	*PAAH (mmol)*	*Yield (%)*	*Conversion (%)*	*Selectivity (%)*
1	0.1	55	99	55
2	0.2	63	94	67
3	0.4	31	64	48

Reaction conditions: *0.15 Pt/Bi_2WO_6 (60 mg), methacrolein, MAC (3 equivalents), reaction time (24 hours), 405-410 nm LED torch, rt, N_2. Yield and conversion were calculated by ^1H NMR using dimethyl terephthalate (DMT) as internal standard. Selectivity is ratio of yield to conversion.*

The above result shows that the acid amount (0.1 – 0.2 mmol) gave a high conversion, but 0.2 mmol of phenylacetic acid (PAAH) slightly improved selectivity. Increasing the PAAH to 0.4 mmol inhibited both the reactivity (64% acid conversion) and the yield (31%). Surface coverage limitations may arise when using an excess amount of acid, potentially poisoning the catalyst by blocking its active sites. This experiment also shows that the acid is the limiting reagent.

Another experiment was conducted to investigate the different amounts of alkene used (Table 4.4). In the absence of alkene, the NMR spectrum shows a peak of bibenzyl which is formed when two benzyl radicals are coupled. Adding the alkene methacrolein to the reaction resulted in the formation of the Giese adduct in preference of bibenzyl (Figure 4.1).

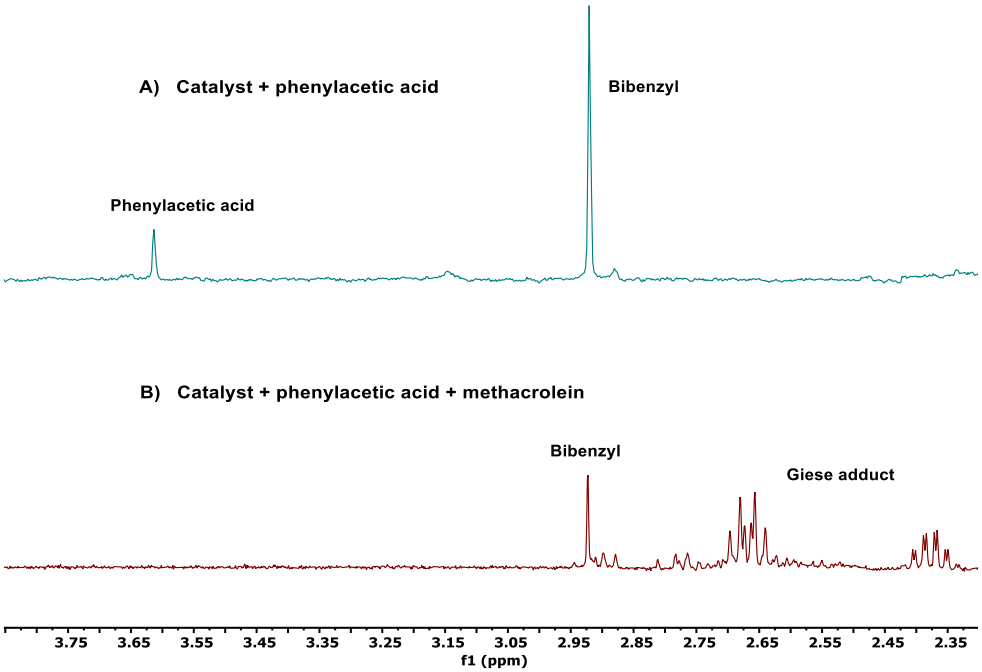

Figure 4.1: ^{1}H NMR spectrum showing reaction outcome of (A) reaction of phenylacetic acid (0.2 mmol in 2 mL CH_3CN) with 60 mg Pt/Bi_2WO_6 and (B) reaction of phenylacetic acid (0.2 mmol in 2 mL CH_3CN) in presence of methacrolein 0.6 mmol with 60 mg Pt/Bi_2WO_6.).

Increasing the amount of alkene makes it less likely that bibenzyl will form because radical addition to alkene will outcompete bimolecular dimerization to form bibenzyl. The fact that bibenzyl can form even in the presence of a large excess of alkene suggests that benzyl radicals react on the surface rather than in solution, as similar reactions with homogeneous catalysis showed a different reactivity pattern. For instance, an experiment was performed by Nishibayashi et al. to study the addition of benzyl radical (using 4-dimethylamino phenylacetic acid as radical source) to electron-deficient alkene (ethyl (E)-2-cyano-3-phenylpropenoate) using homogenous Ir photoredox catalyst. [3] The homocoupling (dimerization) leading to (bibenzyl) was not observed in the homogenous reaction when alkene used in equivalent amount only. With the heterogeneous Pt/Bi_2WO_6, bibenzyl is still formed even in the presence of a 6-fold excess of alkene, suggesting the radical addition occurs on the catalyst surface.

Table 4.4: Effect of alkene amount on yield, conversion, and selectivity.

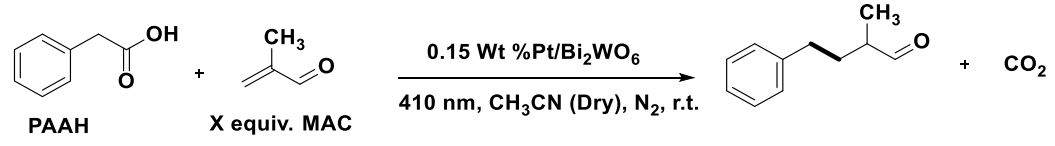

Entry	*MAC (equiv.)*	*Yield (%)*	*Conversion (%)*	*Selectivity (%)*
1	1	16	99	16
2	3	55	99	55
3	6	52	99	52

Reaction conditions: 0.15 Pt/Bi_2WO_6 (60 mg), phenylacetic acid, PAAH (0.1 mmol), reaction time (24 hours), 405-410 nm LED torch, N_2. Yield and conversion were calculated by ^{1}H NMR using dimethyl terephthalate (DMT) as internal standard. Selectivity is ratio of yield to conversion.

Table 4.4 shows that using only one equivalent of alkene significantly reduced the selectivity. The adsorption study in Chapter 3, Section 3.6.1, reveals that alkene is weakly adsorbed on the catalyst surface, and increasing the amount of alkene could potentially enhance collisions with benzyl radical molecules in solution or on the surface. The rate of bimolecular coupling of benzyl radicals ($k = 1.9 \times 10^9$ M^{-1} s^{-1})[4] is much faster than addition to alkene (10^6 M^{-1} s^{-1}).[5] However, because the concentration of benzyl radicals is very low, addition to alkene outcompetes dimerization. Addition to alkene is also facilitated by matching the polarity of the radical (electron-rich) and alkene (electron-deficient). Further increases in alkene amounts did not increase selectivity. This can be tentatively explained if one assumes that the radical addition to alkene occurs on the catalyst surface (e.g., by Langmuir-Hinshelwood mechanism).

After optimising the amount of starting materials and catalyst loading, the reaction time was varied to check if the Giese adduct could undergo further oxidation.

4.1.4 Reaction time and stability of product

One of the problems identified in photocatalysis by metal oxide semiconductors is the possible overoxidation of the formed product due to the high oxidation power of continuously formed holes in Bi_2WO_6.[6,7] The results of this experiment are shown in (Table 4.5).

Table 4.5: Stability of Giese adduct over period of three days reaction.

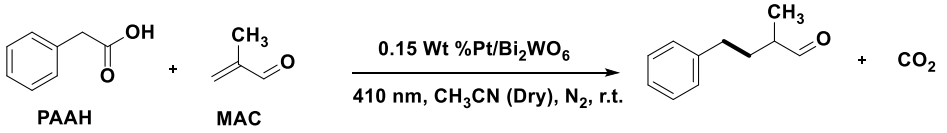

Entry	**Time (h)**	**Yield (%)**	**Conversion (%)**	**Selectivity (%)**

1	12	36	50	72
2	24	64	99	64
3	48	65	99	65
4	72	62	99	62

Reaction conditions: 0.15 Pt/Bi_2WO_6 (60 mg), phenylacetic acid, PAAH (0.2 mmol) and methacrolein, MAC (0.6 mmol), 405-410 nm LED torch, N_2. Yield and conversion were calculated by ^1H NMR using dimethyl terephthalate (DMT) as internal standard. Selectivity is ratio of yield to conversion.

In the first 12 hours of the reaction, half of the phenylacetic acid was consumed, yielding 36% of the Giese adduct with 72% selectivity (Table 4.5, entry 1). In 24 hours, PAAH was completely consumed; however, yield around 64% was obtained (Table 4.5, entry 2). Here, selectivity was slightly higher in shorter reaction time (12 hours) and that might be due to catalyst is getting poisoned a bit at long reaction time. After 48 and 72 hours of reaction, 65% and 62% of the product were obtained (Table 4.5, entries 3 and 4). The negligible change in product yield indicates that the product is stable, and no further oxidised products, apart from benzyl alcohol and benzaldehyde, were noticed. The conclusion of this experiment is that Giese adduct is stable and does not undergo further oxidation.

4.1.5 Light source wavelength

The light wavelength, the driving force of the photocatalytic reaction, is one of the crucial optimisations in photocatalysis, as each metal oxide has its own unique bandgap that absorbs specific wavelengths. The LED torches with different emission wavelength were used in the standard Giese reaction to study the influence of different light energies (Table 4.6).

Table 4.6: Light source wavelength effect on yield, conversion and selectivity.

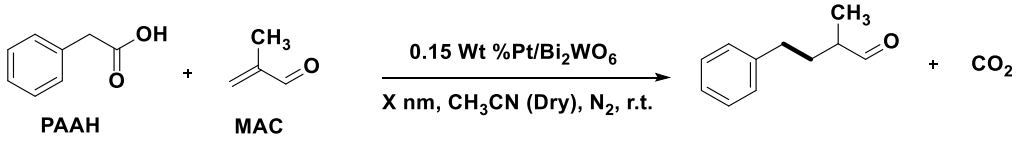

LED (nm)	*Yield (%)*	*Conversion (%)*	*Selectivity (%)*
410	53	99	53

450	21	50	41

Reaction conditions: *0.15 Pt/Bi_2WO_6 (108 mg), phenylacetic acid, PAAH (0.1 mmol) and methacrolein, MAC (0.25 mmol), reaction time (24 hours), N_2. Yield and conversion were calculated by ^{1}H NMR using dimethyl terephthalate (DMT) as internal standard. Selectivity is ratio of yield to conversion.*

The above results suggest that using 450 nm light source with 420 nm catalyst (bandgap ≈ 2.9 eV) should give very poor conversion but medium conversion was obtained. This suggests that platinised particles can facilitate absorption of low energy light followed by energy transfer to Bi_2WO_6. The conclusion from this experiment is that high conversion requires light with energy above the bandgap.

4.1.6 Light intensity

Increasing light intensity should increase production of charge carriers which should lead to faster reaction rate. However, at high light intensity, charge recombination would also increase due to an increase in charge population or accumulation of charges on surface. So, this increase might affect the photocatalytic activity negatively. The following experiment was run to check if light intensity could increase or decrease the rate of the reaction (Table 4.7). The reaction duration was reduced so that the conversion with low light intensity was significantly below 100%.

Table 4.7: Effect of light intensity on yield, conversion and selectivity.

Light source	***Yield (%)***	***Conversion (%)***	***Selectivity (%)***
One torch	28	66	42
4 torches	51	88	59

Reaction conditions: *0.15 Pt/Bi_2WO_6 (40 mg), phenylacetic acid, PAAH (0.2 mmol) and methacrolein, MAC (0.6 mmol), reaction time (15 hours), 405-410 nm LED torch, N_2. Yield and conversion were calculated by ^{1}H NMR using dimethyl terephthalate (DMT) as internal standard. Selectivity is ratio of yield to conversion.*

The above table shows that adding more torches (increasing light intensity) increased the reaction rate. At high light intensity, the rate of charge carriers formation increases. This suggests that the increase in recombination is not significant under these conditions. Moreover, increasing light intensity could enhance light penetration inside semiconductor pores, exposing more surface area to light.[8]

4.1.7 Other optimisations

There were some further optimisation carried out, such as using Ar gas instead of N_2 and using ozonation technique to clean the catalyst surface. When replacing Ar with N_2, no major difference was noticed. The reason for using Ar is that Ar is denser than N_2 making it easier to maintain inert atmosphere in the reaction vessel and to eliminate O_2.

Cleaning solid surfaces using ozonation is an efficient method for the oxidative removal of organic residuals at the catalyst that could arise during catalyst preparation or from exposure to laboratory aerosols. It was found that there was no major difference between ozonated and untreated platinized catalysts.

4.2 Crystallinity vs surface area

One of the main factors affecting the photocatalytic activity is micro-structure and morphology. In Chapter 2, Section 4, Bi_2WO_6 was synthesised with different morphologies and surface areas. Hydrothermal treatment was used to improve material crystallinity without using high temperature treatment such as calcination. The synthesised catalyst was tested in the Giese reaction to reveal the best active catalyst. (Table 4.8) shows different Bi_2WO_6 samples prepared with different surface areas and different degrees of crystallinity. Here, FWHM values are used to represent the broadening in the PXRD diffraction peak of Pt/Bi_2WO_6 which may be related to the particle size as discussed in chapter 2, section 2.4.1.

Table 4.8: Photocatalytic activity of different Pt/Bi_2WO_6 samples synthesised at different morphology

Entry	***catalyst synthesis condition***	***SA (m^2/ g)***	***FWHM (º)***	***Yield (%)***	***Conversion (%)***	***Selectivity (%)***
1	(EG _ MW)	86	7.07	12	54	21
2	(EG _ MW _ Hydro)	31	0.66	36	85	42
3	(Hydro_ CH)	21	0.57	20	65	30

Reaction conditions: 0.15 Pt/Bi_2WO_6 (10 mg), PAAH (0.2 mmol), and MAC (0.6 mmol), 24 h rt, N_2. Yield and conversion were calculated by ^{1}H NMR using dimethyl terephthalate (DMT) as internal standard. Abbreviations: SA stands for surface area, FWHM stands for full width half maxima and it represent the XRD peak with. It is related to crystalline size, the bigger the number, the smaller the crystallite. (EG _ MW _ Hydro) stands for samples synthesised in ethylene glycol EG using microwave MW then the sample being treated hydrothermally. (Hydro_ CH) stands for

samples synthesised in water using conventional heating, this is the standard sample. (EG _ MW) stands for samples synthesised in EG using MW.

Sample synthesised in ethylene glycol (EG) using microwave (MW) has a high surface area (86 m^2/g), entry 1. This sample converted 54% of phenylacetic acid and gave 21% product selectivity. This sample showed poor crystallinity according to PXRD (Figure 2.8 B).

The samples synthesised in EG using MW and hydrothermally treated (SA = 31 m^2/g), entry 2, exhibited the highest photoactivity, converting 85% of phenylacetic acid and giving 42% Giese adduct selectivity. So, two-step synthesis looked promising; however, increasing the quantity of catalyst using microwave was not feasible due to instrument limitations.

The samples synthesized via one-step hydrothermal (Hydro_ CH), the standard samples, (SA = 21 m^2/g) still showed good photocatalytic activity (65% conversion and 30 % selectivity, entry 3). Because only 10 mg of catalyst was used, yield and conversion dropped compared to using 60 mg of catalyst.

So, from above table we can see that (i) surface area decreases with hydrothermal treatment but crystallinity improves; using these methods, it does not appear to be possible to make a sample with high surface area and high crystallinity at the same time. (ii) samples with high surface area showed lowest activity and also lowest selectivity. This suggest that the Giese reaction product is formed on the active sites on crystalline materials, and at low crystallinity, the number of “good” active sites is small and the reaction is dominated by side reactions on “bad” active sites. Therefore, not that only conversion is low but also the selectivity stays low.

In conclusion, in samples with high crystallinity, there are more ‘’good’’ active sites, hence both conversion and selectivity increase.

A study by Amano et al. on Bi_2WO_6 photocatalytic activity was carried out with two reaction systems. It gave a demonstration of how crystallinity plays a crucial role in photocatalytic performance.[9] Reaction 1 was the oxidative decomposition of acetic acid in an aqueous solution. Reaction 2 was the oxidative decomposition of acetaldehyde in air. They found that reaction 1 rate was strongly affected by the crystallinity content of Bi_2WO_6, while the rate of reaction 2 showed a potential relationship with the Bi_2WO_6-specific surface area having same degree of crystallinity (Figure 4.2 A and B), respectively.

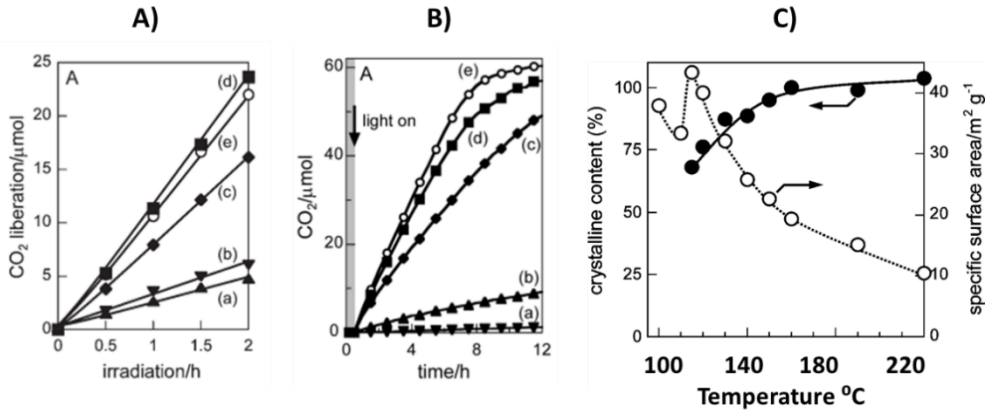

Figure 4.2: photocatalytic decomposition of acetic acid in aqueous solution, reaction 1 (A) and photocatalytic decomposition of acetaldehyde in air, reaction 2 (B). samples a,b,c,d, and e stand for samples synthesised at 100 ºC, 110 ºC, 115 ºC, 120 ºC and 130 ºC, respectively. C) A diagram showing the relationship between preparation temperature, crystallinity (black circles) and specific surface area (white circles).[9]

The above graph shows the amount of released CO_2 from acetic acid and acetaldehyde decomposition after irradiating Bi_2WO_6 (Figure 4.2). In graph A, samples a–e represent Bi_2WO_6 that were synthesised at different temperatures (100–130 °C). Bi_2WO_6 synthesised at 120 and 130 °C showed noticeable activity in the degradation of acetic acid (reaction 1). These samples have a high degree of crystallinity due to high-temperature synthesis.

In graph B), crystallinity also played a big part in how quickly acetaldehyde broke down in air (reaction 2). However, they found that the rate of CO_2 liberation using sample synthesised at a temperature higher than 130 °C reduced, as thermal treatment reduced the sample's surface area. They explained this observation as fewer adsorption sites were available due to reduce in surface area.

They also studied the correlation between degree of crystallinity and charge carrier's lifetime and they concluded that as the degree of crystallinity increased, the photogenerated charges increased as well as their lifetime.

In this literature example the crystallinity clearly determined catalytic activity, so that catalysts with the highest crystallinity showed best activity despite having low surface area. Crystallinity could improve photocatalytic activity by facilitating charge separation and suppressing recombination. Also, the fast recombination of charges is most likely to happen in amorphous materials synthesised at low temperatures due to the presence of defects that could act as recombination centres, or these crystal defects could trap charges, which would result in the depletion of these energetic charges.

From the optimisation described above, the standard conditions of 0.15 Pt/Bi_2WO_6 (60 mg), phenylacetic acid (0.2 mmol), methacrolein (0.6 mmol), reaction time (24 hours), 405–410 nm LED torch, room temperature, and under N_2 typically result in a high conversion of approximately 94% for phenylacetic acid, but the yield remains between 60–70%. We conducted a substrate scope analysis based on this optimization.

4.3 Substrate scope

4.3.1 Alkene scope

To study the effect of different substrates on reaction selectivity and catalyst efficiency, different substituted alkenes and substituted phenylacetic acids were used. A range of alkenes with electron-withdrawing groups (Michael acceptors) of different electron-withdrawing power that are potentially leading to interesting products were chosen (Table 4.9)

Table 4.9: Alkene scope with phenylacetic acid.

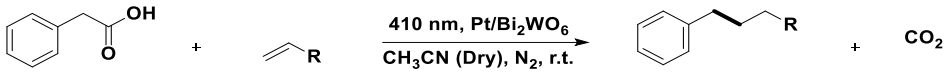

Entry	Alkene	Yield (%)	Conversion (%)	Selectivity (%)
1		63	94	67
2	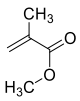	10	51	20
3	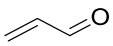	26	74	34
4	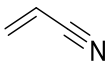	30	86	33
5	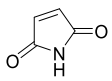	28	88	32
6	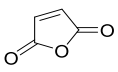	78	96	82

Reaction conditions: 0.15 Pt/Bi_2WO_6 (60 mg), phenylacetic acid, PAAH (0.2 mmol) and alkene (0.6 mmol), reaction time (24 hours), 405-410 nm LED torch, N_2. Yield and conversion were calculated by ^1H NMR using dimethyl terephthalate (DMT) as internal standard. Selectivity is ratio of yield to conversion.

It is worth mentioning that, as far as we know, the photocatalytic formation of substituted propylbenzenes from phenylacetic acid and substituted alkenes has not been previously reported in the literature. It can be noted that the reaction between PAA and methyl methacrylate, MAA, resulted in moderate conversion (51%) and low selectivity (20%) (Table 4.9, entry 2) compared to the standard reaction between PAA and MAC (94% conversion and 67% selectivity, respectively). It might be suggested that the ester group of MMA could compete with acid binding on the surface but this is unlikely to happen as acid will bind stronger. Another reason to consider is that the methoxy group as an electron-donating group decreases electron-withdrawing ability of the carbonyl group which hinders radical addition and hence results in lower selectivity. In the case of acrolein, conversion was reduced to 74% and the product selectivity was also low (34%); see (Table 4.9, entry 3). Thus, using MAC as a Michael acceptor often shows excellent conversion and good product selectivity compared to acrolein which could undergo oligomerisation reducing both conversion and selectivity (see below NMR, Figure 4.3)

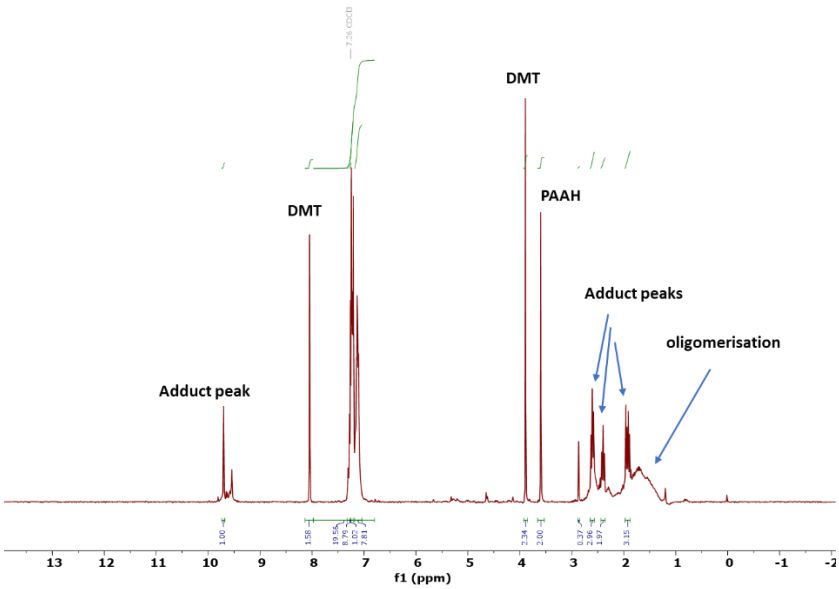

Figure 4.3: ^{1}H NMR spectrum of Giese adduct resulting from reaction of phenylacetic acid and acrolein.

Maleimide and maleic anhydride (Table 4.9, entries 5 and 6) both showed high conversion, but the selectivity was low with maleimide (32%). In contrast, maleic anhydride Giese adduct selectivity was around 82%. The variation in conversion, in general, might not only depend on electronic properties of alkene which confirms our conclusion that the reaction is heterogenous.

The selectivity of these reactions could be tentatively attributed to a combination of surface and electronic effects. According to Hammett parameters in homogenous reactions, the most electron-deficient alkene would be nitrile, phosphate, aldehyde,

anhydride, imide and then ester.[5] However, this order does not match the observed trend with substituted electron-deficient alkene which suggests that the reaction outcome could be determined by the surface interactions.

So, from this alkene scope, it is difficult to identify specific reasons for variation in selectivity, but it can be said that in addition to the electronic effect of alkene, binding mode may play a role. The next set of experiments is to study the effect of substituents on PAAH.

4.3.2 Acid scope

After alkene scope exploration, acid scope was also investigated with phenylacetic acid derivatives and phenylglyoxylic acid (Table 4.10).

Table 4.10: Acid scope with methacrolein.

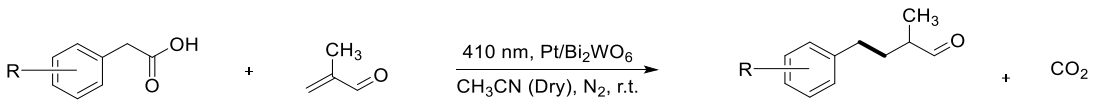

Entry	***Acid***	***Yield (%)***	***Conversion (%)***	***Selectivity (%)***
1	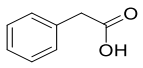	63	94	67
2	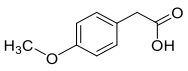	17	44	39
3	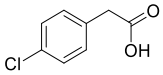	60	99	60
4	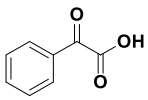	45	99	45

Reaction conditions: 0.15 Pt/Bi_2WO_6 (60 mg) acid (0.2 mmol) and methacrolein, MAC (0.6 mmol), reaction time (24 hours), 405-410 nm LED torch, N_2. Yield and conversion were calculated by ^1H NMR using dimethyl terephthalate (DMT) as internal standard. Selectivity is ratio of yield to conversion.

The reaction of 4-methoxyphenylacetic acid, 4-MeOPAAH, which has an electron-donating substituent, with methacrolein reduces both conversion and selectivity to 44%

and 39%, respectively (Table 4.10, entry 2). Here, low conversion was surprising as methoxy group makes this acid easier to oxidise so high conversion was expected. It is possible that the 4-MeOPAAH-derived benzyl radical binds strongly to surface thus blocking the active sites. This was consistent with the adsorption experiment in Chapter 3, Section 3.6.2, where 4-methoxyphenylacetic acid binds stronger than phenylacetic acid. This relatively strong binding could result in slow radical desorption from the surface which hinders the adsorption of new acid molecules. An alternative explanation could be that oxidation could occur on the electron-rich aromatic ring, and not on the carboxylic group, and this aromatic radical cation stays adsorbed on the surface, not undergoing further reaction and blocking the active sites. In terms of selectivity, methoxyphenylacetic acid is easier to oxidise and therefore is more likely to undergo overoxidation which reduces adduct selectivity. Moreover, MeO group might stabilises benzyl radical leading to slower adduct formation, which could lead to oxidation and dimerization. On the other hand, 4-chlorophenylacetic acid gave similar conversion and slightly lower selectivity as standard phenylacetic acid (Table 4.10, entry 3). Apparently, chloroPAAH undergoes full conversion, although it is more difficult to oxidise compared to methoxyPAAH. This could be explained by assuming that electron transfer from adsorbed chloroPAAH results in the irreversible oxidation of carboxylate ion, while with the methoxy derivative, the electron transfer leads to reversible oxidation of the aromatic ring. However, the presence of the Cl group could slow down the addition of benzyl radicals to alkenes, leading to other side reactions such as dimerization, as seen in the NMR below (Figure 4.4).

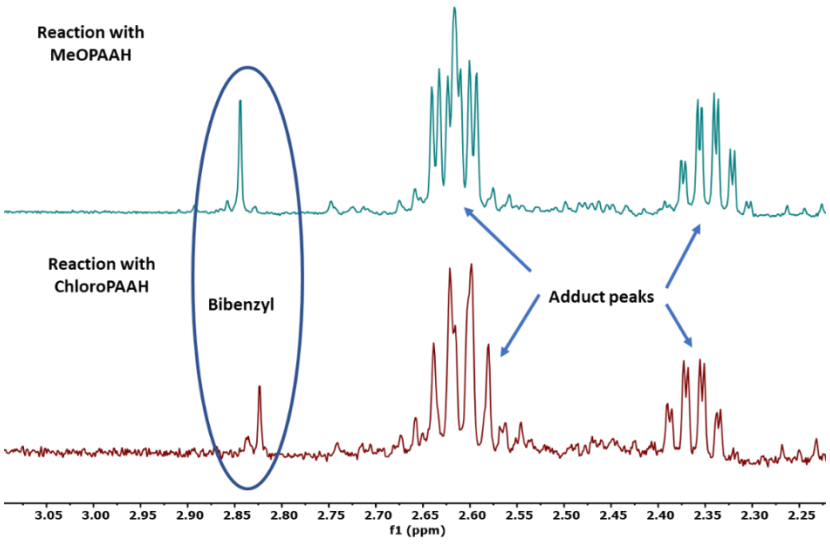

Figure 4.4: ^{1}H NMR spectrum of alkylation of methacrolein with 4-methoxyphenylacetic acid (top) and 4-chlorophenylacetic acid (bottom) showing bibenzyl formation in both reaction, 0.5 % in first reaction and 3 % in second reaction.

A reaction with phenylglyoxylic acid gave high conversion but low selectivity (table 4.10, entry 4). Nonetheless, the applicability of our reaction to the generation of acyl radicals is very encouraging.

Acyl radicals play a crucial role as nucleophilic intermediates in various chemical reactions. The significance of reactions that enable the incorporation of an acyl group is seen in the ability to directly obtain carbonyl-containing compounds, which include essential functional groups in organic synthesis, such as ketones and related derivatives.[11,12] The intermolecular cyclization of acyl radicals is also beneficial in organic synthesis.[13] Conventional techniques for producing acyl radicals necessitate the use of unstable initiators, stoichiometric oxidants, or reductants. Photochemistry offers a viable alternative for conducting acylation reactions due to its modest reaction conditions. Acyl radicals can be generated photochemically from α-keto carboxylic acids (like phenylglyoxylic acid), followed by decarboxylation.[14]

Due to such important synthetic value, an alkene scope with phenyglyoxylic acid was investigated (Table 4.11).

Table 4.11: Alkene scope with phenylglyoxylic acid

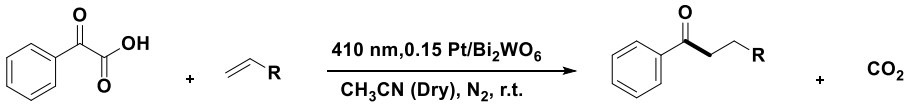

Entry	Alkene	Yield (%)	Conversion (%)	Selectivity (%)
1	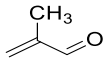	45	99	45
2	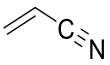	14	75	19
3	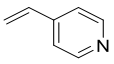	24	95	25
4		13	97	14
5	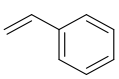	0	10	0

Reaction conditions: 0.15 Pt/Bi_2WO_6 (60 mg), phenylglyoxylic acid, (0.2 mmol) and alkene (0.6 mmol), reaction time (24 hours), 405-410 nm LED torch, N_2. Yield and conversion were calculated

by ^{1}H NMR using dimethyl terephthalate (DMT) as internal standard. Selectivity is ratio of yield to conversion.

Unlike electron-rich benzyl radicals formed from phenylacetic acids, the acyl radical generated from phenylglyoxylic acid is relatively electron-poor. It can therefore add to both electron-poor and electron-rich alkenes, significantly expanding the scope of the reaction. It can be seen that the best selectivity was obtained with methacrolein 45%. When electron-rich alkene (styrene) used, no Giese adduct was detected. Despite the low selectivity of this system, it is promising that this type of coupling can be achieved with platinized bismuth tungstate. For comparison with homogenous system, Melchiorre et al, utilised benzoyl chloride as acyl radical precursor for addition to olefins with different withdrawing groups including aldehydes, phosphonates, sulfones and ketones. They used xanthate catalyst activated by blue LEDs with presence of base. They obtained low to good yields (37 % - 84 %).[11]

To the best of our knowledge, there is no reported direct reaction between phenylglyoxylic acid and methacrolein, but there are only two reports on the same reaction of phenylglyoxylic acid with acrylonitrile and an alkene similar to methyl vinyl ketone (Table 4.11, entry 4), amyl vinyl ketone (Scheme 4.1). For the phenylglyoxylic acid and acrylonitrile coupling reaction, both studies used a homogenous system. The first report was by Wang et al., who obtained 63% of the coupled product.[15] They used an Ir-based catalyst in the presence of blue LEDs. Their system gave a good yield compared to our system; however, those high-cost transition metal catalysts, such as Ir, are toxic and cannot be recovered. The second study was published recently by Gao et al., where around 70% of the Giese adduct was obtained.[16] They used BuPPTNO (pyrimidopteridine N-oxide) as a photocatalyst in the presence of a base. The synthesis of BuPPTNO consists of many steps compared to the synthesis of Pt/Bi_2WO_6.

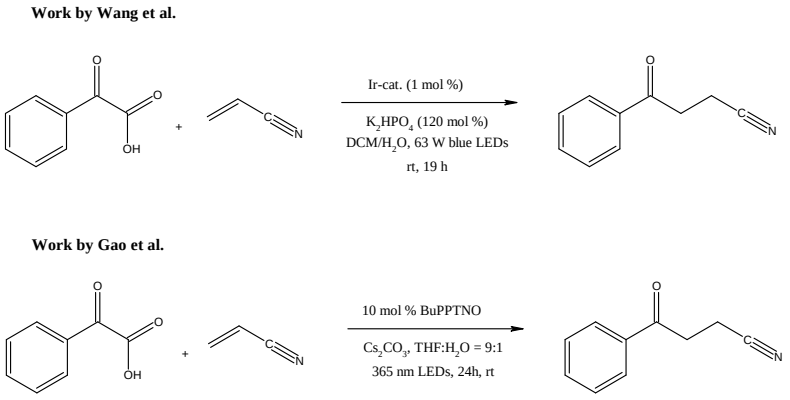

Scheme 4.1: Reaction scheme of phenylglyoxylic acid with acrylonitrile photocatalyzed by homogenous photocatalysts.

In this work, we were able to utilise a metal oxide semiconductor (Pt/Bi_2WO_6) as a heterogenous photocatalyst to carry out such transformations with a selectivity around 19% when acrylonitrile was used (Table 4.11 entry 2). The reactions with 4-vinylpridine (Table 4.11, entry 3) and vinyl methyl ketone (Table 4.11, entry 4) yielded 24 and 13%, respectively.

Apart from the electronic factors, the difference in alkenes trends could be due to a different mode of binding. The binding of phenylglyoxylic acid would be predicted to be stronger than that of phenylacetic acid due to the extra oxygen atom that could contribute to its binding to the surface (Figure 4.5) via different configuration.

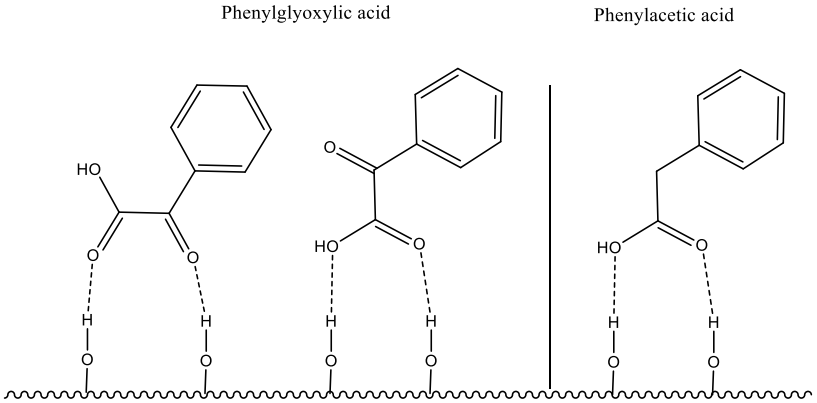

Figure 4.5: Comparison between phenylacetic acid and phenylglyoxylic acid possible binding modes to surface via H-bonding.

4.4. Conclusion and future work

It was concluded from this chapter that the presence of Pt is crucial to aid both catalytic activity and reaction selectivity when an optimum amount of Pt of ~0.15% is used. Having less or more Pt affects both conversion and selectivity. It was also found that light intensity had impact on the reaction where high intensity accelerated the rate suggesting that there is no saturation.

A range of substrates (both substituted alkenes and acids, including phenylglyoxalic) were used in this reaction, giving rise to a diverse range of products, but yields in many cases are moderate, which limits the application of this reaction without further optimisation.

The electronic properties of alkenes were not only the limiting factors in reaction selectivity, but other factors such as binding to surface might also play a crucial role. However, this needs further investigation.

In terms of the effect of crystallinity on selectivity and conversion, conversion depends on the rate of charge recombination. In amorphous materials, recombination is rapid due to defects. So, fewer holes are available for oxidation. In contracts, effective separation in bulk occurs due to structural regularity, resulting in less recombination. Selectivity, on the other hand, depends on the reactivity of different active sites in the catalyst. We hypothesise that in crystalline materials, there is a smaller number of sites (due to the low surface area), but these sites yield the desired products, while in amorphous materials, there is a higher proportion of sites which do not contribute to catalysis or result in overoxidation.

The future research aims to investigate other organic reactions such as hydroaminoalkylation, Menisci-type alkylation, trifluoromethylation, and cross-coupling reactions. The reaction can be carried out in a more controlled environment, such as by using a glove box.

References

(1) Mayer, J. M. PROTON-COUPLED ELECTRON TRANSFER: A Reaction Chemist's View. *Annu. Rev. Phys. Chem.* **2004**, *55* (Volume 55, 2004), 363–390. https://doi.org/10.1146/annurev.physchem.55.091602.094446.

(2) Cheng, N.; Stambula, S.; Wang, D.; Banis, M. N.; Liu, J.; Riese, A.; Xiao, B.; Li, R.; Sham, T.-K.; Liu, L.-M.; Botton, G. A.; Sun, X. Platinum Single-Atom and Cluster Catalysis of the Hydrogen Evolution Reaction. *Nat. Commun.* **2016**, *7* (1), 13638. https://doi.org/10.1038/ncomms13638.

(3) Miyake, Y.; Nakajima, K.; Nishibayashi, Y. Visible Light-Mediated Oxidative Decarboxylation of Arylacetic Acids into Benzyl Radicals: Addition to Electron-Deficient Alkenes by Using Photoredox Catalysts. *Chem. Commun.* **2013**, *49* (71), 7854–7856. https://doi.org/10.1039/C3CC44438D.

(4) Lund, T.; Christensen, P.; Wilbrandt, R. Direct Determination of Rate Constants for Coupling between Aromatic Radical Anions and Alkyl and Benzyl Radicals by Laser-Flash Photolysis. *Org. Biomol. Chem.* **2003**, *1* (6), 1020–1025. https://doi.org/10.1039/B209594G.

(5) Giese, B. Formation of CC Bonds by Addition of Free Radicals to Alkenes. *Angew. Chem. Int. Ed. Engl.* **1983**, *22* (10), 753–764. https://doi.org/10.1002/anie.198307531.

(6) Huang, B.; N. Hart, J. DFT Study of Various Tungstates for Photocatalytic Water Splitting. *Phys. Chem. Chem. Phys.* **2020**, *22* (3), 1727–1737. https://doi.org/10.1039/C9CP05944J.

(7) Chen, T.; Liu, L.; Hu, C.; Huang, H. Recent Advances on Bi2WO6-Based Photocatalysts for Environmental and Energy Applications. *Chin. J. Catal.* **2021**, *42* (9), 1413–1438. https://doi.org/10.1016/S1872-2067(20)63769-X.

(8) Bloh, J. Z. Intensification of Heterogeneous Photocatalytic Reactions Without Efficiency Losses: The Importance of Surface Catalysis. *Catal. Lett.* **2021**, *151* (11), 3105–3113. https://doi.org/10.1007/s10562-021-03573-0.

(9) Amano, F.; Yamakata, A.; Nogami, K.; Osawa, M.; Ohtani, B. Effect of Photoexcited Electron Dynamics on Photocatalytic Efficiency of Bismuth Tungstate. *J. Phys. Chem. C* **2011**, *115* (33), 16598–16605. https://doi.org/10.1021/jp2051257.

(10) Guo, T.; Zhang, L.; Fang, Y.; Jin, X.; Li, Y.; Li, R.; Li, X.; Cen, W.; Liu, X.; Tian, Z. Visible-Light-Promoted Decarboxylative Giese Reactions of α-Aryl Ethenylphosphonates and the Application in the Synthesis of Fosmidomycin Analogue. *Adv. Synth. Catal.* **2018**, *360* (7), 1352–1357. https://doi.org/10.1002/adsc.201701285.

(11) Beato, E. de P.; Mazzarella, D.; Balletti, M.; Melchiorre, P. Photochemical Generation of Acyl and Carbamoyl Radicals Using a Nucleophilic Organic Catalyst:

Applications and Mechanism Thereof. *Chem. Sci.* **2020**, *11* (24), 6312–6324. https://doi.org/10.1039/D0SC02313B.

(12) Raviola, C.; Protti, S.; Ravelli, D.; Fagnoni, M. Photogenerated Acyl/Alkoxycarbonyl/Carbamoyl Radicals for Sustainable Synthesis. *Green Chem.* **2019**, *21* (4), 748–764. https://doi.org/10.1039/C8GC03810D.

(13) Jiang, H.; Mao, G.; Wu, H.; An, Q.; Zuo, M.; Guo, W.; Xu, C.; Sun, Z.; Chu, W. Synthesis of Dibenzocycloketones by Acyl Radical Cyclization from Aromatic Carboxylic Acids Using Methylene Blue as a Photocatalyst. *Green Chem.* **2019**, *21* (19), 5368–5373. https://doi.org/10.1039/C9GC02380A.

(14) Banerjee, A.; Lei, Z.; Ngai, M.-Y. Acyl Radical Chemistry via Visible-Light Photoredox Catalysis. *Synthesis* **2019**, *51* (2), 303–333. https://doi.org/10.1055/s-0037-1610329.

(15) Wang, G.-Z.; Shang, R.; Cheng, W.-M.; Fu, Y. Decarboxylative 1,4-Addition of α-Oxocarboxylic Acids with Michael Acceptors Enabled by Photoredox Catalysis. *Org. Lett.* **2015**, *17* (19), 4830–4833. https://doi.org/10.1021/acs.orglett.5b02392.

(16) Gao, F.; Liao, Z.-Y.; Ye, Y.-H.; Yu, Q.-H.; Yang, C.; Luo, Q.-Y.; Du, F.; Pan, B.; Zhong, W.-W.; Liang, W. Photomediated Hydro(Deutero)Acylation of Olefins by Decarboxylative Addition of α-Oxocarboxylic Acids. *J. Org. Chem.* **2024**, *89* (4), 2741–2747. https://doi.org/10.1021/acs.joc.3c02838.

Chapter 5: Conclusion and future work

In this thesis, semiconductor nanoparticles were used as a visible light photocatalyst in a model Giese reaction. We were particularly interested in developing mechanistic understanding of this process, with the aim to expand applications of heterogeneous visible light photocatalysis to fine organic synthesis.

In chapter 2, bismuth tungstate nanoparticles were prepared by hydrothermal and solvothermal methods, employing both conventional and microwave-assisted heating approaches. The aim of this study was to develop a synthetic protocol to prepare these nanoparticles with high crystallinity and large surface area. Best crystallinity was observed in samples synthesised in water using either conventional or microwave heating. SEM analysis indicated that these samples exhibited a distinctive flower-like shape. Samples synthesised in ethylene glycol had greater surface area but showed tiny spheres and lower crystallinity. Post-hydrothermal treatment of these samples improved crystallinity, but surface area was reduced. Due to time constraints, alternative synthetic strategies, such as employing various surfactants, were not feasible. Future work could focus on increasing the surface area of Bi_2WO_6 without sacrificing its crystallinity, e.g., by testing different solvents and surfactants, especially biosurfactants such as glycolipids, lipopeptides, and lipids, to develop as green synthesis as possible. Microwave synthesis is advantageous due to its reduced energy and time requirements, yet its application is limited by scaling constraints. Consequently, using a large commercial microwave with large capacity would be advantageous.

The catalyst was modified by Pt nanoparticles through photoreduction of Pt (IV) with visible light photocatalyst. The utilisation of the photocatalysis for the deposition of metal particles shows great potential and can be employed across various photocatalysts, such as bismuth vanadate ($BiVO_4$). In future research, it would be interesting to explore the feasibility of replacing Pt with less expensive metal nanoparticles, such as nickel (Ni), as an alternative cocatalyst.

In chapter 3, the successful synthesis of Giese adducts was achieved by utilising visible-light-irradiated Bi_2WO_6 adorned with Pt co-catalyst nanoparticles for decarboxylation of phenylacetic acid, which resulted in the formation of benzyl radicals that underwent addition to methacrolein (Giese reaction). The Giese adduct yield was around 60–70%, with by-products identified as bibenzyl, benzyl alcohol, and benzaldehyde. The presence of Pt proved crucial for the photocatalytic reactivity, as no reaction occurred in its absence. Furthermore, loading of Pt was optimised (0.15 wt%) to achieve best reactivity and selectivity. Higher or lower Pt loading led to low reactivity and selectivity. The importance of Pt is probably not solely limited to facilitating charge separation; it could

be also crucial for catalysis as was concluded from time-resolved photoluminescent spectroscopy where there was no significant difference between unmodified and platinised catalyst. The role of oxygen vacancies and their relation to metal particles cannot be ignored in catalysis, but further investigation is needed. For instance, Bi_2WO_6 can be reduced in absence of Pt (to create oxygen vacancies) and used in the Giese reaction to judge its ability to induce this transformation.

By varying the amount of water in the photocatalytic Giese reaction mixture, we found that water is essential for catalytic activity and must be present in the optimal quantity. Excess water considerably decreased the reaction rate. Water can promote the creation of surface OH groups and the protonation of intermediate enolate. This will facilitate adsorption of starting materials and intermediates on the catalyst surface. Excess water might block active sites for catalysis. In order to confirm the source of protons in the product, efforts have been made to exchange labile protons by deuteration of acid and catalyst, but we found that complete exchange of surface protons with deuterons is challenging. This could be due to the presence of some surface sites that are resistant to exchange. The addition of D_2O led to complete D incorporation in the α-position to the carbonyl group of the product, confirming that the final product is formed by the protonation of the intermediate enolate or abstracting an H from Pt surface. The KIE study concluded that the rate-determining step (RDS) is not the breaking of O-H bonds or the formation of C-H bonds. It is likely that the reaction rate is determined by the rate the oxidation of carboxylic acid and the selectivity depends on the competition between oxidation of the surface-adsorbed benzyl radical and its addition to the alkene

Substrate binding is an essential and pivotal stage in the present mechanism. Using NMR titrations, we assessed the strength of binding of reactants and products to the catalyst in the presence of MeCN solvent. The results showed that carboxylic acid exhibits a higher binding affinity compared to alkene and Giese adduct. The strength of binding does not have a direct correlation with acid conversion. Binding is predominantly reversible, although the possibility of slower dissociation of the acid or a reaction intermediate from certain binding sites cannot be ruled out. This dissociation of surface-bound species can have an impact on the yield and selectivity of the resulting product. Neither the alkene nor the product exhibit strong binding to the surface, indicating that the dissociation of the product is unlikely to play a significant role or be a critical step in the overall reaction. Apart from the strength of binding, the NMR titration experiments made it possible to estimate the number of binding sites on the catalyst surface. The results are suggested that a loosely packed monolayer of the carboxylic acid is formed on the catalyst surface at saturation, with coverage ca. 0.38 molecules / nm^2.

The result from this work showed that amorphous catalysts with high surface area showed low activity and selectivity. The poor crystallinity could be the reason behind low activity. Regarding the impact of crystallinity on selectivity and conversion, conversion is contingent upon the rate of charge recombination. In materials lacking a definite crystalline structure, the process of recombination could occur quickly as a result of imperfections or irregularities. Therefore, fewer charge carriers will migrate to the catalyst surface leading to low conversion. Structural regularity (crystallinity) in contrast would lead to successful charge carrier separation in the bulk, reducing recombination, and migration of charge carriers to the surface (high conversion). The impact of crystallinity on selectivity is more difficult to interpret. We propose the presence of different active sites on the catalyst surface which show different activity and selectivity. Crystalline materials have a lower surface area, resulting in a smaller number of active sites for catalysis which catalyse the target transformation. On the other hand, amorphous materials have a higher surface area, leading to a larger number of active sites. However, some of these sites might be inactive or might promote side reactions such as overoxidation.

Mechanistic understanding obtained in this work can be applicable to different metal oxide semiconductors. Future research might explore and evaluate the potential for tuning catalyst morphology and surface chemistry to improve substrate binding and catalysis. For instance, catalysts with different amount of surface water can be compared to check if there is a difference in binding constant and the number of binding sites. This comparison can help establish a correlation between the role of surface OH and water in facilitating or impeding substrate binding and catalysis. Furthermore, the use of various acids with distinct functional groups and different physical size can be employed to investigate the impacts of functional groups and steric factors.

In chapter 4, it was confirmed that the photocatalytic reactivity was influenced by the intensity of light, with higher intensity leading to a faster reaction rate, suggesting that the photocatalyst is not saturated under reaction conditions. In addition, a variety of substrates, such as substituted alkenes and acids, were employed in this reaction, resulting in a wide array of products. However, the yields in several instances are moderate, which restricts the practicality of this reaction. Furthermore, the electronic effect of alkenes was not the only factor determining reaction selectivity, as the selectivity trend was not comparable to those in homogenous systems, suggesting the incorporation of other factors, such as surface reactions. Regrettably, the catalyst recycling experiment was not examined as a result of time limitations.

For future work, the reaction can be conducted in a highly controlled atmosphere, such as using a glove box to control water and oxygen concentration. The amount of water needs further optimisation to obtain clear results and draw a proper conclusion. The future research will also focus on exploring other organic redox reactions, including hydroaminoalkylation, Menisci-type alkylation, trifluoromethylation, and other cross-coupling reactions.

Another avenue to explore in future work could be aimed at improving photocatalytic reactions by using different reactor types, such as photocatalytic flow reactors, to ensure efficient mixing and separation, improve yield, and reduce reaction time. The current reaction reactor design can be further improved to ensure efficient light penetration into the mixture, either by using a more intense LED torch (heat generated can be eliminated by circulating water around the reactor) or by shortening the length of the glass tube to reduce the light path and increase focus. Future work will also focus on scaling up reactions and using less catalyst to meet sustainable goals.

Chapter 6: Experimental

6.1 Instrumentations for nanoparticles characterisation

6.1.1 Powder X-ray diffraction

Powder X-ray diffractograms (p-XRD) were acquired utilising an Aris diffractometer equipped with a Lynxeye detector and Cu K-alpha source (= 1.5406 Å) as X-ray source. The samples ≈ (100 mg) were placed on an aluminium disc and measurements were taken between 5 and 90°. Peaks full width half maximum (FWHM) and average crystallite size were calculated using Gaussian function and Scherrer equation, respectively.

6.1.2 Scanning electron microscopy

A JEOL 7800 SEM Field Emission Scanning Electron Microscope was used to record electron micrographs. A carbon conductive tape was used to establish electrical connections between sample surfaces and aluminium stubs. A small amount of sample was put on the carbon conductive tape fixed to the aluminium stubs. Then, the aluminium stub was transferred into specimen chamber and left under vacuum for 15 minutes or until vacuum reached 10^{-4} mbar. At working distance of 10 mm, images were taken with an acceleration voltage of 5 kV. Lower electron detector (LED) was utilised to detect backscattered electrons.

Two Oxford Instruments UltiMax 170 Silicon Drift Detector Energy Dispersive X-Ray (EDS) Spectrometers were utilised to acquire EDS measurements. The incident beam of electrons was maintained at 15 keV.

6.1.3 Transmission electron microscopy

TEM images and electron diffraction patterns were carried out by Mr. Connor Murrill (University of York) using a 200 kV-accelerating-voltage JEOL 2011 transmission electron microscope. Gatan Digital Micrograph software was used to extract CCD images. Solid samples for TEM imaging were dispersed in methanol and sonicated for 15 minutes prior to analysis. On a 3 mm holey carbon-coated copper grids, one drop of the dispersion was deposited and permitted to dry in the air.

6.1.4 BET surface area measurement

Using a Micromeritics Tristar 3000 Porosimeter, the surface area measurement and the pore size distribution were determined by BET (Brunauer-Emmett-Teller) and BJH (Barret-Joyner-Hslenda) technique, respectively. Prior to analysis, 150 mg of catalyst powder was placed in quartz tubes activated at 100 °C for 12 hours under vacuum to remove residual water. The tubes were then allowed to cool down to room temperature

and backfilled with nitrogen. The tubes were then connected to the Tristar 3000 porosimeter machine to start the analysis.

6.1.5 Thermo-Gravimetric analysis

TGA analysis was carried out by Mrs Suranjana Bose using NETZSCH STA 449F5. The solid catalyst was placed in alumina crucible and weighed accurately (20 mg). Then, the crucible was inserted in TGA instrument and heated to 650 ºC with heat ramp 10 ºC / min^{-1} under oxidative atmosphere. Then, the mass loss was recorded.

6.1.6 Infra-red spectroscopy

The PerkinElmer Fourier Transform IR spectroscopy (FT-IR) Spectrum Two spectrometer was used to acquire infrared spectra, with a resolution of 1 cm^{-1} and range of 4000-400 cm^{-1} over eight scans. A solid sample was placed on a diamond-attenuated total reflection (ATR) crystal, and pressure was applied to ensure good contact between the crystal and the sample. The data was processed with Spectrum software.

6.1.7 Inductive coupled plasma – Optical emission spectroscopy

ICP-OES measurements were conducted by Mr. Niall Donaldson (University of York) using an Agilent 5100 spectrometer, and analysis was performed in ICP Expert version 7.6.2.12331. Measurements for Bi (223.061 nm), Pt (214.424 nm), and W (248.923 nm), were made with comparison to certified reference material (SUPELCO® Periodic table mix 1 for ICP, SUPELCO® Periodic table mix 2 for ICP). Samples were analysed with internal standard Y (371.029 nm). Suspensions of nanoparticles were prepared in 5% HNO_3 and analysed without further processing.

6.1.8 CHN analysis

Using an Exeter CE-440 elemental analyser, Dr. Scott Hicks (University of York) performed elemental analysis on solid sample using around 100 mg of the sample. The elemental composition of the combustion products was determined by heating samples to 1500 °C under Helium flow.

6.1.9 Diffuse reflectance UV-Vis spectroscopy

An Ocean Optics HR2000+ spectrometer coupled with a Mikropak DH-2000-BAL UV-VIS-NIR light source was used to acquire diffuse reflectance spectra of catalyst powders. Recorded spectra were averaged over 10 scans with a 5 second integration time and a boxcar width of 20. A flat surface of pressed $BaSO_4$ powder was used as a reference spectrum in the dark and under illumination. To obtain a flat surface for measurement, catalyst powders were compressed between two glass microscope slides. Prior to

recording spectra, the upper slide was removed, and the optical fibre probe was placed over the powder.

For bandgap energy (Eg) calculation, the Kubelka-Munk formalism (Equation 6.1) allows for the collection and reporting of the diffuse reflectance spectrum in place of absorbance.

Equation 6.1 $F(R) = \frac{(1-R)^2}{2R}$

where R represents the sample's collected percent reflectance (%R) as a function of wavelength, and F(R) is the Kubelka-Munk value (unitless). According to the equation (Equation 6.2), F(R) is directly proportional to the absorption coefficient.

Equation 6.2 $F(R) = \frac{k}{s}$

where *k* stands for the absorption coefficient, *s* is the scattering coefficient. The Tauc plot can be built for powder samples, enabling bandgap energy (Eg) to be measured (Figure 6.1).

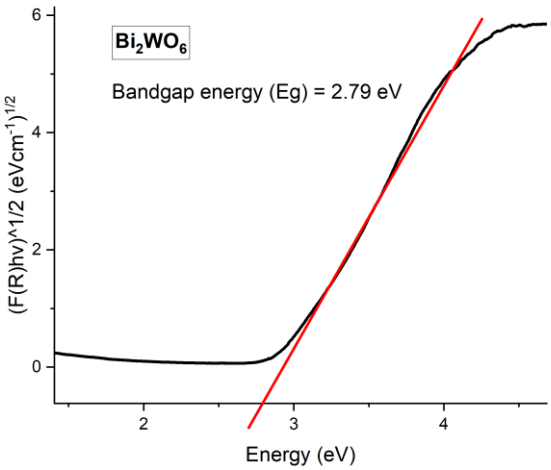

Figure 6.1: Tauc plot showing Bi_2WO_6 bandgap

6.3 Chapter 2 experiments

6.3.1 Materials and reagents

Bismuth nitrate pentahydrate (98%), sodium tungstate dihydrate (99%), chloroplatinic acid hydrate (98%), and ethylene glycol (99%) were purchased from Sigma Aldrich. Ethanol (99%) was purchased form Fisher Scientific and used as received. Millipore water was obtained from Millipore Milli-Q system equipped with QPAK2 column.

6.3.2 Bismuth tungstate powder synthesis

6.2.2.1 Hydrothermal synthesis

Bismuth nitrate pentahydrate (1 g, 2.06 mmol) was dissolved in Millipore water (60 mL), sonicated, and stirred for 2 hrs until white homogenous slurry was formed. In a different beaker, sodium tungsten dihydrate (0.340 g, 1.03 mmol) was dissolved in Millipore water (20 mL) then added dropwise into the bismuth nitrate slurry. The mixture was stirred for 2 h. Then, the final solution was transferred into a 125 mL Teflon tube which was placed in a Parr® stainless steel hydrothermal reactor with max temperature ≈ 250 ºC and max pressure ≈ 130 bar. This autoclave was put in an electrical furnace with heating rate of 5 ℃ min^{-1} to reach 180 ℃ and held at this temperature for 12 hours. After cooling, the obtained white solid was transferred into a centrifuge tube and centrifuged out of suspension at 4400 rpm for 30 min using an Eppendorf Centrifuge 5702. The resulting pale-yellow coloured powder was washed with deionised water and left to dry overnight at 80 °C. Yield was 0.695 g, (97%).

6.2.2.2 Microwave synthesis of Bi_2WO_6

Microwave synthesis of catalyst powders was carried out using CEM Discover Microwave SP equipped with magnetron to induce sample self-heating and connected with local monitor to set stirring, synthesis time, temperature (ºC), pressure (PSI) and input power (W).

Bismuth nitrate pentahydrate (1 g, 2.06 mmol) was dissolved in ethylene glycol (20 mL) and stirred at room temperature until complete dissolution. Then, sodium tungsten dihydrate (0.340 g, 1.03 mmol) was added as a solid. The mixture was stirred until white slurry was formed. The mixture was then transferred into a 50 mL microwave tube and sealed with Teflon cap and heated to 170 ºC for 1 hr. The reaction mixture was left to cool to room temperature and the obtained white solid was transferred into a centrifuge tube and centrifuged out of suspension at 4400 rpm for 60 min using an Eppendorf Centrifuge 5702. The resulting pale-yellow coloured powder was washed with deionised water and ethanol several times and left to dry overnight at 80 °C. Yield was 0.682 g, (95 %)

6.3.3 Preparation of bismuth tungstate decorated with platinum nanoparticles (0.15 Pt/Bi_2WO_6)

Chloroplatinic acid (40 mg, 0.077 mmol) was dissolved in distilled water (10 mL) to make chloroplatinic solution (4 mg mL^{-1}). Bismuth tungstate powder (1 g) was transferred into a dry Schlenk vessel and evacuated for 30 min using Schlenk line. After that, the tube

was filled with N_2 and evacuated again 3 times. Then, ethanol: water (1:4 v: v) 20 mL was added to Schlenk tube followed by addition of chloroplatinic acid solution (1 mL). After that, the Schlenk tube was sealed, and the solution was evacuated to remove excess air and purged with N_2. The mixture then was stirred for 10 min and irradiated with a 30 W blue LED array (λ = 420 - 550 nm) for 20 hours. After irradiation, the mixture was transferred into a centrifuge tube and span for 30 minutes at 4400 rpm to separate the solid catalyst. The supernatant was decanted, and the obtained grey-coloured solid was washed (three times) with distilled water and ethanol alternately and left overnight at 80 °C for drying. Yield was 0.98 g, (98 %).

6.4 Chapter 3 experiments

6.4.1 Photochemical reactor for Giese reaction

The photochemical kit was designed by Prof Richard Douthwaite (Figure 6.2.) Reaction vessel was equipped with Young's tap for Schlenk line connection and vessel mouth sealed with LEDs torch using Teflon ring fitted with quartz window. The LEDs constant current is 350 mA and their wavelengths range between 405-410 nm with intensity powers = 75 mW/cm^2. The reaction vessel is equipped with magnetic stir bar.

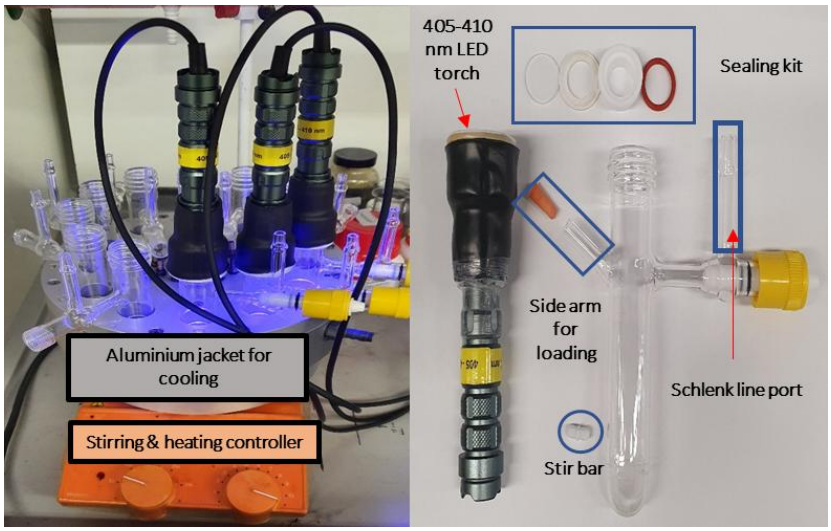

Figure 6.2: A photo of the carousel reactor (left) and a photo of the reaction vessel (right).

6.4.2 Instrumentations for Giese products characterization and mechanistic study.

6.4.2.1 Nuclear magnetic resonance (NMR) Spectroscopy

On a JEOL ECX400 (400 MHz) spectrometer, solution ^{1}H NMR spectra were acquired by dissolving samples (crude or worked up) in $CDCl_3$ solvent. For quantitative ^{1}H NMR, 100 µL of crude reaction mixture was transferred into NMR tube and a spiked with 100 uL of an internal standard solution (dimethyl terephthalate, DMT, 5 mg in 10 mL $CDCl_3$). Then, the NMR was topped off with $CDCl_3$ to reach 700 µL and submitted to NMR. All peaks were referenced to the $CHCl_3$ residual solvent peak. ^{2}H NMR spectra was recorded on Bruker AVIIIHD 500 deuterium at 298 K by Heather Fish using 0.7 mL of protonated crude reaction with 100 µL $CDCl_3$.

6.4.2.2 Gas Chromatography-Mass Spectrometry

GC-MS analysis was conducted by Mr. Karl Heaton (University of York) on a JEOL AccuTOF GCx-plus mass spectrometer coupled to an Agilent 7890B GC system containing a Phenomenex ZB-5MS plus column (30 m $_x$ 0.25 mm $_x$ 0.25 m). Electron ionization (EI) was used as ionization source. Helium was used as carrier gas.

6.4.2.3 EPR measurement.

Continuous wave (CW) X-band solution EPR spectra were recorded by Professor Victor Chechik on a Bruker micro EMX spectrometer operating at ca. 9.4 GHz, 0.4 G modulation amplitude modulation amplitude, microwave power of 5 mW at 298.15 K and 40 millisecond constant time and 60 millisecond conversion time.

6.4.2.4 Steady-state photoluminescence spectroscopy

Spectra of steady-state luminescence were acquired using a Hitachi F-4500 spectrometer, employing solution and solid cell receptacles. Finely ground solid samples (100 mg) were positioned in a quartz cell at a 90° angle to the incident light and detector. The solution sample was made of 1 mg of solid powder dispersed in 1 mL dry acetonitrile to mimic the actual reaction condition. The excitation wavelength was λ = 300 nm.

6.4.2.5 Time-resolved photoluminescence spectroscopy

A time resolve photoluminescence analysis was conducted using a FLS 980 spectrometer from Edinburgh Photonics. A 5 mg of solid catalyst was dispersed in 5 mL dry acetonitrile to obtain a suspension. 1 mL of suspension was placed in quartz cuvette and was illuminated using a picosecond pulse light emitting diode from Edinburgh Instruments, with excitation wavelength of λ = 315 nm.

6.4.3 Materials and reagents for Giese reaction and mechanistic study

Phenylacetic acid (Sigma Aldrich, 99%), N-tert-butyl-a-phenylnitrone (PBN) and 5,5-dimethyl-1-pyrroline N-oxide (DMPO), were used as received form Victor Chechik's lab. Methacrolein (95%), chloroform-d (99.8 atom % D), deuterium oxide (99.8 atom % D) were purchased from Sigma Aldrich. Dry acetonitrile was obtained from Puresolve PS-400-3-D solvent purification system and kept under N_2 in presence of molecular sieves. Deuterated acetonitrile (99.8 atom % D) was purchased form ACROS organics. Dry acetonitrile-d_3 was purified by vacuum distillation.

6.4.4 Procedure for Photo-Giese reaction

Platinized bismuth tungstate (60 mg) was transferred into Schlenk tube along with a magnetic stirrer. The tube was then fitted with a 405-410 nm LED torch and connected to Schlenk line and evacuated and backfilled with N_2 several times and left under N_2 flow. After that, 2 mL of stock solution of phenylacetic acid (100 mM) and methacrolein (300 mM) in acetonitrile was transferred into the same Schlenk tube. The reaction mixture was then stirred and illuminated for 24 hours at room temperature, standard conditions. At the end of the reaction, the resulted crude reaction mixture was transferred into centrifuge tube and span at 4000 rpm for 30 minutes to separate the catalyst from liquid reaction mixture.

6.4.5 Radical detection experiment of Giese reaction

For radical detection in actual Giese reaction: spin trap, either N-tert-butyl-α-phenylnitrone (PBN) (35 mg, 0.2mmol), or 5,5-dimethyl-1-pyrroline N-oxide (DMPO), (22.6 mg, 0.2mmol), was added in a Schlenk tube along with platinised catalyst (60 mg) and evacuated and backfilled with N_2. After adding the reagents (2 mL acetonitrile solution of phenylacetic acid (0.2 mmol) and methacrolein (0.6 mmol)), the reaction mixture was stirred and irradiated with 410 nm LED torch for 10 minutes.

For radical detection with phenylacetic acid only (photo Kolbe), the above procedure was performed expect no methacrolein was added. The control experiment with solvent only (acetonitrile) was also carried out.

For radical detection, a small aliquot (100 uL) of each reaction was transferred into EPR tube and submitted for EPR measurement.

6.4.6 Deuterium exchange experiment

6.4.6.1 Phenylacetic acid deuteration

Phenylacetic acid (1 g) was refluxed with D_2O (50 mL) overnight under N_2. Then, the reaction was cooled to room temperature and the volume was reduced using rotary evaporator. The resulting white solid was subjected for further drying under vacuum (10 $^{-1}$ mbar) at 60 ºC for 2 h. The final solid was kept under N_2 and transferred into dry box.

For quantification of D % in deuterated acid, a small amount of deuterated acid was dissolved in $CDCl_3$, that was dried over $MgSO_4$, and analysed by ^{1}H NMR. The degree of D incorporation was 96 % as determined by integration the signal of OH protons relative to internal standard.

6.4.6.2 Platinised Bi_2WO_6 deuteration

Platinized catalyst (300 mg) was transferred into a round bottom flask, and 50 mL of D_2O was added. The catalyst suspension was stirred and refluxed overnight under N_2. Then, the reaction was cooled to room temperature. The RBF was left until the powder had settled. The clear supernatant was syringed out, and the wet powder was dried using a Schlenk line at 80 °C for 2 h. The obtained dry powder was then transferred into a glove box.

6.4.6.3 Photo-Giese reaction with deuterated conditions

The procedure of photo-Giese reaction with deuterated acid and catalyst (Section 6.3.3) was used with the following modifications. In the first experiment, deuterated phenylacetic acid (PAAD) was used instead of protonated phenylacetic acid (PAAH). In the second experiment, both deuterated phenylacetic and deuterated catalysts were used. In the third experiment, both deuterated phenylacetic acid, deuterated catalyst, and dry deuterated acetonitrile instead of dry protonated acetonitrile were used. In the fourth experiment, the same reaction conditions were used as in the third experiment with the addition of 100 uL of D_2O.

6.4.7 Adsorption experiments of substrate onto catalyst nanoparticles

6.4.7.1 Adsorption experiments of phenylacetic acid and methacrolein onto Bi_2WO_6

Bismuth tungstate nanoparticles (30, 60, 125, 250, 375, and 500 mg) were transferred into six (2 mL) Eppendorf tubes, and each tube was spiked with 1 mL of stock solution containing phenylacetic acid (18 mM) and methacrolein (17.6 mM). The reaction mixture was shaken using a vortex mixer for 10 minutes. Then, each tube was centrifuged at

13000 rpm for 10 minutes for nanoparticle separation. After that, an aliquot of supernatant (600 µL) was transferred into an NMR tube and spiked with 100 uL of dimethyl terephthalate (8 mM) as an internal standard.

6.4.7.2 Adsorption experiments of phenylacetic acid and other acids

Bismuth tungstate nanoparticles (125 mg) were transferred into a 2 mL Eppendorf tube and mixed with 1 mL of phenylacetic acid solution (0.5 mM). The tube was shaken after each addition using a vortex mixer to ensure mixture homogeneity. Then the mixture was centrifuged at 13000 rpm for 10 minutes to separate solid nanoparticles. After that, an aliquot of supernatant (600 µL) was transferred into an NMR tube and spiked with 100 uL of dimethyl terephthalate (4 mM) as an internal standard. Then the NMR spectrum was acquired with 64 scans to enhance the signal-to-noise ratio. These steps were repeated several times, starting with adding a new aliquot of acid solution (0.7 mL) to the remaining acid solution (0.4 mL) with a catalyst. The evolution of CH_2 protons in phenylacetic acid was monitored and used to calculate the corresponding concentration. The same procedure was performed for the other acids, 4-methoxyphenylacetic acid and 4-chloropehylacetic acid.

6.5 Chapter 4 experiments

6.5.1 Materials and reagents

Phenylacetic acid (Sigma Aldrich, 99 %), 4-methoxyphenylacetic acid (Sigma Aldrich, 99 %), 4-chlorophenylacetic acid (Tokyo Chemical Industry, >97 %), methyl methacrylate (Sigma Aldrich, 90 %), acrolein (contains hydroquinone as stabilizer, 90%), acrylonitrile (99 %) diethyl vinyl phosphonate (fluorochem), n-decane (Alfa Aesar 99 %), maleimide (Sigma Aldrich, 99 %), maleic anhydride (Sigma Aldrich, 99 %) and dimethyl terephthalate (Sigma Aldrich, 99 %), styrene (Sigma Aldrich, stabilised) and methylene cyclohexane (Acros Organics, 98 %) were used as received. Methacrolein (95 % stabilised) and Chloroform-d (99.8 atom % D) were purchased from Sigma Aldrich. Acrylamide (99 %), alpha-methylene-gamma-butyrolactone (95 % stabilised) and acetonitrile-d3 (99.8 atom %D) were purchased form Across Organics. Dry acetonitrile was obtained from PureSolve PS-400-3-D solvent purification system and kept under N_2 in presence of 3 Å molecular sieves. Water content was measured by Karl Fischer coulometric titrator C20S.

6.5.2 General procedure for Photo-Giese reaction

Platinized bismuth tungstate (60 mg) was transferred into Schlenk tube along with a magnetic stirrer. The tube was then fitted with a 405-410 nm LED torch and connected to Schlenk line and evacuated and backfilled with N_2 several times and left under N_2 flow.

After that, 2 mL of reactants mixture containing acid (100 mM) and alkene (300 mM) was transferred into the Schlenk tube under N_2 flow. The reaction mixture was then stirred and illuminated for 24 hours at room temperature, standard conditions. At the end of the reaction, the resulted crude reaction mixture was transferred into centrifuge tube and span at 4000 rpm for 30 minutes to separate the catalyst from liquid reaction mixture. For ^{1}H NMR analysis, 0.1 mL of the crude mixture was transferred into NMR tube and spiked with 0.1 mL of dimethyl terephthalate (DMT) dissolved in $CDCl_3$ or CD_3CN.

To calculate Yield, following equation 6.3 was used;

Equation 6.3

$$Yield\ (\%) = \frac{mmol\ of\ Product\ in\ crude\ mixture}{mmol\ of\ Starting\ material\ (before\ reaction)} * 100$$

Where;

$$mmol\ of\ product\ in\ crude\ mixture = \frac{\left(\frac{integral}{\#\ protons}\right)Product}{\left(\frac{integral}{\#\ protons}\right)Int.\ Stand.} * mmol\ of\ int.stand.$$

And;

$$mmol\ of\ starting\ material\ (SM) in\ crude\ mixture = \frac{\left(\frac{integral}{\#\ protons}\right)SM}{\left(\frac{integral}{\#\ protons}\right)Int.Stand} *$$

$$mmol\ of\ int.stand.$$

To calculate conversion, equation 6.4 can be used.

Equation 6.4

$$Conversion\ (\%) = \frac{mmol\ of\ SM\ (before\ Rx)\ - mmol\ of\ SM\ in\ crude\ mix\ (after\ Rx)}{mmol\ of\ SM\ (before\ \ Rx)} * 100$$

Then selectivity can be calculated using following equation 6.5

Equation 6.5

$$Selectivity\ (\%) = \frac{Yield\ (\%)}{Conversion\ (\%)}$$

6.5.3 Experiment to check light intensity effect

The normal Giese reaction between phenylacetic acid and methacrolein was carried out with one torch and multiple torches, as shown in Figure 6.3. This reaction was run for 15 hours, but the photo was taken 2 hours after the reaction started by temporarily switching off the light.

Figure 6.3: A photo shows two experimental setups of photochemical Giese reaction using one torch and four torches.

List of abbreviations

(MOSC) metal oxide-based semiconductors

(LED) light diodes emission

(HOMO) higher occupied molecular orbital

(LUMO) lower unoccupied molecular orbital

(Eg) bandgap energy

(VB) valence band

(CB) conduction band

(ROS) reactive oxygen species

(TEMPO) 2,2,6,6-tetramethylpiperidine 1-oxyl

(LSPR) Localised surface plasmon resonance

(OVs) Oxygen vacancies

(MNPs) metal nanoparticles

(MB) methylene blue

(SEM) scanning electron microscopy

(pXRD) powder X-ray diffraction

(DRS) diffuse reflectance UV spectroscopy

(PL) Photoluminescent spectroscopy

(EPR) electron paramagnetic resonance

(RhB) Rhodamine B

(SA) surface area

(EG) ethylene glycol

(CH) conventional heating

(MW) microwave heating

(FWHM) full width half maxima

Appendices

A) List of tables

Table 1: The effect of changing atmosphere on yield, conversion and selectivity of Giese reaction.

Atmosphere	Yield %	Conversion %	Conversion %
N_2	49	99	50
Ar	51	99	51

Conditions: oven dried 0.15-Pt/Bi_2WO_6 (60 mg), 0.1 mmol PAA: 0.3 mmol MAC, 2 mL dry-MeCN, 24 hrs.

Table 2: The effect of using UV irradiation for nanoparticles surface cleaning on yield, conversion and selectivity of Giese reaction.

Catalyst condition	Yield %	Conversion %	Selectivity %
A	49	88	56
B	45	75	60

Conditions: Before A and after B treating with UV for 20 min. (0.2 mmol) phenylacetic acid, PAA and (0.6 mmol) methacrolein, MAC, reaction time (24 hours), 405-410 nm torch, 0.15Pt/Bi2WO6 (60 mg). and dry MeCN (2mL).

Table 3: Phenylacetic acid adsorption with Bi_2WO_6

Experiment	NMR integration of acid peak	Acid (mmol)	Acid (mg)	Acid loss (mg)	Acid left %
Acid only (no catalyst)	1.99	7.8×10^{-3}	1.07	0	100 %
Acid + 30 mg BT28 (0.043 mmol)	1.83	7.2×10^{-3}	0.99	0.083	92.26 %
Acid + 60 mg BT28 (0.086 mmol)	1.74	7×10^{-3}	0.94	0.127	88.17 %
Acid + 125 mg BT28 (0.18 mmol)	1.52	6.1×10^{-3}	0.83	0.234	78.15 %

Acid + 250 mg BT28 (0.358 mmol)	1.25	5.0×10^{-3}	0.68	0.390	63.66 %
Acid + 375 mg BT28 (0.537 mmol)	1.06	4.2×10^{-3}	0.57	0.495	53.90 %
Acid + 500 mg BT28 (0.716 mmol)	0.87	3.5×10^{-3}	0.48	0.592	44.88 %

Acid = 16 mM, 1 mL acid soln. is added to different tubes containing different catalyst loadings. 0.5 mL acid aliquot + 0.2 mL internal standard into NMR tube.

Table 4: Calculation of number of binding sites (BS) (mmol) and binding constant (K) (M-1) of phenylacetic acid (PAAH) with Bi_2WO_6 nanoparticles.

Total [A] in the system before adsorption (mol/L)	**[A] in the system after adsorption (mol/L)**	**Volume of Eppendorf, mL**	**Number of binding sites (BS) (mmol)**	**[A] calculated**
3.402×10^{-4}	2.437×10^{-5}	1.004	1.60×10^{-3}	2.09×10^{-5}
6.563×10^{-4}	6.156×10^{-5}	1.100	**Binding constant K (M^{-1})**	5.83×10^{-5}
8.991×10^{-4}	1.223×10^{-4}	1.199	1.20×10^{4}	1.18×10^{-4}
1.075×10^{-3}	1.983×10^{-4}	1.292		2.01×10^{-4}
1.198×10^{-3}	2.909×10^{-4}	1.386		2.97×10^{-4}
1.263×10^{-3}	3.579×10^{-4}	1.476		3.77×10^{-4}
1.296×10^{-3}	3.579×10^{-4}	1.567		4.38×10^{-4}
1.301×10^{-3}	4.821×10^{-4}	1.649		4.75×10^{-4}

Bi_2WO_6 (125 mg), phenylacetic acid (0.5 mM). CD_3CN (10 mL) as solvent.

Table 5: Calculation of number of binding sites (BS) (mmol) and binding constant (K) (M^{-1}) of 4-methoxyphenylacetic acid (4-MeOPAAH) with Bi_2WO_6 nanoparticles.

Total [A] in the system before adsorption (mol/L)	**[A] in the system after**	**Volume of Eppendorf, mL**	**Number of binding sites (BS) (mmol)**	**[A] calculate d**

	adsorption (mol/L)			
3.148×10^{-4}	1.285×10^{-5}	1.004	2.02×10^{-3}	0
6.133×10^{-4}	3.989×10^{-5}	1.100	**Binding constant K (M^{-1})**	4.55×10^{-5}
8.568×10^{-4}	8.292×10^{-5}	1.199	9.85×10^{4}	8.57×10^{-5}
1.035×10^{-3}	1.459×10^{-4}	1.292		1.37×10^{-4}
1.161×10^{-3}	2.058×10^{-4}	1.386		1.98×10^{-4}
1.247×10^{-3}	2.681×10^{-4}	1.476		2.62×10^{-4}
1.300×10^{-3}	3.208×10^{-4}	1.567		3.20×10^{-4}
1.326×10^{-3}	3.546×10^{-4}	1.649		3.67×10^{-4}

Bi_2WO_6 (125 mg), 4-methoxyphenylacetic acid (0.5 mM). CD_3CN (10 mL) as solvent.

Table 6: Calculation of number of binding sites (BS) (mmol) and binding constant (K) (M-1) of 4-chlorophenylacetic acid with Bi_2WO_6 nanoparticles.

Total [A] in the system before adsorption (mol/L)	[A] in the system after adsorption (mol/L)	Volume of Eppendorf, mL	Number of binding sites (BS) (mmol)	[A] calculated
3.305×10^{-4}	3.319×10^{-5}	1.004	1.44×10^{-3}	3.81×10^{-5}
6.260×10^{-4}	1.046×10^{-4}	1.100	**Binding constant K (M^{-1})**	9.99×10^{-5}
8.313×10^{-4}	1.834×10^{-4}	1.199	6.75×10^{3}	1.78×10^{-4}
9.717×10^{-4}	2.464×10^{-4}	1.292		2.62×10^{-4}
1.067×10^{-3}	3.400×10^{-4}	1.386		3.43×10^{-4}
1.114×10^{-3}	4.255×10^{-4}	1.476		4.03×10^{-4}
1.122×10^{-3}	4.483×10^{-4}	1.567		4.38×10^{-4}
1.123×10^{-3}	4.400×10^{-4}	1.649		4.63×10^{-4}

Bi_2WO_6 (125 mg), 4-chlorophenylacetic acid (0.5 mM). CD_3CN (10 mL) as solvent.

Derived equations for number of binding sites and binding constants

$$S + L = SL$$

$$K_a = \frac{[SL]}{[S][L]} = \frac{\theta}{(1-\theta)[L]}$$

Acid or ligand (A) or (L) + catalyst sites (S) = Catalyst + acid or ligand (SA) or (SL)

$$K = \frac{(V/N\ ([A0]\ -\ [A])])}{\left(1\ -\frac{V}{N}([A0]-\ [A])\right) * [A]}$$

Let N/V = Z

$$K = \frac{Z\ ([A0]\ -\ [A])}{1-\ Z\ ([A0]-\ [A]) *\ [A]}$$

$$K = \frac{Z\ [A0]\ -\ Z[A]}{[A] - Z\ [A0][A] + Z[A]\text{^}2}$$

$KA - ZKAA_0 + ZKA^2 = ZA_0 - ZA$

$ZKA^2 + A\ (K - ZKA_0 + Z) - ZA_0 = 0$

$$[A] = \frac{ZK[A0] - Z - K + \sqrt{((ZK[A0] - Z - K)2\ +\ 4Z\text{^}2K[A0])}}{2Zk}$$

$$[A] = \frac{V/N * K[A0] - V/N * -K + \sqrt{(((V/N * K[A0] - V/N * -K)2 + 4(V/N)2K[A0]))}}{2 * V/N * K}$$

Solver function was used to calculate binding constant (K) and number of binding sites (Z)

B) List of figures

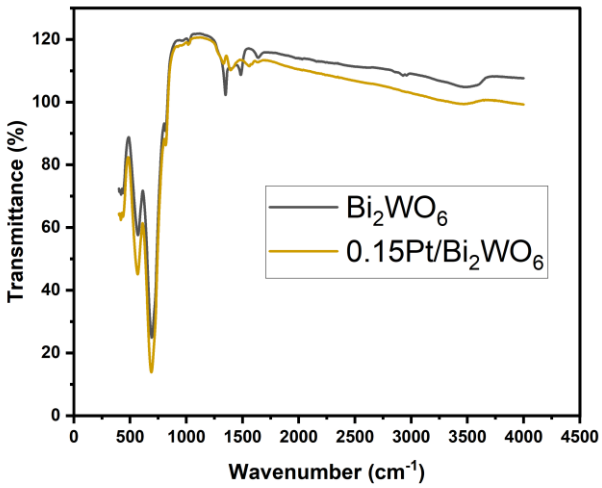

Figure 1: IR spectrum of Bi_2WO_6 and 0.15Pt/Bi_2WO_6

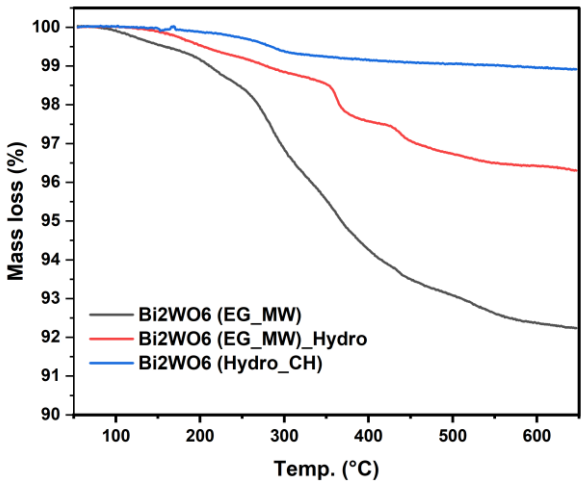

Figure 2: TGA of Bi_2WO_6 samples synthesised with different conditions.

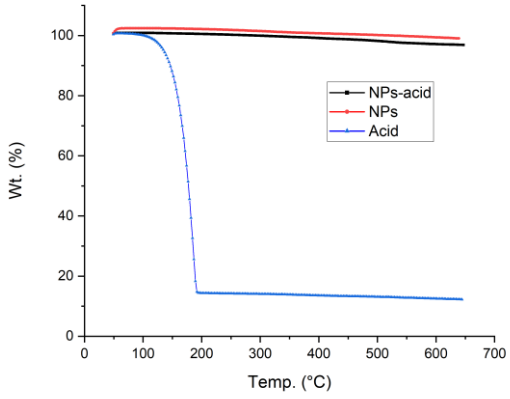

Figure 3: TGA analysis of acid, NPs-acid and NPs only. No detection for organic material on NPs.

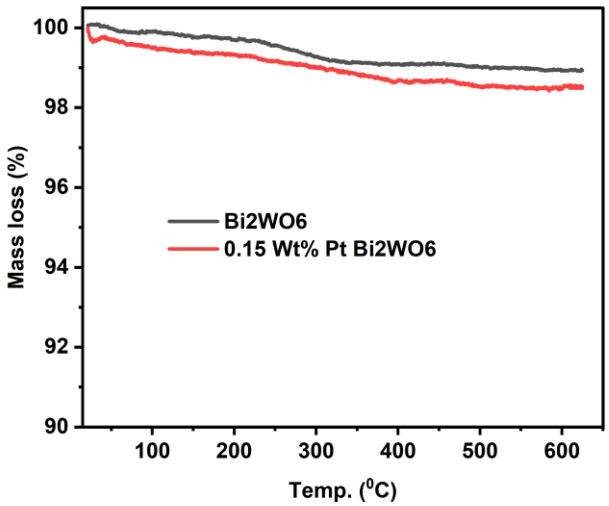

Figure 4: TGA Bi_2WO_6 and Pt/Bi_2WO_6 showing no difference in mass loss upon platinization

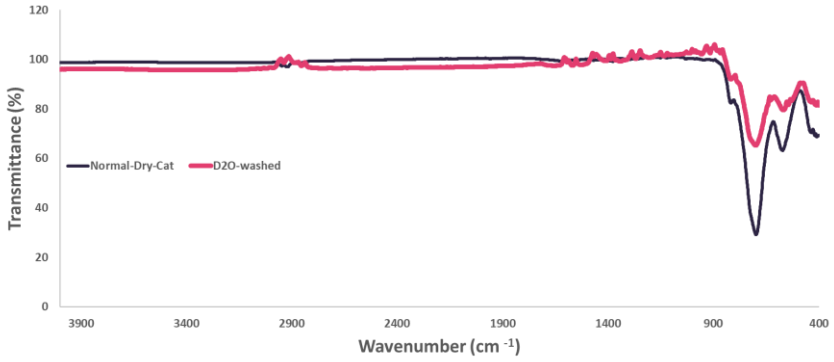

Figure 5: IR of normal and deuterated catalyst.

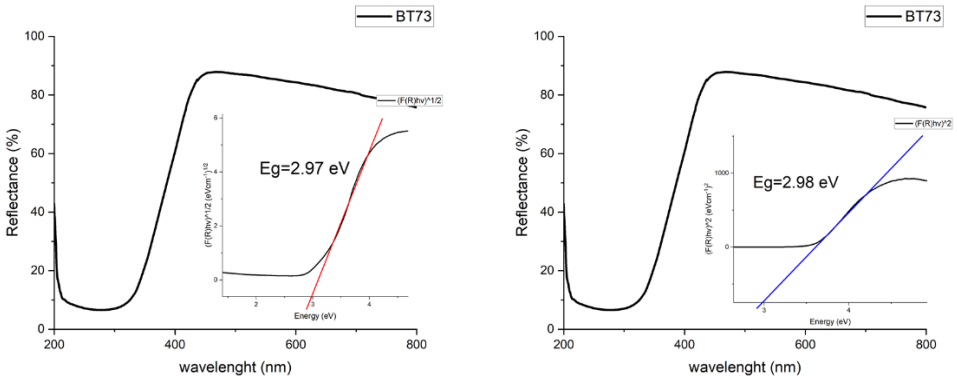

Figure 6: UV-Vis diffuse reflectance spectroscopy of Bi_2WO_6 and energy band gap value (inset) obtained using Kubelka-Munk's function and Tauc's plot where it is direct and not direct transition

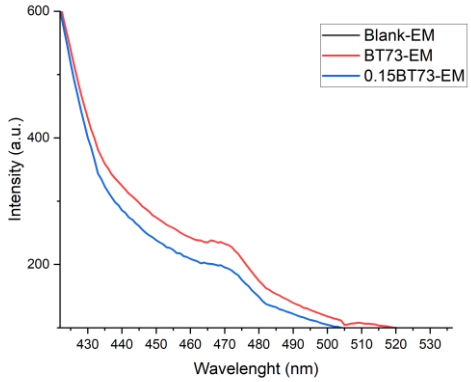

Figure 7: Photoluminescence (PL) emission mode of Bi_2WO_6 and 0.15Pt/Bi_2WO_6. excited at λ = 390 nm.

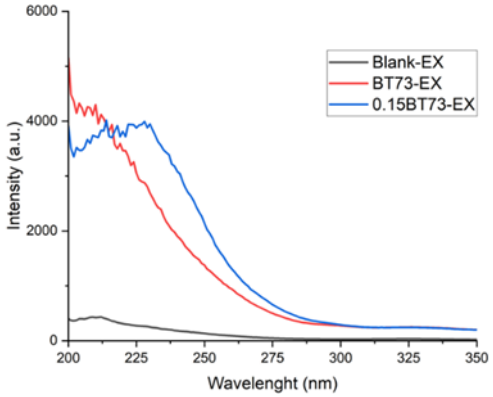

Figure 8: Photoluminescence (PL) excitation mode of Bi_2WO_6 and 0.15Pt/Bi_2WO_6. excited at λ = 390 nm, emission λ = 420 nm.

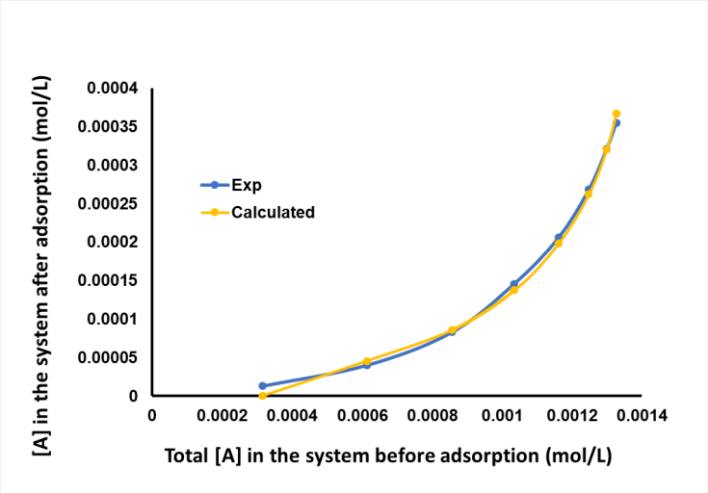

Figure 9: Binding curve with fitting of 4-methoxyphenylacetic acid with Bi_2WO_6 nanoparticles. Bi_2WO_6 (125 mg), phenylacetic acid (0.5 mM). CD_3CN (10 mL) as solvent.

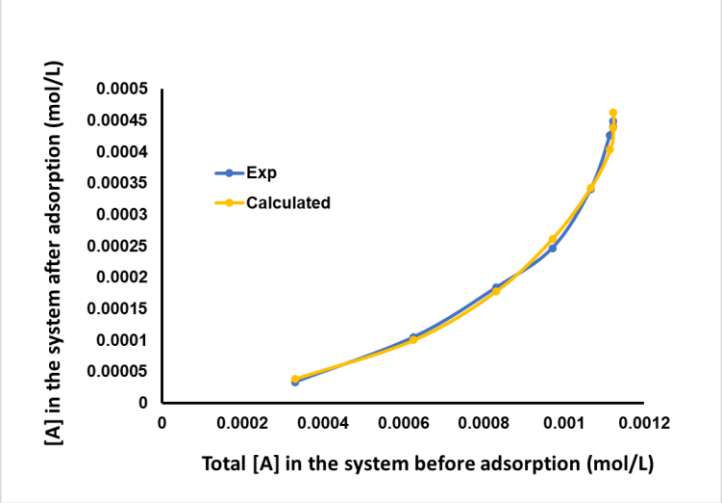

Figure 10: Binding curve with fitting of 4-chlorophenylacetic acid with Bi_2WO_6 nanoparticles. Bi2WO6 (125 mg), phenylacetic acid (0.5 mM). CD_3CN (10 mL) as solvent.

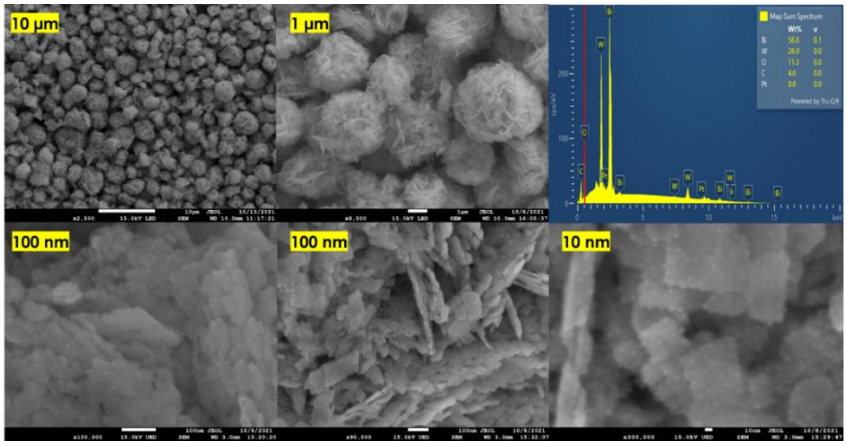

Figure 11: SEM and EDX of 0.15 Pt/Bi_2WO_6 patch no (5).

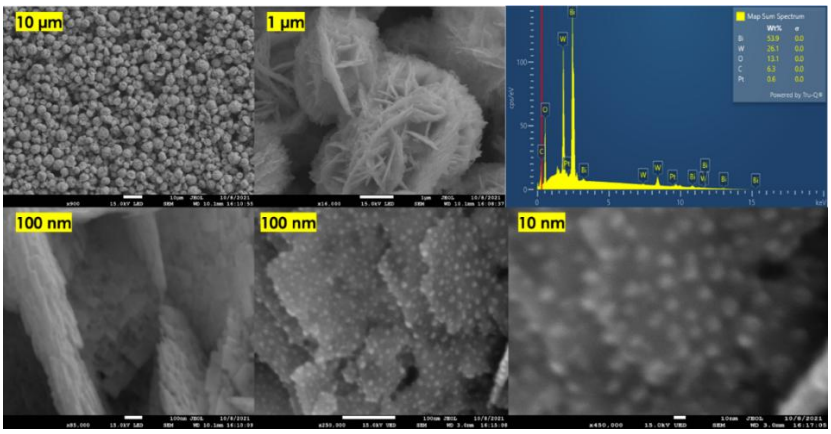

Figure 12: SEM and EDX of 0.15Pt/Bi_2WO_6 patch no (6)

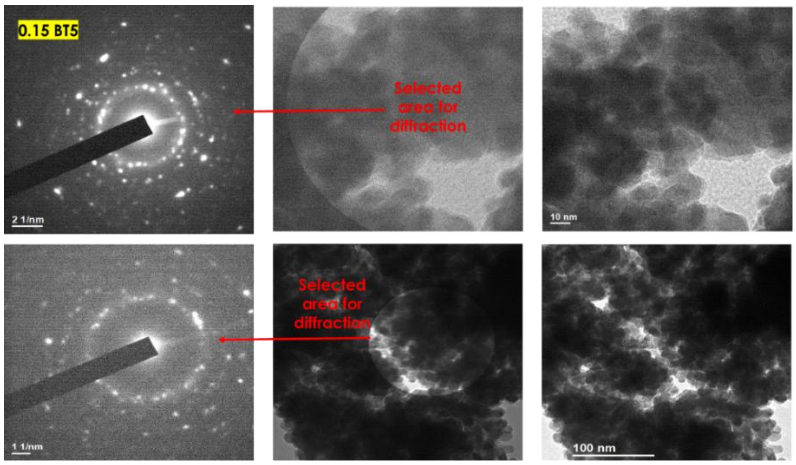

Figure 13: TEM of 0.15 Pt/Bi2WO6 (5) (BT5).

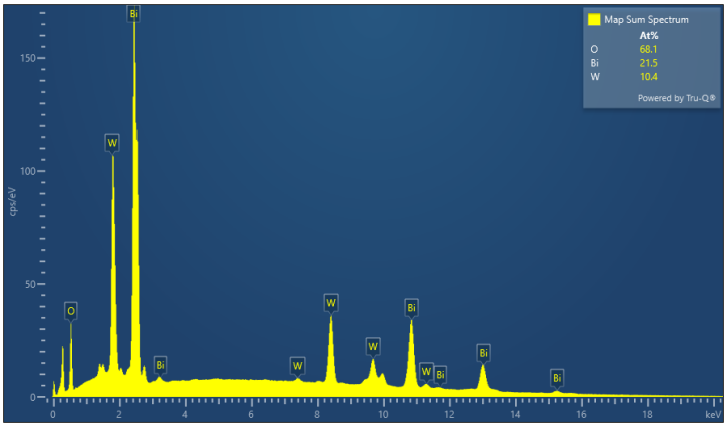

Figure 14: EDX of Bi2WO6 synthesised in EG using MW then treated hydrothermally bt50(13,15) MW + Hydro

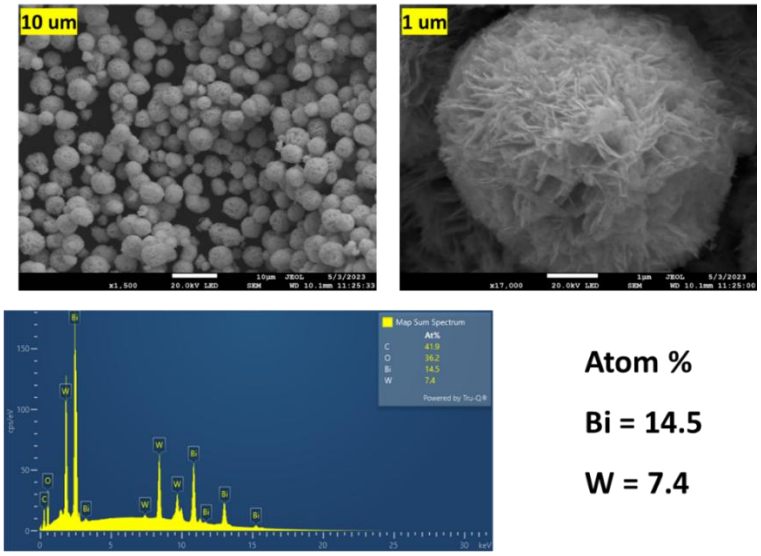

Figure 15: SEM and EDX of Bi_2WO_6 synthesised hydrothermally.

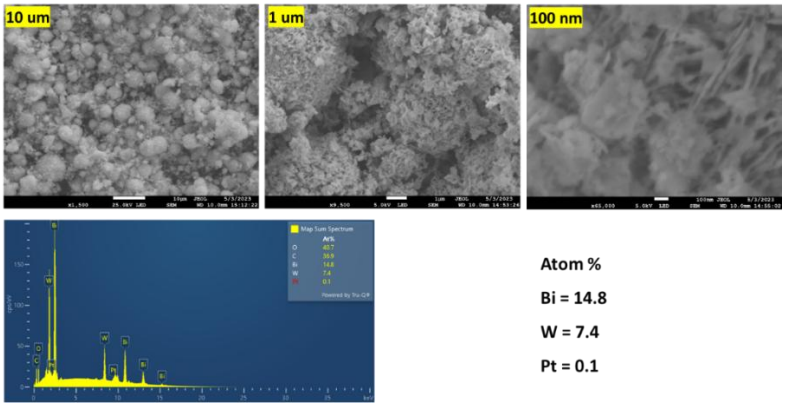

Figure 16: SEM and EDX of 0.15Pt/Bi_2WO_6 synthesised hydrothermally.

C) GC-MS

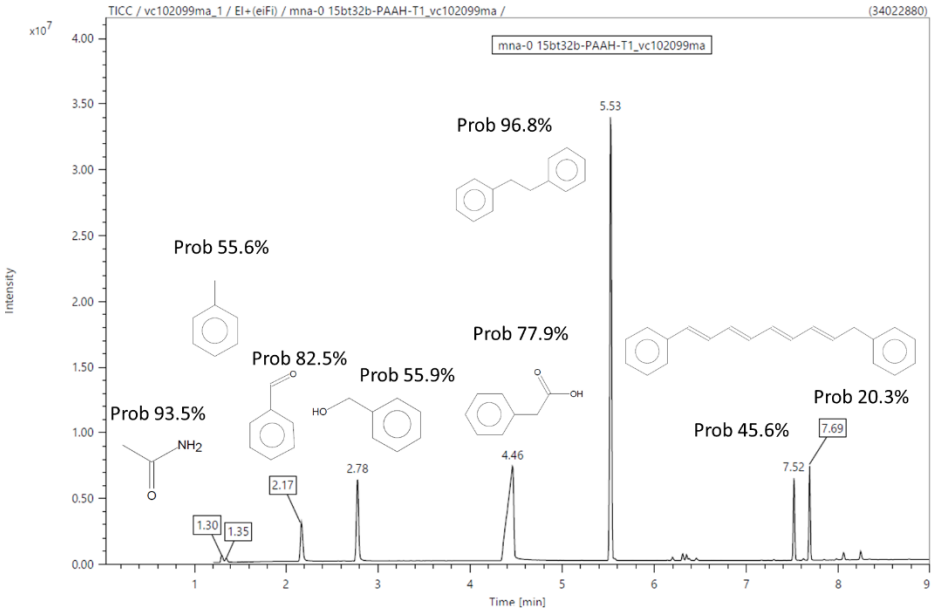

Figure 17: photo-Kolbe reaction of phenylacetic acid with platinised catalyst. BB is major product, others include benzyl alcohol, benzaldehyde. Some phenylacetic left. Reaction was performed in dry acetonitrile.

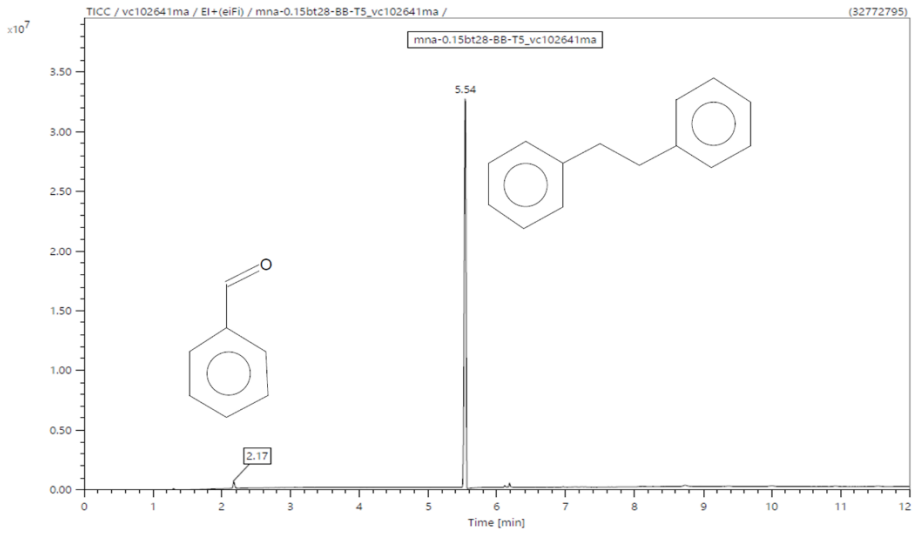

Figure 18: Reaction of BB only with platinised catalyst showing no reaction. Reaction was performed in dry acetonitrile.

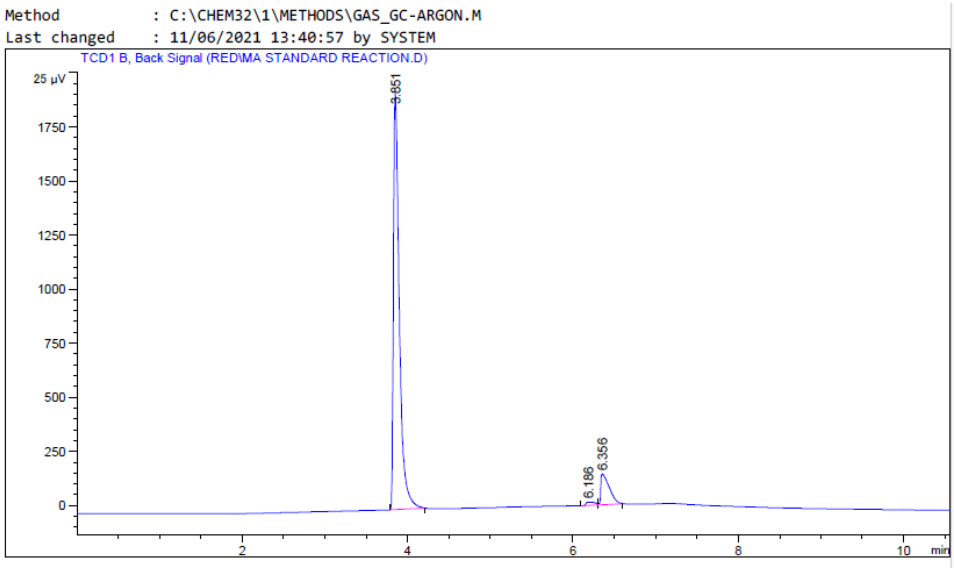

Figure 19: Gas GC chromatogram of standard Giese reaction between phenylacetic acid and methacrolein. Large peak is N_2 and the second intense peak is CO_2.

D) NMR spectrum

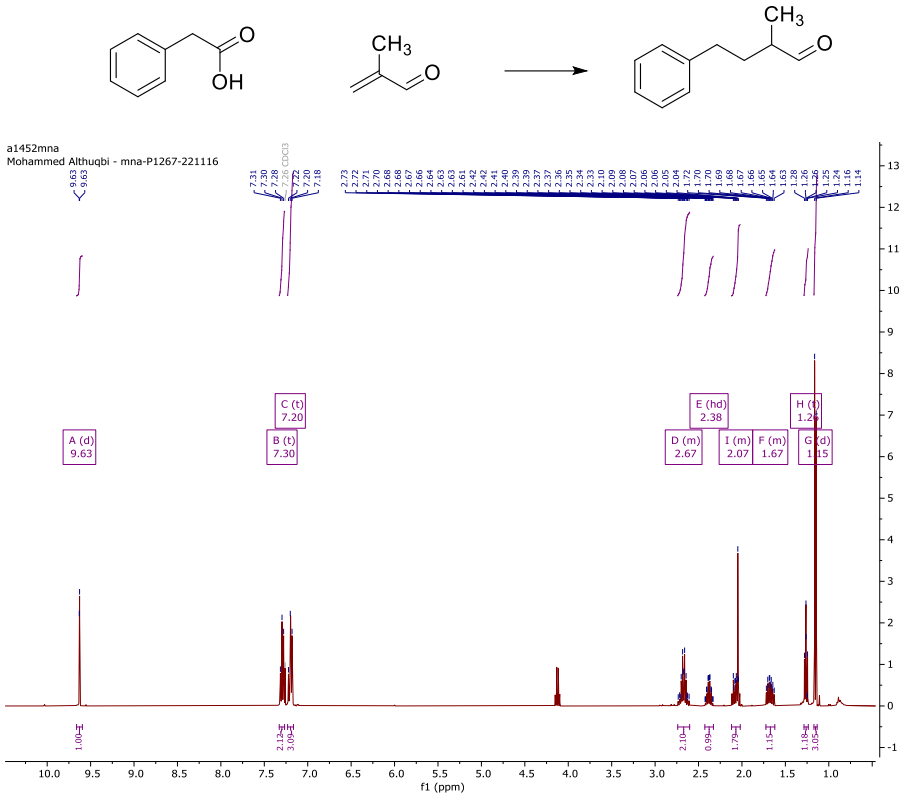

Figure 20: Giese product resulting from reaction between phenylacetic acid (PAAH) and methacrolein (MAC). (^{1}H NMR (400 MHz, CHLOROFORM-*D*) δ 9.63 (d, *J* = 1.4 Hz, 1H), 7.30 (t, *J* = 7.3 Hz, 2H), 7.20 (t, *J* = 8.2 Hz, 3H), 2.74 – 2.60 (m, 2H), 2.38 (hd, *J* = 6.9, 1.8 Hz, 1H), 2.12 – 2.02 (m, 2H), 1.72 – 1.62 (m, 1H), 1.26 (t, *J* = 7.1 Hz, 1H), 1.15 (d, *J* = 7.3 Hz, 3H).

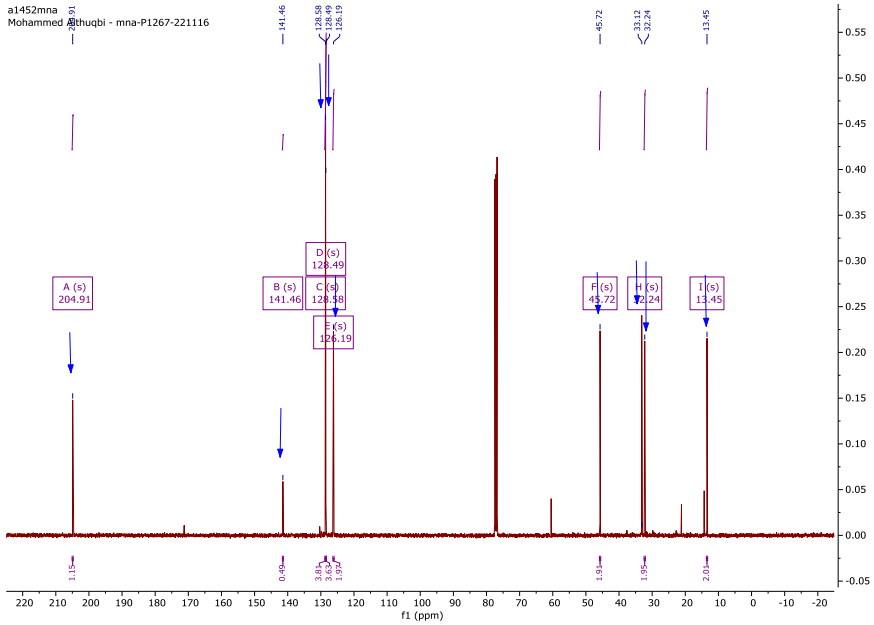

Figure 21: 13C NMR of Giese product (13C NMR (101 MHz, CHLOROFORM-D) δ 204.91, 141.46, 128.58, 128.49, 126.19, 45.72, 32.24, 13.45).

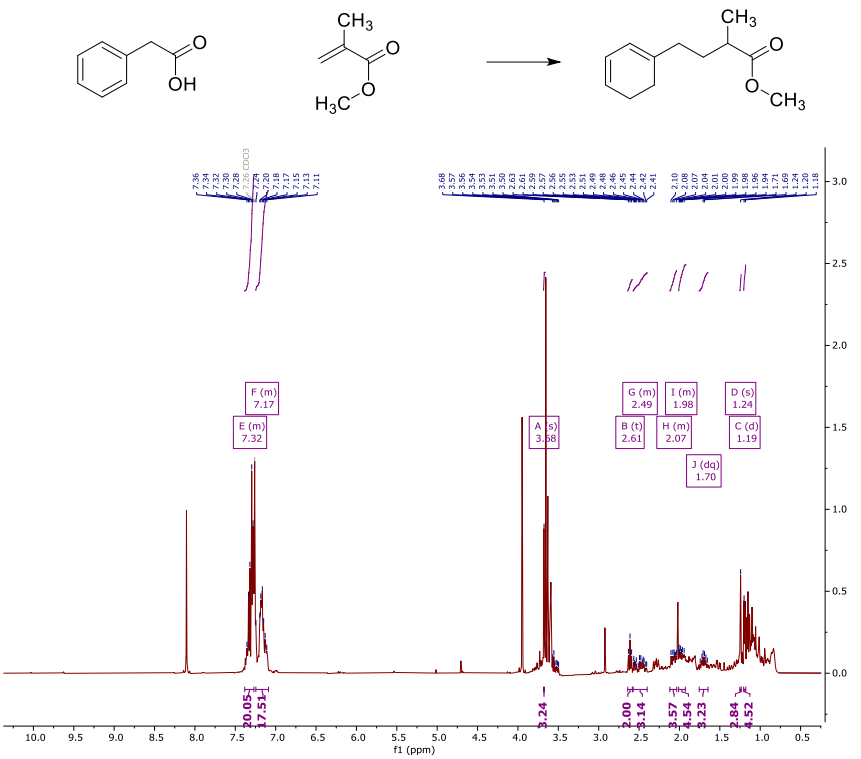

Figure 22: Reaction of PAAH with methyl methylacrylate.

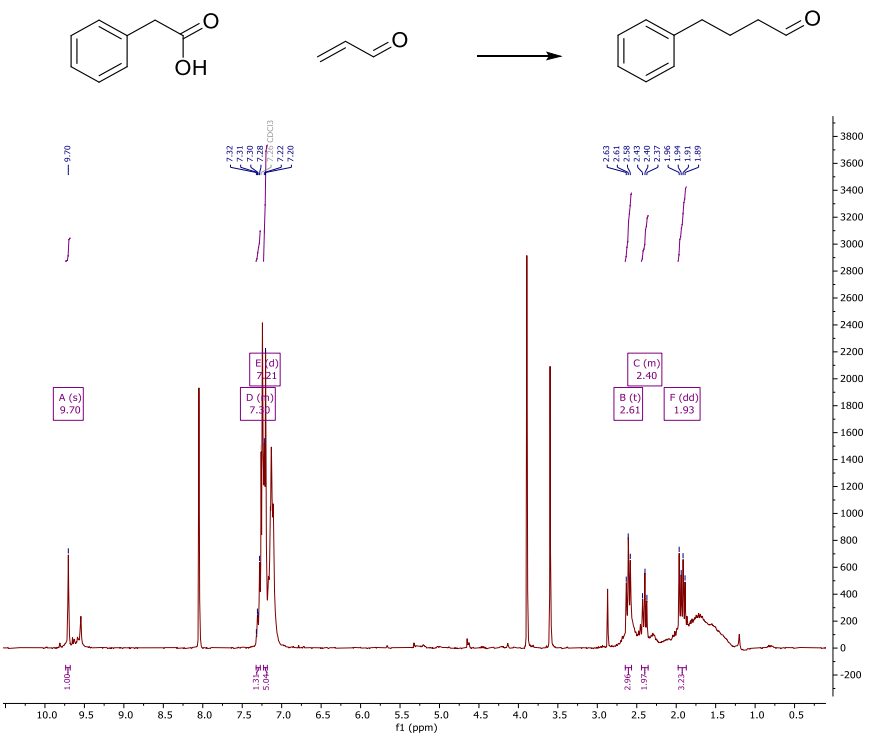

Figure 23: Reaction of PAAH with acrolein.

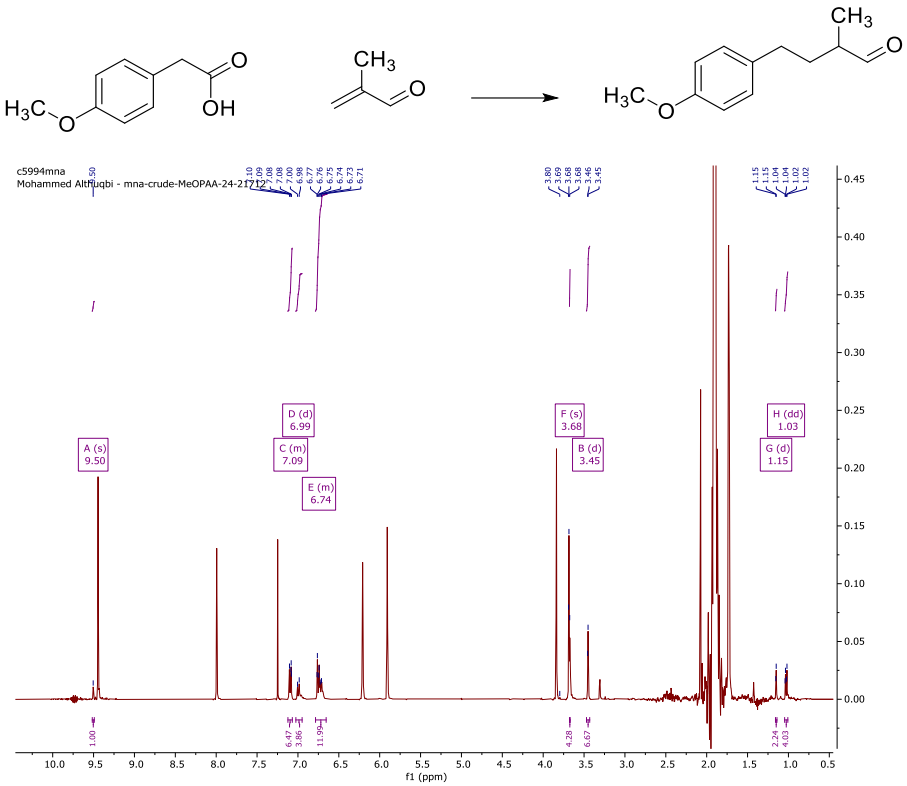

Figure 24: Reaction of 4-MeOPAAH with MAC. Crude

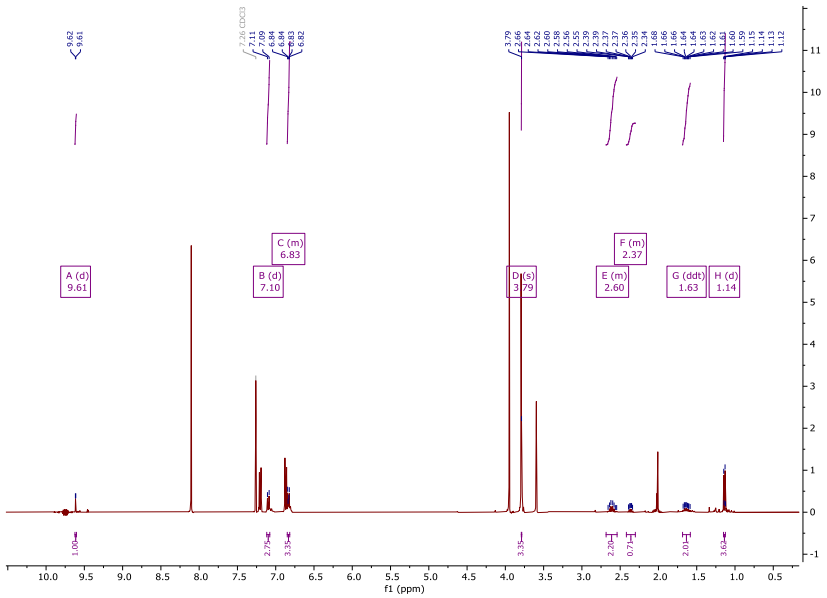

Figure 25: Reaction of 4-MeOPAAH with MAC. Rotavap

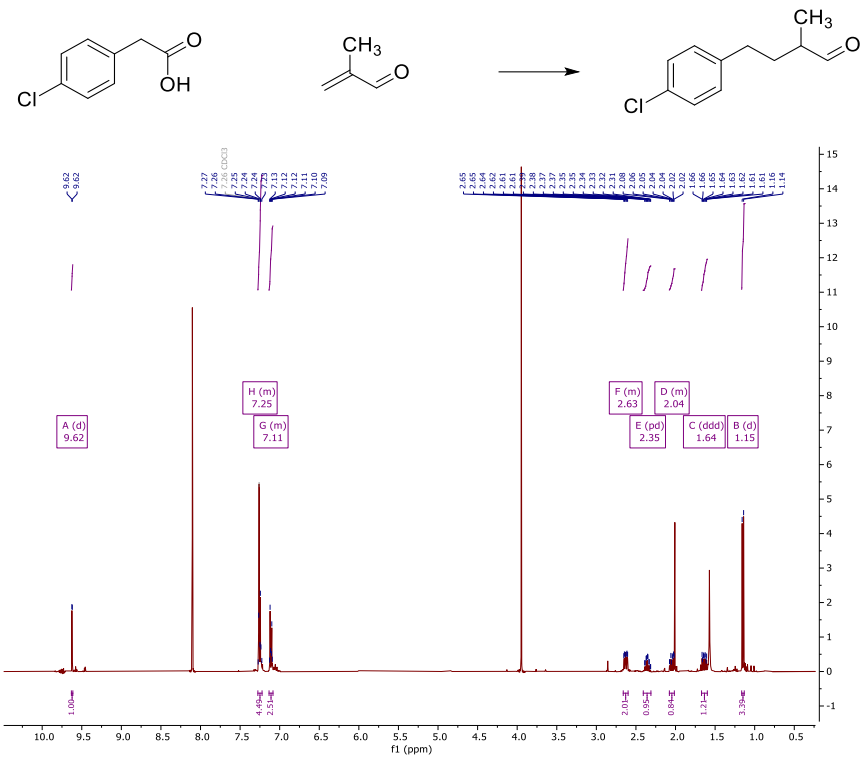

Figure 26: Reaction of 4-chloroPAAH with MAC rota.

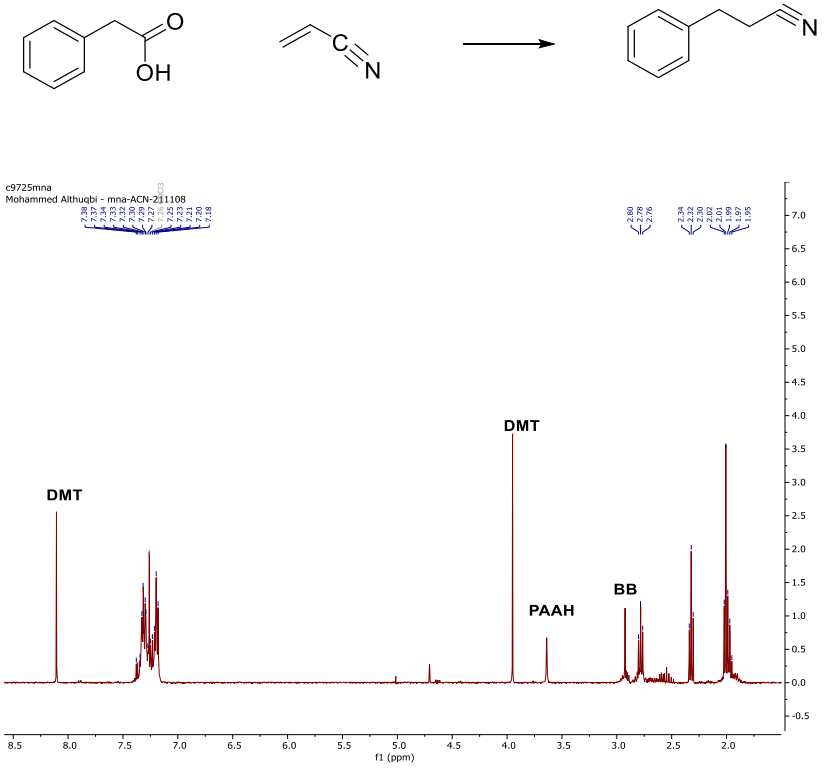

Figure 27: Reaction of PAAH with CAN. Rotavap. DMT dimethyl terephthalate, BB bibenzyl.

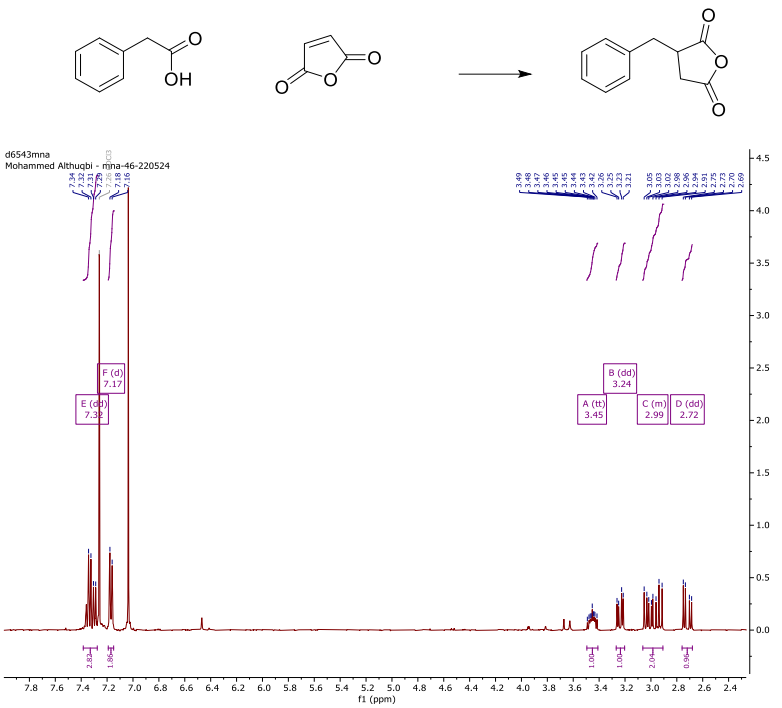

Figure 28: Reaction of PAAH and maleic anhydride (^{1}H NMR (400 MHz, CHLOROFORM-D) δ 7.32 (dd, J = 14.9, 7.1 Hz, 3H), 7.17 (d, J = 6.9 Hz, 2H), 3.45 (tt, J = 9.6, 5.7 Hz, 1H), 3.24 (dd, J = 14.2, 5.0 Hz, 1H), 3.06 – 2.91 (m, 2H), 2.72 (dd, J = 19.0, 6.6 Hz, 1H).

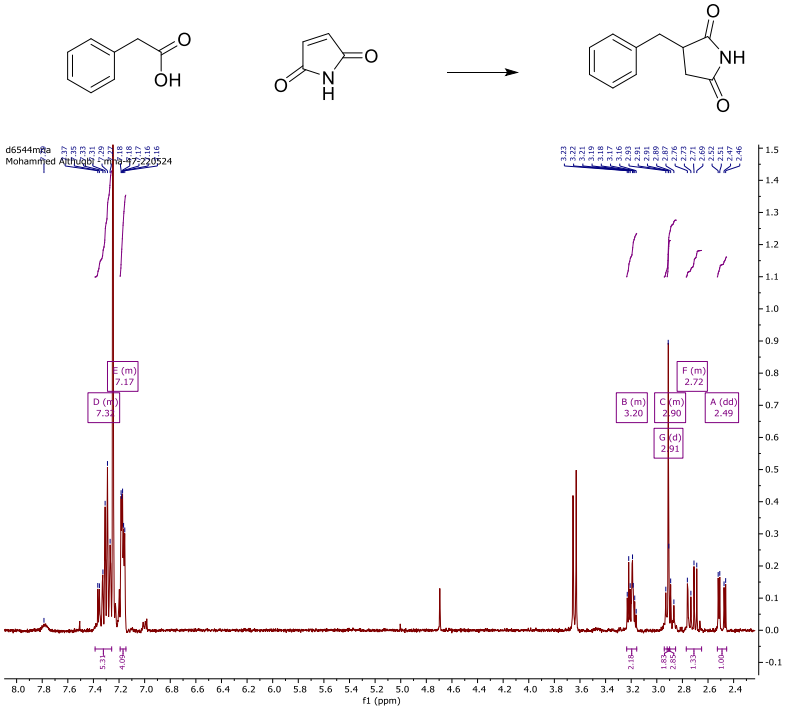

Figure 29: Reaction of PAAH with maleimide (^{1}H NMR (400 MHz, CHLOROFORM-D) δ 7.39 – 7.26 (m, 5H), 7.19 – 7.15 (m, 4H), 3.24 – 3.16 (m, 2H), 2.94 – 2.85 (m, 3H), 2.77 – 2.65 (m, 1H), 2.49 (dd, J = 18.3, 5.0 Hz, 1H).

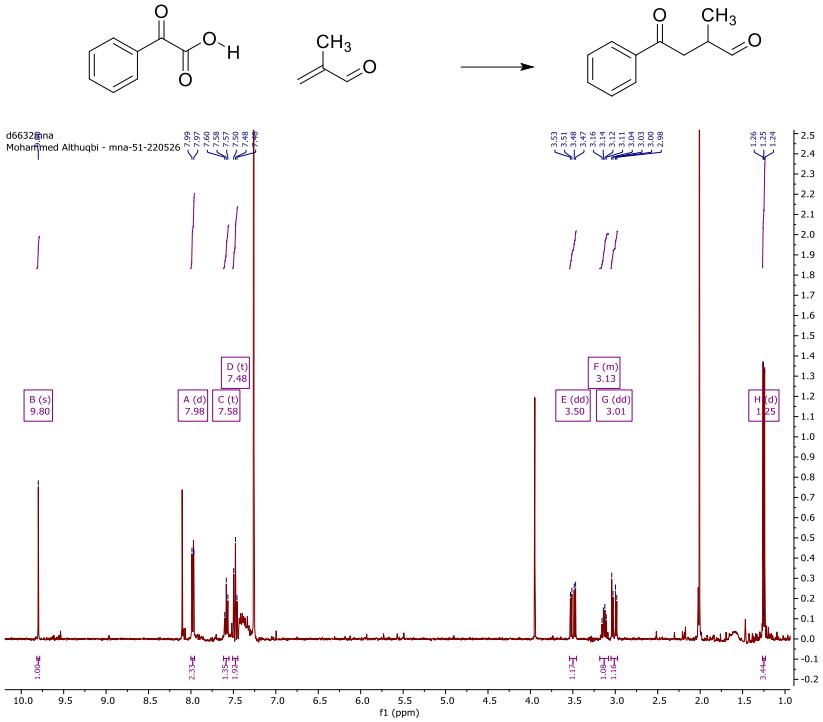

Figure 30: Reaction of *phenylglyoxylic* acid with MAC. Rotavap

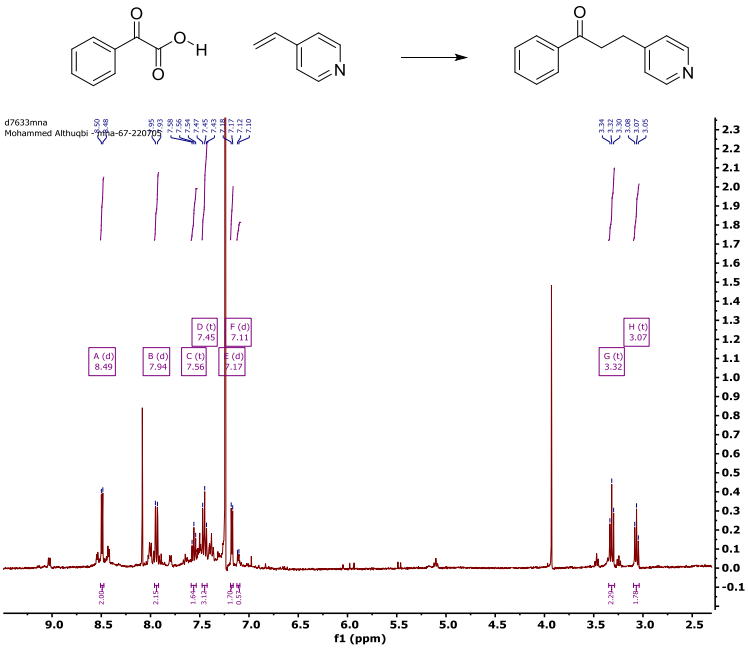

Figure 31: Reaction of *phenylglyoxylic* acid with 4-vinyl pyridine

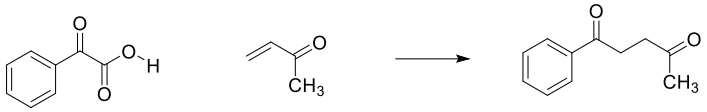

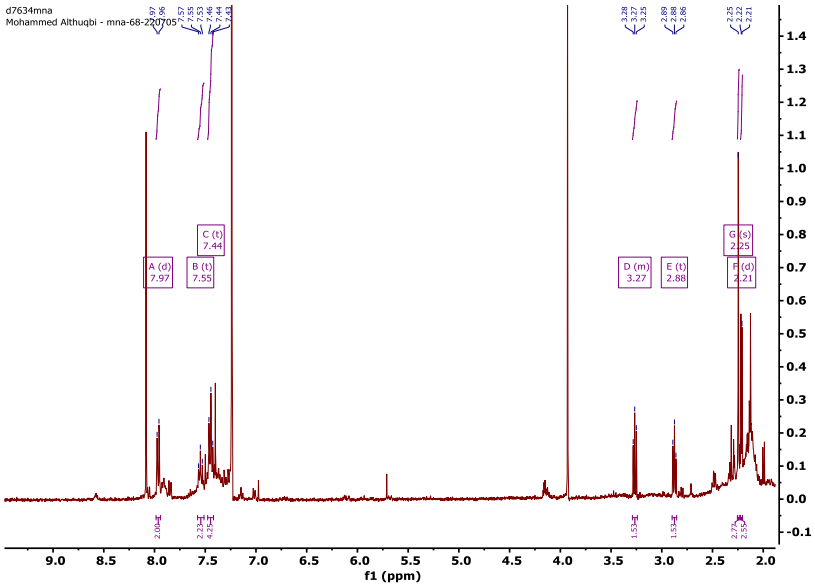

Figure 32: Reaction of *phenylglyoxylic* acid with methyl vinyl ketone

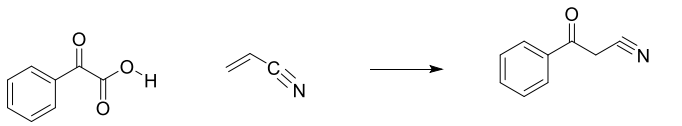

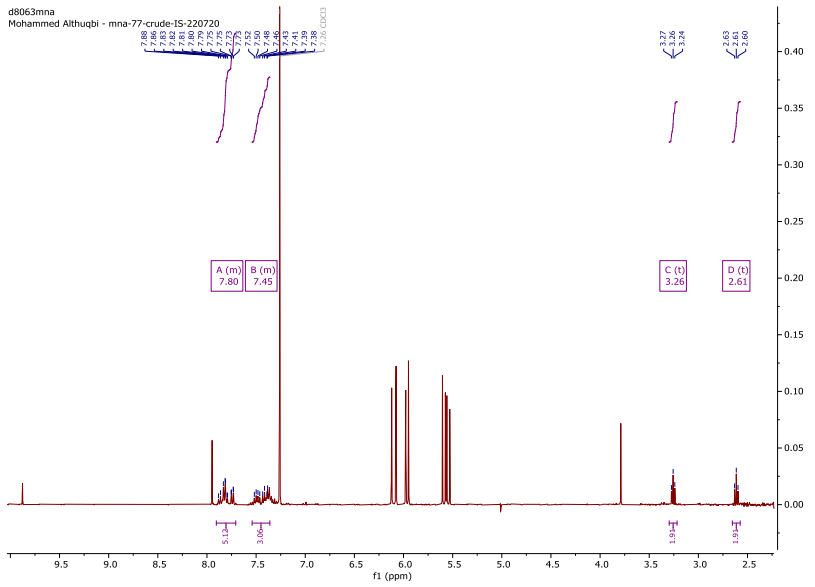

Figure 33: Reaction of *phenylglyoxylic* acid with CAN

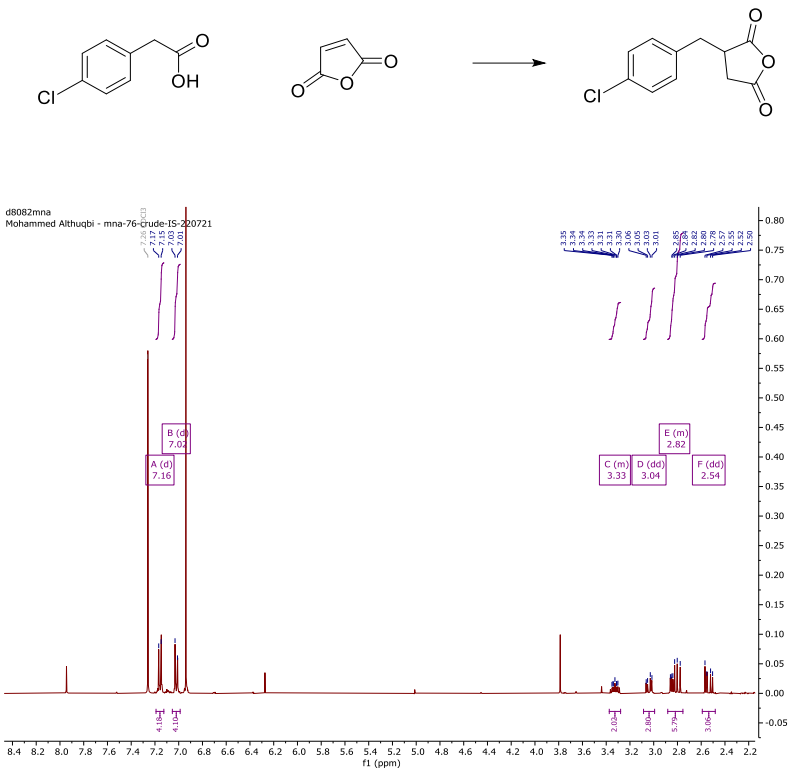

Figure 34: Reaction of 4-chloroPAAH with maleic anhydride

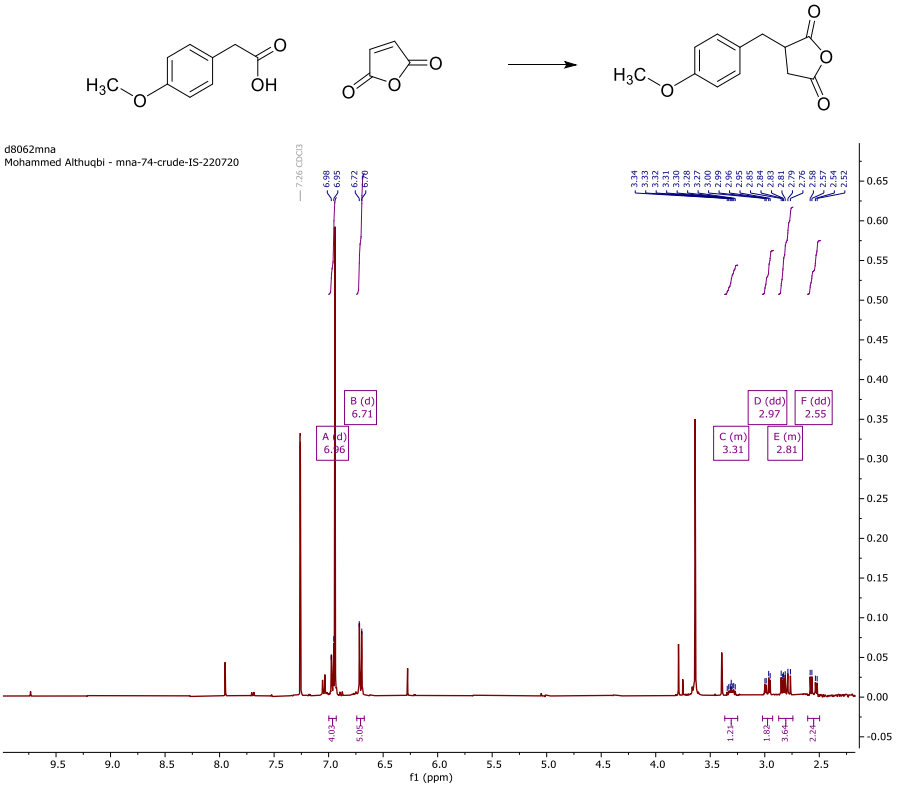

Figure 35: Reaction of 4-meoxPAAH with maleic anhydride.